VNiVERSiDAD
Ð SALAMANCA

Advanced Nanofabrication and Characterization of High-Aspect-Ratio Fresnel Zone Plates and 2D Transition Metal Dichalcogenides for Next-Generation Nanodevices

Author:
Maha Labani

Thesis Directors:

Mario Amado Montero
Giancarlo Gatti

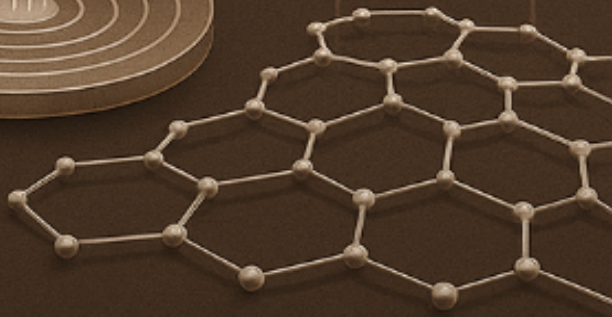

Salamanca, May 26, 2025

Acknowledgements

In every moment of doubt, there was a small faith whispering quietly to me: Continue, the road is yours. This journey was not just papers to be written, or milestones to be passed, but a mirror in which I saw my weakness and strength, my fall and rise, my fear and courage. I am here today not because the road was easy, but because my heart chose not to stop, and because I have always believed that in every darkness there is a light, waiting for those who look for it. This thesis is not only the result of a scholarly effort, but a testimony of a life that says: He who carries in his heart the belief in the light, makes a path for himself, no matter how dark it is.

I would like to express my sincere gratitude and appreciation to my esteemed supervisors, Professor Mario Amado Montero and Professor Giancarlo Gatti, for the support and guidance they have provided me throughout this research. Their supervision has played a pivotal role in refining my ideas and guiding my academic path, both through their careful observations and through the continuous encouragement they provided me during challenging moments. The combination of their expertise and profound scientific insights has been a fundamental reference for me in developing this dissertation, and I will remain grateful for their generosity of knowledge, their open-mindedness, and their belief in my ability to complete this work. It has been a pleasure to work under their guidance, and I will carry their influence with me as I continue my academic and professional journey.

Of all the stations I've been through on this academic journey, the most extraordinary and ingrained support comes from Dr. Ana Pérez Rodríguez and has left the strongest impression on me. Her involvement extended beyond academic guidance to remarkable human support, striking the right balance between academic rigor and warmth of human relationships, reason and emotion. She invested much time and effort in me, and had open arms and an open mind available to me at all times. Not merely a mentor but indeed, in earnest and careful presence, in times of struggle and doubt,

she provided the insight and assurance that allowed me to continue. She was a beacon figure at several points along this journey, moving with me in unstinting dedication, both in my study and in those moments when I needed most genuine human comfort. No matter how much I try to express my gratitude, it will remain inadequate. But I hope that these words are evidence of my sincere appreciation and respect for her, and for the valuable help she has given me.

I am very grateful to both Dr.Vito Clericò and our Research Team Head, Prof.Enrique Diez Fernández, for their huge contribution throughout the journey. Dr.Vito Clericò did a gigantic amount of work in the lab, happily guiding me through the empirical aspect of research. His guidance on teaching me to work and use various fabrication processes and lab facilities was essential in my growth. His regular availability to share his expertise played a significant role in my technical development. Likewise, I owe a lot to Prof.Enrique Diez Fernández, whose motivation and encouragement went far beyond academic advice. Sending me to different scientific conferences and research meetings was his way of opening opportunities that diversified my academic and professional lives and made a great contribution to my research development.

My father was, without a doubt, the greatest source of strength and inspiration in my life. His presence, guidance and constant support have shaped not only my academic path, but also the person I have become. He has always stood by me steadfastly and calmly, encouraging me, lifting my spirits when I stumble, and believing in me through all my doubts and difficulties. His role in my life has gone beyond that of a father; he has been a foundation, a compass, and a light in moments of confusion.

"إلى من لم يكن فقط ظلّي حين اشتدّ وهج الطريق، بل كان النور ذاته... إلى أبي، الذي كان الحضور الأعمق في لحظات ضعفي، والسند الأصدق حين خذلتني الحياة، شكرًا لأنك كنت دائمًا المعنى الأجمل لكلمة وطن."

To my wonderful husband, who has always been a source of encouragement and support in my life. In my moments of weakness, you were the one who gave me strength, and in times of sadness, you were the one who filled my heart with hope. I have spent the most beautiful days of my life with you, and you have lit up my life with joy and happiness, most notably the day we got married and the day you came to Spain to join

me. You have always been by my side, and you have been my source of strength and inspiration. I thank God for your presence in my life, and I thank him for the days that brought us together; every moment with you is a gift from destiny. I'd also like to thank my marvelous brothers, Abdou and Taha, for their encouragement and affection, which made my life full of joy and happiness. They contributed significantly to bringing joy and support into my life. I also cannot but remember my dear cousin Fatima, who was always close to my heart, with her warmth, support, and love. I dedicate my love to her two children, Maryam and Mohammed.

I cannot fail to mention my two most beautiful, affectionate, and wonderful friends, Fatna and Amina, whose presence in my life gave me a special warmth and love. I still keep in my memory the moments of our first meeting, and all the situations that brought us together during and outside academic life. The times of laughter, fun, and happiness that we shared together were some of the most beautiful things I have ever experienced. Although I don't have sisters, life has given me two sisters in every sense of the word. I thank them from the bottom of my heart for their presence, and I hope that our friendship will remain strong, eternal, and timeless.

Finally, and most importantly, I would like to express my sincere gratitude to Algeria, my country and its government, for giving me the opportunity to realize my dreams and ambitions, while simultaneously developing myself personally and academically. Their tremendous moral and financial support has been invaluable in this endeavor. I extend my sincere gratitude and respect to this country, to which I am proud to belong.

Abstract

Nanofabrication plays a crucial role in nearly every scientific field, and its importance in technology cannot be overstated. Among the various methods available, electron beam lithography (EBL) stands out as one of the most widely used techniques for creating high-resolution and high-density structures. However, the resolution, density, and aspect ratio of the resulting nanostructures are often constrained by the lithography process itself and the challenges of transferring the pattern to the underlying substrate. Additionally, an innovative method called ICP RIE etching is intended to provide fast etch rates, great selectivity, and minimal processing damage. The plasma may be kept at low pressures, which also results in excellent profile control.

The Nanotechnology group at the University of Salamanca has a long experience with EBL and ICP/RIE in the fabrication of structures on thin substrates. However, it has been a longstanding challenge to determine the optimal patterning conditions for the Fresnel zone plate, a circular diffraction-grating focusing element consisting of zones with decreasing widths for increasing radii.

This thesis starts with a theoretical background, which is divided into two sections. The first section provides a detailed presentation of the Fresnel lens, covering both theoretical information and its applications. The second part is an introduction to two-dimensional (2D) Van der Waals materials, covering their fabrication methods and give a short report on transition metal dichalcogenides (TMDs).

Moreover, an additional chapter entitled Methodology presents the instruments used in this thesis for fabrication and analysis. This includes a comprehensive description of their operation principles, definitions, and different applications. The tools covered include scanning electron microscopy (SEM), atomic force microscopy (AFM), Kelvin probe force microscopy (KPFM), profilometry, inductively coupled plasma/reactive ion etching (ICP/RIE), Raman spectroscopy, and others.

In the first part of this thesis's results, we demonstrate a novel approach combining electron beam lithography (EBL) and cryoetching to produce silicon-based FZP prototypes as a test bench to assess the strong points and limitations of this fabrication method. Through this method, we obtained FZPs with 100 zones, a diameter of 20 µm, and an outermost zone width of 50 nm, resulting in a high aspect ratio that is suitable for use across a range of photon energies. The process incorporates a chromium mask in the EBL stage, enhancing microstructure precision and mitigating pattern collapse challenges. This minimized issues of under- and over-etching, producing well-defined patterns with a nanometer-scale resolution and low roughness. The refined process thus holds promise for achieving improved optical resolution and efficiency in FZPs, making it viable for the fabrication of high-performance, nanometer-scale devices.

In the second part, this thesis explores the structural, chemical, and electronic characterization of two transition metal dichalcogenides (TMDs). In the case of MoSeTe, grown by vapor deposition, we performed thorough analyses via Raman spectroscopy, profilometry, and scanning electron microscopy (SEM) before and after a successful exfoliation and transfer onto SiO_2 substrates.

For ReS_2, known for its 1T' crystal structure and remarkably low interlayer coupling, we exfoliated and transferred flakes of varying thicknesses and stacking configurations (AA or AB) onto different substrates. Raman spectroscopy confirmed the number of layers and stacking modes by analyzing frequency shifts of characteristic vibration peaks. Atomic force microscopy (AFM) validated thicknesses and corroborated the Raman findings. Kelvin probe force microscopy (KPFM) studies revealed distinct, domain-like electrostatic contrasts unrelated to topography or thickness alone, suggesting that sliding ferroelectricity, strain, or domain boundary effects can induce pronounced surface-potential modulations. Temperature dependent measurements indicated that thermally activated processes can irreversibly modify these domains. Correlative ultraviolet photoemission electron microscopy (UVPEEM) further supported the presence of domain-dependent work-function variations in ReS_2, emphasizing its inherent electronic inhomogeneity.

Resumen

La nanofabricación desempeña un papel fundamental en casi todos los campos científicos y su importancia para la tecnología no puede subestimarse. Entre los distintos métodos disponibles, la litografía con haz de electrones (EBL, por sus siglas en inglés) destaca como una de las técnicas más utilizadas para crear estructuras con alta resolución y alta densidad. Sin embargo, la resolución, la densidad y la relación de aspecto de las nanofabricaciones resultantes a menudo se ven limitadas por el propio proceso de litografía y por las dificultades inherentes a la transferencia del patrón al sustrato subyacente. Además, existe un método innovador llamado grabado ICP/RIE, diseñado para ofrecer altas velocidades de grabado, gran selectividad y daños mínimos en el proceso. El uso de presiones bajas en el plasma también proporciona un excelente control del perfil.

El grupo de Nanotecnología de la Universidad de Salamanca cuenta con una larga trayectoria en el uso de EBL e ICP/RIE para la fabricación de estructuras en sustratos delgados. Sin embargo, aún constituye un desafío duradero determinar las condiciones óptimas de patrón para la placa de zonas de Fresnel, un elemento de difracción circular con zonas de anchura decreciente a medida que aumenta el radio, y que se emplea como dispositivo de enfoque.

Esta tesis comienza con un contexto teórico dividido en dos secciones. En la primera sección se presenta en detalle la lente de Fresnel, abarcando la información teórica y sus aplicaciones. En la segunda parte se introducen los materiales bidimensionales (2D) de van der Waals, explicando sus métodos de fabricación y ofreciendo un breve panorama de los dicalcogenuros de metales de transición (TMDs).

Asimismo, se incluye un capítulo adicional, titulado “Metodología”, donde se describen los instrumentos utilizados en esta tesis para la fabricación y el análisis. Aquí se ofrece una descripción completa de sus principios de funcionamiento, definiciones y diversas aplicaciones. Entre las herramientas mencionadas se encuentran la microscopía

electrónica de barrido (SEM), la microscopía de fuerza atómica (AFM), la microscopía de fuerza Kelvin (KPFM), la perfilometría, el grabado con plasma acoplado inductivamente y grabado por iones reactivos (ICP/RIE), la espectroscopía Raman, entre otras.

En la primera parte de los resultados de esta tesis, se presenta una aproximación novedosa que combina la litografía con haz de electrones (EBL) y el grabado a bajas temperaturas (cryoetching) para producir prototipos de placas de zonas de Fresnel (FZP) de silicio, concebidos como banco de pruebas a fin de evaluar las ventajas y los límites de este método de fabricación. Mediante este método, se obtuvieron FZP con 100 zonas, un diámetro de 20 m y una zona más externa de 50 nm de anchura, lo que da lugar a una alta relación de aspecto adecuada para un amplio rango de energías de fotones. El proceso incorpora una máscara de cromo en la etapa de EBL, lo que mejora la precisión de la microestructura y mitiga problemas de colapso de patrones. Esto reduce los inconvenientes de subgrabado y sobregrabado, generando patrones bien definidos con resolución a escala nanométrica y baja rugosidad. El proceso refinado muestra un gran potencial para lograr mejoras en la resolución y la eficiencia óptica de las FZP, haciendo factible la fabricación de dispositivos de alto rendimiento a escala nanométrica.

En la segunda parte, esta tesis profundiza en la caracterización estructural, química y electrónica de dos dicalcogenuros de metales de transición (TMDs). En el caso de MoSeTe, obtenido mediante deposición en fase de vapor, se llevaron a cabo análisis exhaustivos de espectroscopía Raman, perfilometría y microscopía electrónica de barrido (SEM) antes y después de una exfoliación y transferencia exitosas sobre sustratos de SiO_2.

Por otro lado, en el caso de ReS_2 —caracterizado por su estructura cristalina 1T' y por la notablemente débil interacción entre capas— se exfoliaron y transfirieron láminas de espesores y configuraciones de apilamiento variables (AA o AB) sobre diferentes sustratos. A través de espectroscopía Raman se confirmó el número de capas y los modos de apilamiento, analizando los desplazamientos de frecuencia de los picos de vibración característicos. La microscopía de fuerza atómica (AFM) validó los espesores y corroboró los hallazgos de Raman. Estudios de microscopía de fuerza Kelvin (KPFM)

revelaron diferencias electrostáticas en forma de dominios que no están vinculadas ni a la topografía ni al espesor, lo que sugiere que la ferroelectricidad por deslizamiento, la deformación o los límites de dominio pueden generar modulaciones pronunciadas en el potencial de superficie. Experimentos con dependencia de temperatura mostraron que dichos dominios pueden modificarse de forma irreversible mediante procesos activados térmicamente. Observaciones complementarias mediante microscopía de fotoemisión ultravioleta (UVPEEM) apoyaron la existencia de variaciones dependientes de dominios en la función de trabajo de ReS_2, subrayando así su naturaleza electrónicamente heterogénea.

Contents

1 | Motivation

In recent years, photovoltaic power generation has undergone a significant transformation. This change is driven by remarkable progress in commercial high-efficiency multi-junction solar cells achieving 40% conversion efficiency, combined with advancements in optical design for solar concentrators that can deliver flux levels ranging from hundreds to thousands of suns with high collective efficiency. A solar concentrator system utilizes lenses, reflectors, or a combination of both, along with a tracking mechanism, to focus sunlight from a large area into a concentrated beam. Unlike heat receivers, concentrator photovoltaic (CPV) panels are more sensitive to the distribution of focused sunlight. As a result, they require an optimized optical design to ensure the concentrated sunlight is evenly distributed across the receiver's surface.

The development of electron storage rings dedicated solely to producing synchrotron radiation has been a major factor in the advancement of X-ray optics. New optical components are needed to fully utilize the unique properties of this light, which can uncover the secrets of matter and reveal the microscopic world. Synchrotron light's potential went beyond theoretical predictions; it turned out to enable many experiments that increased the understanding in different scientific domains. With the passage of time, synchrotron radiation sources have developed into important instruments for specialists in almost all branches of science, such as biology, chemistry, physics, material science, and even archaeology.

X-ray microscopy is a nondestructive method that creates an image of the internal characteristics of the materials under examination. The contrast of the image is based on how differently the various materials' constituents absorb X-rays. The first X-ray microscope was developed in the late 1940s.It has become a method for observing structures that are not possible to view with traditional optical microscopy. It offers advantages over electron microscopy because of the x-ray radiation's longer penetration depth and chemical sensitivity.

The optics of the x-ray microscopes, synchrotrons, and concentrator photovoltaics include components such as the Fresnel zone plate lenses, which are made by means of

microfabrication techniques.

Only a handful of research groups worldwide are focused on developing diffractive optical elements for X-ray radiation. Fresnel zone plate lenses, in particular, are expensive and have limited commercial availability. Additionally, their lifespan in an operational X-ray microscope is relatively short. Producing these lenses in-house is often challenging, as it requires access to a micro- and nanofabrication laboratory and specialized expertise in diffractive optical elements.

The primary objective of this thesis is to present the initial efforts toward in-house production of a Fresnel zone plate (FZP) prototype in our lab, highlighting both the strengths and limitations of the fabrication process. The manufacturing of FZPs involves significant challenges, primarily due to the need for extreme precision and control. Achieving nanometer-scale resolution, essential for advanced applications, requires the fabrication of lenses with sharp and smooth edges. Furthermore, the process demands meticulous control over the full 3D structure of the device, spanning transverse sizes of tens of micrometers and thicknesses at the micrometer scale.

Secondly, two-dimensional (2D) materials have triggered a wave of innovation in electronics, spintronics, and optoelectronics. Among 2D materials, Transition Metal Dichalcogenides (TMDs) have attracted a lot of attention. TMDs such as MoSeTe or ReS_2 display a wide range of unique properties—tunable bandgaps, reduced dimensionality, strong spin–orbit coupling, and exotic excitonic phenomena— make them promising materials for next-generation devices such as sensors, solar cells, batteries... However, there are several open questions, mainly related to their behaviour at the nanoscale. In particular, subtle modifications in thickness, crystallographic stacking, or defect concentration can drastically alter a TMD's electrical and optical behavior.Studying these parameters and understanding the microscopic origin of their distinctive phenomena, such as sliding ferroelectricity in ReS_2, requires a broad set of characterization tools that can provide a correlated characterization reveal the phenomena occuring at the nanoscale.

2 | Introduction

2.1 | Fresnel zone plates theoretical background

2.1.1 | Diffraction theory

The key concept in science behind microscopy and optics is diffraction, which describes the rearrangement of the path for the propagation of the wave when it encounters an aperture or an obstacle [1]. Light diffraction happens when light waves hit obstacles or pass through small openings [2, 3]. The scattering and bending of light rays cause patterns of interference and the spreading out of light. This phenomenon plays a critical role in various practical applications, from analyzing small structures under a microscope to measuring light spectra, as well as in common observations like the colorful display of clouds overhead [4–7]. Interference is a phenomenon that occurs with all types of waves, not just light. It happens when a waveform passes through a slit or around barriers and consequently spreads. This can also be observed in the case of sound waves [8], water waves [9] and particles of sizes comparable to the wavelength of the wave [10, 11]. The degree of bending is influenced by the wavelength relative to the size of the opening. Extensive bending occurs when the aperture's width is close to the wavelength of the wave passing through it [12]. Moreover, a diffraction pattern can be produced when light waves interfere with each other as they go through an aperture or obstruction [13].

When light travels through a uniform medium, ray optics assumes it moves in a fixed direction in a straight line. It changes direction when it encounters the surface of a different medium or if the medium's optical characteristics are nonuniform in space or time. According to the ray approximation, light moving through a homogeneous medium will follow a path that is straight and perpendicular to the wavefronts, as depicted in Figure 2.1.a . There are three possible outcomes if the wave reaches a barrier with a circular opening in it. The outcome depends on the width of the slit in

relation to the wavelength of the light and wave. If the slit diameter is larger than the wavelength, as seen in Figure 2.1.b ,the ray approximation is correct because the wave that emerges from the aperture continues to move straight forward (with the exception of a few minor edge effects). If the diameter of the opening is on the order of the wavelength, the waves radiate forth from the aperture in all directions as shown in Figure 2.1c. This is known as the diffraction effect. Lastly, as seen in Figure 2.1.d , if the aperture is significantly smaller it may be roughly represented as a point source of waves; when waves come into contact with an opaque object of size d, similar results are observed [14].

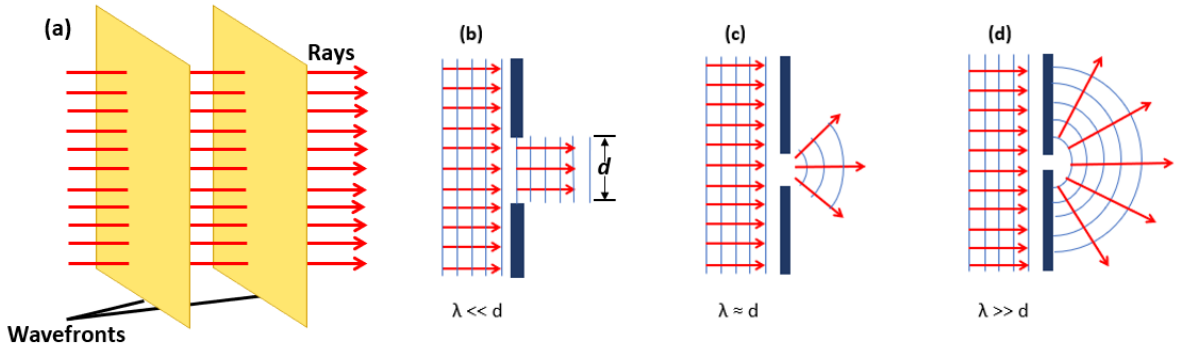

Figure 2.1: (a) A plane wave propagating to the right. (b) A plane wave of wavelength λ strikes on a barrier in which there is an opening of diameter d. The rays maintain their linear trajectory and the ray approximation is true when $\lambda \ll d$. (c) The rays spread out after entering the aperture when $\lambda \approx d$. (d) The opening acts as a point source that emits spherical waves when $\lambda \gg d$.

As seen above, light spreads out in all forward directions after passing through a slit if its wavelength is equal to or greater than the slit's width, This is known as the diffraction phenomenon. It is reasonable to assume that light traveling via a small aperture would only produce a wide area of light on a screen since light disperses. Conversely, Diffraction patterns are seen, resembling the interference patterns in some ways, with bright and dark sections. Figure 2.2.a depicts the diffraction pattern that light can create when placing an opening or slit between a screen and a light source or laser beam. The pattern is made up of a broad, bright central band known as the central maximum, which is surrounded by a number of smaller, less intense side bands known as secondary maxima or side maxima, as well as a number of dark bands known as minima that appear in between [15]. A pattern of light diffraction related to light

traveling by an object's edge is seen in Figure 2.2.b. Once more, we observe fringes that are both bright and black, evoking memories of an interference pattern.

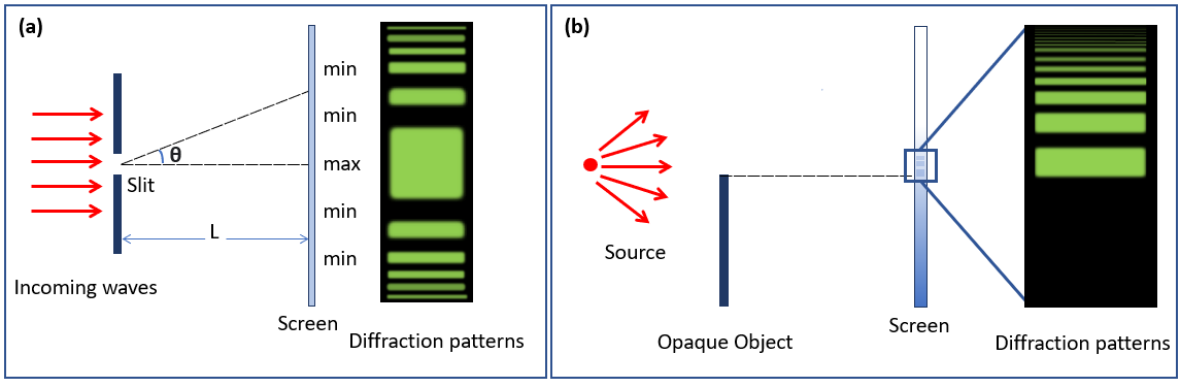

Figure 2.2: **(a)** Patterns that arise from light passing through a slit. This pattern features a brilliant fringe in the center, bordered by somewhat weaker maxima that alternate with dark fringes. **(b)** the outcome of light coming through a little source, passing through an untransparent object, and emerging onto a screen. The area above the object's edge on the screen displays a diffraction pattern made up of light and dark fringes.

2.1.2 | Fresnel and Fraunhofer Diffraction

Fresnel diffraction and Fraunhofer diffraction are two general types of diffraction phenomena. Fraunhofer diffraction refers to diffraction patterns where the light source and the screen displaying the pattern are both situated at an infinite distance from the aperture producing the diffraction. On the other hand, Fresnel diffraction refers to diffraction patterns observed when either the source or the screen, or both, are at finite distances from the aperture [16].

The main differences between Fraunhofer and Fresnel diffraction are enumerated in the following:

- **Source and Screen Distance:** In Fresnel diffraction, the source and screen are at a finite distance from the obstruction/hole It's known as **near-field diffraction**, while in Fraunhofer diffraction both the source and the screen are at an infinite distance from the obstruction/hole and this known as **far-field diffraction**[17].

- **Wave Front:** A spherical or cylindrical wave front strikes the obstruction or aperture during Fresnel diffraction. Conversely to this, a plane wavefront strikes the obstruction or aperture in Fraunhofer diffraction[18].

- **Central spot:** In Fresnel diffraction patterns the central spot is either dark or bright however, in Fraunhofer the central spot is usually bright [19].

- **Intensity:** In the Fresnel case, the intensity of consecutive maximas drops gradually as the order grows, whereas in the Fraunhofer case, the intensity reduces suddenly as the order increases [17].

- **Shape of patterns:** In the Fraunhofer class, the wavefront is planar and the diffraction pattern is not significantly affected by the distance from the aperture. However, in the Fresnel class, the diffraction pattern is more dependent on the distances between the source, aperture, and screen, since the wavefront is diverging [20].

2.1.3 | Huygens-Fresnel Theory

Without the advantage of Maxwell's equations to support them, Huygens and Fresnel developed an intuitive explanation of wave motion.The Huygens-Fresnel theory states that every point on a wavefront acts as a source of *secondary* waves. As the wavefront propagates through a medium, the sum of these secondary waves forms the new wavefront. This principle helps explain phenomena such as diffraction and interference (see Fig.2.3). Therefore, if one knows the surface that describes the wavefront at a given time, we can determine its new position shortly thereafter by considering each point on the previous wavefront [15]. The sequential "*emissions*" of these secondary waves provide a clear explanation for the propagation of spherical and plane waves. Every secondary wave has a phase associated with it, based on how far it has progressed from its starting place. Moreover, the phases of all secondary waves that reach a spot at any given instant in time indicate the state of vibration in the medium at that place.

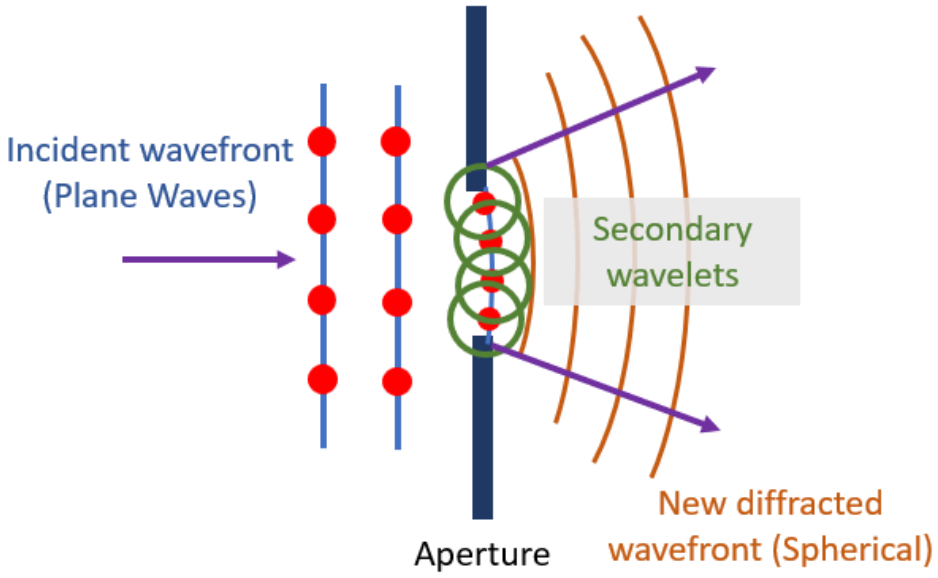

Figure 2.3: Huygens' Principle where every point on a wavefront acts as a source of secondary waves and As the wavefront propagates through a medium, the sum of these secondary waves forms the new wavefront

Using these concepts, Augustine Jean Fresnel explained in 1815 how a wave is obstructed from passing through an aperture in a screen, causing diffraction. Secondary waves are generated from various points on the aperture determine how the wavefront moves into the diffraction area. The overall wave disturbance in the diffraction area is the result of summing the effects of these secondary waves at each point [21].

A spherical wavefront's disturbance at a given position can be expressed using the wave equation $Ae^{\frac{ikr1}{r1}}$ where k is the wave vector. A describes the amplitude of the spherical wavelet at point **S**. According to the Huygens-Fresnel principle, the disturbance contribution dU(**P**) at a position **P** caused by the element dS is written as Eq.2.1 [21, 22]:

$$dU(P) = K(X) \cdot \frac{Ae^{ikr1}}{r1} \frac{e^{ikr2}}{r2} dS \tag{2.1}$$

where r_1 is the distance from the source point **S** to the wavefront, and r_2 is the distance from that wavefront to the observation point **P**, see Figure 2.4. $\mathbf{K(x)}$ is an inclination factor that indicates how the secondary wave's propagation direction affects

its amplitude. The angle between the main wavefront's normal and the secondary wavefront's normal is represented by the variable **x**.

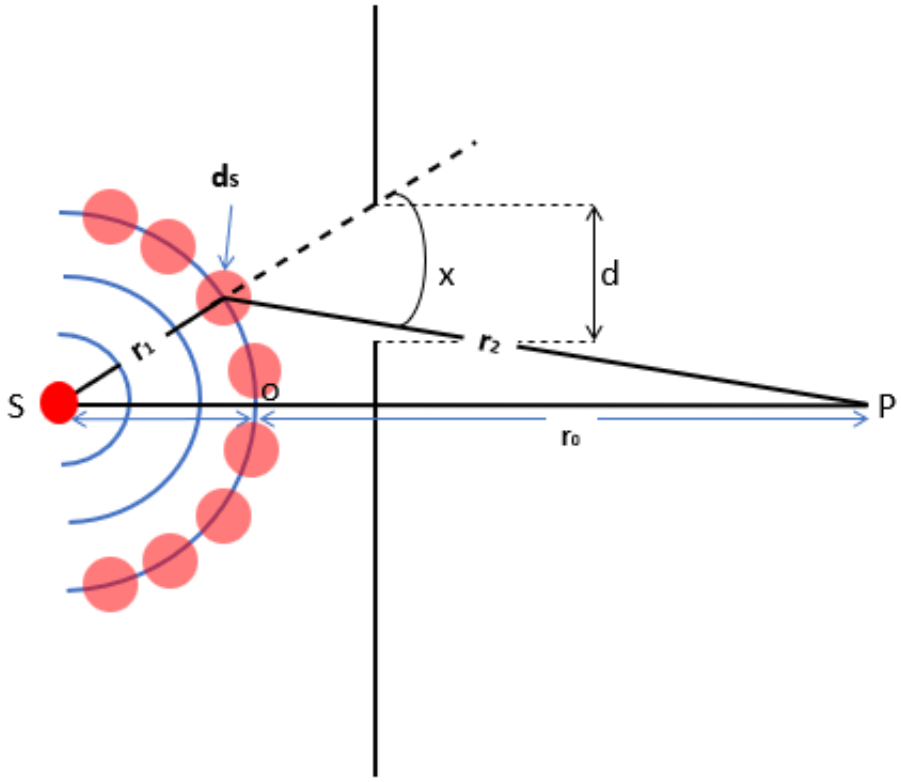

Figure 2.4: Illustration of geometric configuration for Fresnel calculation. Every point on the wavefront may be thought of as a source of spherical wavelets, However, the amplitude of the secondary wavelets decreases as the angle of departure from the primary wavelets' direction increases. The portion of the wave that is not blocked by aperture **d** adds to the disruption at point **P**.

Kirchhoff succeeded in giving an explicit equation for **K(x)** [23]:

$$K(X) = \frac{1}{2\lambda}(1 + \cos(X)) \tag{2.2}$$

K(X) has a high value in the initial propagation direction **(X=0)**, according to Eq.2.2, and it rapidly drops as **X** increases toward $\pi/2$. It illustrates the fact that the secondary spherical waves don't move backward.

Furthermore, Fresnel made the assumption that the disturbance at point **P** is exclusively caused by the portion of **dS** that is unobstructed. Therefore, by integrating

across the surface area of **S**, the total disturbance at point **P** may be obtained according to equation .2.3, also known as the Fresnel diffraction integral:

$$U(P) = \frac{Ae^{ik_1}}{r_1} \iint_S \frac{e^{ikr_2}}{r_2} K(X)\, dS \tag{2.3}$$

2.1.4 | Fresnel's assumptions

According to Fresnel, the effect of a wavefront at an external point depends on certain factors. In figure 2.5., **ab** shows a small aperture. **S** is a monochromatic point source of light, **cd** is the screen and **so** is perpendicular to **cd**.The incident spherical wavefront caused by the point source **S** is represented by **axb**. To determine the outcome at point **P** on the screen, Fresnel made the following assumptions:

- A wave front can be split up into a lot of zones, or strips, known as Fresnel's zones. The total influence of all the secondary waves coming from the different zones will determine the final effect at any given time [24].
- Only when the wavefront strikes a sharp object or travels through slits a diffraction pattern appears [25].
- The impact of a specific zone on a given point depends on the distance between that point and the zone [26].
- The angle at which a point is tilted compared to the area we're looking at (obliquity) will affect the impact at point **P**. For example, this happens because of the part of the wavefront at point **x**. The impact decreases as the angle increases and reaches its highest point at **O**. It is strongest when moving outwards from **x** and weakens in the opposite direction. Due to the obliquity factor, The effect at a point is proportional to $(1 + \cos(\theta))$, where $\angle pxo = \theta$. The effect is strongest at point **o** when considering a small wavefront at point **x**, because $\theta = 0$ and $\cos(\theta) = 1$. Similarly, when $\theta = 90°$ and $\cos(90°) = 0$, the effect along the path **xh** (which is tangent to the main wavefront at **x**) is half of that along **xo**. The effect is zero in the direction **xs** because $\theta = 180°$, $\cos(180°) = -1$, and

$1+\cos(180°) = 1-1 = 0$. This characteristic of the secondary waves removes one of the challenges with the Huygens principle's simplified version. Both a forward and a backward wave should result from the secondary waves spreading out in all directions from each location on the main wavefront. However, there won't be a back wave since the wave's amplitude at its rear is zero [27].

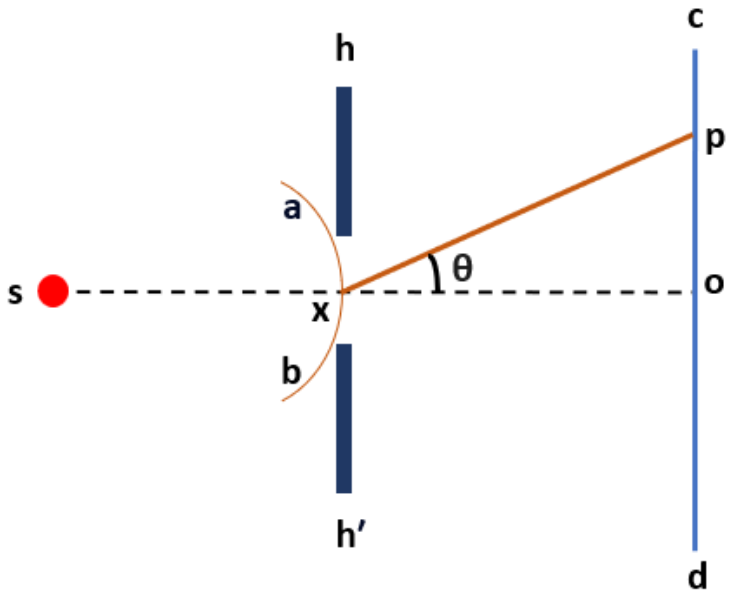

Figure 2.5: Light diffraction via a narrow aperture **hh′**, where **ab** is a spherical wavefront and **s** is a light source. One of the diffracted points in the screen **cd** is projected onto **p** with an angle $\boldsymbol{\theta}$.

2.1.5 | Fresnel's Half-Period Zones (Rectilinear Propagation of Light)

To illustrate Fresnel's method for solving diffraction challenges, let's first look at his approach to determining the effect of a slightly divergent spherical wave at a point located in the wave's forward path. Figure 2.6 illustrates **klmn** which stands for a spherical wavefront of monochromatic light moving. We can think of every point on this sphere as the source of secondary wavelets. In order to determine the influence of these wavelets at a given point **P**, the wavefront is divided into zones via fresnel construction. This results in a set of circles that are spaced half a wavelength apart from **P**, around the point **O**, which is the foot of the perpendicular to **P**. The radius

of the circles, measured along the arc from **O** to S_n, is $S_1, S_2, S_3, ..., S_n$. This is the denominated Fresnel's half-period zones technique [28]. If the distance **OP** = **b**, the circles will be separated by $\boldsymbol{b + \frac{\lambda}{2}, b + \frac{2\lambda}{2}, b + \frac{3\lambda}{2}, \ldots, b + \frac{n\lambda}{2}}$ from **P**. Every zone has a phase difference of $\boldsymbol{\pi}$ or a path difference of $\frac{\lambda}{2}$ from its neighbor. OS_1 is the radius of the first zone. OS_2 is the radius of the second zone and so on, as illustrated in Fig 2.6.

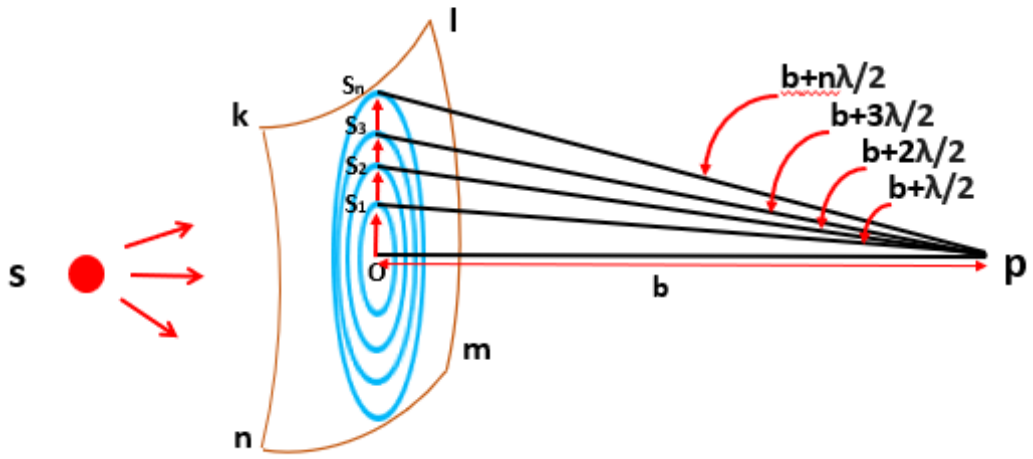

Figure 2.6: Construction of half-period zones on a spherical wavefront. The wavefront is separated into zones using fresnel construction to determine the impact of these wavelets at a certain point P. Assuming that **OP** = **b**, the circles will be separated from Pby $\boldsymbol{b + \frac{\lambda}{2}, b + \frac{2\lambda}{2}, b + \frac{3\lambda}{2}, \ldots, b + \frac{n\lambda}{2}}$. There is a $\frac{\lambda}{2}$ path difference or a $\boldsymbol{\pi}$ phase difference between each zone and its neighbor.

In general, the areas Z_n of successive zones are equal, i.e., the area of the zone with radius S_1 is equal to the area of the zone with radius S_2 and so on [29]. Figure 2.7 depicts a schematic of this, where a big aperture centered at **O**, at a distance **a** from the point source **P**, is illuminated. The intensity at **P'**, **a'** way from **O** is sought. Considering a point **Q** in the aperture that is situated at the position where **OQ** = **S**. Because of diffraction, light moves from **Q** to **P'** (see Huygens's assumptions). lets take $\mathbf{s} \ll \mathbf{a}, \mathbf{a}'$. **PQ** differs from **PO** by $\boldsymbol{\delta}$. whereas **P'Q** differs from **P'O** by $\boldsymbol{\delta'}$. $\boldsymbol{\delta}$ is related to **a** and **s**:

$$a^2 + s^2 = (a + \delta)^2. \tag{2.4}$$

Because **s** is small and $\boldsymbol{\delta}$ is small. Thus, the square can be expanded and the term $\boldsymbol{\delta^2}$ can be removed, yielding: Eq.2.5

$$\delta \cong \frac{s^2}{2a} \tag{2.5}$$

Which is referred to as the sag formula. (In reality, the sag is the perpendicular distance between **Q** and the circle; nevertheless, at small angles, it is almost equal to $\boldsymbol{\delta}$.) As with $\boldsymbol{\delta'}$, **a'**, and **s**, the sag formula also applies. The entire path difference is represented by Δ and equal to ($\boldsymbol{\delta'}$+$\boldsymbol{\delta}$). between PQP' and PP' is thus: Eq.2.6

$$\Delta = \frac{s^2}{2a'} + \frac{s^2}{2a} \tag{2.6}$$

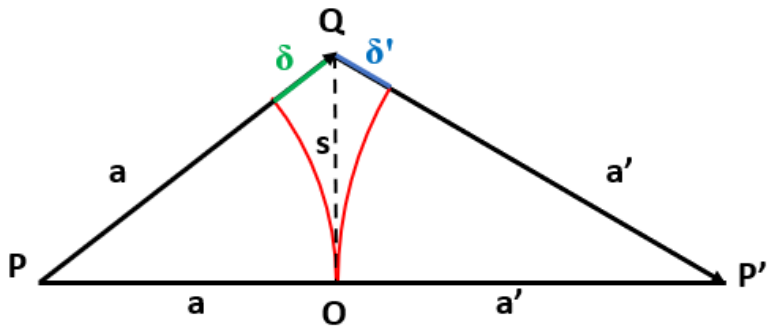

Figure 2.7: The construction of Fresnel, where a big aperture centered at **O** at a distance **a** from the point source **P** is illuminated. The goal is to find the intensity at **P'**, **a'** way from **O**, Considering a point **Q** in the aperture that is situated at the position where **OQ** = **S**.

Determining radius $S_1, S_2, S_3, \ldots$, so that $\boldsymbol{\Delta_1 = \frac{\lambda}{2}}$, $\boldsymbol{\Delta_2 = \frac{2\lambda}{2}}$, $\boldsymbol{\Delta_3 = \frac{3\lambda}{2}}$, ..., or, more broadly, $\boldsymbol{\Delta_n = \frac{n\lambda}{2}}$, constitutes Fresnel's construction. The zones that are created by two consecutive radii are known as Fresnel half-period zones because the field that emerges at **P'** from one annulus is often $\boldsymbol{\pi}$ out of phase with the field from the next annulus. We can calculate the radius by assuming $\mathbf{S_n \propto \sqrt{n}}$:

$$m\lambda/2 = \frac{s_n^2}{2}\left(\frac{1}{a'} + \frac{1}{a}\right) \tag{2.7}$$

Any annulus's surface area is: 2.8

$$Z_n = \pi s_n^2 - \pi s_{n-1}^2 \tag{2.8}$$

that can be written as :2.9

$$Z_n = \pi \frac{aa'}{a' + a} \lambda \tag{2.9}$$

in addition, for a given geometry each zone contributes approximately the same amplitude as every zone to the field at P'. This is due to the fact that each Fresnel zone's area is equal[30]. Let A_n denote the resulting amplitude of the light from the n^{th} zone. Because reversing the direction of the amplitude vector implies altering the phase by π, the consecutive values of A_n will have alternating signs. The amplitude that results from the whole wave, denoted as **A**, may be expressed as the total of the following sum:

$$A = A_1 - A_2 + A_3 - A_4 + \ldots + (-1)^{n-1} A_n \tag{2.10}$$

Thus, the amplitude resulting from the n^{th} zone may be expressed as:

$$A_n = \text{const} \cdot \left(\frac{Z_n}{d_n} \right) \cdot (1 + \cos\theta) \tag{2.11}$$

where the angle at which light departs the zone is $\boldsymbol{\theta}$, and **dn** is the average distance to **P'**. Currently, a precise computation of the $\boldsymbol{Z_n}$'s reveals that the factor **a'** in Eq. 2.9 has to be changed to $\boldsymbol{a' + \delta'}$, where $\boldsymbol{\delta'}$ is the path difference for the middle of the zone. Given that $\boldsymbol{d_n = a' + \delta'}$ at the same time, we may conclude that the ratio $\boldsymbol{Z_n / d_n}$ is constant and not dependent on **n**. As a result, the only component remaining is the obliquity factor $\boldsymbol{I + cos\theta}$ impact, which results in the extremely slow decline of the subsequent terms in Eq. 2.11. Due to the quick change in $\boldsymbol{\theta}$ with **n**, the drop is least gradual at first, but the amplitudes soon become nearly equal.

Assuming that **n** is odd,

$$\begin{aligned} A &= \frac{A_1}{2} + \left(\frac{A_1}{2} - A_2 + \frac{A_3}{2} \right) + \left(\frac{A_3}{2} - A_4 + \frac{A_5}{2} \right) + \ldots + \frac{A_n}{2} \\ &= A_1 - \left(\frac{A_2}{2} \right) - \left(\frac{A_2}{2} - A_3 + \frac{A_4}{2} \right) - \left(\frac{A_4}{2} - A_5 + \frac{A_6}{2} \right) - \ldots - \frac{A_{n-1}}{2} + A_n \end{aligned} \tag{2.12}$$

The amplitudes A_1, A_2,..., do not decrease at a steady rate. Therefore, each one is smaller than the average of the amplitudes before and after it. This means the following inequalities must be true, and all the values in the parentheses in the given equations are positive:

$$\frac{A_1}{2} + \frac{A_n}{2} < A < A_1 - \frac{A_2}{2} - \frac{A_{n-1}}{2} + A_n \tag{2.13}$$

Since the amplitudes for any two neighboring zones are almost the same [31], we can set A_l equal to A_2, and A_{n-1} equal to A_n. Therefore we find the equation 2.14

$$A = \frac{A_1}{2} + \frac{A_n}{2} \tag{2.14}$$

Assuming that **n** is even, we can determine:

$$A = \frac{A_1}{2} - \frac{A_n}{2} \tag{2.15}$$

Therefore, we can conclude that the amplitude at **P'** resulting from the **n** zones is **half of the total (n is odd)** amplitude provided by the first and final zones or **half of the difference (n is even)** [32].

When **n** is big enough to split the entire spherical wave into zones, for the last zone, $\boldsymbol{\theta}$ approaches 180°. Consequently, the total amplitude from the whole wave is only half of what it would be from just the first zone working alone, as the obliquity factor makes $\boldsymbol{A_n}$ insignificant. The graphical construction shown in Figure 3.7 displays an interpretation of these results. The amplitudes $\boldsymbol{A_1, A_2, A_3}$,..., which alternate between positive and negative, are usually added together on the same line. In this figure, they are separated horizontally for clarity's sake. Every vector has its tail positioned at the same height as its head. The final arrowhead height above the horizontal baseline is the amplitude **A** that results from a given number of zones.

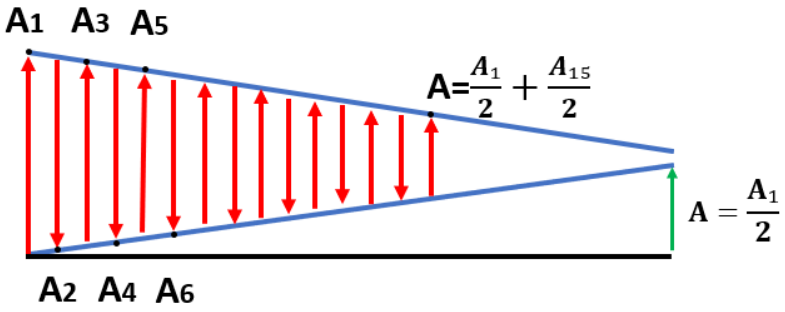

Figure 2.8: Half-period zone amplitudes summation. The amplitudes A_1, A_2, A_3,..., which alternate between positive and negative re separated horizontally for clarity's sake and added together on the same line. For a given number of zones, the amplitude A is the ultimate arrowhead height above the horizontal baseline. In this schema, we represent 15 zones (n is odd) so the resultant amplitude is given by $A = \frac{A_1}{2} + \frac{A_{15}}{2}$.

2.1.6 | Fresnel zone plate fundamentals

As discussed above, a zone plate is a specially designed-screen that selectively blocks light in specific zones. Its construction allows for light to be blocked in either even-numbered or odd-numbered zones. This design takes advantage of Fresnel's method for splitting a wavefront into half-period zones [33]. Two zone plates consisting of opaque alternating zones between concentric circles are seen in Figure 2.9. These zone plates block either even (b) or odd (a) indexed zones. The radii of the zone boundaries are proportional to the square root of natural numbers [34]. In one configuration, the odd-numbered annular spaces are transparent, while the even-numbered spaces are opaque. Conversely, in another possible configuration, the odd-numbered spaces are opaque, and the even-numbered spaces are transparent. Therefore, there are two types of zone plates based on which zones are blocked, which are explained in more detail in the following [35]:

- **Positive zone plate:** A zone plate is referred to as a positive zone plate when the first half period zone, or the central circular zone, is visible on a thin glass plate. Even-numbered half-period zones (the second, fourth, sixth, etc.) in a positive

zone plate are blackened to make them opaque to light, whereas odd-numbered half-period zones (the first, third, fifth, etc.) are left transparent. as shown in Figure 2.9.a.

- **Negative zone plate:** A zone plate is referred to as a negative zone plate when the whole central circular zone, or the first half period zone, is opaque on a thin glass plate. Evenly numbered half-period zones in the negative zone plate —the first, third, and fifth— are transparent, as shown in Figure 2.9.b.

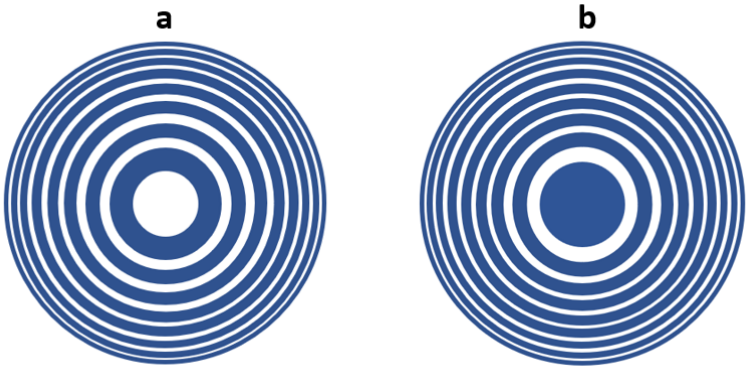

Figure 2.9: **(a)** Positive zone plate: A positive zone plate is a zone plate that has odd zones that are translucent and even zones that are dark.**(b)** Negative zone plate: A negative zone plate is a zone plate that has odd zones dark and even zones translucent.

Diffraction gratings can be used to conceptualize Fresnel zone plates. Figure 2.10 illustrates a comparison between a simple transmission grating, a circular grating, and a Fresnel zone plate. In the simple transmission grating 2.10.a the entering beam is split into multiple beams that exit the element at various angles, with each beam corresponding to a different diffraction order. First-order constructive interference occurs at angles where the path length difference is equal to one wavelength, as described in:

$$\sin\theta = \frac{\lambda}{d} \tag{2.16}$$

This happens at both positive and negative angles, resulting in the grating's $\pm$1st orders, in addition to the $\mathbf{0}^{\text{th}}$ order moving forward. As the path length differences

increase by integer multiples of the wavelength $\boldsymbol{n\lambda}$, higher orders are produced at angles $\boldsymbol{\theta_n}$, meaning that:

$$\sin\theta_n = \frac{n\lambda}{d} \tag{2.17}$$

where $n = 0, \pm1, \pm2, \pm3, \ldots$. The condition for constructive interference can be easily shown for light hitting the grating at an angle θ_i, measured from the normal;

$$\sin\theta - \sin\theta_i = \frac{n\lambda}{d} \tag{2.18}$$

Equation 2.17 is known as the grating equation, and Eq. 2.18 describes a special case for normal incidence.

The incoming beam is divided differently in the circular grating figure 2.10.b. Positive convergent orders are partially focused onto a segment on the optical axis of the element because of the element's circular symmetry, but negative orders are divergent from a virtual focus that is similarly composed of a segment but is upstream of the element. The local line spacing in a Fresnel zone plate, as shown in Figure 2.10.c, is designed so that all first-order rays converge at a single point, which is the element's focus. In the negative orders, which are similarly divergent, a virtual point of focus is located in front of the element. The grating period must be larger in the inner regions and smaller in the outer regions of the element because the deflection angle is proportional to the line density [36].

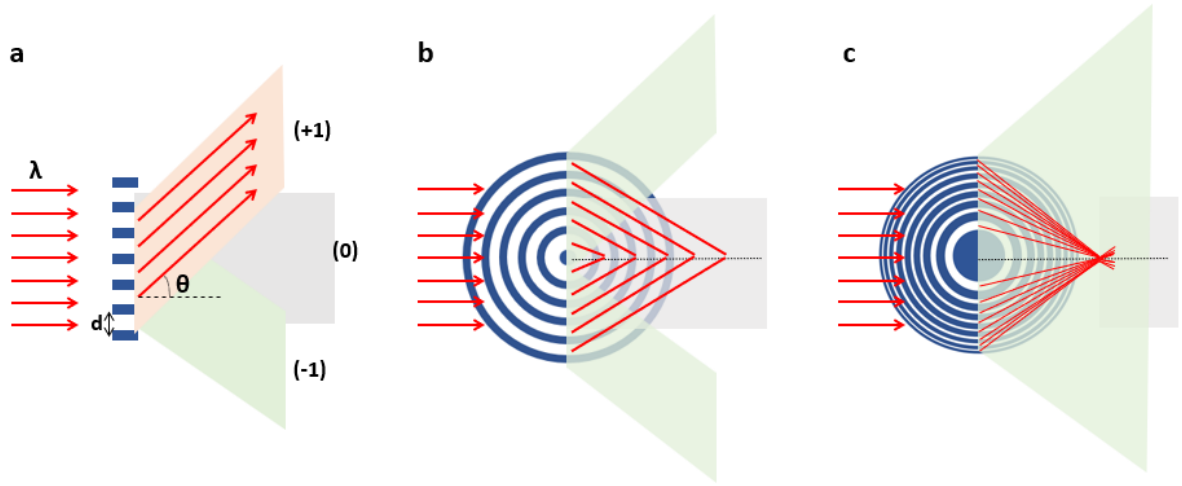

Figure 2.10: A simple grating (a), a circular grating (b), and a Fresnel zone plate (c) are compared. For every element, the zeroth (grey), first (red), and minus first (green) ordering are displayed. The circular grating and the Fresnel zone plate concentrate the radiation onto a segment and a point of the optical axis, respectively, whereas the simple grating just splits the incoming beam.

2.1.7 | Relevant parameters of Fresnel zone lens

Radius and zone area

To understand how a Fresnel zone plate lens focuses light, we need to consider the first-order diffraction from a circular grating. The spacing between the zones decreases as you move further from the center. This creates a real first-order focus, as shown in Figure 2.11, because the diffraction angle increases according to Eq.2.16. When a screen is moved to capture an image while the zone plate is held perpendicular to an incident light beam, the screen's maximum brightness can indeed be achieved at a certain location, which might be **f** centimeters from the zone plate [37]. The top half of the incident plane wavefront is denoted by **XO**. The light intensity should be taken into consideration at point **P**. Point **P** is located **f** distance from the wavefront. $\boldsymbol{OM_1 = r_1}$, $\boldsymbol{OM_2 = r_2}$, etc. are the radii of the zones. The zonal radii are provided by the Pythagorean theorem if a right triangle is drawn with the focal length **f** as one side, the radius of any zone $\boldsymbol{r_n}$ as a second side, and $\boldsymbol{f + \frac{n\lambda}{2}}$ as the length of the hypotenuse:

$$f^2 + r^2 n = \left(f + \frac{n\lambda}{2}\right)^2 \text{ where } \quad \lambda \text{ is the wavelength of light.} \tag{2.19}$$

which becomes:

$$r_n^2 = nf\lambda + \frac{n^2\lambda^2}{4} \tag{2.20}$$

For $\boldsymbol{f \gg \frac{n\lambda}{2}}$, the spherical aberration factor, $\boldsymbol{\frac{n^2\lambda^2}{4}}$, can be neglected. This condition is is typically the case for x-ray wavelengths. It corresponds to a lens with a small numerical aperture $\boldsymbol{NA = \sin\theta = \frac{\lambda}{2\Delta r} \ll 1}$. This phrase should be kept in situations when this condition does not hold, such as when using a higher **NA** optic at an extreme ultraviolet (EUV) wavelength. For the low **NA** case, we have:

$$r_n \approx \sqrt{n\lambda f} \tag{2.21}$$

demonstrating that when consecutive zones increases by $\boldsymbol{\sqrt{n}}$, a true first-order focus is reached. This provides the required prescription for reducing the radial grating period required to produce a common focus. Lord Rayleigh's 1871 report is the earliest documented use of alternately opaque Fresnel zones to concentrate light [38, 39].

Once the radius for $\boldsymbol{n}$ zones is determined, we will discuss other relevant parameters of the Fresnel Zone plate: depth of focus, focal length $\boldsymbol{f}$, lens diameter $\boldsymbol{D}$, numerical aperture $\boldsymbol{NA = \sin\theta}$, and spatial resolution. These characteristics will be explained in terms of the outer zone width $\boldsymbol{\Delta r}$, the total number of zones $\boldsymbol{N}$, and the wavelength $\boldsymbol{\lambda}$. But before, lets pay attention to the zone area. As shown earlier in the half-period zone section, the area of consecutive zones is constant and can be expressed as follows:

$$\pi(r_n^2 - r_{n-1}^2) = \pi\lambda f \tag{2.22}$$

Outermost zone width and zone diameter

Now, let's describe the first important parameter, which is the outermost zone width $\boldsymbol{\Delta r}$. As each zone is an annulus, $\boldsymbol{\Delta r}$ differs from the radius of the zones and represents the width of the selected zone for study, By replacing **n** with **N**, we have:

$$\Delta r = r_N - r_{N-1} \tag{2.23}$$

where N is the total number of zones, including both the opaque and transparent zones. The outcome is as follows once **n** is replaced by **N** and $\boldsymbol{r_N}$ and $\boldsymbol{r_{N-1}}$ are substituted with the appropriate values from Eq. 2.21:

$$r_N^2 - r_{N-1}^2 = N\lambda f - (N-1)\lambda f = \lambda f \tag{2.24}$$

Applying Equation 2.23, we get:

$$r_N^2 - (r_N - \Delta r)^2 = 2r_N\Delta r - (\Delta r)^2 \approx 2r_N\Delta r \tag{2.25}$$

given that $\Delta r \ll r_N$ for large values of **N**. When the two equations above are combined (2.24 and 2.25), the following result is obtained:

$$\lambda f \approx 2r_N\Delta r \tag{2.26}$$

Now we are able to define the zone diameter, denoted by D and equal to $\boldsymbol{2r_N}$, from Eq.2.26 we have :

$$\lambda f \approx D\Delta r \tag{2.27}$$

Moreover, we observe from Eq.2.21 that $\lambda f \approx \frac{r_N^2}{N}$, so that from Eq. 2.27 we get:

$$D\Delta r \approx \frac{r_N^2}{N} = \frac{D^2}{4N} \quad \text{that can be simplified to} \quad D \approx \Delta r \cdot 4N \tag{2.28}$$

Focal length

Consequently, by also using Eq.2.27, the focal length can be determined as follows, showing a strong dependence on the wavelength:

$$f \approx \frac{\Delta r D}{\lambda} \tag{2.29}$$

or in conjunction with Equation 2.28 :

$$f \approx \frac{4N(\Delta r)^2}{\lambda} \tag{2.30}$$

Since Eq.2.30 shows that the focal length scales directly with the number of zones and the square of the outer zone width (which essentially determines the resolution), and inversely with the wavelength, it introduces a strong chromatic effect. This relationship is extremely significant for the design of zone plate microscope lenses.

Numerical aperture NA

Another important parameter is the numerical aperture **(NA)** of a lens is defined as:

$$NA \equiv \sin\theta \tag{2.31}$$

As shown in Figure 2.11, $\boldsymbol{\theta}$ is the half angle measured back to the lens from the optic axis at focus. So, the numerical aperture of a zone plate lens can be found as $\boldsymbol{NA = \frac{r_N}{f} = \frac{D}{2f}}$ or using Eq 2.27 as:

$$NA \approx \frac{\lambda}{2\Delta r} \tag{2.32}$$

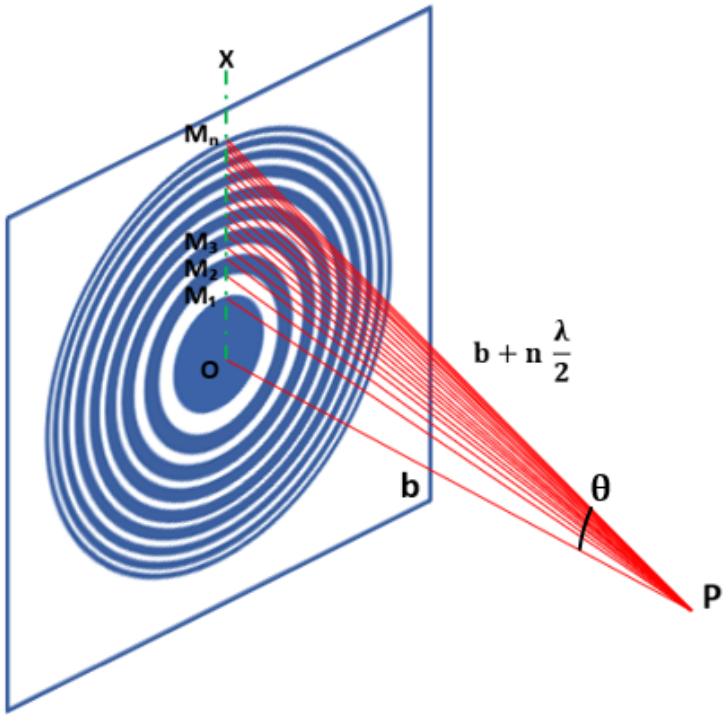

Figure 2.11: A plane wave-illuminated Fresnel zone plate lens that only displays the convergent **(+1st)** order of diffraction. In the straightforward transmission zone plate, alternate zones are opaque. The zone plate lens has a total of **N** zones, which is one of its important specifications. In order to ensure that the incremental path length to the focal point is $n\lambda/2$, successive zones of radius r_n are defined.

Magnification

The magnification explains how the object's dimensions have changed in relation to the picture may be found [40], as seen in Figure 2.12. But before onto that parameter let's look at point-by-point, imaging of an item at a limited distance **q** from the zone plate to an image plane at a distance **p**. Once more, the progressively transmissive and opaque zones are built to increase the path lengths by $\boldsymbol{\lambda/2}$. This means that:

$$q_n + p_n = q + p + \frac{n\lambda}{2} \tag{2.33}$$

where for lower numerical aperture lenses

$$q_n = \left(q^2 + r_n^2\right)^{\frac{1}{2}} \approx q + \frac{r_n^2}{2q} \tag{2.34}$$

$$p_n = \left(p^2 + r_n^2\right)^{\frac{1}{2}} \approx p + \frac{r_n^2}{2p} \tag{2.35}$$

therefore we have

$$q + \frac{r_n^2}{2q} + p + \frac{r_n^2}{2p} \approx q + p + \frac{n\lambda}{2} \tag{2.36}$$

$$\frac{r_n^2}{2q} + \frac{r_n^2}{2p} \approx \frac{n\lambda}{2} \tag{2.37}$$

$$\frac{1}{q} + \frac{1}{p} \approx \frac{1}{f} \tag{2.38}$$

using $f = \frac{r_n^2}{n\lambda}$ from Eq.2.21 . The focal length of an ordinary visible light refractive lens is related to the image and object distances by equation 2.38. The transverse magnification can also be demonstrated:

$$M = \frac{p}{q} \tag{2.39}$$

Fresnel zone plate lenses are employed for magnified imaging ($M \ll 1$) or focusing ($M \gg 1$).

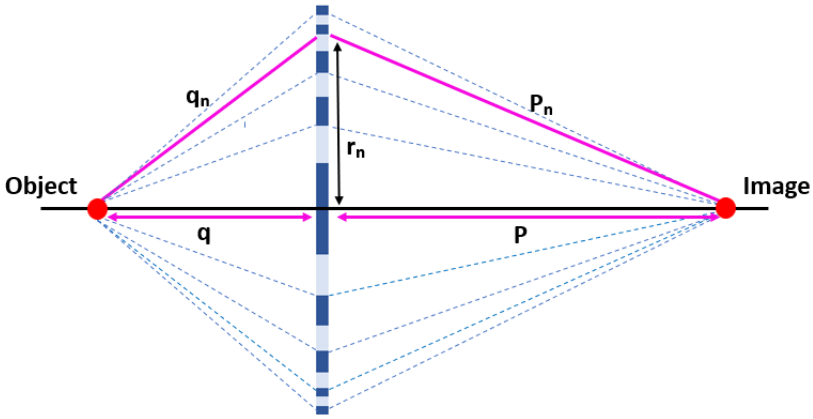

Figure 2.12: An illustration of point-by-point imaging using a Fresnel zone plate lens is provided. Propagation pathways grow successively by $\boldsymbol{\lambda/2}$.

A Fresnel zone plate, like other linear diffraction gratings, yields several focus points in addition to the first order. The $\boldsymbol{n^{th}}$ diffraction order focal length, $\boldsymbol{f_n}$, can be expressed as follows:

$$f_n = \frac{nr_N^2}{M\lambda} \tag{2.40}$$

where N is the total number of zones and n is the diffraction order (positive convergent or negative divergent). Real focus points are associated with positive diffraction orders, whereas virtual focal points are associated with negative order [23], thereby making the Fresnel zone plate a multifocal device. Since there are multiple diffraction orders, a pinhole needs to be placed near the chosen order to block the radiation from the other orders. Order selecting aperture (OSA) is the common term used to describe the pinhole, shown in Figure 2.13. A clear focus is achieved by placing the aperture close to the focal point and using a central stop i.s. an opaque disc that covers the low-order rings for the lens.

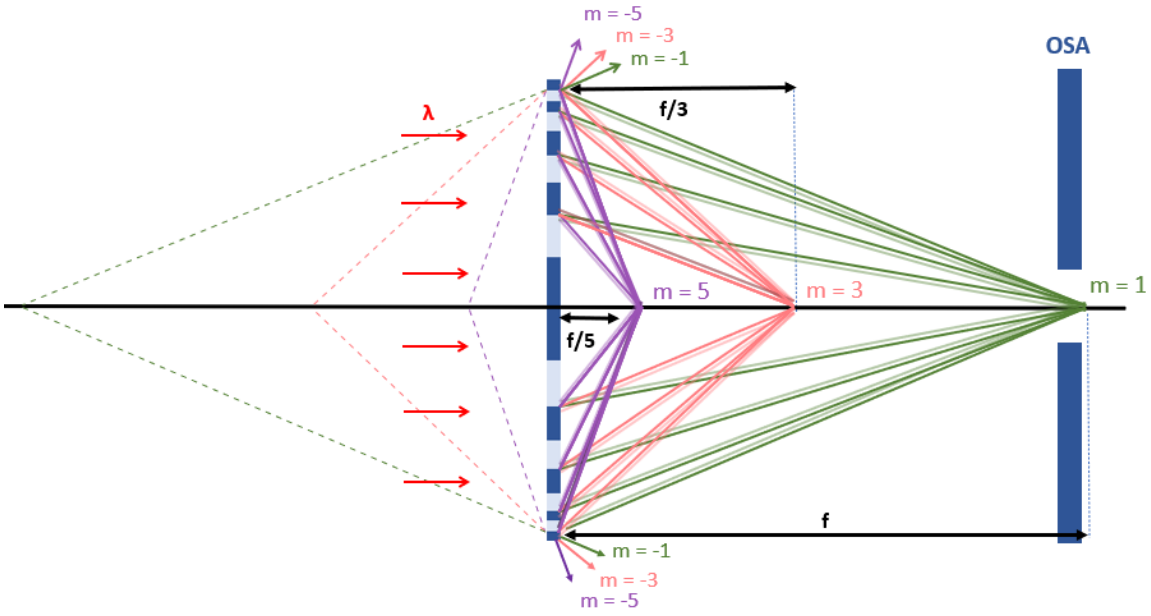

Figure 2.13: A Fresnel zone plate focuses light into the first three positive orders. There are also three negative divergent orders with virtual focal points before the lens. Most of the unwanted radiation from other orders can be blocked by placing an order selecting aperture (**OSA**) near the first-order focus.

The depth of focus and maximum spectral bandwidth acceptance are two more crucial characteristics in any imaging equipment, and they are likewise determined in the case of a Fresnel zone plate as [41]:

$$\text{Depth of Focus, DOF} = \pm\frac{1}{2}\frac{\lambda}{(\text{NA})^2} = \pm\frac{(\Delta r)^2}{\lambda} \tag{2.41}$$

$$\text{Maximum Spectral Bandwidth, } \frac{\Delta\lambda}{\lambda} \leq \frac{1}{N} \tag{2.42}$$

2.1.8 | Spatial resolution of Fresnel zone plate

The theory states that the de Broglie wavelength of the atomic beam, $\boldsymbol{\lambda}$, sets the smallest focus width, $\boldsymbol{\omega}$, possible when using a Fresnel zone plate. The focus width is the size of the focused spot. This relates to spatial resolution, which is the smallest distance between two objects that can be distinguished. It defines the ability of an

imaging device to see small details of the object. One of the most often used techniques for estimating the spatial resolution $\boldsymbol{\delta}$ is the Rayleigh criteria [23, 42, 43] which for a zone plate states:

$$\delta = \frac{0.61\lambda}{\mathrm{NA}} \tag{2.43}$$

where **NA** is the numerical aperture. **NA** is a dimensionless number that indicates the largest angle at which the wave enters or exits the zone plate. by substituting the value of NA provided in Eq.2.32, equation 2.43 may so be rewritten as follows:

$$\delta = 1.22\frac{\lambda f}{2r_N} = \frac{\lambda}{2(NA)} \tag{2.44}$$

To get optimal resolution for a given focal length $\boldsymbol{f}$ and wavelength $\boldsymbol{\lambda}$, one must increase the zone plate diameter $\boldsymbol{D}$, therefore increasing the number of zones in the zone plate. The spatial resolution of a zone plate can be expressed in terms of the outermost zone width $\boldsymbol{\Delta}$r using Eq 2.27 and Eq 2.44. By doing this, we obtain that spatial resolution $\boldsymbol{\delta_{ZP}}$ is proportional to the width of the outermost zone $\boldsymbol{\Delta}$r.

$$\delta_{ZP} = 1.22\Delta r \tag{2.45}$$

Thus, the manufacture of the Fresnel zone plate, how precisely the outer zones of the Fresnel zone plate are made, determines the theoretical resolution limit. The $\boldsymbol{N^{th}}$ zone has the lowest zone width and is often the hardest zone to produce via lithography methods[44].

2.1.9 | Fresnel Zone Plate Diffraction Efficiency

The proportion of incoming radiation intensity that is diffracted into a certain diffraction order is indicated by the diffraction efficiency of a Fresnel zone plate. When a Fresnel zone plate has completely opaque and bright zones, the diffraction efficiency may be expressed using the following formula [41]:

$$\eta_m = \frac{I_m}{I_{\text{incoming}}} = \begin{cases} \frac{1}{4} & m = 0 \\ \frac{1}{m^2\pi^2} & m \text{ odd} \\ 0 & m \text{ even} \end{cases} \quad \text{and} \quad \frac{1}{4} + \sum_{m \text{ odd}} \frac{1}{m^2\pi^2} = 0.5 \tag{2.46}$$

Thus, without being focused, **25%** of the incoming radiation is transferred in the forward direction **(m = 0)**. About **10%** of the diffraction efficiency is directed toward the first order focus **(m = 1)**, another **10%** toward the first divergent **(m = -1)**, and less than **5%** toward the other orders. Conversely, only **50%** of the radiation is capable of passing through the lens because the remaining **50%** is absorbed by the opaque rings. Because of this, a binary Fresnel zone plate has a poor focusing efficiency by construction.

Currently it is challenging to produce Fresnel zone plates with entirely opaque zones at the x-ray regime. For typically used materials, the required zone thickness **(h)** to absorb all the radiation is of a few microns. When this is combined with the need for a small outermost zone width **Δ**r, the resultant high aspect ratio structures are not easily generated. Kirz et al [45] demonstrates that in order to acieved the described zone plate, equation 2.46 needs to be revised. The following factor determines how the electromagnetic wave field transmitted across transmissive and opaque zones differs from one another:

$$A = e^{-i\left(\frac{2\pi\delta}{\lambda}\right)h} e^{-\left(\frac{2\pi\beta}{\lambda}\right)h} \tag{2.47}$$

The first term provides the additional phase, while the second word explains absorption. Then, using a similar development of equation 2.46, the diffraction efficiency may be recalculated, and one gets:

$$\eta_m = \begin{cases} \left|\frac{1+A}{2}\right|^2 & m = 0 \\ \left|\frac{1-A}{m\pi}\right|^2 & m \text{ odd} \\ 0 & m \text{ even} \end{cases} \tag{2.48}$$

This allows to arrange the odd diffraction orders as:

$$\eta_m = \frac{1}{(m\pi)^2}\left[1 + e^{-2\frac{2\pi}{\lambda}\beta h} - e^{-\frac{2\pi}{\lambda}\beta h}\cos\left(\frac{2\pi}{\lambda}\delta h\right)\right] \tag{2.49}$$

The given formula 2.49 demonstrates that the diffraction efficiency is dependent upon the refraction index ($n = 1 - \delta - i\beta$) and thickness of the material. When the material and zone thickness are properly selected, the additional phase change the material introduces may strengthen the constructive interference in the focal point, which will boost the diffraction efficiency of a Fresnel zone plate.

When $\boldsymbol{\beta h}$ approaches to zero, the diffraction efficiency reaches its maximum when $\frac{2\pi}{\lambda}(\boldsymbol{\delta h}) = \boldsymbol{\pi}$. This circumstance would equate to a pure phase Fresnel zone plate. Since the zone thickness can be adjusted to cause a phase lag of $\boldsymbol{\pi}$ in the radiation passing through the zones,n the radiation passing through, up to 40% diffraction efficiency can be achieved. When the product $\boldsymbol{\beta h}$ is sufficiently big, the expression approaches Eq.2.46, as all radiation passing through the opaque zones is absorbed.

2.2 | Fresnel zone plate lenses VS different types of lenses

Doubly-Hyperbolic Lens: In layout and functionality, the FZP is engineered to imitate the feature of a doubly-hyperbolic lens, presenting a lighter and thinner opportunity (25% thickness, 32% weight loss) in comparison to the bulkier and heavier doubly-hyperbolic lens. However, the bandwidth is limited by the diffractive nature of the FZP, while the doubly hyperbolic lens has no such constraints. FZP has a non-continuous profile. This can cause problems with phase uniformity and amplitude taper. However, the doubly-hyperbolic lens is smooth. It has better phase uniformity as a result. The FZP could become part of free-space focused-beam setups. Why? because Its source and focal point are close to the zone plate. The doubly-hyperbolic lens is mainly utilized in the focused beam system. [46].

X-ray refractive lenses: X-ray refractive lenses are primarily useful for controlling nearly diffraction-limited beams in the hard X-ray spectrum. Because of their strong X-ray absorption, they are unique in that they have an intrinsic soft (Gaussian) aperture. The critical Fresnel number (CFN) governs the optical characteristics of these

lenses. X-ray Fresnel lenses are hailed as the best-focusing instruments for hard X-rays, with high-efficiency rates reaching up to 100% and beam modification possible with the use of numerous lenses. However, problems like color chromaticity and manufacturing complexity come with their use [47].

Plano-convex lenses : plano-convex lenses are larger than fresnel lenses and are made from one piece of material; they are used in concentrated solar power systems. Both types of lenses focus light, but Fresnel lenses work better when spherical aberrations are reduced by their shape and enable a higher amount of light ray concentration. In a comparison of plano-convex lenses with Fresnel lenses having spherical facets, the latter are better in performance due to reduced spherical aberration. The preferred solar concentrators for various applications are fresnel lenses because they are feather-weight and constructed effectively. However, employing plano-convex lenses on a large scale can be expensive and problematic. When it comes to concentrating solar energy, practicality and efficiency are some of the benefits that can come from using Fresnel lenses, particularly those with spherical facets [48].

Ordinary Refractive Lens Antennas: When thinner, lighter, and simpler focusing devices are needed for manufacturing, FZP lenses are chosen over standard refractive lenses. However, even though the FZP lenses and antennas have undergone extensive theoretical analysis, their usefulness in real-world applications is still underestimated. The gain, beamwidth, cross-polar isolation, and input-mismatch of terahertz grooved-dielectric FZP lenses/antennas with four or more phase-correction steps are similar to those of the equivalent conventional lens antenna in a constrained frequency range. Moreover, the diffractive plane-step FZP lenses exhibit superior fabrication-error tolerance and ease of production [49].

2.3 | Applications of Fresnel zone lenses

2.3.1 | X-ray microscopy

When Roentgen discovered X-rays in 1895, he quickly came to the conclusion that it would be difficult to focus these X-rays using lenses because of their near refractive

index of 1 [50]. Thus, even though X-rays with short wavelengths were first utilized to assess things like crystal structures shortly after Roentgen's discovery, for almost eight decades, X-ray microscopy was hindered by inadequate X-ray optics. However, over time, it became evident that Fresnel zone plates are an excellent choice for diffractive X-ray optics in X-ray microscopes [51]. Soft X-ray microscopes based on FZP optics come in two varieties: a full-field (imaging) transmission X-ray microscope (TXM) and a scanning version, the scanning transmission X-ray microscope (STXM).

- **Transmission X-ray Microscopy:** In 1980, Gottingen University constructed the first full-field transmission X-ray microscope, which achieved a resolution of around 150 nm and a focal depth of 3.3 μm in the soft ray band [51]. Full-field transmission X-ray microscopes are now being effectively used worldwide in synchrotron radiation systems. The imaging system TXM has achieved a resolution of 30 nm in the hard-line group and 15 nm in the soft-line group, owing to the utilization of sophisticated processing technologies [52–54]. The working principle of a Transmission X-ray Microscopy which is comparable to that of a traditional microscope, is sketched in Figure 2.14. Through condenser optics (mirror or zone plate), the incoming X-ray beam is focused on the sample, and an objective FZP lens projects the photons onto a screen or 2D image detector (CCD camera). Although the picture resolution is determined by the objective FZP resolution, the condenser FZP requirements are less strict, and a capillary condenser can be employed in its place [55].

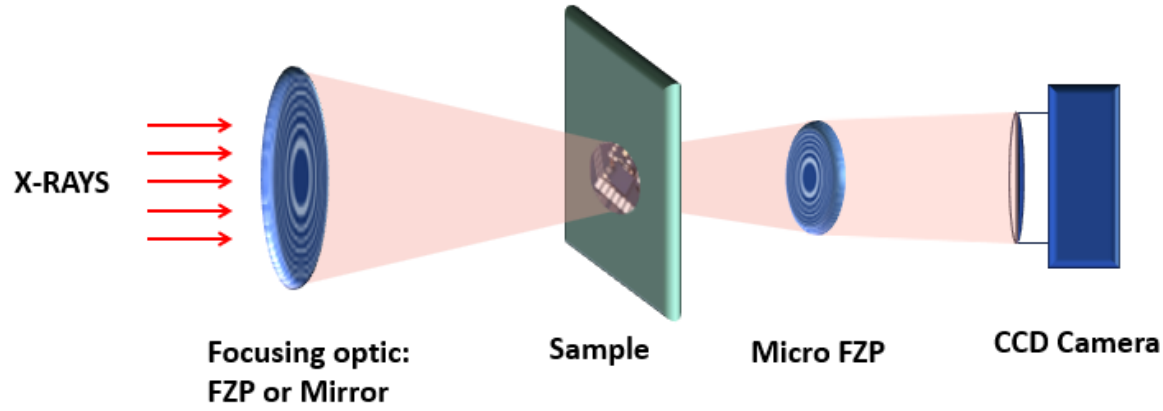

Figure 2.14: Transmission X-ray microscope schematic diagram. Condenser lens illumination is used to illuminate the sample, just like in a traditional microscope, and after that, an objective lens is used to display the beam onto a screen (CCD camera). Objective lenses that are diffractive Fresnel zone plates must be utilized since X-rays have a tiny refractive index.

TXM has an easy-to-use experimental setup that produces a picture immediately, aside from the focusing FZP. In contrast to some microscope types, such as photoelectron emission microscopes (PEEM), TXM is regarded as a photon-in, photon-out approach that is not affected by magnetic fields produced by the sample or its surroundings. The width of the outer ring of the Fresnel zone plate determines the spatial resolution of TXM, and its photon efficiency diminishes with increasing magnification. Therefore, TXM is most appropriate for studies that need a larger field of view at intermediate magnifications, such as imaging the mesoscale development of domain patterns. By utilizing the full-field imaging mode, which reduces the sample size to less than the spot size at the sample site, TXM is able to acquire the sample's two-dimensional transmission picture in only one exposure. For this reason, it has a big benefit over the scanning imaging approach, which is the fast imaging speed.

According to studies by Ehrenfried et al [56], Fresnel zone plates have been shown to provide the best spatial resolution available in a full-field imaging microscope over the complete electromagnetic spectrum when it comes to TXM/XCT with sub-50 nm resolution, where A zone height of around 1.6 μm is needed for a

30 nm resolution Au zone plate in order to attain an ideal focusing efficiency of approximately 33% while operating at 8 keV X-rays.

A multi-layer fresnel zone plate (ML-FZP) with an outermost zone width of 40 nm, a total zone thickness of 10 um, and an aspect ratio of 157 has been fabricated by Yanli et al.[57] using atomic layer deposition (ALD) and focused ion beam (FIB) milling. A half-pitch cut-off resolution of 29 nm was attained during the testing of the ML-FZP in transmission X-ray microscopy at 9 keV.

- **Scanning X-ray microscopy:** Compared to transmission microscopy TXM, scanning transmission X-ray microscopy STXM is more sophisticated as it needs a precise scanning stage that is controlled by a computer. However, it is by far the easiest method for examining the pictures that the scanning microscope captured. this technique was pioneered by Horrowitz et al in 1972 [58]. The X-ray beam in STXM is focused on the tiniest possible spot using a FZP (see figure 2.15). Higher diffraction orders of the FZP are removed using an order separating aperture. The resultant illumination spot for an STXM establishes the imaging resolution. Similar to other scanning microscopy methods, piezo-controlled nanopositioners are used to scan the sample through the X-ray spot, and an X-ray-sensitive detector subsequently gathers the photons that are passed through the sample. An STXM does not require spatially resolving detectors because the image is created by scanning the sample; in fact, several detectors can be used simultaneously, such as an avalanche photodiode (APD) to detect transmitted photons and a sensitive ammeter to measure the total electron yield (TEY), or the drain current of electrons ejected from the surface [59]. Since each pixel in the picture is measured separately, a computer is required to create the sample's two-dimensional image.

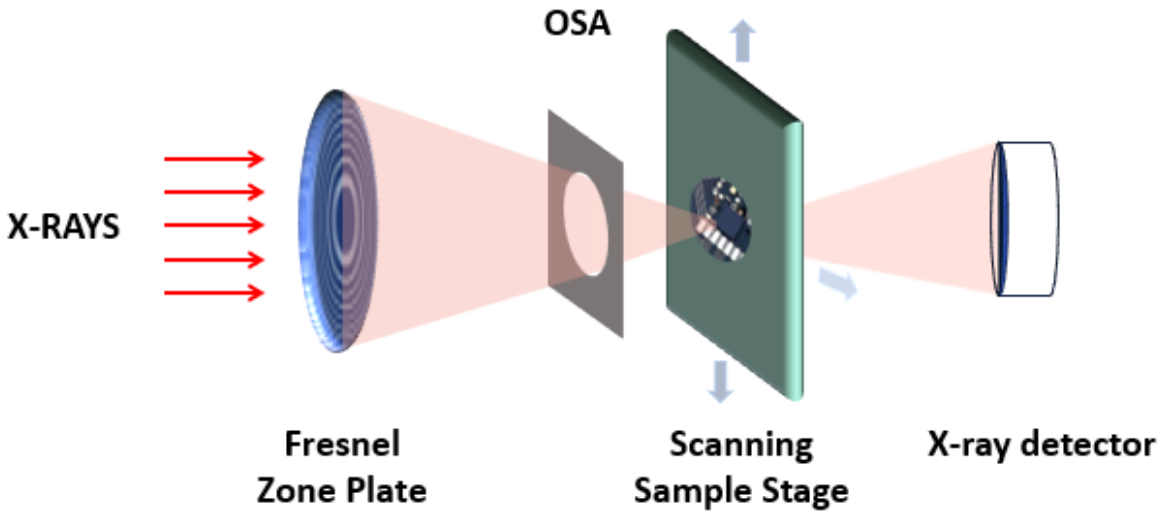

Figure 2.15: Diagram of a scanning transmission X-ray microscope. A Fresnel zone plate is used to concentrate the X-ray beam on the illumination spot size that limits resolution. Using an order separating aperture, the higher diffraction orders of the FZP are eliminated. Arbitrary detectors can be used to measure the X-ray absorption contrast while the X-ray spot scans the sample. The photos are then produced using a computer.

At large magnifications, Compared to the previously stated methods, STXM has an advantage since all photons are employed at the smallest focused point. Nevertheless, STXMs suffer from sluggish measurements when scanning a wide field of view at low magnification due to the requirement to reconstruct the picture from individual pixels of the focus spot size, for the same reasons. Similar to TXM, STXM has the advantage of being a magnetic field-insensitive photon-in, photon-out method. Combined with the ability to use any kind of detector, STXM is the most adaptable platform for complex sample settings. For example, it may be used to deliver RF fields, currents [60–63], or even gases and liquids to the sample while it is being measured [64, 65], But this also increases the experimental complexity of STXM. STXM can be surface-, bulk-, or both simultaneously sensitive, depending on the type of detector that is being utilized.

A novel class of Fresnel zone plate lenses targeted at the sub-20 and sub-10 nm resolution range is presented by Istvan et al in their work [66]. A beam focussing test for scanning transmission X-ray microscopy was conducted using the 7nm

zone plate. In order to take the measurement, a test item with feature sizes as small as 10 nm was continually scanned where Extremely good optical characteristics with focus spots as small as 7.8 nm are revealed by the thorough evaluation of these lenses.

Yasuo *et al.* present a compact scanning transmission X-ray microscope recently created and engineered at the Photon Factory [67]. To make the microscope compact, steady, and appropriate for usage at multifunctional beamlines' endstations that are now in service they used piezo-driven linear stages for all of its coarse stages. Fresnel zone plate with a diameter and an outermost zone width of 150 μm and 30 nm, respectively is used to provide images with a spatial resolution of 20-100 nm.

2.3.2 | Solar Energy Concentration

Recently, Fresnel lenses have emerged as one of the finest options for concentrated solar energy applications due to their many advantages, including small volume, lightweight, low cost of mass production, as well as increase in effective energy density [68]. Glass is a desirable material to utilize for glazing or when lenses are to be used at high temperatures. However, a good material for making Fresnel lenses is polymethylmethacrylate (PMMA), a transparent, sturdy, and lightweight polymer with optical properties almost identical to those of glass. Fresnel lenses have become more high-quality, and designing Fresnel lenses for solar energy concentration applications has become more feasible because to the development of new polymers, molding processes, and computer-controlled diamond-turning equipment[69]. Despite the fact that Fresnel lens concentrators have been utilized in systems for concentrating solar energy since the 1960s, The prospective development of Fresnel lenses for commercial solar energy concentration is still underway. Nonetheless, there are two primary areas in which significant research on focused solar energy applications employing Fresnel lenses for diverse objectives may be categorized: **imaging Fresnel lens systems and non-imaging systems.**

- **Imaging systems**: The majority of Fresnel lenses that were first chosen for solar energy applications weren't made to gather solar radiation; instead, they were intended to be imaging devices. The imaging Fresnel lens creates an image on the focus plane by refracting light from an object. this image is influenced by deviations because of the inaccurate manufacturing of the prism tips and grooves. Following the development of the glass Fresnel lens on a lighthouse, the imaging Fresnel lens started to be utilized extensively in the field of concentrated solar power, including solar illumination, solar-pumped lasers, concentrated photovoltaic, solar thermal utilization and power production, and imaging solar concentrators. The first plastic Fresnel lenses with superior surface quality and great accuracy were created in 1951 by Miller *et al* [70].

  A new area of imaging Fresnel lens application that received some interest is solar illumination. Tsangrassoulis *et al.* [71] reported the creation of a technique to regulate the amount of light produced by a prototype hybrid lighting setup that used a massive core liquid fiber optic to transfer daylight from a heliostat with a focusing Fresnel lens to a luminaire in a windowless room. Solar-pumped laser by high-focusing Fresnel lens is a different line of inquiry that is highly widespread in Japan. Yabe *et al.*[72] used Cr-codoped Nd: yttrium aluminum garnet ceramic and Fresnel lens focusing from ambient sunlight to obtain 11%–14% slope efficiency of the solar-pumped laser. Plastic Fresnel lenses were quickly employed in concentrated photovoltaic power generation due to their lightweight nature and ability to increase solar energy density. Based on spectral distribution considerations, Oshida *et al.* [73] investigated photovoltaic applications using Fresnel lenses. Using an acrylic Fresnel lens to focus sunlight on high-intensity solar cells, Donovan *et al.*[74] built a photovoltaic concentrator array that was tuned to produce the affordable photovoltaic power output. One of the major research projects in the realm of solar thermal use and power generation was the linear Fresnel Reflector (LFR) technology. Utilizing a series of linear mirror strips, Linear Fresnel Reflector technology focuses light onto a stationary receiver positioned atop a linear tower. For it, Fresnel reflectors are regarded as the archetypal imaging tools. Giorgio Francia.[75], a renowned solar pioneer, was the

first to use this technique in the 1960s to construct linear and two-axis tracking Fresnel reflector systems in Genoa, Italy.

- **Non-imaging systems**: Since its discovery in 1965, non-imaging concentrators have been utilized in solar energy-gathering systems on a larger scale. The concentration of solar energy necessitates extremely uniform flux concentrators with adaptable designs that can accommodate variations in solar disk size, solar spectrum, and tracking errors, rather than imaging quality. that's why convex Fresnel lenses are typically used in non-imaging designs to achieve a high concentration ratio and flux distribution at a short focal length. Concentration ratios, or the geometric concentration ratio C, are the primary features of non-imaging systems. These ratios are often categorized as low for $C \leq 10$, medium for $10 < C \leq 100$, or high for $C > 100$.

  The design and manufacturing processes for the medium and high-concentration non-imaging Fresnel lenses were thoroughly examined by several researchers. Lin et al.[76] simulated a non-imaging Fresnel lens with a pitch size of 0.3 mm and a focus distance of 200 mm using the optical program TracePro. For a non-imaging Fresnel with a flat upper surface, Akisawa *et al.*[77] looked into a novel design technique to make production easier. Prisms were designed using non-linear optimization to achieve optimum acceptability at half angle using the edge-ray concept. It was demonstrated that creating lenses larger than 500× Fresnel was feasible.

It may be said that FZPs are widely used tools in many science fields. People use them to make particle accelerators. They also help make terahertz imaging systems, which see heat. FZPs assist astronomy by improving how good telescopes are at seeing X-rays and visible light [78, 79]. Scientists employ FZPs in numerous applications. FZPs are great for making images very detailed and clear. They work well for imaging using X-rays and gamma rays too. Overall, these tools are very helpful in many technical areas. FZPs are very important tools in X-ray and gamma-ray imaging. This is because normal lenses cannot focus short-wavelength radiation like these [80]. FZPs are also

used in particle accelerators. They help separate energy parts, focus charged particle beams, and filter space to make things more precise [81]. In terahertz imaging systems, FZPs are used for security checks, testing without damage, and looking at materials[82].

2.4 | 2D materials

Nanotechnology has been developing for many years, but in the twenty-first century, it really picked up speed. Due to their widespread availability, two-dimensional (2D) materials provide many material substrates for scientific investigation in technology and the development of atomic-level applications [83]. Two-dimensional (2D) materials are characterized as crystalline substances made up of one or a few layers of atoms, where the interatomic interactions are substantially stronger in-plane than they are in the stacking direction[84].

Due to its potential applications in a number of industries, including energy storage, optoelectronics, spintronics, sensors, thermoelectric, photoelectric, and superconductors, the research of 2D materials has recently attracted attention [85–91]. Following the initial isolation of graphene [84], the family of two-dimensional (2D) materials [92] has significantly expanded. With their qualities typically vastly different from their 3D counterparts, the discovery of novel materials is always exciting and riddling. Moreover, 2D materials provide a high degree of control over the tuning of their electrical characteristics. Therefore, altering the number of layers in a particular material can be used to do band-gap engineering [93, 94]. More intriguing is the unique 2D physics seen in these materials [e.g., Kosterlitz-Thouless (KT) behavior, which is characterized by the formation of topological order as a result of vortices and antivortices coupling below a critical temperature]. Transition metal-containing crystals are especially vulnerable to many-body phenomena in stability, including spin density waves (SDWs), charge density waves (also known as CDWs), and superconductivity. If such crystals are positioned between two different 2D materials, then proximity can likewise produce similar effects.

2.4.1 | Van der Waals materials

A platform for the development of heterostructures with a range of characteristics is provided by two-dimensional (2D) materials. Nowadays, a wide family of these materials consisting of crystals one atom thick has a very wide variety of features. When

many 2D crystals are combined into a single vertical stack, a multitude of opportunities become apparent. More combinations are possible with such heterostructures than with any conventional growth process since they are kept together by van der Waals forces, which are also responsible for holding layered materials together [95].

The currently employed method of assembly (micromechanical stacking), allowed for specific interface combinations only. However, a different method—sequential growth of monolayers—that may enable the mass manufacturing of these structures has drawbacks of its own and is still in its early stages of development. Van der Waals heterostructures have, however, previously been used in a wide range of innovative experiments and prototypes, suggesting that these materials are adaptable and useful instruments for upcoming research and applications.

Direct mechanical assembly is the most flexible method for assembling heterostructures Fig 2.16.a. With the work of Dean et al.(2010) [96] demonstrating the extremely excellent performance of graphene devices mounted on a hBN substrate, this approach began to flourish. However, the mentioned approach is regarded as a laborious procedure with a low yield of devices [97]. Thus, methods pertaining to the transfer of large-area crystals produced via chemical vapor deposition (CVD) Fig 2.16.b. Direct heterostructure growth by CVD, physical epitaxy, or one-step growth in solution are now under development.

Many applications, including tunneling devices [98] , photovoltaics [99], and optical sensors [100], have made use of these Vander Waals heterostructures. An electrochemical sensing mechanism for the detection of acetaminophen (AC) was published in 2013 [101] using a biosensor composed of MoS_2 graphene van der Waals heterostructure.

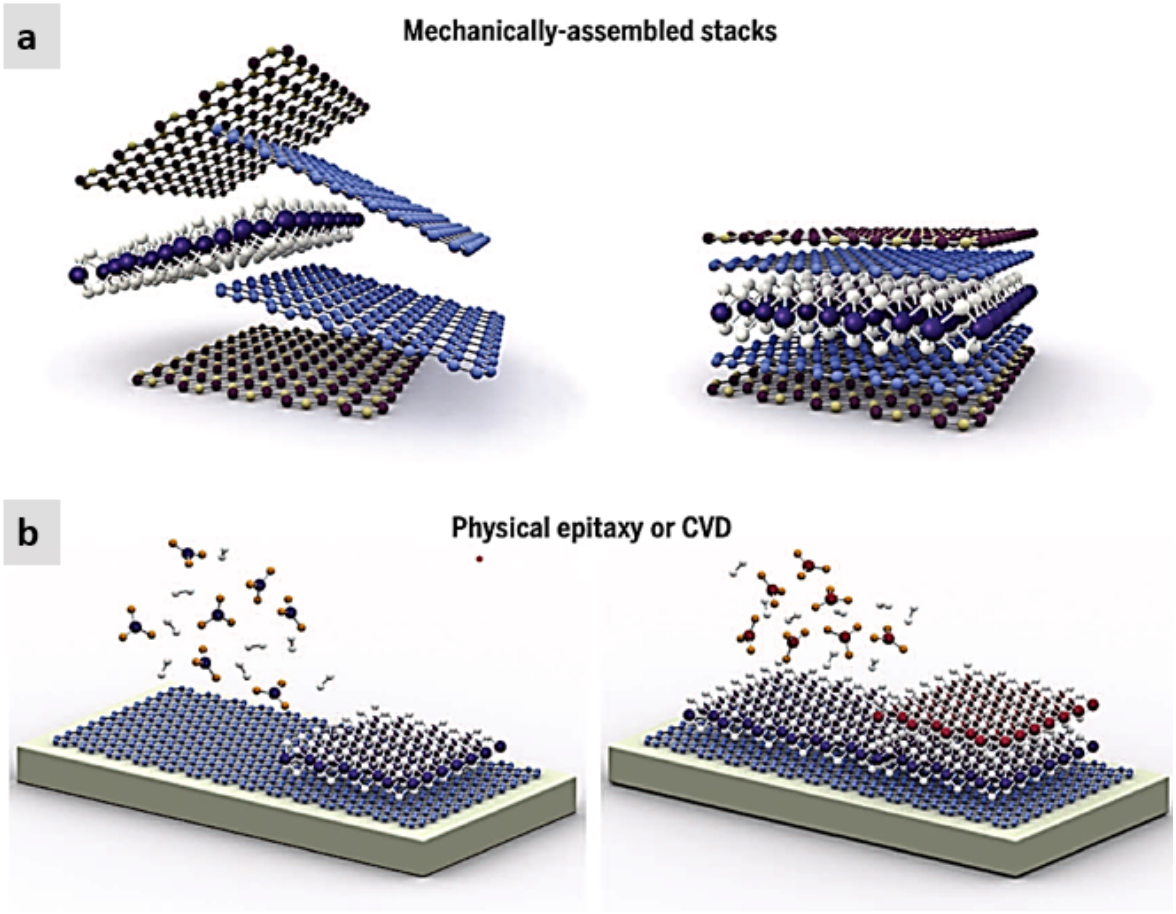

Figure 2.16: Fabrication of van der Waals heterostructures. (a) Mechanically-assembled 2DM stacks using individual flakes. (b) Large-scale CVD or physical epitaxy growth of 2D stacks.(image adapted from [102]).

2.4.2 | Fabrication of 2D materials

There are numerous methods for fabricating 2D materials. Though these methods differ greatly from one another, they can be broadly categorized as either bottom-up methods, which see the desired 2D material generated to specification, or top-down methods, which extract the 2D material from a source bulk material. There are advantages and disadvantages to each strategy, and this section will discuss the two main strategies.

2.4.2.a Top-down techniques

Numerous methods that are often categorized as top-down or bottom-up can be used to create 2D materials. Commonly, bottom-up methods comprise chemical vapor deposition, hydrothermal synthesis, and pulsed laser deposition (PLD), while top-down methods comprise mechanical exfoliation [103], electromechanical exfoliation [104], and solution processing [105]. Various ways for fabricating 2D materials are depicted in a flowchart in Figure 2.17.

Top-down methods are often easier to use than bottom-up methods, but they come with a greater learning curve for managing the thickness of the created 2D material. The most straightforward production method for exfoliating bulk 2D material into few-layer or monolayer structures is mechanical exfoliation, which is carried out by periodically peeling the bulk material using an adhesive tape [106].

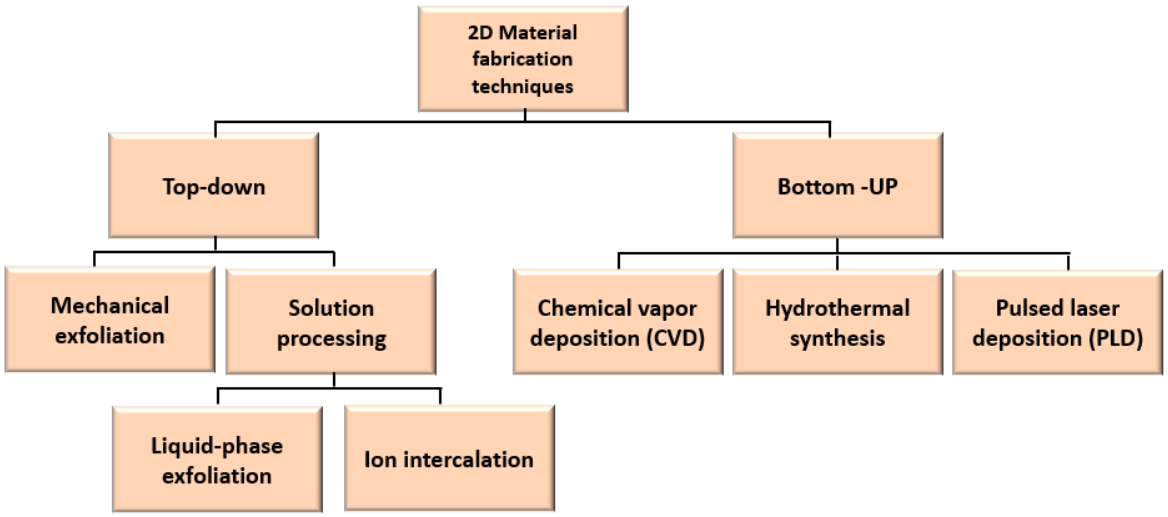

Figure 2.17: An overview of the methods used to fabricate 2D TMDs adapted from [106].

However, solution processing methods are a little more involved and fall into two groups: ion intercalation and liquid-phase exfoliation. The more popular method for creating 2D materials is called liquid-phase exfoliation [107], which entails a number of steps including (i) dispersing the bulk material into a solvent; (ii) sonicating the material; and (iii) centrifuging the material. In order to guarantee optimal dispersion of the two-dimensional substance, the least amount of mixing enthalpy in the solvent

is optimal. Because of its great efficiency, lithium-ion is the intercalant that is most frequently utilized in the intercalation process. submerged for more than 24 hours in a solution containing lithium, such as n-butyllithium. Lithium ions work to improve bulk material interlayer separation, which facilitates the hydrothermal exfoliation process that follows. Lithium ions in between layers react violently with water during the exfoliation process to release H_2 gas. The 2D material layers are separated by tiny bubbles created by the production of H_2 gas.

2.4.2.b Bottom-up techniques

In addition to removing 2D materials from their parent materials or bulk equivalents, bottom-up methods can also be used to grow these nanomaterials [108]. In order to facilitate vaporization, a solid precursor must be heated to a high temperature using the CVD process [109]. On a substrate, the volatile compound created during the heating process will be deposited as a thin layer of 2D material. The concentration of the first precursor can be changed to regulate the eventual thickness of the 2D material film. The nucleation rate of the substrate has a major impact on the formation of 2D material films by CVD. High pressure and temperature conditions are necessary for the hydrothermal synthesis process to produce 2D material. The lateral sizes of 2D materials created by hydrothermal synthesis are frequently in the range of sub-micrometers to a few micrometers. The intended bulk material is ablated in order to fabricate few-layer 2D material films using PLD. During the fabrication process, the bulk 2D material is put in a vacuum chamber and exposed to radiation from a pulsed laser source. The 2D material was extracted from its bulk and subsequently placed onto a substrate by means of a strong-intensity laser beam [106]. The pros and cons of the various top-down and bottom-up fabrication approaches are compiled in Figure 2.18.

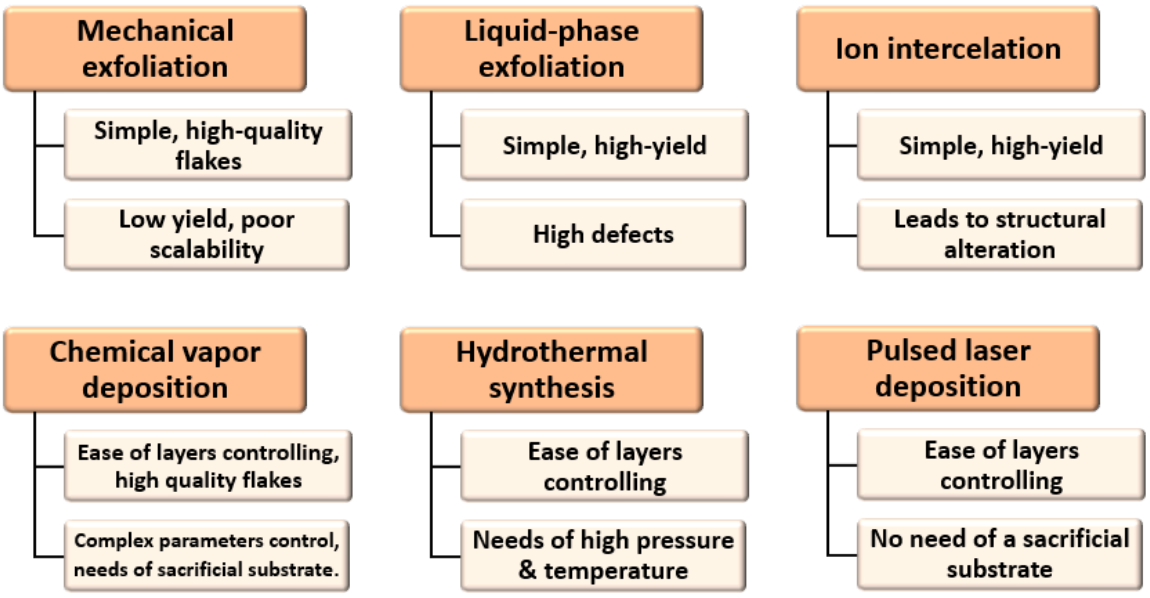

Figure 2.18: Comparison of various fabrication methods comprising (top) top-down and (above) bottom-up. adapted from [106].

2.4.3 | Transition metal dichalcogenides (TMDs)

The transition metal dichalcogenides are one of the main classes of 2D materials that have been successfully manufactured and investigated up to this point, along with graphene, black phosphorus, and topological insulators. 2010 marked the experimental isolation of 2D TMDs, which are atomically thin semiconductors of type MX_2 , where X is a chalcogen atom and M is a transition metal atom [110]. The typical band gaps of TMDs span the visible to near-infrared spectrum, from 1 to 2.5 eV. As the material thickness reduces from multilayer to monolayer, one of the notable characteristics of the TMD group is the indirect-to-direct bandgap transition. This evolution of the band structure is caused by altered confinement effects and the interaction of the adjacent layers. Due to the sluggish and ineffective second-order radiative recombination of indirect excitons aided by phonons, photoluminescence for a bulk or multilayer TMD is insignificant. The TMD shifts from an indirect to a direct bandgap when the thickness is reduced to a monolayer, resulting in an orders-of-magnitude greater photoluminescence enhancement, but with a relatively low quantum yield. The semiconducting TMD may show various absorption peaks from ultraviolet to near-infrared frequencies due

to excitonic and interband transitions, in contrast to the universal optical conductance in graphene. Exciton resonance peaks often occur in two groups, where the optical excitation of electrons from the spin-orbit-split valence band hill to the degenerate conduction band valley at the K point and band nesting, respectively, is credited [106].

TMDs with the chemical formula MX2 usually consist of a plane with the transition metal atoms M (groups 4–10) arranged hexagonally in Figure 2.19 situated in the middle of two hexagonal planes X made of chalcogen atoms (e.g., S, Se, Te). Most of the M-X bonds inside the layers are covalent, and the sandwiched layers are held together by weak Van der Waals forces [111]. TMDs have been known about since the 1960s, and in 1969, a review was conducted on a set of 40 TMDs and their basic characteristics [112].

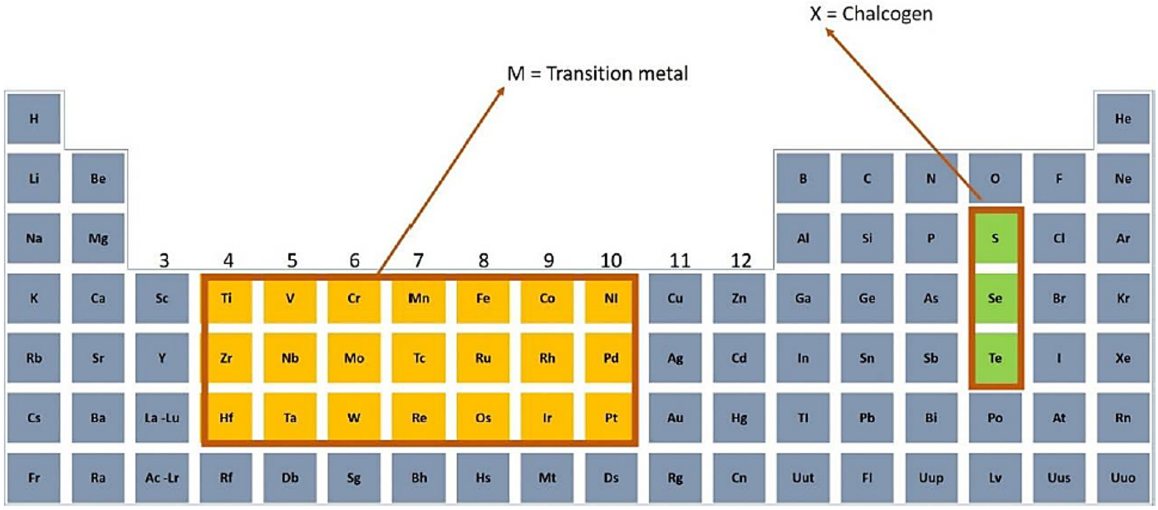

Figure 2.19: Periodic table displaying the components of TMD materials, which include three chalcogen X elements and transition metal M. Image adapted from [113]

2.4.3.a Rhenium Disulfide ReS_2

The last stable element in the periodic table [114], rhenium, was initially discovered in 1925 by Noddack, Tacke, and Berg [115]. One way to conceptualize the atomic arrangement of a ReS_2 layer is as a deformed 1T configuration. Along the lattice's b-axis, the layer is made up of zigzag Re-Re chains (Figure 2.20.a) [116]. Eight S and four Re atoms make up the ReS_2 unit cell as a result of doubling brought on by metal-metal

bonding (Figure 2.20.b).

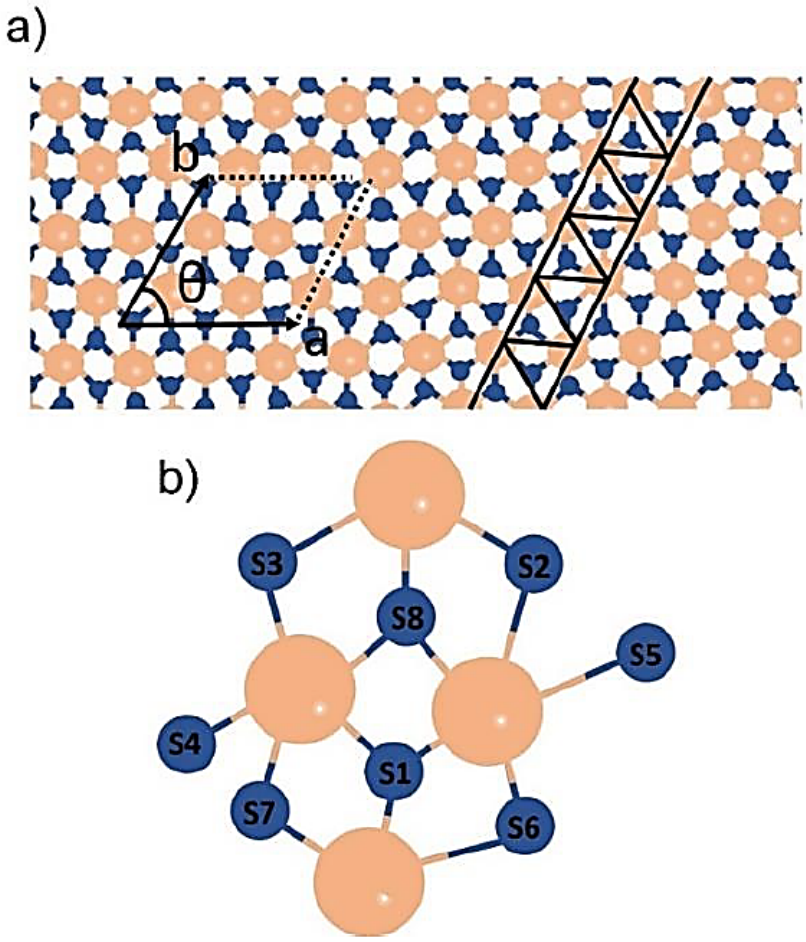

Figure 2.20: (a) Atomic configuration of a single-layer ReS2. Re chains and the unit cell are displayed. (b) Unit cell atom reveals the top view of the ReS2 monolayer. Image adapted from [113].

Due to its unusual electro-optical, structural, and chemical properties, rhenium disulfide (ReS_2) in group 7 has received the most attention lately [117]. In contrast to the very symmetric 2H structures that group 6 TMDs stabilized in, ReS_2 has a unique deformed 1T structure that gives its physical characteristics an in-plane anisotropy [114]. Moreover, bulk ReS_2 acts as electrically and vibrationally dissociated monolayers because of the remarkably small interlayer coupling, resulting in a pronounced layer-independent character in several properties [116]. ReS_2 has various novel uses, including energy storage, optoelectronic devices, catalysis, and sensing, thanks to its special qualities [118–120].

As the first part of this thesis we will describe in detail the fabrication techniques

that have been used in the laboratory to produce the optical elements (FZP). We will describe in detail some problems that had to be overcome during the fabrication of the elements, and taking into account that the solutions had to be compatible with the other steps involved in the fabrication process.

In the second section, we will thoroughly characterize ReS_2 with the goal of applying it to various optoelectronic devices. However, surface, structural, and chemical characterization techniques yield the primary results given here, which concentrate on understanding it behavior at the nanoscale. This segment will specifically address the characterization of ReS_2 using a range of tools, including Raman spectroscopy, atomic force microscopy (AFM), and Kelvin probe force microscope (KPFM).

3 | Methodology

3.1 | Instruments and equipment for FZPs fabrication

3.1.1 | Plasma cleaner

These days, surface cleaning of some kind is an essential first step in nearly all industrial applications. The surface to be cleaned will undergo a chemical reaction when using conventional procedures like heat treatment or chemical treatment [121]. Very thin layers, particularly hydrocarbons, and oxides, that cling after traditional cleaning can be removed with plasma cleaning. Using plasma gases like O_2, H_2 , N_2 , and so on, surface polymer groups are removed to create surface-level novel functional groupings, which is how plasma surface activation is accomplished. Choosing the proper plasma gas is crucial since various gases react and eliminate impurities in different ways. By means of oxidation and reduction, oxygen eliminates impurities. Other neutral gases, such as argon, are surface-cleaned using sandblasting [122].

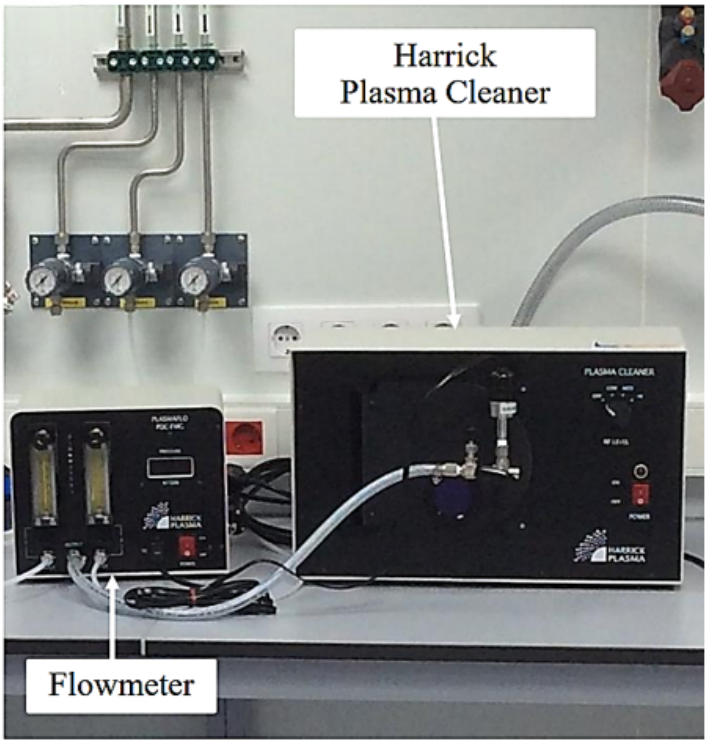

Figure 3.1: Harrick Plasma cleaner

A plasma cleaner machine is needed to accomplish the plasma cleaning procedure; in our lab, we utilize the Harrick Expanded Plasma Cleaner with PlasmaFlo Gas Flow Mixer (See Figure 3.1)which minimizes the danger of thermal damage by enabling the use of ambient air, N_2 , O_2, or a combination at temperatures close to room temperature. Apart from superficial cleaning, many surface engineering applications can make use of our plasma cleaner, such as the activation of surfaces, the change in surface energy, surface adhesion, and bonding preparation, surface chemistry modification, and surface handling of biomaterials and polymers via surface coating, activation, and grafting.

In addition to surface cleaning, another intriguing use of this machine in our study is improving the adhesion of the resistive coat to the substrates. Depending on the materials we use to spin, there are resist materials that stick better or worse to the substrates. For example, polymethylmethacrylate (PMMA) adheres to silicon very well but the same does not happen with Hydrogen Silsesquioxane (HSQ), which has more difficulties. We use radio frequencies to generate an O_2 plasma with this apparatus. Surface flaws and roughness are removed from the substrate by the isotropic interaction between the plasma and the substrate. The smoother the surface, the more contact it will have with the resist, and the higher the probability of the molecules of the resist material sticking to the substrate.

3.1.2 | Resist cabin

By using the principles of surface tension and centripetal force to the creation of homogenous and uniform thin films on surfaces, spin coating is a widely used technique [123]. This procedure is carried out in what is known as the resist cabin Figure 3.2.b, which houses two hot plates and a spin coater SÜSS MicroTec with an 8000 rpm maximum speed. During this process, a tiny quantity of solution is dropped into the substrate's center, covering the majority of it. The substrate is then spun at a high speed for a predefined period (a few seconds) in order to disperse the coating material across the substrates uniformly. If the substrate spins during the injection of the material's precursor solution, the process is referred to as dynamic spin covering, otherwise, it is known as static spin coating. A vacuum is required so that the substrate stays

on the rotating holder throughout the coating process. Lastly, the hot plate is used to bake the resist. Wet etching, cleaning, and lift-off procedures are commonly carried out using the magnetic hotplate and ultrasonic cleaner located in the chemical cabin. A diagram illustrating the spin-coating process method of thin film creation is presented in Figure 3.2.a.

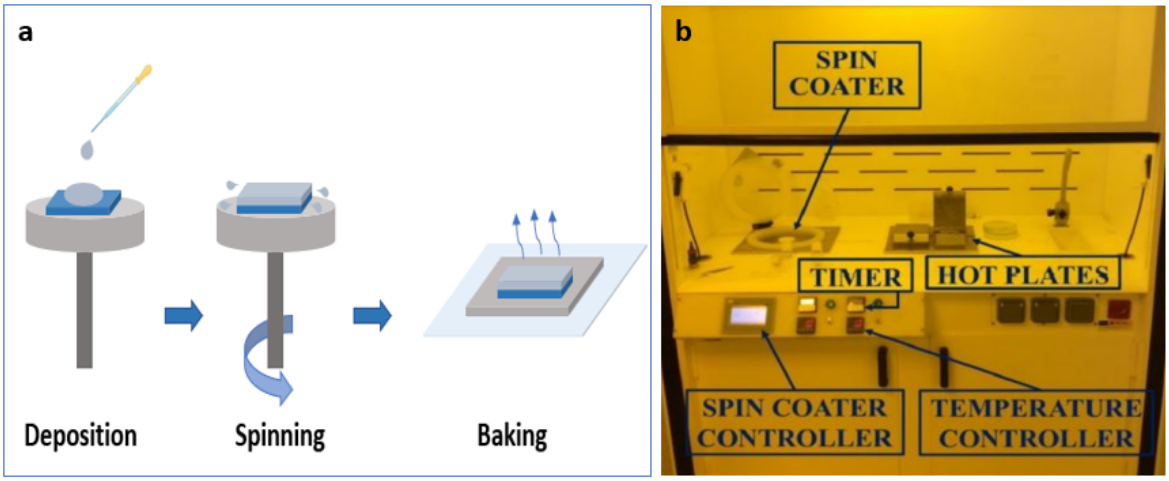

Figure 3.2: **(a)**Diagram showing the spin-coating steps for thin-film deposition. **(b)** the resist cabin which prominently displays the spin coater, timer, two hot plates, and the controllers of temperature and coating recipes

A benefit of the spin-coating method is its ability to cover homogenous thin films with varying thicknesses quickly and effectively. Although the technology is cost-effective, it has certain limitations, such as using just one substrate and losing a large amount of solution (between 80% and 90%) during the spin-coating process [124].

3.1.3 | E-beam evaporator

Whenever one wants to evaporate materials with a high melting point, the problem of choosing the right material for a resistant or thermally heated boat always arises. This issue is solved by the electron beam (e-beam) technology, which heats the source material from the same direction that the evaporant exits [125]. At comparatively low substrate temperatures, the electron beam evaporation technique produces a high rate of deposition ranging from 0.1 μ /min to 100 μ/min by physical vapor deposition. Many different choices are available for regulating the shape and structure of films, with

the goal of achieving certain attributes like high productivity, minimal contamination, high thermal efficiency, dense coating, and high dependability [126]. Through the use of electromagnets or permanent magnets, an electron beam produced by an e-beam cannon is directed and accelerated toward the substance to be evaporated. The electrons will lose energy when the e-beam is focused on the material; nevertheless, the electrons' interactions with the substance will transform that energy into various forms. The heat generated by the electrons causes the evaporating material to heat up and either melt or sublimate. The substance will finally begin to evaporate from the melted material or sublimate from the solid material if appropriate evaporation conditions have been met [127].

- **Tecnovac E-beam evaporator with Telemark e-beam gun emitter:** Two separate chambers make up the e-beam prototype that our lab team designed with Tecnovac's assistance. Figure 3.3.a shows how a manual guillotine may be used to join or separate them. Typically, the bigger main chamber operates at a high vacuum ($10^{-}9$ mbar or below). When the chamber reaches an appropriate pressure range (lower than $10^{-}5$ mbar in less than 60 minutes), the sample is loaded and unloaded using the smaller secondary chamber, also known as the load-lock chamber Figure 3.3.a. High control over the evaporation rate (less than 1 Å/s) is ensured by the great distance (nearly 1 m) between the material and the sample and the extremely low pressure during operation, resulting in high homogeneity thin layers on the samples but with a significant metal consumption. A quartz crystal that is managed by a TTL (Transistor-Transistor Logic) controller measures the rate of evaporation as well as the thickness of the vaporized metal. The device is furnished with a Telemark e-beam gun that uses an e-beam source model 244 to produce electrons through a tungsten filament (see image 3.3.b.).To keep from becoming polluted by evaporant, the emitter assembly is placed outside of the evaporation zone. The equipment is controlled by means of an external rack. Applying a tiny emission current to the filament allows it to become hot enough to excite the filament to release electrons when it reaches a certain temperature. In our framework, electrons are applied at a high voltage

(8 kV) and are guided to the center of the pocket containing crucibles containing various metals (the target) by the magnetic field. These metals may first take the form of rods or ingots (Figure 3.3.c,d). The magnetic fields load and sweep the e-beam over the whole crucible during the "XY Sweeping" process, ensuring that all of the material evaporates uniformly. It is possible to evaporate and apply a thin film coating to the sample.

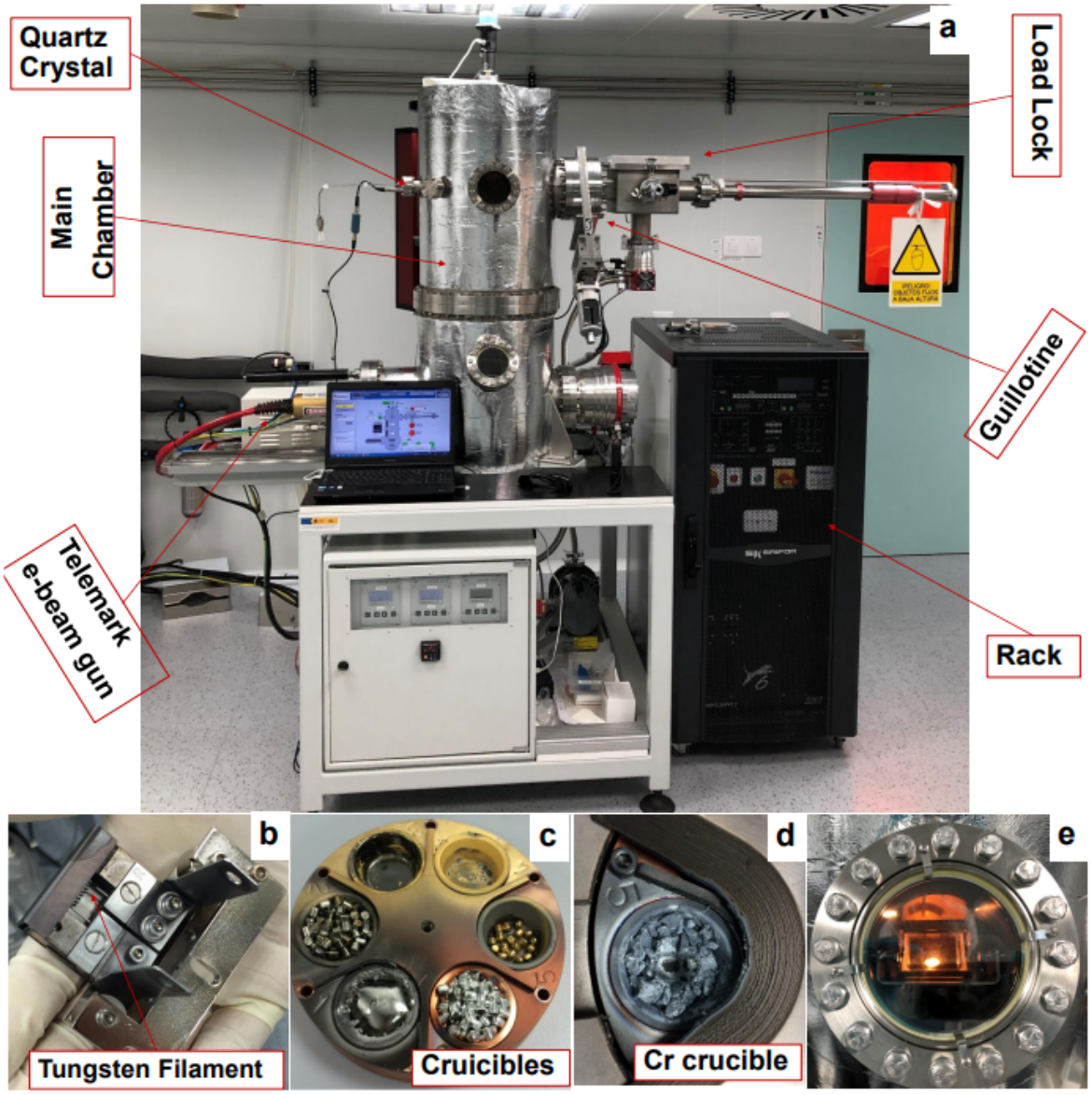

Figure 3.3: **(a)** Tecnovac invented an e-beam evaporator that uses a Telemark e-beam cannon. **(b)** Model 244 (E-beam source). **(d)** Detailed Cr-crucible; **(c)** Crucible pocket. **(e)** A picture taken during an evaporation, seen from an inside periscope through an exterior window. Image adapted from [127].

Figure 3.3.e. depicts a typical evaporation process in which the metal is heated

as the emission current is raised until it turns into a gas. The e-beam evaporator in our system can evaporate many materials (Au, Cr, Ti, Al, Ni, Co, Pt) including dielectrics SiO_2, Al_2O_3, HfO_2). Since evaporating ohmic connections is the primary goal of the machine, its application is really restricted to metals in order to prevent any contamination with dielectrics.

3.1.4 | FE-SEM and Raith nanolithography system

FE-SEM

Zworykin described and created the first scanning electron microscope (SEM) in 1942. He demonstrated how secondary electrons (SE) offered topographic contrast by biasing the collector positively with respect to the specimen. By pre-amplifying the SE emission current with an electron multiplier tube, he was able to achieve a resolution of 50 nm [128]. Field emission, which emits electrons using a field emitter gun (FEG), is the sole electron source intended for high-resolution imaging of a variety of materials [129]. The emission capability of these electron emitters is up to 1000 times greater than that of a tungsten filament. But they did require far higher vacuum levels [130]. the combination of SEM and a field emitter gun creates the so-called Field Emission Scanning Microscope (FE-SEM), Thus, in order to differentiate it from the traditional SEM, the emitter type is included in the nomenclature.

The field emission scanning electron microscope is one type of electron microscope that takes pictures of a sample surface using a high-energy electron beam that is scanned in a raster pattern. this technique allows us to observe structures that may be as small as 1 nanometer (= billion of a millimeter) [131]. With a significantly brighter electron source and a smaller beam size than a standard SEM, the FE-SEM can see and image objects up to 500000 times more clearly than a regular SEM [132]. Moreover, An FE-SEM differs from a normal SEM in that it features a field emission cannon that enables the use of low-energy, highly focused electron beams. This feature includes the ability to operate at very low potentials (0.01–5 kV) and increased spatial resolution. By using a low voltage, the charging impact is minimized and the risk of damaging delicate samples, like 2D materials, is decreased [133]. In the domains of nanomaterials research,

the FE scanning electron microscope is a highly helpful instrument for high-resolution surface imaging [134].

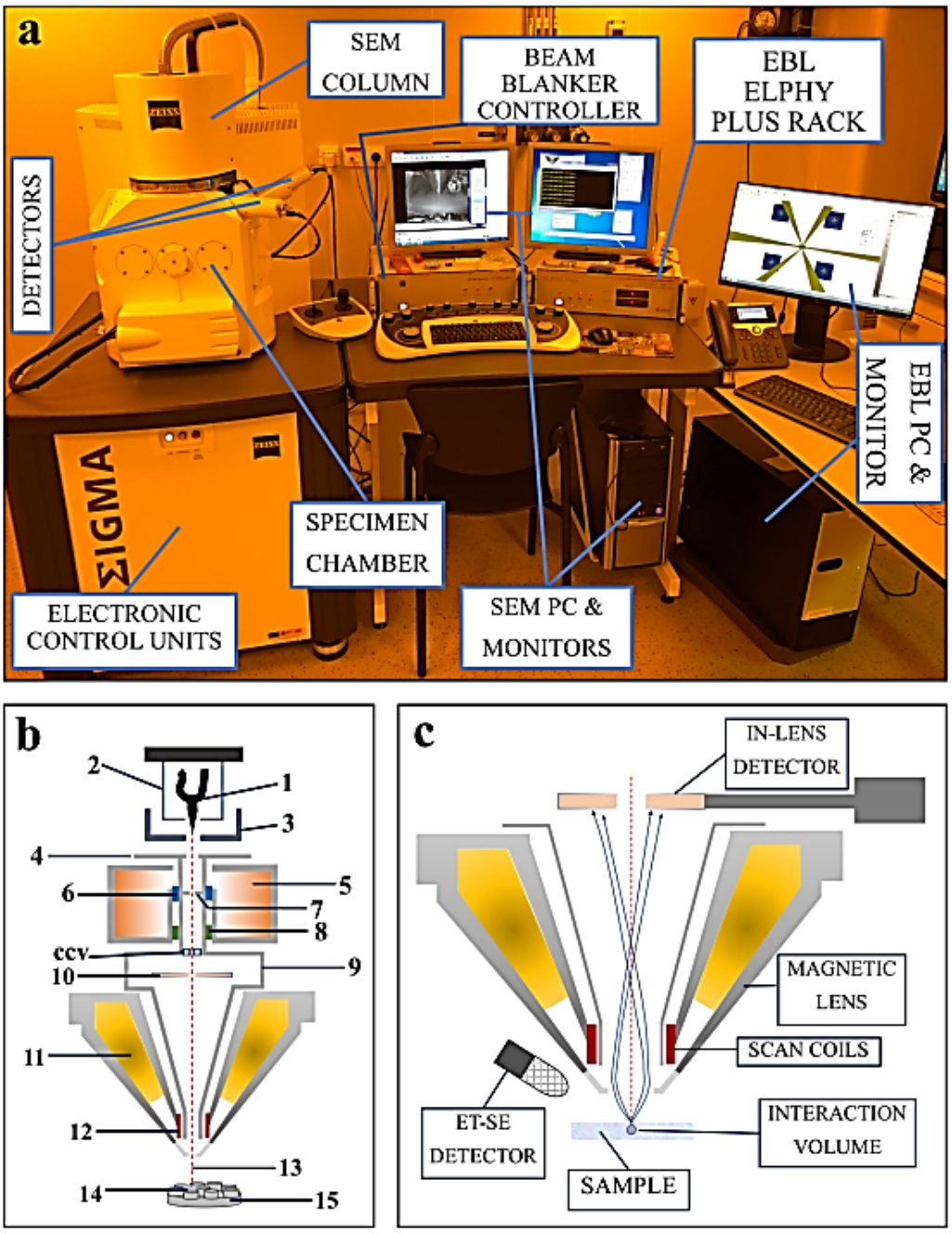

Figure 3.4: **(a)** An image of our clean room featuring the Raith nanolithography machine and the FE-SEM with its major components.**(b)** FE-SEM schematic illustration: Filament (1), suppressor electrode (2), extractor electrode (3), anode (4), condenser lens (5), gun/aperture alignment system (6), multi-hole aperture (7), stigmator (8), liner tube (9), In-lens detector (10), electromagnetic lens (11), scan coils (12), primary electron beam (13), specimen (14), holder (15), column chamber valve (CCV) **(c)** A sketch showing the locations of the ET-SE detector and In-Lens detector (2) in relation to the column and specimen. Image adapted from [127, 135].

Figure 3.4.(a) provides a schematic picture of a typical FE-SEM with a Zeiss Gemini column and its major parts located in the clean room of our nanotechnology lab. Bundled high-energy electrons produced in the source are the fundamental energy source for electron microscopes. These electrons are released in the filament shown in figure 3.4.(b), position (1), under the suppression electrode's control (2), and gathered through the extractor (3), and at last picked up speed towards the anode (4). Before being collimated by the aperture (5), the electron beam exits the source and travels via the anode's and the condenser's boreholes (7).

Filaments in EBL can be made of a variety of materials, which are closely tied to the various operating theories and anticipated characteristics. A modest vacuum ($10^{-6} - 10^{-7}$ mbar) was suitable in the pioneer systems when thermionic filaments (W and LaB_6) were frequently utilized. These devices free electrons from the well-known thermal electrode emission, which is achieved by raising the filament's temperature to the point where the carriers' energy exceeds the material's work function [136]. The progression of thermionic sources is represented by Schottky sources, often referred to as thermal field emission sources. These sources are based on tungsten filaments coated with zirconium oxide. They can be found in several of the most recent EBL system versions [137]. Because of the reduction in their operating temperatures, electron tunneling brought on by electric field-induced emission is predominant. The emission current is significantly increased by the combination of the ZrO coating, which decreases the work function to be overcome, and the sharp tips, which locally improve the electric field at their apex, so lowering the energy barrier.

Following the creation of the electron beam at the source, it has to be directed and focused by the optics in the column. The e-beam is bundled and deflected by magnetic or electrostatic lenses (see position 11 in Figure 3.4(b)). The electron beam will be guided by electromagnetic fields, much like in geometric classical optics. In an electron microscope, access to high-resolution beam spots is permitted when the electron wavelength λ is reduced, much like in optical microscopes where the resolution is constrained by diffraction inside the various lenses and relies on the wavelength of the light itself. The momentum and the wavelength λ are connected by the following

formula:

$$\lambda = \frac{h}{p} \tag{3.1}$$

where h is the Planck constant ($h = 6.626 \times 10^{-34}$ J·s) and p is the momentum of the electrons. We may represent the electron wavelength λ as a function of the accelerated voltage V using the relativistic equations [130].

$$\lambda = \sqrt{\frac{1.5}{V(1 + 10^{-6}V)}}\,\text{nm} \tag{3.2}$$

where a nominal resolution of 0.017 nm may be obtained for a typical value of the accelerated voltage (5kV).

The vacuum tube has many mounted apertures. They can effectively be used to restrict the beam (lessening the quantity of beam striking the specimen) or to disrupt it. The majority of SEMs use 30 microns as the standard aperture for imaging processes; however, for EBL in particular, various apertures (usually 7.5, 10, 20, 30, 60, and 120 microns) are available in any commercial system, allowing one to obtain a good compromise between resolution and exposure time.

A scanning electron microscope , uses the electron beam's deflection as it passes through scan coils, also known as deflector plates, to scan the sample's surface (see position 12 in Figure 3.4 (b)). The electron beam begins to scan in a raster style across a rectangular region of the sample's surface with extremely high accuracy where it is deflected in the X or Y direction by the magnetic field (or electric field in the case of the deflector plate) that is formed in the scan coils. Based on magnification, the size of the scan field on the sample is selected. The magnification is determined by calculating the ratio between the field's dimensions on the SEM display and its actual size on the sample. Higher magnifications are possible because the SEM screen's size is fixed., which shrinks the size of the field on the sample.

Important details about the sample, such as its location, topography, size, and shape, will be returned to us by the interaction between the beam and the specimen beam. Electrons near the sample's surface will get a portion of the incident electron

beam's energy when it interacts with it; these electrons may eventually escape the specimen. If their energy is less than 50 eV, they are called secondary electrons (SEs), and if their energy is more (up to the original beam's energy), they are called backscattered electrons (BSEs). In the EBL method, resist exposure can be achieved by the employment of BSEs and SEs for imaging.

Selective SEM detectors can be used to gather the electrons that are exiting the sample. The most common ones in commercial systems are the Everhart-Thornley and In-Lens detectors (figure 3.4(c)). They employ two distinct types of secondary electrons for their work:

- **SE1:** These are directly created when the beam hits the sample and are expelled from the surface close to the impact point of the incoming beam—possibly as near as a few nanometers.
- **SE2:** These particles are produced by repeated scattering within the specimen and are released from it up to a few micrometers away from the incoming beam's impact point.

For non-conductive samples, In-Lens detectors (figure 3.4(b)) are useful because they can capture high-quality topography and compositional images of the surface at relatively low applied energy (approximately 5 kV). These detectors are typically mounted inside the electron column of the microscope and gather BSEs and SEs that are emitted from the sample's surface.

The SEs are collected using Everhart-Thornley (ET) detectors, which are positioned laterally and intended to function over a range of working distances of 5 to 12 mm. The ET-SE detector is seen on the lower left corner of figure 3.4(c)). The primary use of ET detectors is topographical imaging; tilted sample scanning increases their sensitivity.

The chamber in which the specimen is inserted and the cannon are separated by a column chamber valve (shown as CCV in Figure 3.4(b)). Where the cannon is positioned, the normal pressure range with the usage of an ion-getter pump (IGP) is 10^{-10} mbar. Turbo pumps, which typically have a pressure of 10^{-6} mbar, are responsible for

creating the vacuum in the sample's main chamber. There are several ways to install and arrange the sample within the various holders that are accessible. These can be secured using pressure clamps, screwed directly, or adhered to with a certain type of double-sided conductive tape. The many standards needed for the astigmatism, focus, and current calibration are usually housed by sample holders.

FE-SEM ADVANTAGES

- the capability of using energy dispersive spectroscopy to scan smaller contamination areas at electron-accelerating voltages [132].
- Probes with low kinetic energy electrons have less difficulty penetrating materials when they are near the surface.
- Superior quality, low voltage pictures with little or no electrical charge of items that accelerate voltages between 0.5 and 30 kV [131].
- Essentially, insulating materials don't require conducting coatings to be applied.

Raith (Elphy Plus) nanolithography

A Raith (Elphy Plus) nanolithography equipment is included with our FE-SEM to facilitate the creation of an appropriate lithography configuration.

In electron beam lithography [138, 139], an exposure is created by concentrating an accelerated electron beam on an electron-sensitive resist [140, 141]. Then, to create sequential patterns, this electron-beam spot, which has a diameter of only a few nanometers, is scanned dot-by-dot across the resist surface. PMMA (polymethyl methacrylate), which is made up of large organic molecules, is the most widely used as an electron-sensitive resist. When an electron beam is directed towards a PMMA, the molecules are broken up into little fragments that are readily dissolved by the developer. As a result, the illuminated areas by the electron beam during development vanish, which is why the PMMA resist is known as a positive resist [142]. HSQ (Hydrogen Silsesquioxane) is also a well-known negative resist, among other prominent ones. Earlier research has demonstrated that the HSQ has the characteristics of an inorganic e-beam resist with

a negative tone and high resolution, producing single lines that are smaller than 10 nm [143] Fig.3.5.(a).

An EBL instrument may be used for two different types of pattern generation: vector scanning Fig.3.5.(c) and raster scanning Fig.3.5.(b). When a controlled stage moves the substrate beneath the beam, the exposing beam is scanned in a single direction at a set rate using a raster-scanning system to pattern the substrate. With every scan, the electron beam is blanked on and off thousands of times to create a predetermined pattern. It is comparable to a television's raster scanning. By directing the exposure beam just toward the areas of the substrate that need to be exposed, the vector-scanning approach aims to increase throughput. Because the beam bypasses the areas without a pattern, a substantial amount of time may be saved by this method [144].

Following the developing process, the exposed resist either stays on the substrate or departs it, depending on the tone, and the weaker chemical bonds are eliminated. There are several uses for the sample's resist mask [145]. In etching procedures, it can be employed as a mask to shield the covered portions, allowing the etched areas to be free of resist [146]. Another alternative has to do with metal evaporation, in which case all of the metals are deposited on the sample,but only the metals associated with the sample remain after the well-known lift-off procedure, and the metal deposited on the resist is removed along with the resist [147].

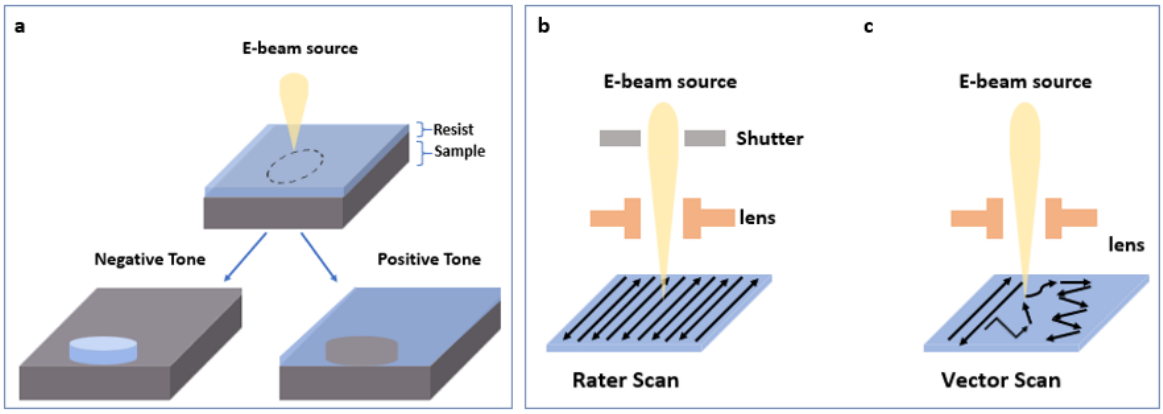

Figure 3.5: **(a)** Diagram illustrating the exposure procedure for electron beam lithography.**(b)** Rater Scan. **(c)** Vector Scan.

With the help of Elphy Plus, an electron beam writing system used in conjunction

with an FE-SEM, it is possible to build micro- and nanostructures. With a digital control unit and a separate thermocontrolled analog electronics box, the hardware assembly is housed on a 19" rack. It features a video out to a display (BAS out) and an X-Y beam shift input. With the help of an integrated SCSI interface, the PC data system may fully operate the electronics units remotely [127].

Our nanolithography equipment has an electronic beam-blancked controlled device in addition to the ELPHY Plus rack. Positioned on the SEM column is the beam-blanched hardware. There are two parallel plates that make up this structure; one is grounded while the other is linked to a high voltage. The electrons are able to enter the sample through a spray aperture when the voltage is zero. In contrast, electrons are deflected and are prevented from reaching the specimen by the aperture when a nonzero voltage is applied. a TTL voltage from the ELPHY Plus rack is accepted by The Beam Blancker control unit is a high-voltage power supply.

The Raith Elphy-Plus system has several useful features, such as bit-mapped pattern exposure, support for data representation in polar coordinates (which significantly reduces the amount of data needed to represent circles), and a "path writing" mode. The stage is moved along the length of the line or curve while the beam is guided in a circular pattern to define the width of the line in the path writing mode. Although it takes longer to write a long line this way, stitching mistakes that are spatially specific are avoided. Rather, the mistakes related to placement and drift are averaged across the feature's length. In addition to being utilized for SEM conversions, the Raith Elphy-Plus serves as the pattern generator for Leica's LION-LV1 e-beam system [148].

3.1.5 | Inductively Coupled Plasma Etching (ICP-RIE)

Etching is a popular procedure that comes after electron beam lithography (EBL) in nanofabrication, and depending on many factors, including the materials being used and the desired outcome, it might be wet or dry etching. Although wet-etching procedures are primarily dependent on chemical exchanges and usually exhibit remarkable selectivity, they are typically isotropic since the liquid solution moistens both the bottom and the construction's lateral walls. Strongly basic or acidic solutions or tempera-

tures significantly higher than room temperature are needed for wet etching [149]. Wet etching is frequently thought of as a low-cost, dependable technique that works well in large production settings with good selectivity [150]. On the other hand, dry etching is frequently an anisotropic process in which the target materials are physically removed and etched utilizing an advancing ion species velocity toward the substrate in conjunction with a masking approach [151]. This etching technique has the potential to etch tiny patterns with a higher aspect ratio and a smaller undercut as compared to wet etching [152].

Planar etching (PE), deep reactive ion etching (DRIE etch), inductively coupled plasma etching (ICP etch), and reactive ion etching (RIE) are some of the many dry etching techniques. All of the etching methods previously discussed require plasma, but they vary from one another in terms of how the electrodes for plasma formation are set up. In physics, plasma is a conductive medium for electricity created when atoms in a gas get ionized without direct contact with the material being processed. It is composed of charged ions, electrons, neutral radicals, and other neutral species, (e.g., excited molecules)[153]. Radiofrequency (RF) energy, microwave radiation, and electromagnetic (EM) fields ionize the gas, which is regarded as a plasma source, with an energy greater than the binding energy of an electron of the gas atom/molecule. The atom or molecule determines the ionization energy, which for our gases varies from 11.6 eV in Cl_2 to 15.7 eV in Ar. In the dry etching process, reactive ion combination selection, temperature control, as well as time procedure are critical parameters [150]. Once the EBL process is complete, or patterned polymer (i.e., resist), functions as a mask to transfer the patterns to the substrate by an etching approach Fig.3.6.(a). where the sections behind the mask will remain safe while the exposed parts will be etched.

let us describe the reactive ion etching (RIE) or ICP-RIE processes that are the most important techniques in our study. High resolution can be attained via reactive ion etching (RIE) as well as ICP-RIE, which combines chemical and physical principles. In both industry and research, the procedure is among the most varied and often employed. The procedure is significantly quicker since it incorporates both chemical and physical interactions. The etchant molecules split off into more reactive species as a result of

the high-energy collision caused by the ionization.

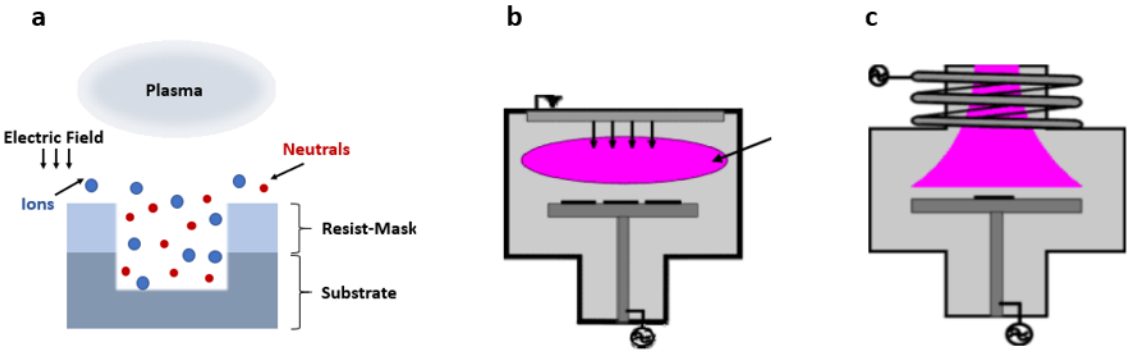

Figure 3.6: **(a)** A typical procedure for plasma etching.**(b)** Working principle of RIE process.**(c)** Working principle of ICP-RIE process.Image adapted from [127]

The first step in the RIE process is to apply a powerful radiofrequency within a vacuum chamber at low pressure to a substrate, which is usually a silicon wafer covered in a patterned mask (i.e., resist, metal). During the etching process, plasma can react in different ways with the sample surface: ion-assisted chemical reaction, radical chemical reaction, and ion bombardment (sputtering). To achieve a vertical profile in the etching process, anisotropic etching requires ion bombardment to facilitate the reaction. Conversely, in processes with pure chemical etching (similar to wet etching), ion bombardment is not needed, and in this instance, the etching lacks direction. When an inert gas, like argon (Ar), is introduced, the ions in it accelerate, strike the substrate, and split the atomic bonds there. The etching rate is higher in the vertical direction because those ions clash more on the horizontal surface than on the sidewalls. since Etching proceeds more quickly in a vertical orientation, whereas sidewall etching proceeds more slowly. Better anisotropy can only be attained by actively protecting the sidewall [152]. The primary distinction between RIE and ICP-RIE is seen in Figures 3.6.(b),(c). In contrast to RIE, an ICP-RIE has a physical barrier separating the acceleration of ions from the plasma formation, that is accomplished via an inductive coil. As a result, an ICP-RIE has greater control over the etching process than a regular RIE. This includes deeper etching due to increased confinement and ion flux homogeneity with a more powerful plasma.

PlasmaPro 100 Estrelas system

In our laboratory, reactive ion etching and inductively coupled plasma are both possible with the PlasmaPro 100 Estrelas system (Figure 3.7), wherein plasma production at 13.56 MHz is achievable. The employment of various gases and, consequently, different plasmas allows for the etching of a variety of materials, including dielectric, metals, semiconductors, organic compounds, etc. This mechanism can load wafers up to 4 inches in diameter. Other than He and N_2, which are utilized for wafer stability management and venting, our system has access to a variety of gas lines, including O_2, Ar, H_2, CH_4, SF_6, C_4F_8, CHF_3, Cl_2, and BCl_3, and BCl_3. Their application is dependent on the material (and mask) that has to be etched.

The DC bias parameter in our system allows us to gather important real-time process information. It is characterized as the wafer electrode's average direct current (DC) offset from zero (earth potential). The cause behind DC bias is the faster electrons (about 2000 times faster than ions) that are produced in the process. These electrons charge a blocking capacitor and respond quickly to changes in electric fields at RF frequencies. Our equipment is accoutered with a cryogenic module allowing it to work below $-120°$ to perform cryo-etching.Furthermore, it features an endpoint detector interferometer system that gives complete control over the etching throughout the procedure.

Figure 3.7 shows the current configuration of the etching equipment in our lab, where only the load lock (used to load and unload samples) and one of the two controller PCs are located within the clean room (Figure 3.7(a)). The technical room houses the majority of the equipment, which includes the gas line, pumps, nitrogen tank, and Clean Solution (CS) system for the disposal of harmful gases (Figure 3.7 (b)).

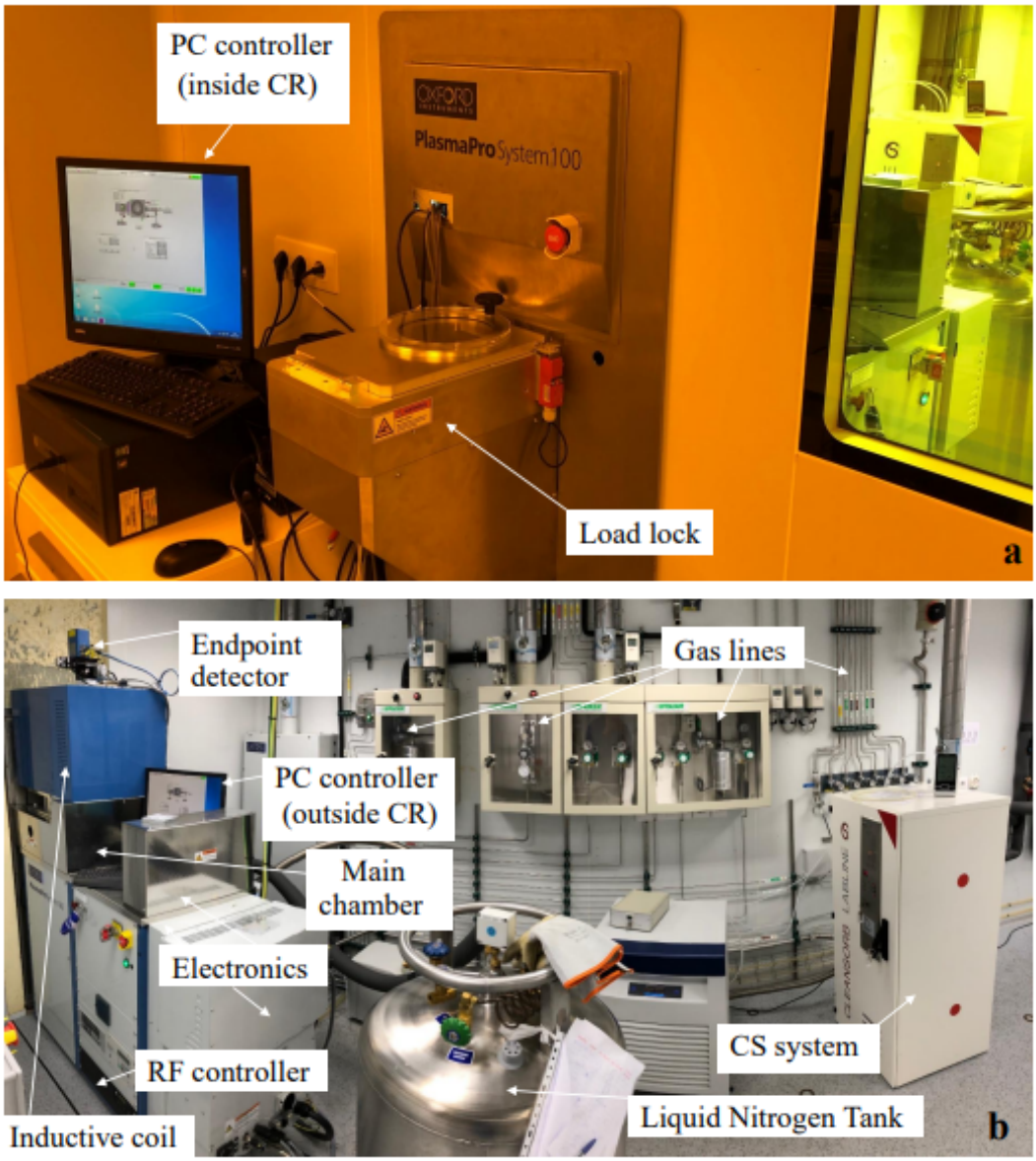

Figure 3.7: **(a)** ICP-RIE load lock and PC controller inside the clean room.**(b)** The remaining of the equipment installation in the technical room. image took from [127]

3.2 | Instruments and equipment used for 2D materials characterizations

3.2.1 | LabRam HR Evolution MicroRaman spectroscopy

The vast opportunities that Raman Spectroscopy presents for identifying molecules as well as learning about their structure and characteristics. This novel scattering effect

was discovered in India in 1928 by Chandrasekhara Venkata Raman. For nearly a decade, the approach was widely and infrequently employed, laying the groundwork for molecular spectroscopy.The first Raman microscope was introduced independently in 1974 at the National Bureau of Standards (Washington) and in Lille, France [154].

In our lab, the MicroRaman is situated in the technical room, which is not within the clean area (see Fig.3.8). Its application is essential for the quality control of stacked heterostructures and the characterization of hBN, graphene, and other 2D materials.

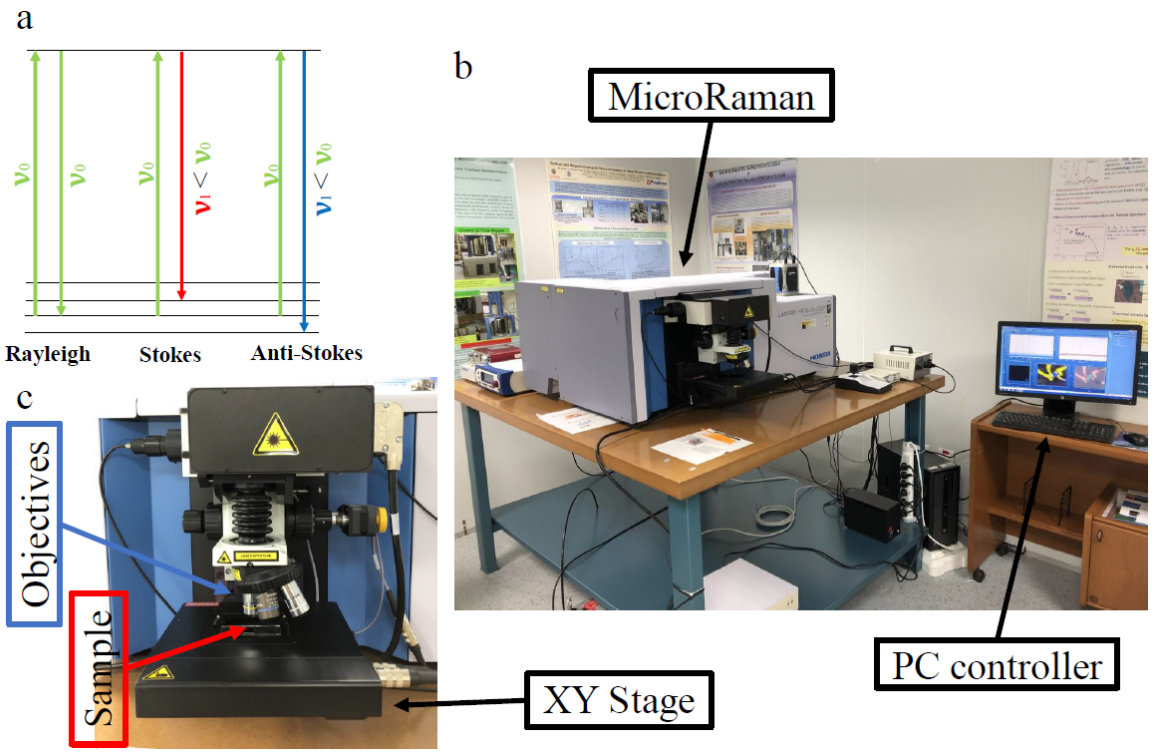

Figure 3.8: **(a)** Rayleigh, Stokes and Anti-Stokes processes. **(b)** LabRam HR Evolution MicroRaman. **(c)** Front view of the equipment. Image adapted from [127]

Principles:

A material can interact with an electromagnetic wave (usually UV, visible, or infrared light) in two ways: it can be scattered or absorbed. One way to divide the final procedure is as shown in Figure 3.8.a:

Rayleigh elastic scattering: The energy and wavelength (same frequency)of photons are identical to those of the incident light.

Raman inelastic scattering (Stokes): The photons that are incident have a

higher wavelength and a lower frequency, indicating lower energy.

Raman inelastic scattering (Anti-Stokes): The photons that are incident have a smaller wavelength and a greater frequency, indicating increased energy.

Raman spectroscopy uses the Raman effect, which is based on the inelastic scattering of photons, to examine low-energy excitations of a chemical or physical system, such as vibrational rotation.Just one out of every $10^5 - 10^8$ photons has a Raman scattering process, indicating a very low chance of the inelastic scattering process respecting a Rayleigh process. Raman spectroscopy therefore requires a strong, monochromatic laser source.The information pertaining to the intensity of light scattered by a material, or the quantity of scattered photons, is provided by a Raman spectrum as a function of the frequency shift with regard to the stimulating incident light. In a Raman spectrum, wavenumber ($D_w = \frac{1}{\lambda_0} - \frac{1}{\lambda_1}$) sually takes the place of frequency. A Raman spectrum can provide several types of information about the sample based on the quantity, location, height, and width of its peaks and bands in the spectra.

MicroRaman :

Raman measurements were performed using the Micro Raman Spectrometer – LabRAM HR Evolution (Figure 3.8(b)(c)). In order to provide light, the apparatus uses three distinct lasers:

- Ventus Solo laser at 532 nm with an output power of 100 mW.
- He-Ne laser at 633 nm with an output power of 17 mW.
- Diode laser at 770-795 nm with an output power $>$ 200 mW.

The confocal imaging capabilities of the LabRAM HR system allow for the acquisition of both macro and micro measurements in two and three dimensions. it has three distinct aims With a lengthy working distance of 10x and 50x and a very high resolution of 100x at a very short working distance. Attenuation of incoming light can be achieved using filters up to 0.01% of the output power. The Raman spectrum's range can exhibit a frequency shift starting at a comparatively low wavenumber (cut-off 50 cm^{-1} and ending with an accurate step below 2 cm^{-1}.

The XY motorized stage (Figure 3.8(c)) allows for a 0.05 mm step. After being gathered in a confocal configuration, the scattered light is examined using two distinct diffraction gratings (1800 grooves/mm or 600 grooves/mm). A Synapse CCD detector with 256x1.024 pixels and a spectral range of 200–1.050 nm is used to obtain Raman spectra.

There are many different uses for Raman spectroscopy. These comprise not just conventional quantitative and qualitative analysis but also scalable imaging techniques used in microscopic applications, depending on the characteristics of the target samples. Both inorganic and organic chemical species can be studied using Raman spectroscopy. Numerous electron atoms, like metals found in coordination compounds, typically have a large number of loosely bonded electrons, making them Raman active. Compound composition, structure, and stability can be determined by using Raman Spectroscopy to provide information on the metal-ligand link.Metal compounds with low vibrational absorption frequencies in the infrared can benefit greatly from this.Determining the functional groups and fingerprints of organic compounds is another area in which Raman is highly helpful. Because molecules vibrate as a whole rather than in small groups, Raman vibrations are frequently very distinctive to a particular molecule. The vibrations of the groups that do show up in Raman spectra are generally concentrated inside the group and frequently involve several bonds [155].

3.2.2 | Atomic force microscopy AFM

Atomic force microscopes and scanning tunneling microscopes (STM) are the two main types of scanning probe microscopy (SPM). Gerd Binnig and Heinrich Rohrer conceptualized and built the first STM in the early 1980s, for which they were awarded the Nobel Prize in 1986. A STM measures the tiny tunneling current between a sharp tip and a conductive surface, creating atomic-scale images of that surface. The fact that STM can only scan materials that have the ability to conduct a tunneling current, however, is by far its greatest drawback. In order to get over it, Binnig and Quate created the Atomic Force Microscope in 1986 [156].

In surface science, AFM remains one of its primary tools. A major advantage of

AFM is its ability to image surfaces with atomic-scale resolution, enabling detailed analysis of surface morphology, defects, and lattice structures Its versatility extends to evaluating mechanical, electrical, and magnetic properties. [157–160]. Its versatility extends to evaluating mechanical properties such as elasticity, adhesion forces, and viscoelastic behavior through force spectroscopy [161–163].AFM operates in multiple environments (air, liquid, vacuum), making it indispensable for studying biological systems like cell membranes, protein interactions, and bacterial adhesion in physiologically relevant conditions [164–167]. Also, Dynamic modes such as tapping mode allow non-destructive imaging of soft materials like polymers and biomolecules [168].

Principles: AFM interacts with the material (sample) by means of a sharp probing tip at one end of a flexible cantilever that resembles a spring. The tip-sample interaction involves attractive and repulsive forces that deflect the cantilever, which is tracked via a laser and photodetector system. The attractive forces (such as van der Waals) dominate when the tip is near but not touching the sample, bending the cantilever toward the surface. Repulsive forces (elastic/contact forces) dominate when the tip touches the sample, bending the cantilever away from the surface.The AFM's schematic diagram of its operation is displayed in Figure 3.9.a and Figure 3.9.b shows the AFM instruments that are located in our lab.

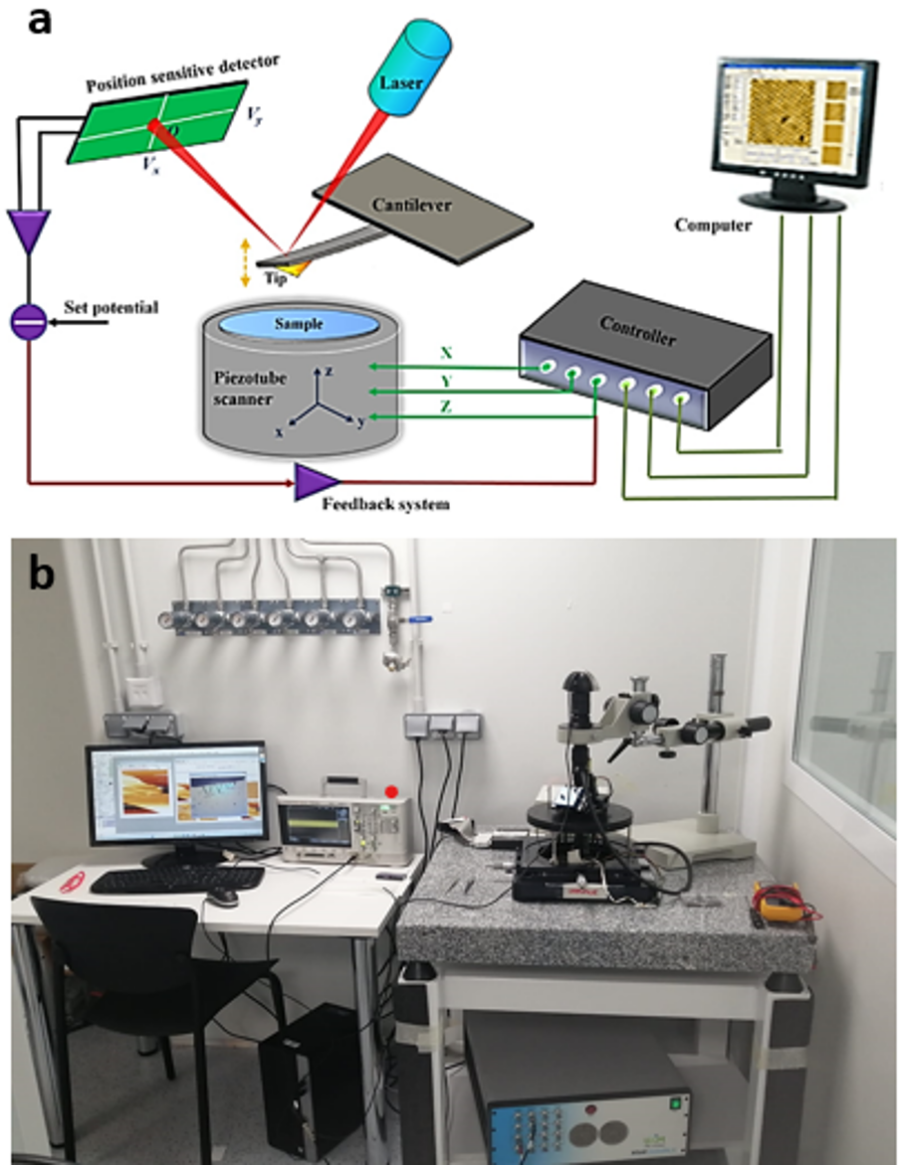

Figure 3.9: (a)AFM working principle schematic diagram showing how the cantilever deflection is caused by the contact between the sample and the probing tip [169]. (b)the AFM at our laboratory

The three primary modes are contact, non-contact, and tapping (intermittent contact) mode. In contact mode, the tip directly touches the sample surface. This method is capable of providing high-resolution images even on air, but its also likely to damage soft samples. Conversely, non-contact mode operates in the attractive force regime, with the cantilever oscillating close to the surface without touching it. Tapping mode, also known as dynamic force mode or intermittent contact, oscillates the cantilever so that it briefly contacts the surface in each image point. This mode aims at obtaining high resolution with reduced sample damage.

There are various sources and contributions of the forces operating between the probe and the sample. The key interactions between tip and sample will be covered in the following.

- **Short-range forces :** The overlapping wave functions and the ion cores' repulsion are what generate these forces. They act in the region of around 0.2 Å–1 nm and can be either repulsive or attracting.

- **Friction forces :**A frictional force acts in the opposite direction of the movement experienced by the tip as it slides through the sample. The twisting of the cantilever caused by friction allows for the imaging of the dissipation energy, which occasionally yields more information than topographic pictures [170].

- **Van der Vaals forces:** relatively modest attractive forces that develop as a result of each particle's internal electric polarization brought on by the presence of other particles and that operate on neutral atoms and molecules. An atom with a limited dipole will polarize an atom nearby when it approaches it with its generated electric field. This will lead to the appearance of an attractive contact between these two atoms in the vicinity of 0.2 nm and 10 nm [171].

- **Electrostatic forces:** These long-range forces act in accordance with Coulomb's law. The force that results from treating the tip-sample distance as a capacitor, applying a potential difference between the tip and sample (V_{bias}), and varying the contact potential difference (V_{CPD}) as a result of the different work functions of the tip and sample is: Eq.3.3

$$F_{\text{el}} = -\frac{1}{2} \cdot \frac{\partial C}{\partial z} \cdot (V_{\text{bias}} - V_{\text{CPD}})^2 \tag{3.3}$$

where **z** is the tip-sample distance and **C** is the capacitance of the system.This interaction is used by Kelvin Probe Force Microscopy (KPFM) to measure the contact potential difference (CPD) with nanometric resolution between the tip and the sample. Later on, it will be clarified.

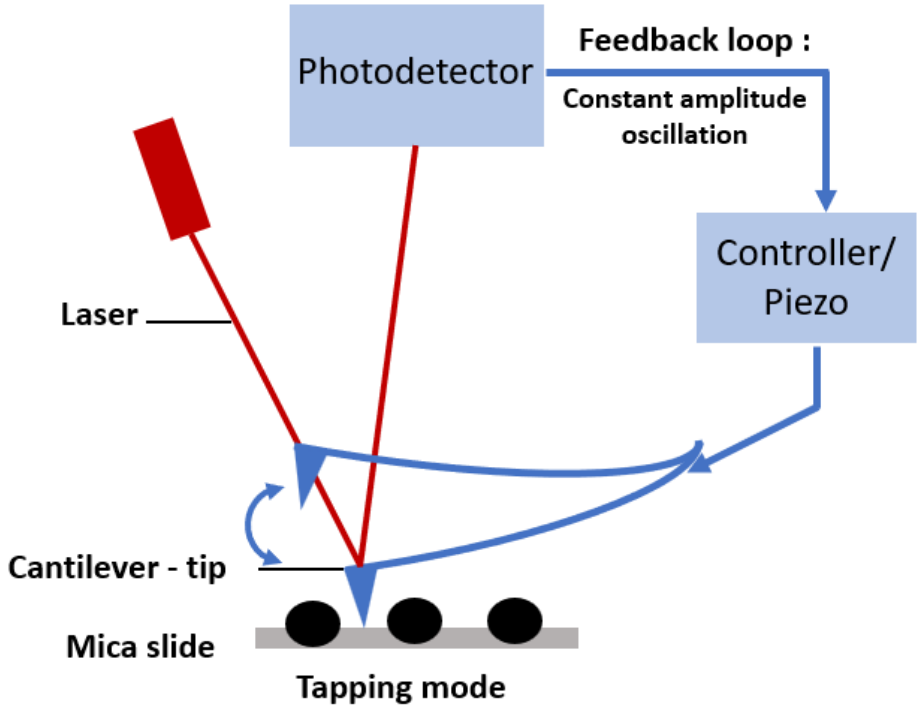

Figure 3.10: The fundamental principle of atomic force microscopy in tapping mode involves analyzing the photodetector output signal to determine the phase and amplitude of the cantilever oscillation. The oscillation's amplitude is maintained constant by the feedback loop. Image adapted from [172]

3.2.3 | Kelvin probe force microscopy KPFM

Kelvin Probe Force Microscopy (KPFM) is technique derived from Atomic Force Microscopy (AFM) that measures the surface potential and work function of materials with nanometer-scale resolution. Based on the principle of a vibrating capacitor [173], it works by applying an external voltage to nullify the electrostatic force between the probe tip and the sample. By applying a feedback-controlled DC bias to nullify electrostatic forces, KPFM obtains values of the contact potential difference (CPD) between the top and the sample, generating detailed maps of electronic properties, revealing phenomena such as doping, band bending, charge trapping among others [174, 175].

Kelvin Probe Force Microscopy (KPFM) is a powerful technique for high-resolution imaging of surface potential and electrostatic forces. KPFM provides information about the local electronic properties of materials, including surface potential and work function, which are crucial for understanding their structure and response in devices. For

instance, it is employed study doping profiles, band bending, and surface states in semiconductor materials and devices [176], to characterize the electrical properties of ferroelectric materials [177], to imaging operational electrical devices and providing high-resolution potential profiles [178], to study the surface properties of heterogeneous catalyst [177] and to investigate emerging perovskite photovoltaics materials and assessing surface photovoltage [179, 180] among many other applications.The applications of KPFM also include the study of surface states and defects under different environmental conditions, and the characterization of semiconductor devices such as high electron mobility transistors [181], resistors, solar cells [182], and light-emitting diodes (LEDs) [183]. Additionally, KPFM plays a crucial role in surface photovoltaic spectroscopy, aiding in the development of more efficient solar technologies [184]. By providing quantitative, nanoscale measurements of surface potential and work function, KPFM has become an essential method for understanding and optimizing the performance of advanced materials and devices. In the following, the working principle of KPFM will be briefly explained.

As mentioned before, the work function (ϕ) of a material can be directly measured using this method. The work function is defined as the amount of energy required to transfer one electron from its initial position in the Fermi level (E_F) to a location above the vacuum state in the free space (E_{vac}).

Figure 3.11.(a) shows the energy level scheme when two metallic materials (such as the AFM tip and the sample) with different work functions are taken into consideration. Electrons move from the material with the lowest work function (the sample, in Figure 3.11 diagram) to the material with the highest work function when they are electrically coupled until their Fermi levels line up. A contact potential difference and electrostatic force form between the tip and sample as a result of this charge movement (Figure 3.11.(b)). This electrostatic force can be nullyfied by introducing an external bias between the probe and the sample, as shown in Figure 3.11.(c). The vacuum levels flatten at the bias value known as V_{CPD} , which is the point at which this force is nullifye. The definition of the two materials' contact potential difference is:

$$CPD = \frac{\phi_{\text{sample}} - \phi_{\text{tip}}}{q} = \frac{\Delta\phi}{q} \tag{3.4}$$

where q is the elementary charge and ϕ_{tip} and ϕ_{sample} are the work functions of the tip and sample, respectively.

The electrostatic force between the tip and the sample, assuming that they are forming a planar capacitor, can be expressed by equation 3.3. An AC bias V_{AC} with a frequency of ω is provided to the KPFM tip, keeping the sample grounded, in order to isolate the contribution of other forces (mostly van der Waals and chemical forces). Equation 3.3 then becomes:

$$F_{\text{el}} = -\frac{1}{2}\frac{\partial C}{\partial z}\left[(V_{\text{DC}} - V_{\text{CPD}}) + V_{\text{AC}}\sin(\omega t)\right]^2 \tag{3.5}$$

Where V_{DC} is an applied bias to the tip. We may divide the electrostatic force into three terms by developing equation 3.5:

$$F_{\text{el}} = F_{\text{DC}} + F_{\omega} + F_{2\omega} \tag{3.6}$$

where;

$$F_{\text{DC}} = -\frac{1}{2}\frac{\partial C}{\partial z}\left[(V_{\text{DC}} - V_{\text{CPD}})^2 + V_{\text{AC}}^2\right] \tag{3.7}$$

$$F_{\omega} = -\frac{\partial C}{\partial z}(V_{\text{DC}} - V_{\text{CPD}})V_{\text{AC}}\sin(\omega t) \tag{3.8}$$

$$F_{2\omega} = \frac{1}{4}\frac{\partial C}{\partial z}V_{\text{AC}}^2\cos(2\omega t) \tag{3.9}$$

There is a harmonic response at ω and 2ω frequencies in the amplitude due to the F_{ω} and $F_{2\omega}$ components; the V_{CPD} is measured using F_{ω} . F_{DC} adds to a static deflection of the cantilever, and F_{ω} is commonly utilized for capacitance microscopy [185]. The KPFM works by applying a changing DC voltage to the tip V_{DC}, which is equivalent to V_{CPD}, hence nullifying the term F_{ω}. To create a V_{CPD} map, also known as a surface

potential map, V_{DC} is adjusted to the local CPD value at each scanning site. Amplitude mode Kelvin probe force microscopy (AM-KPFM) is the term for this technique. FM-KPFM is an alternate operating mode that is characterized by the following equation and is based on monitoring the electrostatic response in the frequency shift (Δf) at a specific omega:

$$\Delta f(\omega) \propto \frac{\partial F_\omega}{\partial z} = \frac{\partial^2 C}{\partial^2 z}(V_{DC} - V_{CPD})V_{AC}\sin(\omega t) \tag{3.10}$$

Instead of using F_ω as a physical magnitude in the feedback loop, FM-KPFM uses ∂F_ω. The lateral resolution and signal-to-noise ratio are improved by this technology, which also avoids the cantilever and tip cone's contribution to the electrostatic force [186].

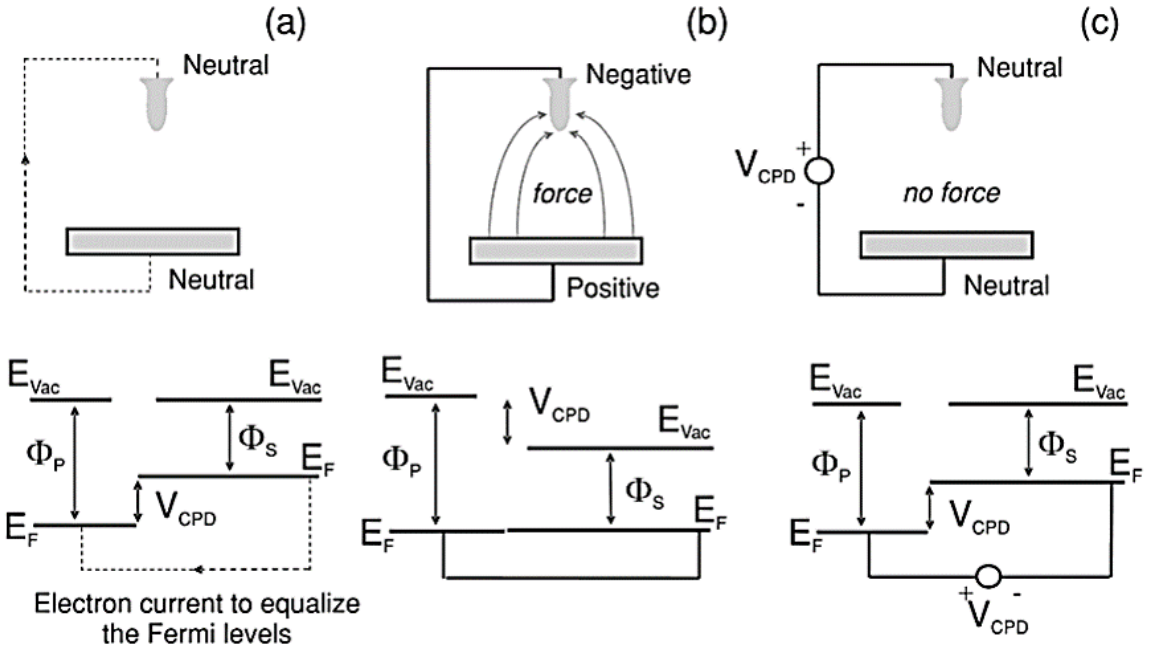

Figure 3.11: graphs showing the energy levels in the basic contact potential difference measurement setup, where the sample and probe act as a capacitor with work functions ϕ_p and ϕ_s, respectively. The metals are in isolation in (a). The alignment of the Fermi levels (EF) when they are electrically coupled (b) may cause a decrease in their vacuum levels. following the application of V_{CPD}. The vacuum levels have become flattened (c). Image adapted from[187].

3.2.4 | 2D-Transfer setup

A 2D-Transfer system setup is installed in the Nanolab Cleanroom. The transfer system (shown in Figure 3.12) is built with an optical microscope (a Nikon microscope). With large focal distance optical objectives (magnification x10, numerical aperture 0.30, working distance 16 mm, and magnification x20 optical, numerical aperture 0.40, working distance 11 mm). The transfer procedure can be seen on an external screen because the microscope is connected to a camera.

The transfer system is supported by an anti-vibration table and honeycomb optical breadboards. It is made up of a micrometric rotator, a hot plate with a temperature controller, an X-Y micrometric stage, and a stage-Z. To effectively fix the sample, the hot plate is attached to the vacuum line. in order to cool the hot plate at the desired rate, we also have an adjustable compressed air line. An adjustable tilt base that is attached to a magnetic base to reduce vibration during transfer is included to provide the required tilt during transfer.

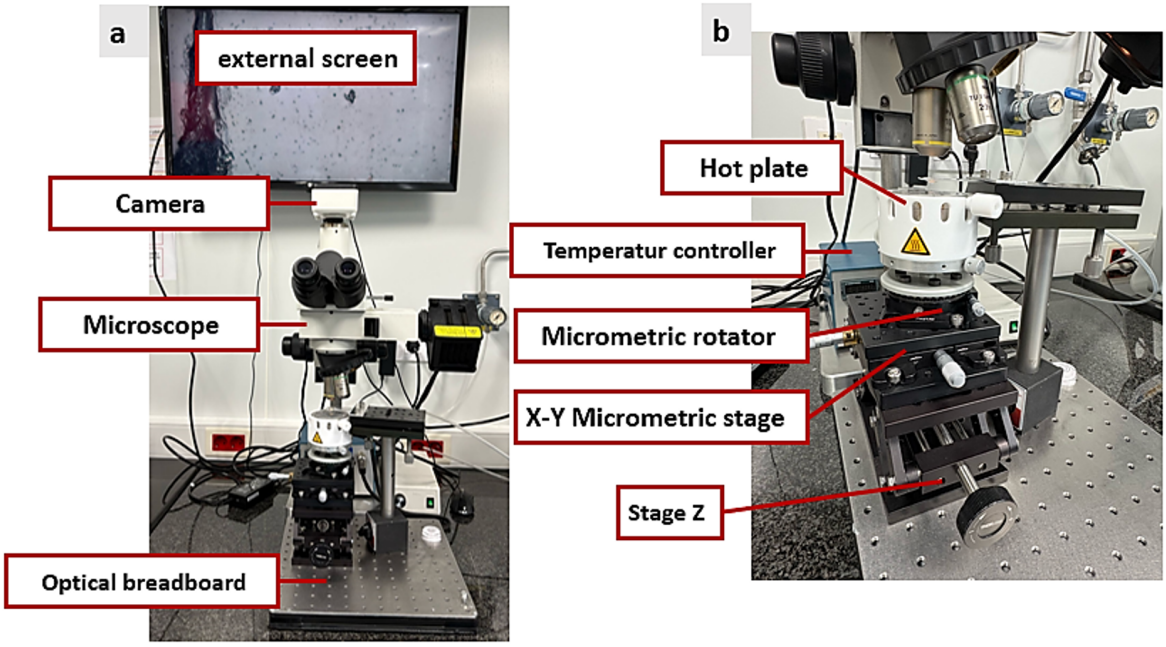

Figure 3.12: Transfer system that highlights the different components.(a) An illustration of the entire transfer system.(b) image shows the Various phases are employed to correct the alignment.

3.2.5 | DektakXT Bruker Profilometer

The DektakXT system Figure 3.13 is sophisticated equipment designed to measure the step height of both thick (up to hundreds of mm) and thin (down to a few nm) films.

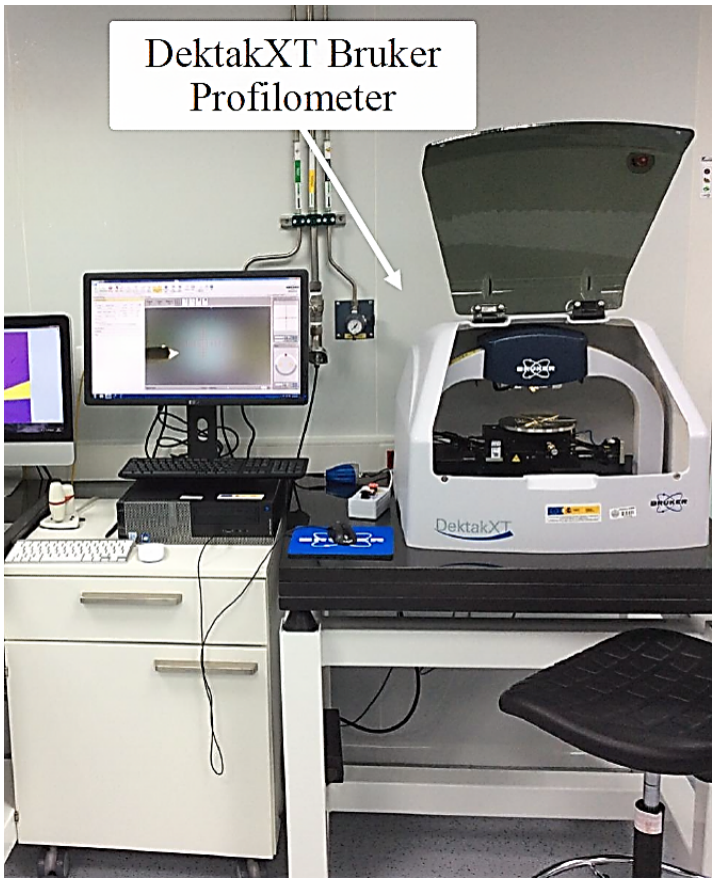

Figure 3.13: DektakXT Bruker Profilometer. Image adapted from[127].

It was utilized to measure the thicknesses of the dry etching and 2D-flakes during this thesis. In addition to surface topography and waviness profiling, the system can quantify roughness down to the nanoscale range. Along with step-height nanoscale resolution, it features automated X-Y-theta stages. The DektakXT system is capable of performing three-dimensional measurements in addition to two-dimensional surface profile measurements, producing three-dimensional maps in the (x,y) plane with micrometer resolution. A diamond-tipped stylus is electromechanically operated over the sample surface based on the required line speed, duration of scan, and stylus force (ranging from 3 to 15 mg). A Linear Variable Differential Transformer (LDVT), which

generates a feedback signal by processing electrical signals, is attached to the stylus. This signal corresponds to surface variations of the sample. After being transformed to a digital format, the surface data is retained for study and display. We employed the Vision64 software for this purpose because it can compute and show the output of user-selectable analytical functions for determining surface texture and other characteristics that describe the profile data.

4 | Design and fabrication of FZP

The results obtained during this part have been published in this paper [188].

4.1 | Introduction and work motivation

In the rapidly evolving field of nanotechnology, the ability to fabricate structures at the nanometer scale is crucial for advancing a myriad of applications. Among the techniques that have emerged to meet this demand, lithography and cryo-etching stand out for their precision and versatility [127]. Lithography, a process that uses electrons to transfer a pattern onto a substrate, and cryo-etching, which involves etching at cryogenic temperatures to achieve smooth high-resolution patterns, together provide a powerful toolkit for nanofabrication. This combination is pivotal in the creation of intricate nanometric structures essential for the miniaturization and enhancement of various devices encompassing high-density memory elements, structural elements and functional surfaces, such as cantilevers or lamellae, the fabrication of arrays of Josephson junctions for quantum computing to cite just a few of them. This chapter will particularly emphasize the application of these nanofabrication techniques in creating optical elements and devices useful for X-ray manipulation (e.g., imaging, condensing, filtering, etc.). More in detail, the production of Fresnel Zone Plates addresses challenges at the forefront of nanofabrication technology capabilities. The present work illustrates a combination of nanolithography and cryoetching techniques as a promising path to overcome such issues. This innovative approach aims to enhance the performance and scalability of optical devices, demonstrating the transformative potential of integrating advanced nanofabrication techniques.

A soft X-ray beam can be successfully monochromatized and focused at photon energies below 1400 eV with high transmittance up to 20% using reflection zone plates (RZPs), which are made up of elliptical zones constructed as laminar grating structures on a mirror surface. Nevertheless, RZPs can only be built for a single photon energy and are extremely chromatic. A reflection zone-plate array (RZPA), which covers a wide

bandwidth while maintaining pulse form and flux, is the new solution used by Maria B. et al.[189] to mitigate the issue. Unprecedented new methods for examining the electronic structure and dynamics of transition metal systems are made possible by X-ray free electron lasers, or XFELs. One effective method for these kinds of investigations is L-edge absorption spectroscopy, which has been shown to be feasible at XFELs for both liquids and solids. However, further monochromatization is required, and the necessary X-ray bandwidth is an order of magnitude smaller than that of self-amplified spontaneous emission (SASE). A novel method based on self-seeding of linac coherent light source (LCLS) is compared with L-edge x-ray absorption spectroscopy (XAS) of a prototypical transition metal system based on monochromatizing the SASE radiation of the LCLS by Thomas K. et al.[190].

Various approaches have been employed to fabricate such FZPs, such as photolithography [191], focused ion beam milling [57, 192], interference lithography [193], and electron beam lithography [194]. Di Fabrizio et al.[40] fabricated a silicon nitride and nickel FZP with a diameter of 5000 µm and a thickness of 1.3 µm using electron-beam lithography. Rogers et al.[195] utilized ion-beam milling on aluminum to produce a significantly thinner FZP (0.1 µm) with a diameter of 40 µm . Kong et al.[196] employed photolithography to create an ultra-thin graphene FZP with a diameter of 100 µm and a thickness of less than 0.005 µm. Li et al.[197] achieved a 10 µm thick carbon nanotube-based FZP with a diameter of approximately 650 µm using lithography. Additionally, Zheng et al.[198] and Low et al.[199] employed femtosecond direct laser writing (FsDLW) on graphene oxide, utilizing adaptive optics and a 3D stage or Galvano scanner, to fabricate FZPs with thicknesses of 0.28 µm and 0.9 µm and diameters of approximately 8 µm and 656 µm, respectively.

Achieving the nanometer-scale resolution required for cutting-edge applications necessitates the development of diminutive lenses with sharp and smooth edges. To fabricate such high-precision FZPs, it is imperative to push the limits of electron beam lithography (EBL). EBL, known for its exceptional resolution, can define the intricate patterns required for FZPs. When combined with cryoetching, the production of FZPs with sharp and smooth edges would become significantly more feasible. However, achiev-

ing defined nano-metric patterns with EBL presents challenges. During exposure, the energy deposition distribution within the resist significantly influences the patterning performance of the masks produced. Incident electrons penetrate the resist and substrate, undergoing scattering and energy loss [200], which can hinder the technique's applicability at the nanoscale.To mitigate these issues, the implementation of a capping layer is crucial. A capping layer helps minimize backscattering effects, ensuring that electrons are effectively absorbed or scattered away from the underlying layers, thereby reducing the risk of unwanted exposure and pattern distortion [201, 202]. Various materials, such as Al-Cu, Ti, TiN, or Cr, have been evaluated for this purpose, with Cr emerging as one of the most promising options [203, 204].

Selection of materials with high X-ray transmittance, low absorption, and an appropriate refractive index, with commonly utilized options including diamond and silicon nitride,[205, 206] is of fundamental importance. Spatial resolution is determined by the width of individual zones and follows the expression 2.44 , and strongly depends on the fabrication process and methods. Overall efficiency is dependent on parameters such as the number of zones, their thickness, and accurate placement. A zone plate's resolving power depends on the illumination conditions, i.e. the numerical aperture of the condenser system [21]. Specific zone plate parameters, including the number of zones (N), zone diameter (D), zone thickness (t), and outermost zone width (Δr) demand a delicate balance to optimize spatial resolution and efficiency. In the soft X-ray range (wavelengths between 0.3 nm and 5 nm), the best resolutions are achieved by using FZPs [207].

According to the results presented by K. Parfeniukas and J. Rahomäki [208], who demonstrated an improved nanofabrication method of high-aspect-ratio tungsten structures for high-efficiency hard X-ray nanofocusing zone plates, we have addressed the issue of efficiency loss towards the edge of the zone plate. This loss was partly attributed to flaws in the vertical zone profile. In our work, we demonstrate how the use of cryogenic etching for the FZP allows precise control of the sidewall angle and the roughness at the edges [209], crucial for achieving high lens efficiency [210, 211]. We thoroughly report on the fabrication steps of a Si-based FZP structure, with 100

differentiated zones, a lens diameter of 20 µm and an outermost zone width of 50 nm and a thickness of 4.3 µm.

Our goal is to investigate the limits in the combination of electron beam lithography (EBL) and cryo-etching for the design of structures that might be used in prototypical FZPs when conveniently scaled, as the employed aspect ratio of 86 is quite challenging and poses severe issues in the manufacturing as much as in the handling of the FZP. As an example, by using the scaling law given by Eq.2.20, we could use the structure synthesized directly as a Si-FZP for photons of 1.2 KeV, for a focal length of 970.87 µm, as much as for 3 KeV (with 2.5 times the initial focal length), or, conversely, as a masking pattern used to make deposition of conventional absorbing materials (e.g., Ni, Au, Ta, W) suitable for harder X-rays (e.g., 9 KeV). We have developed a robust process utilizing EBL to ensure the fine definition of intricate micrometric structures. This method has been combined with a chromium mask, which guarantees the successful fabrication of a vertically-step FZP comprising a large number of differentiated zones via cryo-etching [127]. This approach aims to significantly improve the focusing performances of the FZP. All parameters of the fabricated FZPs are detailed in Table 4.1

Table 4.1: Fresnel Zone Plate parameters.

Parameter	**Notation**	**Values**
Radiation wavelength	λ	1.03 nm (1.2 KeV)
Outer zone width	$\Delta r_n = \frac{\lambda f}{2r_n}$	50 nm
Number of zones	N	100
Focal length	$f = \frac{r_n^2}{n\lambda}$	970.87 µm
Diameter	$D = 4N\Delta r$	20 µm
Numerical Aperture (1st order)	$\mathrm{NA} = \frac{\lambda}{2\Delta r}$	0.0103
Spatial Resolution (1st order)	$\delta_{\mathrm{res}} = 1.22\Delta r$	61 nm
zone thickness	t	550 µm

4.2 | The resist layer selection for EBL

Before starting any EBL process the first and most important stage is to select the resist layer that will cover our substrate while patterning. This section provides a detailed description of every stage that comes before the EBL process, including Design, sample preparation, and spin coating.

4.2.1 | Design and sample preparation

The process starts with getting the surface ready. A silicon chip about 550 µm thick was cut into 1x1 cm pieces. Before using electron beam lithography, there were some steps to prepare. The silicon surface was put in acetone and heated for 2 minutes at 45 degrees Celsius. After that, it was rinsed with isopropanol (IPA) for 30 seconds to remove any leftover acetone. Next, the sample was cleaned in a plasma cleaner for 5 minutes using 29.6 W of power, 30 mL/min of oxygen flow, and 1000 mTorr of stable chamber pressure. This process is very important. It gets the surface very clean. A dirty surface can mess up the lithography process. Heating and rinsing remove oils and dirt. The plasma cleaner blasts the surface with energetic particles (see section 3.1.1). This further cleans the surface. A clean surface is key for high-quality lithography patterns.

The design of the Fresnel zone plate pattern, as depicted in Figure 4.1**.a** , was carefully constructed in the GDSII file format using the ELPHY PLUS software (see section 3.1.4) where a set of concentric rings were defined as alternate between being opaque and transparent with The dose of 375 μC cm^{-2} in HSQ and 160 μC cm^{-2} in PMMA for each ring. The ELPHY Plus program is combined with a GDSII-based editor that is compatible with ASCII, DXF, CIF, and CAD formats, and it has all the tools required to expose micro and nanostructures (WFs, dosages, etc.). Graphic patterns are created and edited by the superposition of various layers on which various components are drawn. Differentiated components with adjustable beam intensity, dosage, exposure time, focus, and writing field specific to each layer will be constructed for multilayer exposure in these layers. Pattern-generating files are stored in the standard GDSII data

format. It is possible to monitor the current intensities right before the exposure starts using a Faraday cup that needs to be manually moved into the electron beam track.

4.2.2 | Spin coating

After the thorough cleaning of the substrate, we proceeded to the coating phase, Hence, in order to choose the appropriate resist material for our fabrication, The two silicon substrates that were previously clean were equally coated: one with a coating of Hydrogen Silses Quioxane (HSQ) and the other with a single layer of Polymethyl-methacrylate (PMMA with a concentration in chlorobenzene of 2%) .

For the PMMA resist : A spin coater was used to apply the coating(see section 3.1.2), and it was programmed to run for 60 seconds at a constant speed of 5000 rpm and an acceleration of 1000 rpm/s. We were able to attain a constant PMMA resist layer thickness of around 83 nm by using this technology. The prepared substrate was then given one more thermal treatment, put on a hot plate, and heated for 10 minutes to 160 degrees Celsius.

For the HSQ resist : Before coating, we heated the cleaned surface for 5 minutes at 150°C. Then we moved it to the spin coater. The spin coater spun for one minute at an acceleration of 1000 rpm/s and a constant speed of 4000 rpm. This allowed us to make a layer of HSQ that was around 50 nm thick all over the surface. After that, we heated the surface again. We put it on a hot plate and heated it to 80 degrees Celsius for 4 minutes.

4.2.3 | Electron beam lithography for FZP

For the past twenty years, electron-beam lithography (EBL) has been utilized to pattern features at the nano- to micron-scale for cell investigations [212, 213]. This technology was initially described as a substrate material patterning method in the 1960s [214, 215]. In EBL, a resist layer is directly patterned by serially exposing a polymeric resist pixel-by-pixel to create a bespoke pattern using an electron beam that is electronically scanned using FE-SEM (see Section 3.1.4). EBL is a primary method

for creating master templates that are then utilized in nanofabrication procedures with higher throughput, such as nanoimprint lithography and photolithography.Since the finely concentrated beam may be freely deflected by the deflectors and coils, e-beam lithography does not require a mask, in contrast to UV, DUV, and EUV lithography.

EBL offers versatility in the patterning of intricate shapes as well as precise control over the lateral dimensions at a 5-7 nm resolution. Modern EBL systems can effectively handle the uneven surface topology of standard GaN wafers and accompanying wafer bows because they have excellent depth of focus (many hundred nanometers) and can adjust for large-scale height fluctuations of the wafer (of several hundred microns). The ability to produce many designs concurrently on a single wafer is another benefit of EBL. Because of this, one of the methods with the highest resolution is thought to be the EBL. Like UV light, electrons with high energy can change the properties of the resist material. This allows the exposed or non-exposed parts of the resist to be removed. Like all forms of lithography, EBL has advantages and disadvantages [216]. One benefit of employing electrons is the Production method (direct-write format without a mask), which has a resolution higher than that of light because of higher energy, faster electrons provide more resolution and produce far finer patterns with a resolution of less than 10 nm by focusing much more tightly than light. The slow (low energy) electrons that have a wide range (up to 100 nm) and cause relatively little loss when striking resist molecules are the drawbacks; they reduce resolution, particularly in the <0–5 eV region. Low-energy electrons interact poorly with the ionization potential because their kinetic energies are lower. Additionally, in terms of velocity, it is ten million times slower than current optical lithography equipment, especially when printing dense patterns on a wide scale. The most common disadvantage is the proximity effect, which presented a challenge in our investigation and will be covered in the upcoming section along with all available solutions (see section 4.2.4).

In our fresnel zone plate fabrication, after the spin coating of the two substrates, one with PMMA and the other with HSQ, the subsequent electron beam lithography exposures were carried out with a scanning electron microscope Sigma, manufactured by Zeiss. The EBL process was executed precisely, employing a 15 KeV electron beam

energy, a 7.5μm column aperture, and maintaining a typical beam current of 0.016114 nA. Specific details of the EBL settings can be found in Table 4.2.

Table 4.2: Exposure parameters for the e-beam lithography

E-beam lithography parameters	
Substrate	Si chip 1 cm × 1 cm
Resist	PMMA2%
Resist thickness	83nm
Electron beam current	0,016114 nA
Electron beam energy	15 KeV
Step size	2nm
Dwell time	0,000284 ms
Column aperture	7,5µm
Z stage position	17 mm
Working distance	05 mm
Exposure field	100 µm × 100 µm
Magnification	1500

Following the EBL exposure, the samples underwent a sequence of post-processing steps:

The substrate coated with PMMA commenced with a 45-second immersion in a 1:3 mixture of MIBK (4-Methyl-2-pentanone) and IPA, designed to develop the patterned resist. Afterward, the sample was immersed IPA for an additional 45 seconds, ensuring the removal of any residual materials. A final touch was added by gently drying the sample with a controlled nitrogen jet.

Then regarding the chip coated with HSQ, In order to carry out the developing process, tetramethylammonium hydroxide at a 25% concentration in DI-water (TMAH25%) is rinsed with manual gentle agitation at 80°C, stopped in flowing DI-water for one minute, and then dried with a controlled nitrogen jet.

Once the resist mask fabrication was completed, the sample was analyzed using a

scanning electron microscope. The results are displayed in Figure 4.1. Starting from a first viewpoint; it is noticeable that the PMMA mask is more or less like a CAD design (Fig 4.1**.a**) in contrast to the HSQ mask, where the HSQ resist was poorly defined and full of blemishes (Fig 4.1**.b**). This could be due to it being improperly exposed in the EBL process or not being properly adhered to the substrate. HSQ may be contaminated as a result of it being left open for a long time or not being stored properly. Therefore, we chose to use PMMA as the best resist for our fabrication because of the aforementioned reasons. We also considered the fact that PMMA provided few defect sites when compared to HSQ, is cheap, always fresh, and is always available in our laboratory.

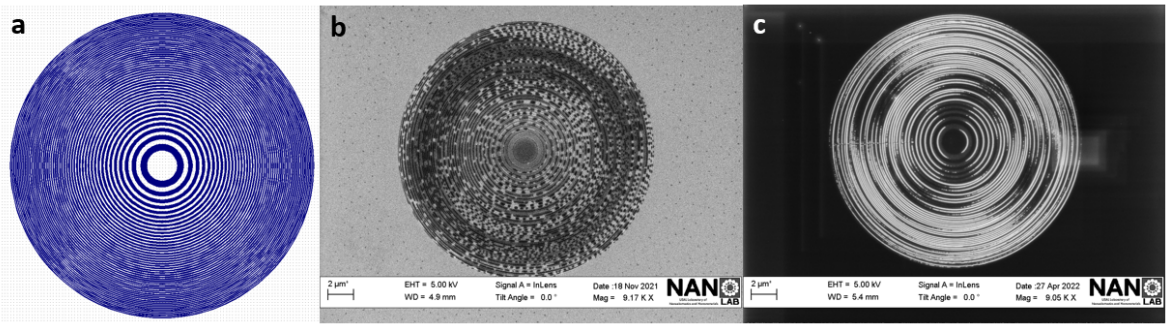

Figure 4.1: (a) Computer-aided common design (CAD) of a Fresnel Zone plate with 100 concentric zones.(b) Scanning electron microscope image of FZP using HSQ with a dose of 375 μC cm^{-2}.(C) Scanning electron microscope image of FZP using PMMA with a dose of 160 μC cm^{-2}.

Upon closer inspection, we can conclude that there was an issue with our resultant PMMA mask that is embodied in the collapse of the patterns all over the zone accompanied by undesired over/under exposure as presented in Figure 4.1**.c**. This issue is related to the shape of standard fresnel lenses produced by EBL where the width of patterns diminishes from the center to the outermost zone as already shown in Figure 4.1**.a**. This decrease in width poses as a kind of difficulties in micrometric-size structures due to high aspect ratios.

It is considered that the approximation effect is the cause of the collapse problem which significantly affects each pattern and its neighbors and leads to the interference of patterns during exposure. The approximate effect and methods to avoid it, in order to eliminate collapse, will be described in detail below.(section 4.2.4)

4.2.4 | Proximity effect

The discrepancy between the design and the exposure outcomes after the development is one of the limiting elements of EBL, as can be shown in the earlier findings (Fig 4.1.c). The absorbed dosage is not limited to the area where the beam has been driven due to the electron-solid interactions. This fact results in dimension errors and design distortions, which are more broadly referred to as the proximity effect (PE).

The acceleration voltage determines how the electron beam interacts with the materials (resist and substrate). Figure 4.2 shows a schematic illustration of this interaction. Because of the bigger aberrations in the microscope, resolution is often poorer at low voltage; nevertheless, this relationship is complex and dependent on a number of parameters. Sometimes it's preferable to work at a high voltage in order to get a higher resolution.

PE refers to the resist that inadvertently gets a non-zero electron dose outside the specified area of exposure. Actually, as Figure 4.2 illustrates, the electron beam collides with the resist or substrate, exposing the resist far from the original incident location due to the production of forward (with small angles) and backscattering (with high angles) electrons. The electrons start a sequence of low-energy elastic collisions as soon as they enter the resist, which will cause the electron to deflect slightly with each impact. This beam widening caused by forward scattering is more noticeable at lower incident energy and rises with thickness [217, 218].

In reference to the backscattering [219], Usually, the majority of the electrons fully enter the substrate and pass through the resist. When enough large-angle collisions occur, some of those electrons will reappear in the resist in a different location than where they originally departed. (see Fig 4.2). Higher energy levels might expose microns [220, 221] farther from the beam entry point due to these backscattered electrons. Exposure at a neighboring feature is increased by electrons writing a feature at one site, resulting in pattern deformation and overexposure. and this is what the proximity effect means [222, 223].

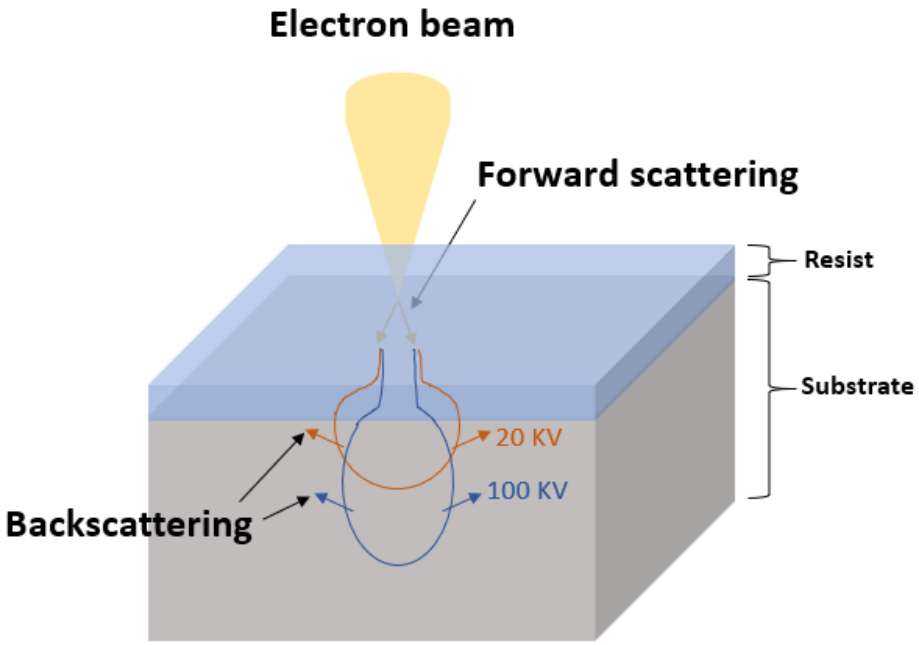

Figure 4.2: A schematic representation of electron beam collisions in an EBL process shows how the forward and backward electrons scatter at different voltages.

PE more particularly impacts submicron structures, resulting in a dispersion of nonuniform exposure across or within pattern elements [224]. A poor choice of pattern geometry in the CAD file or the smaller and more constrained space and size of the neighboring features to be exposed might be the cause of the nonuniformity in the exposure between pattern components. In actuality, isolated elements receive less radiation than packed components, and smaller elements receive less real dose than bigger ones.The nonuniformity in the exposure inside a single element is associated with the writing pattern selection within the single element as well as the variation in exposure between the feature center and its boundaries. The most typical pattern is to scan (therefore write) along parallel lines until the polygon is complete, although when needed, diagonal or radial scans can also be carried out.

Because of fluctuations in the interaction volume of the electron beam in the sample and in the forward scattering angle of the main beam, it is evident from the schematic depiction of the PE in Figure 4.2 that using a higher beam voltage implies substantial changes in the PE effect [225]. Additionally, the backscattering process is greatly influenced by the characteristics of the substrate itself, which in turn affects the interaction

volume.

How to correct or reduce the proximity effect?

Several techniques exist for reducing PE, including varying the dosage at which element fragmentation is introduced in the **CAD** file features, selecting the optimal scan direction [226], and altering the element's form and dimensions. The PE correction may either be computed computationally by the EBL software, essentially replicating the effect due to backscattering electrons, whose contribution is stronger at high voltage, or it can be done manually by the user (although this needs a high degree of knowledge and is quite time-consuming).

Other ways to prevent or lessen PE depend on the setup and system characteristics that are used. If pattern transfer is required, a thicker mask beneath can be used in conjunction with a thin resist layer (< 50 nm) to reduce forward scattering. Furthermore, it can be beneficial to employ multilayer resists, where the lower layer is utilized to lessen backscattering processes while the top layer is employed for patterning [227]. Furthermore, high contrast resists (HSQ) typically exhibit less sensitivity to the PE.

Substrates are also important; using membranes is dependable, and materials with low atomic numbers create less backscattered electrons. For many applications, it can be quite convenient to change the beam energy since low voltages (< 15 keV) limit backscattering and high voltages (> 50 keV) diminish the broadening of forward scattering.

To reduce the return scattering contribution, a PE correction (known as GHOST) [133, 228] can also be carried out with a background dose. It involves printing the inverse of the intended image (after the initial exposure) using a defocused beam to achieve a consistent background dose level everywhere. In addition to extending the exposure period caused by two lower-dose scans, the main characteristic of this technique is low contrast in feature definition.

The approach we chose to address the proximity effect issue and lessen the collapse issue will be covered in the sections that follow.

4.2.5 | Resist mask improvement

After understanding the PE and knowing ways to reduce it, and by projecting the previous results (collapse of patterns in the FZP), we combine two methods to reduce the PE and thus eliminate the collapse. First, a thin chromium layer (typically 7 nm) is deposited directly on top of the bare Si (between the resist PMMA and Si substrate) by metal evaporation technique (Cr evaporation is described in Section 4.3.1), which will avoid the majority of undesired electron backscattering [229–231]. This Cr layer will be used later as an etching mask. Secondly, four novel structures where element fragmentation is introduced will be designed and implemented, alongside with different doses for the lithography applied to different regions of the pattern, allowing for better control and optimization of scan directions [226].

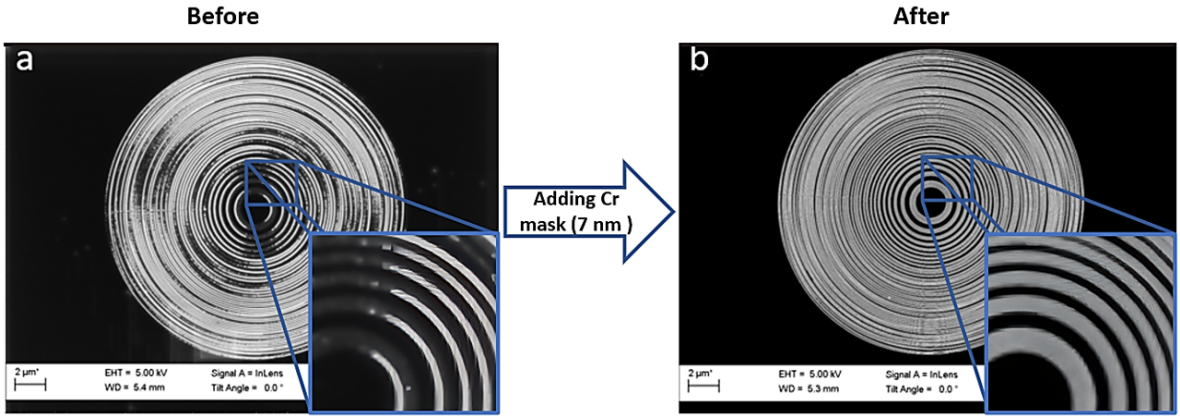

Figure 4.3: Scanning electron microscope images of FZP using a concentric design (a) without and (b) with an extra Cr-layer (7 nm) on top of the Si for a dose of 160 μ C·cm^{-2}. Remarkable improvements in the final FZP can be seen upon the addition of the chromium layer onto the silicon chips which effectively addressed several issues, resulting in a significant enhancement of the overall pattern quality. However, some collapsing can still be observed, particularly in the outermost regions where the separation between concentric rings started to narrow.

The effect of the Cr layer is immediately observed. Figure 4.3.a displays a concentric **PMMA** mask for the generation of FZP without previously deposited Cr on top of the bare Si showing a large portion of undesired overexposed (and hence collapsed areas) throughout the whole structure where the pattern was harmed by excessive clearance of PMMA. The overexposure observed is directly linked to the electron dose applied; in this case, a uniform dose of 100 μC·cm^{-2} was administered across the entire mask

from center to edges. As shown in the zoomed section of Fig.4.3.a, the central region exhibits signs of overexposure. The interline distance and the exposure dose are known to have a significant impact on the possibility of fabricating a high-quality grating. Numerous negative influences exist. Underexposure is the first and most well-known type, which occurs when exposed lines' clearance depth is too little to produce a grating pattern. Overexposure is the other extreme regime; in our fabrication, we experienced this final one when the pattern was damaged by high PMMA removal. On the other hand, Fig.4.3.b presents the final patterned resist mask using the same initial CAD design, the same dose of 100 μC·cm^{-2} with a previous Cr layer showcasing a much improved final structure without any distinguishable damaged areas. The improvement was most evident in the zoomed-in area of Figure 4.3.b, where the collapse is absent and the overexposure has been eliminated. The metal coating, typically 5–20 nm thick, serves to two purposes: i.e., eliminates the charge buildup that occurs during EBL and, henceforth, allows for a more precise beam focusing without obstructing the patterning process and, secondly, it facilitates better adherence of the PMMA [232, 233]. Among the different metals available, chromium is often chosen for the metal coating since it exhibits ease of etching removal and has a low atomic mass, making it easier to image pre-patterned metal structures for alignment purposes.

The four different CAD geometries developed in this work are displayed in Figure 4.4(a-d) with their already developed PMMA counterparts shown in panels (e-h) respectively. Firstly, from the common stem of the concentric-like shape, we added 72 radial lines spaced out by 5 degrees which helped easing the majority of the overexposure at the outermost regions shown in Fig4.4(b) an translated onto a final PMMA mask in 4.4(f). Panel (c) shows an evolution of design shown in Fig.4.4(c) where not all 72 lines start from the first radial structure but commence at different distances from the origin, alleviating the undesired overstructure close to the center. Such design still provokes collapse and stress of the final PMMA mask at next to the edges as shown in Fig.4.4(g). Finally, Figure4.4(d) displays the final CAD design where there majority of the external concentric rings are interrupted at the vicinity of the radius. Different doses of electron beam exposure are applied to different parts of the pattern, allowing

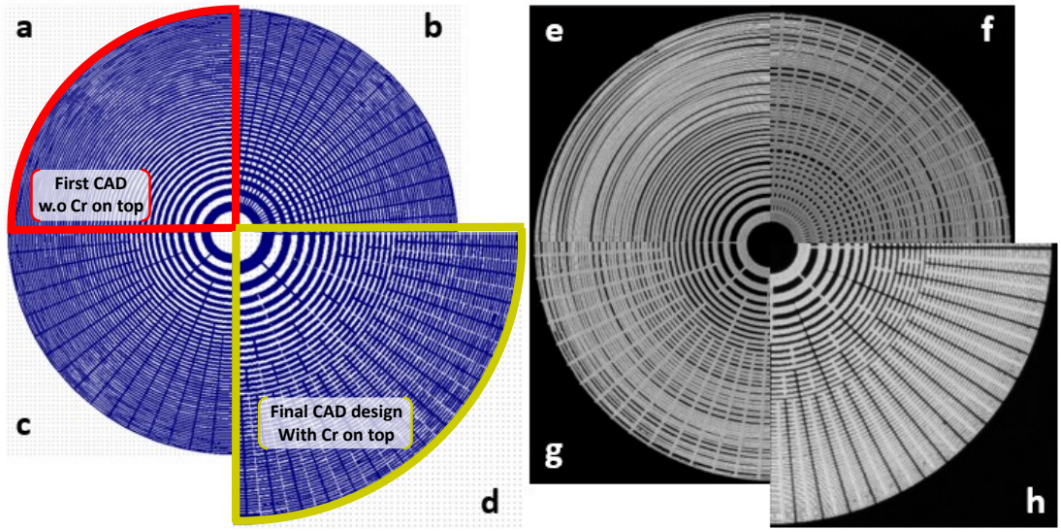

Figure 4.4: **(a)** Computer-aided common design of a Fresnel Zone plate with 100 concentric zones.**(b)** modified CAD design with the inclusion of 72 segments, each 0.05 µm wide, spaced out by a 5-degree angle from the first to the last zone. **(c)** The new segments were modified in the CAD design such that eight of them began in the first zone and ended in the tenth zone while the remaining segments began in the sixth zone and ended in the last zone with varying lengths. **(d)** CAD design that is akin to the one presented in **(c)** but with a set of intermediate segments to lower local exposure there. **(e-g)** are scanning electron microscope images of the already developed PMMA using designs**(a-c)** respectively where it still shows the presence of resist collapse even after adding extra segments both radially and circularly. Panel **(h)** displays the final PMMA mask on top of Cr/Si with no traces of proximity effect within their outermost regions. This final mask was retrieved from the CAD presented in panel **(d)** and demonstrates the effectiveness of this final morphology where the improved design generates final well-defined patterns.

for better control and optimization of scan directions [226].Three different dosages were employed in the four CAD designs (Fig 4.4): 200 μC·cm^{-2}, 170 μC·cm^{-2}, and 185 μC·cm^{-2}. These dosages were used for the middle 6 rings, the last 3 rings, and the rest of the rings in between, respectively. This technique helps mitigate the collapse problem by minimizing the interaction between neighboring patterns and reducing the overall stress on the resist material.

The final optimized PMMA mask onto Cr/Si presented in Figure 4.4(h) shows an overall improvement of the desired structure with no traces of overexposure or collapses. These results demonstrate that the strategy of combining metal coating and element fragmentation has been successful in reducing backscattering during EBL expo-

sure. This approach succeeds in minimizing proximity effects and leads to an efficient optimization of the **PMMA** mask.

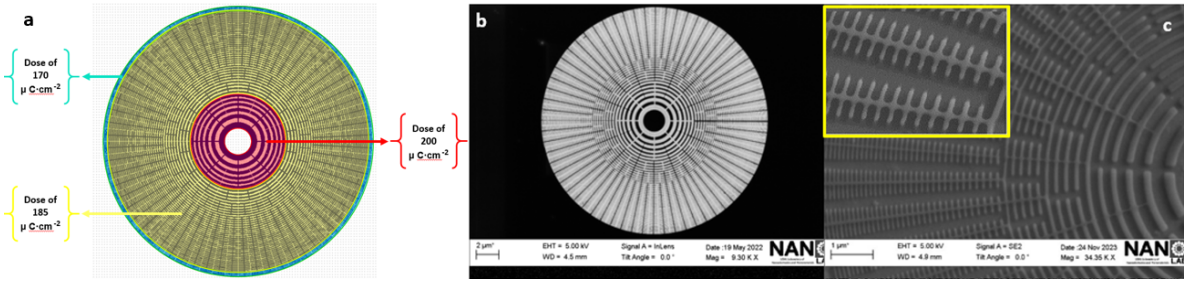

Figure 4.5: (a) Final computer-aided designs where Different doses of electron beam exposure are applied to different parts of the pattern, the first 6 rings with a Dose of 200 μC·cm^{-2}, last three rings with a Dose of 170 μC·cm^{-2} and rings of the middle are with a Dose of 185μC·cm^{-2}.(b)(c) SEM images that display the resulting PMMA mask from afar and zoomed angle of view with highlighting the collapse removal.

A more detailed picture of the produced mask can be shown in Figure 4.5. The optimized **CAD** design with suitable doses is shown in **(a)** while an SEM image of the final mask is displayed in **(b)**, from which a zoomed are **(c)** displays intact and well-defined structures, and no collapsing effects are found.

A detailed examination by SEM of the produced PMMA structures is fundamental to enhance the outer zone patterns in order to identify significant pattern collapse as the ones shown in Figure 4.6.a. This phenomenon was produced due to the presence of resudial resist material, during the development stage. The constraints imposed by the narrowest separation between patterns hindered the developer's efficacy, to overcome this challenge and achieve optimization, we employed descum etching techniques. This strategic approach not only facilitated the removal of the persistent resist material but also played a pivotal role in refining the overall pattern morphology.

The descum process serves as a critical step in the integrated circuit manufacturing process, specifically designed to eliminate residual organic residues persisting after the photolithography stages. It consists of a low-temperature, oxygen-based plasma process operating at low power, and it is specifically engineered to remove a targeted few hundred angstroms of resist material. This process guarantees achieving a clean and uncontaminated surface, setting the stage for subsequent critical process steps, includ-

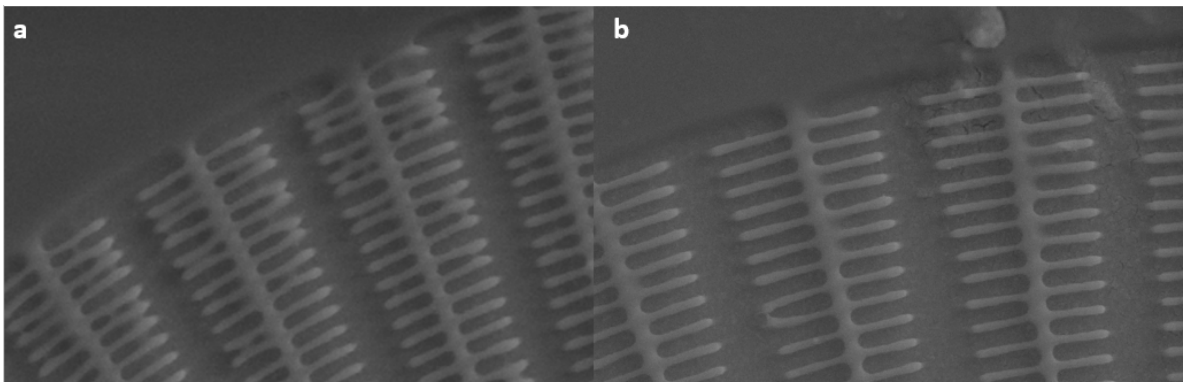

Figure 4.6: Scanning electron microscope overviews of comparative analysis for the outer patterns without (a) and after (b) the descum etching process using a pressure of 60 mTorr and an oxygen flow set at 50 sccm: Emergence of clearly defined patterns.

ing wet and dry etching. By effectively eradicating organic residues, descum improves the overall quality of the structures [234].

The descum process was carried out in the PlasmaPro 100 Estrelas system where the specific etching parameters employed in this study included a pressure of 60 mTorr, an RF power of 50W, O_2 flow set at 50 sccm, and a temperature maintained at 25°C. The etching duration was optimized at 5 seconds.Descum using oxygen plasma produces radical oxygen species to chemically eliminate the silicon wafer's resist layer where oxygen molecules can be broken down by intense electrons in the plasma to produce reactive oxygen atoms moreover, oxygen plasma ashing produces non-toxic byproducts. In comparison to the wet etching method, it is more ecologically friendly. The findings are displayed in Fig.4.6.b, which displays precisely defined and narrow patterns of the outermost zone contrasted to the scenario in which DESSCUM was not used, indicating that the decision to use descum was successful in eliminating the remaining resist that was challenging to eliminate with only development. This result shows that the PMMA 2% resist mask is effective and ready for the next step of chromium etching. The strong and controlled descum process sets the stage for smooth fabrication, guaranteeing the creation of high-quality, well-defined patterns.

4.3 | Chromium mask

Once the PMMA mask has been produced, ensuring the high quality of the desired structures, the Cr layer is ready to be etched, and the pattern is to be transferred in order to create the final mask (as shown in the schematic in Figure 4.7)

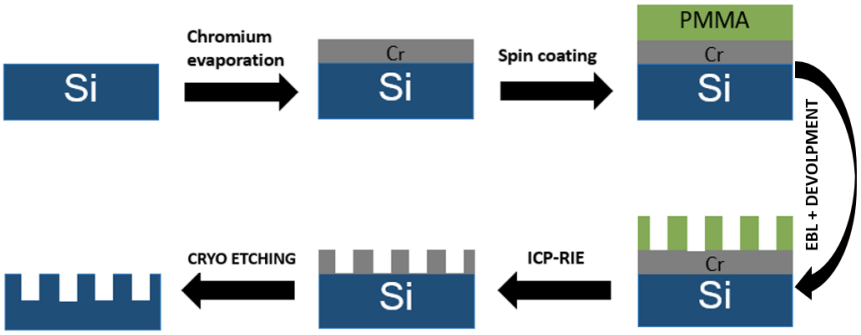

Figure 4.7: Fresnel zone plate manufacturing steps including all the necessary measures to improve the final structure. This sequence will produce the final structures.

4.3.1 | Chromium evaporation

The deposition of the 7 nm chromium layer on a silicon substrate is carried out with the use of a homemade electron beam evaporator (see section 3.1.3). The electron beam technique is able to obtain very high quality and reproducible depositions with a very low level of contaminant. The use of a local electron beam on the target material and the presence of water to cool the walls of the crucible prevent any alloy compositions. In our process, the deposition is very homogeneous thanks to the large separation (~ 1 m) between the target material and the sample and the very low pressure of the main chamber (the base pressure is 8×10^{-10} mbar, the Cr-process pressure around 8×10^{-9}mbar). The sublimation of Chromium is obtained with a beam voltage of 8 kV and an emission current of 20 mA. The target material is commercial chromium in pieces (0.8-6 mms) with a purity of 99.95 %, the e-beam crucible liner is a FABMATE liner.

4.3.2 | Pattern transfer to the intermediary mask

In the cryogenic etching of silicon, the use of plasma etching along with PMMA is not considered to be the most popular approach. This is because PMMA has high-resolution capabilities but poor etch resistance. [235] Additionally, it has poor adhesion on silicon[236], making it suitable as a soft mask in plasma dry etching. In contrast, a hard mask such as a chromium mask is typically required for prolonged etching. Figure 4.8 represents the results of using a PMMA resist as a mask to etch silicon it is obviously clear that the patterns seem to lack smoothness where it is noticeable that the side walls are Peeled and rough.

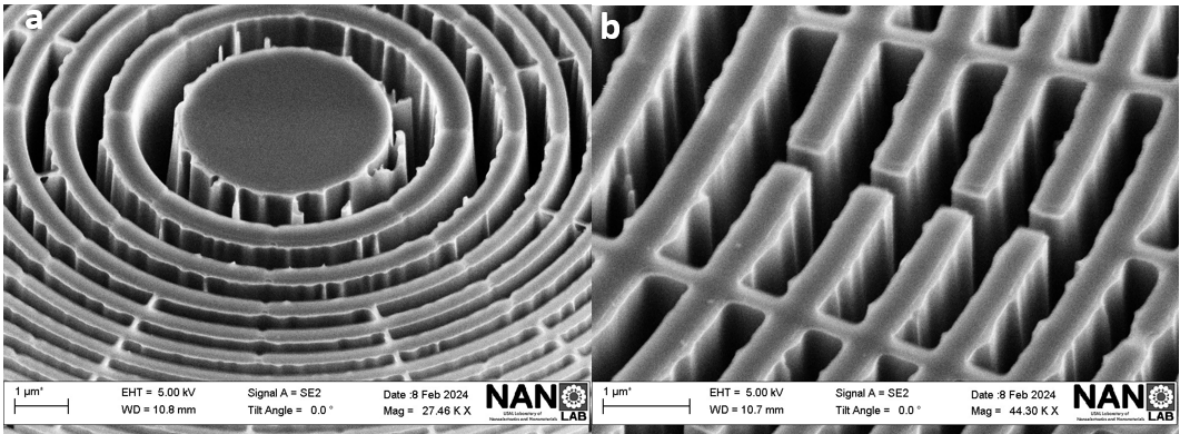

Figure 4.8: Tilted (60°) scanning electron microscope images were used to observe the center (a) and outer patterns (b) of the Fresnel lens. The etching process involved using the resist PMMA as a mask and the following etching conditions: pressure of 10 mTorr, RF/ICP power of 04/1000 W, a gas mixture of SF6/O2 with a flow rate of 60/15 sccm, and a temperature of -120 °C. The etching test was carried out for 2 minutes.

In addition to the fact that using the chromium layer to reduce the proximity effect was effective, the previous test (See Fig 4.8) on using the PMMA layer as an etching mask shows us the additional importance of utilizing the chromium layer, which is to use it as an intermediate mask to transfer patterns from the resist layer to the silicone layer. One of the most common techniques that people use for substrates is to etch them deeply by combining conventional polymer resist with intermediate hard etching masks. In this particular process, the middle-level hard masks are typically made through lithography and pattern transfer, after which they are employed in dry

etching the substrate (or sub-layer) using their designed structures as etching masks. It is possible that, among other materials, Chromium (Cr) is extensively used as a hard mask material in plasma etching because it has high selectivity towards silicon and its compounds when fluorine or chlorine-based etching chemistry is adopted chromium was discovered to be selective to silicon and its compound by researchers. Over the years, since 1976 [237–240], scientists have explored various applications of Cr films such as photomasks containing an opaque layer; production of semiconductor devices involving etching masks; electrodes for field emission displays (FEDs), and so on [241–244]. The resist can be used as a mask for either a lift-off or direct etching process for transferring the pattern into chromium (Cr) from the resist structure.

Chromium is a useful material for photomask and reticle manufacturing [245] because of its high optical density, even in the deep ultraviolet regime. It is wear-resistant, electrically conductive, and simple to deposit using physical vapor deposition techniques [246, 247]. Moreover, it creates a thin, thick oxide coating that self-passivates, protecting the majority from additional corrosion [248]. For instance, adhesion interlayers made of chromium are also common between gold and other materials [233, 249, 250]. It is also an effective hard masking material for dry etching, as it exhibits high sputter resistance and selectivity in fluorine and bromine chemistries. This property allows chromium to serve as an etching mask for various materials, including silicon, SiO_2, ZnO, Si_3N_4, TiO_2, MoSi, and GaAs [251].

In this study, the resistance layer's pattern was transferred to the chromium layer underneath to start the etching process. This layer acts as a mask for the silicon-reactive ion etching (RIE) process. The perfect recipe must be discovered for reactive ion etching (RIE) in order to preserve the chromium mask through the process without negatively impacting the resist or the thinning of the chromium layer. It is important to ensure that the resist layer is completely removed in the areas where etching is required while simultaneously protecting the underlying chromium layer. Table 4.3 outlines the specifications used in the different recipes that were tested.

Each recipe was designed, taking into consideration the etching characteristics of the resist and the chromium layer. Following conventional laboratory procedure, the

Table 4.3: Parameters for chromium dry etching recipes that were tested in this study.

Parameter	**Recipe 1**	**Recipe 2**	**Recipe 3**	**Recipe 4**
Pressure (mTorr)	5	100	12	6.5
Rf power (W)	30	50	10	08
ICP power (W)	500	0	1200	600
Cl_2 flow (sccm)	20	17.2	45	44
O_2 flow (sccm)	20	04	5	06
Temperature (°C)	10	19	50	15

sample was etched for 35 seconds and then subjected to scanning electron microscopy examination. To obtain the desired result, the etching procedure was extended if necessary.However, during the initial 12 seconds of etching using the first recipe, it was observed that the PMMA2% layer was etched before the chromium layer. Furthermore, the second and third etching recipes for the Cr layer were found to be ineffective, as they took a prolonged time of 2 minutes and 1 minute 10 seconds, respectively, leading to the unintended disappearance of our PMMA layer. Ultimately, the fourth recipe was close to being suitable, where it was conducted at various time intervals, specifically 35, 45, 50, 55, and 57 seconds. These different durations were implemented to determine the most effective etching time for our purposes.

As seen in Figure 4.9 which clearly shows the process of successfully etching away the chromium layer. However, upon close examination, it became evident that the shape of the middle rings after etching did not meet the desired standards. After 57 seconds of etching, roughness started to show up in the center rings, and there was some burning of the resist layer. To address this problem, we chose to raise the chamber pressure from 6.5 to 12 mTorr while keeping the same etching parameters as recipe 4 in place. The outcome of this change is shown in Figure 4.10 , where we can see that all roughness and burning have vanished and the chromium mask was well etched. But the chromium mask started to show unexpected black areas, which presented an unexpected difficulty as we dug deeper into improving our methods.

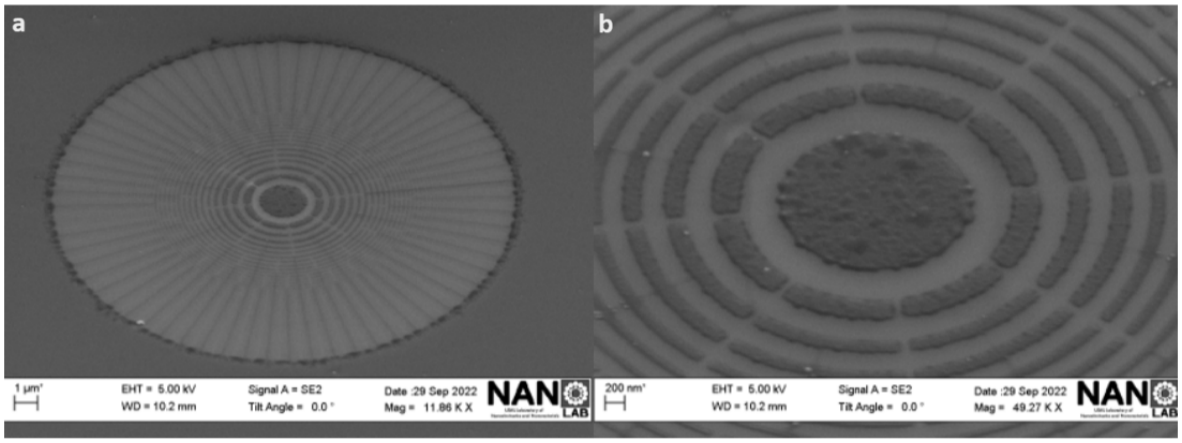

Figure 4.9: tilted view at 45 degrees for both global (a) and central (b) angles provides an insight into the outcome of a PMMA-exposed Fresnel zone plate pattern transferred onto an underlying chromium layer. This transfer was achieved after 57 seconds of dry etching, employing a Cl_2/O_2 gas flow rate of 44/6 sccm, maintaining a chamber pressure of 6.5 mTorr, an ICP power of 600 W, and an RF power of 08 W.T. The visual impression suggests a notable roughness in the etched areas.

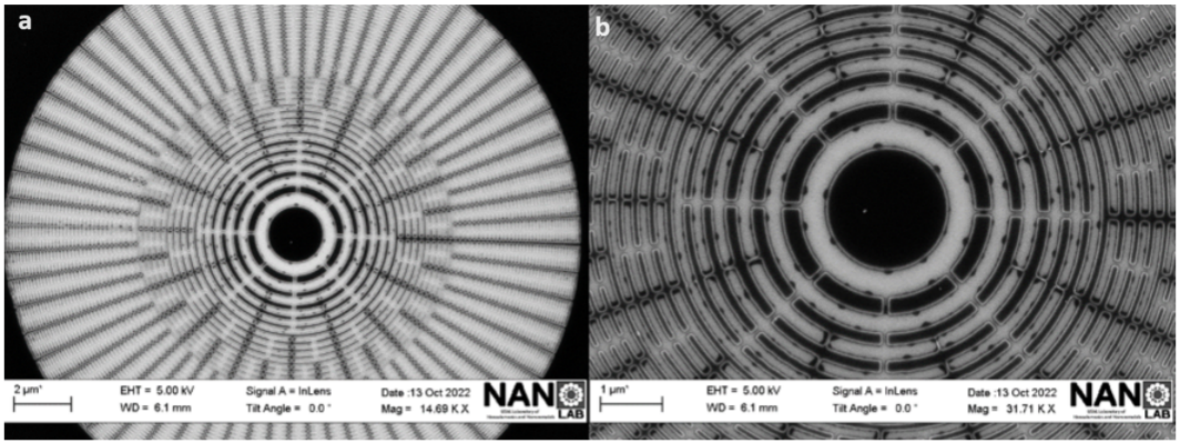

Figure 4.10: Displaying a top view (a) and a detailed zoomed illustration (b) of the Fresnel Zone Plate following 55 seconds of chromium dry etching at a chamber pressure of 12 mTorr.Notably, the photos clearly show the appearance of strange black patches on the chromium mask's surface.

Cr has been etched by plasma in conditions based on chlorine, such as $O_2 + Cl_2$, where oxygen and chlorine radicals etch the material by generating the volatile etch by-product CrO_2Cl_2 according to the reactions [204, 237, 251, 252]:

$$C_r + 2\,O^* + 2\,Cl^* \longrightarrow C_rO_2Cl_2 \tag{4.1}$$

$$C_rO_x + (2 - x)O^* + 2\,Cl^* \longrightarrow C_rO_2Cl_2 \tag{4.2}$$

It was difficult to use Cr as an intermediate etch mask because oxygen and chlorine gas were required for the plasma etching process. However, this leads to unfavorable outcomes since, as shown when employing the first recipe, the polymer are known to exhibit poor etch resistance against plasmas, including oxygen gas [253]. ICP power and chamber pressure had an impact on the lengthening of the etching period and, consequently, the removal of PMMA prior to chromium etching in the second and third recipes. As it is known that the ICP power has a significant impact on the Cr etch rate and etch rate uniformity, recipe 2 exhibits high pressure but no ICP (ICP = 0 W). The Cr etch rate decreases as a result of a reduction in the quantity of reactive species with decreasing ICP power[254].In contrast, recipe 3 has a high ICP power of 1200 W. However, because of the influence of the plasma's physical etch component, there may be a decrease in the etch rate while operating at a low chamber pressure, where the mean free path of plasma species (ions and neutrals) is bigger [255, 256].

We were able to arrive at the ideal chromium mask etching recipe after successfully completing all of the earlier testing. where the complete process of the Inductively Coupled Plasma Reactive Ion Etching (ICP-RIE) technique goes as follows:

Prior to the etching procedure, the whole chamber underwent a conditioning phase lasting 20 minutes in order to stabilize the system. Once the sample was loaded within the chamber, the chromium etching process commenced at room temperature. To achieve optimal results, a specific gas flow rate comprising 14.7 sccm of Cl_2 and 2 sccm of O_2 was maintained within the chamber. Additionally, the chamber pressure was regulated at 12 mTorr, the ICP power set at 600 W, and the RF power at 8 W. The duration of the etching process varied between 30 to 55 seconds, ensuring the desired pattern was accurately transferred to the underlayer material. Following the completion of the chromium etching a thorough cleansing was achieved by utilizing 100 sccm of Argon (Ar) for one minute. This step ensured the removal of any remaining trace materials, resulting in clean and well-defined patterns, as depicted in Fig 4.11 which clearly shows the process of successfully etching away the chromium layer. The

zoomed area in (c) depicts some fine pattern details where the structures can be seen as well-defined and suited for their use as FZPs. By using the recipe mentioned above the etching rate for chromium was 7.64 nm/min. We were able to completely etch the 7nm chromium film after 55 seconds. Regarding the PMMA (with a thickness of 83 nm), the etching rate was 89 nm/min. This indicates that there was a very small amount of PMMA left (about 2 nm) after a 81 nm etch during 55 seconds, as seen in Fig.4.11.c. It is clear that an ultra thin layer of PMMA (around 2nm thick) remains on top of the Cr mask.

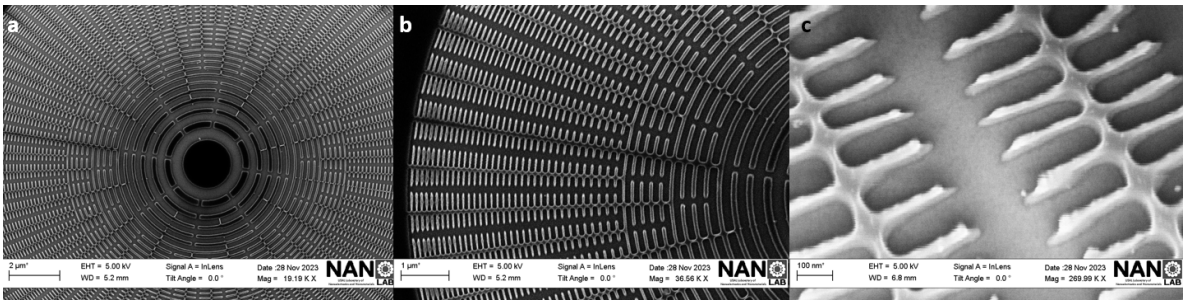

Figure 4.11: A comprehensive view from above reveals the central (a), outermost zone (b), and pattern details of the Fresnel Zone Plate after 55 seconds of dry etching of chromium at a chamber pressure of 12 mTorr. The etching process employed a gas flow combination of 2 sccm of O_2 and 14.7 sccm of Cl_2. In panel (a), the innermost region of the FZP is clearly visible, showcasing high-quality definition of the desired structures, along with a Moiré pattern that contrasts with the highly defined symmetrical structures. Panel (b) presents the outermost region of the structure, where the nm-scale patterns remain well-preserved after the Cr-etching. Finally, panel (c) provides a detailed view of the outermost region of the Cr mask, where the 7 nm-thick metal remains intact as a hard mask, with a thin layer of residual PMMA.

4.4 | Pattern transfer to silicon substrate

To overcome with the faulty definition of the outermost zones of the FZP where nm-size structures are required we've extensively made use of cryo-etching, allowing the production of clean structures with highly-controlled edge definition. In silicon-based devices, it has been successfully implemented with defined low-roughness sidewalls [257], and generating samples with a high aspect ratio and cleaning [258] in nanometric-size structures[209].

4.4.1 | Silicone cryogenic etching

After the first description and understanding of reactive ion etching at low temperatures in 1987 [259], a number of subsequent studies have examined the method of cryogenic etching. A number of investigations looked into the cryogenic etching procedure. Cryogenic etching using a gas combination of SF_6 and O_2 has been selected in this work to transfer the patterns from the chromium mask to the silicon substrate. The following are the benefits of this technique:

- Compared to the SF_6/C_4F_8 based method, the cryogenic SF_6/O_2 etching process offers a number of advantages. One advantage is that the process of etching is carbon-free, making it incredibly clean and preventing the deposition of polymers on the surfaces of the final nanostructures and chamber walls. Additionally, it can offer continuous etching, which could lead to the final silicon nanostructure having a smoother sidewall [260].
- It is possible to improve metallization lift-off on silicon by utilizing the high selectivity of photoresist's etch rate over silicon [261].
- With just low-energy ion bombardment needed, the passivation layer (SiO_xF_y) is extremely thin, allowing for less hard mask damage and better etching selectivity [262, 263].
- Reaction products may be sufficiently eliminated because of the low-frequency pulse, which helps to decrease the undercut effect [260].
- By adjusting the etch parameters, the sidewall profile is very controllable and repeatable [264, 265].
- When combined with extremely low forward bias power methods, cryogenic temperatures can provide significant benefits for nanoscale etching. Great-fidelity pattern transfer is possible even with incredibly thin soft material masks, thanks to their great selectivity [209].

A passivation layer of adhering reactants forms on the silicon surface more readily when the conventional reactive ion etching procedure is combined with maintaining the substrate at cryogenic temperatures [209]. Since fluorine has a higher reaction probability with silicon than other halogens, a mixture of SF_6 and O_2 was used as feed gas in this work's cryogenic etching technique [266]. The achievement of an anisotropic etching outcome depends on both adding oxygen and conducting the procedure at cryogenic temperatures. The favored silicon-surface reaction below −100 °C is Si, O, and F recombining to form SiO_xF_y molecules.As a result of activation energy and Arrhenius' law, the SiO_xF_y halogen compounds evaporate at a slower pace. The passivation layer inhibits the spontaneous reactions between silicon and fluorine radicals [209].

Fluorine can diffuse through around two to five monolayers without bias before interacting with silicon [267]. A very exothermal chemical reaction produces SiF_4, which subsequently desorbs from the surface. At atmospheric pressure, (SiF_4 has a melting point temperature of -86.8 °C, making it a very volatile substance. After then, the pumping system either evacuates it or dissociates it in the plasma. It should be noted that while SiF_4 is the primary byproduct, significantly smaller amounts of other compounds, such as SiF_2, Si_2F_6 or Si_3F_8, can also be formed [267].

At the specified temperatures, therefore, the SiO_xF_y passivation layer on the silicon surface is promoted. Even though cryogenic temperatures are required, the temperature range is typically restricted to be between -100 °C and -140 °C, [268].The restriction is caused by the involatile Si_2F_6 that forms on the silicon surface at temperatures below -196 °C, which prevents fluorine-induced etching. However, at temperatures beyond -140 °C, this condensation is totally forbidden [269]. Within the appropriate temperature range, the passivation layer is developing at the bottom of the pattern and on the side walls, significantly slowing down the etching rate [270]. The ion bombardment accelerates the etching process at the trench bottoms. Ions are accelerated from the plasma to the sample as a result of the DC bias [271]. The angular distribution and kinetic energy (self-bias) of the ions play a major role in the removal of the passivating layer.

In the transfer of fresnel lens patterns from chromium to silicon, it is important to

carefully control the etching parameters to avoid undesired results. Prior to the etching procedure, meticulous conditioning of the reaction chamber was conducted on a silicon wafer, following a well-defined etching recipe for a duration of 20 minutes. This conditioning step has been demonstrated to be of paramount significance in achieving consistent and reproducible outcomes. The cryo-etching was performed using an Inductively Coupled Plasma (ICP) Reactive Ion Etching (RIE) system, specifically, the Oxford Instruments Plasma Pro 100 Cobra. This process involved the controlled introduction of sulfur hexafluoride (SF6) and oxygen (O2) gases and was executed at extremely low cryogenic temperatures, with the operational temperature maintained below -100°C [272]. For a comprehensive overview of the typical operational conditions employed in our cryo-etching process, please refer to Table 4.4

Table 4.4: Typical control values for the silicon reactive ion etching generating under-etched profiles as shown in Fig.4.13

Silicon reactive ion etching	
Pressure	10 mTorr
Rf power	4 W
ICP power	1000 W
SF6 flow	60 sccm
O2 flow	08 sccm
Temperature	-110 °C
Time	15 s
etching rate	2.63 µm/nm

Strong under-etching (In the case of under-etching, the etching procedure is depicted in the schematic in Figure 4.12), as is depicted in Figure 4.13, is the primary issue that silicon cryo-etching faces. This under-etching made the patterns thinner and brittle, which produced damage of the narrowest lines, and the Cr mask was bent. Underetching has implications for device production as well since it affects the faithful etching of resist patterns into silicon through a mask. For device fabrication processes to be optimized, it is imperative to address and comprehend these under-etching effects.

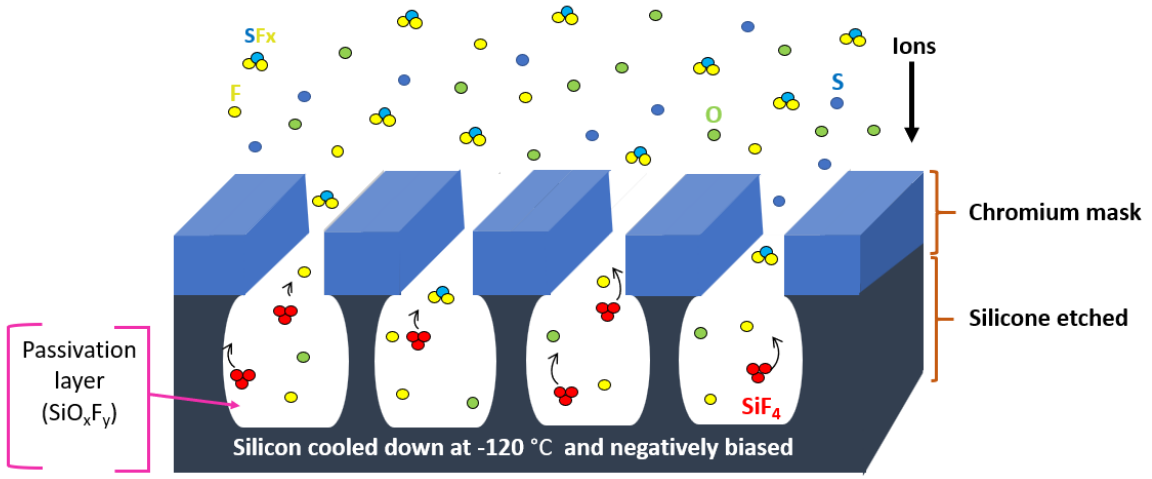

Figure 4.12: Schematic representation of cryogenic etching process revealing under-cutting of silicon beneath chromium mask.

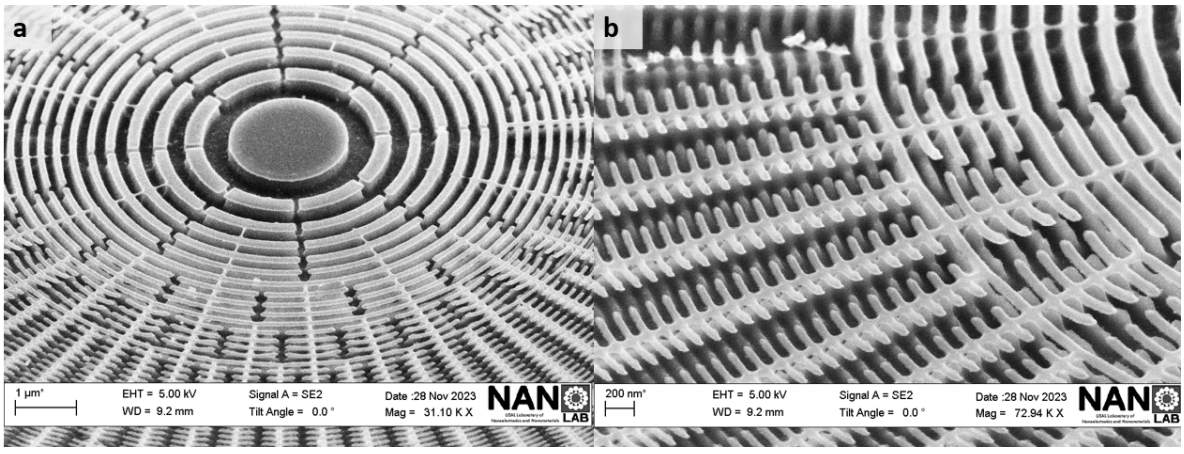

Figure 4.13: Inclined view (60°) of the FZP after 15s of the cryo-etching of the silicon layer under the chamber pressure of 10 mTorr and -110°C with the SF_6/O_2 gas flow rate of 60 / 08 sccm, ICP power of 1000 W and RF power of 04 W . Figure **(a)** SEM image depicts silicon etching results highlighting noticeable undercutting. Figure **(b)** displays bending instances in our chromium mask.

Prior to discussing the taken technique to address this issue, let us clarify what under-etching is and the circumstances behind its occurrence.

Cryogenic silicon etching raises the possibility of under-etching, a phenomena defined by the lateral removal of material beneath a masking layer during the etching process. Under-etching in this case results from sidewall tapering or undercut regions forming as a result of the lateral erosion of silicon material beneath the applied mask. Under-etching is observed during silicon etching at low temperatures in cryogenic reactive ion etching (RIE). As seen earlier in our lens with an outer zone width of 50 nm, the isotropic character of the etching process causes lateral and undercutting effects that are most noticeable in small designs with narrow dimensions. In cryogenic etched trenches, the width of the trenches affects the sidewall angle. The main reason for this variance is because the SiO_xF_y passivation layer must be created by a larger oxygen flow in trenches with narrower gaps due to the reduced oxygen transport in smaller trenches. An increase in trench size will result in a more upright profile as more oxygen becomes accessible for passivation development while utilizing a consistent SF_6 to O_2 ratio that produces vertical sidewalls for a given trench size. In contrast, the profile will exhibit undercutting or bowing as the trench size decreases because not enough oxygen will reach the sidewalls to produce the passivation layer [262].

A different way to lessen under-etching is to change the ion energy. It is possible to regulate the ion energy without affecting the ion density by adjusting the bias voltage. Reactors that use inductively coupled plasma (ICP) technology have the ability to function at low energy, usually a few electron volts (eV). This is very useful when using a sensitive mask to etch small and shallow structures. using this benefit, sidewalls that are smooth and perpendicular can be produced using low-energy plasma while the silicon surfaces' passivation layer is still intact. It's crucial to remember, though, that very low ion energy can lead to the development of silicon spikes, sometimes referred to as black silicon. When the passivation layer on the bottom surfaces is not sufficiently removed, this happens [273].

Temperature and O_2 flow are two obvious characteristics that regulate the trench profile based on the SiO_xF_y passivation mechanism. undercut has a considerable tem-

perature dependency. The sticking coefficient of oxygen on silicon increases when the wafer temperature drops from +20 to -130 °C, strengthening the passivation mechanism and reducing lateral etching, such as undercut[274]. Based on the mentioned suggestions to improve the etching process, the recipe used was changed by introducing 12 sccm (standard cubic centimeters per minute) of oxygen flow and reducing the temperature to -120°C, a marginal improvement in the under-cutting of silicon was observed. However, despite these adjustments, some bending and under-cutting still persist as seen in Figure 4.14.

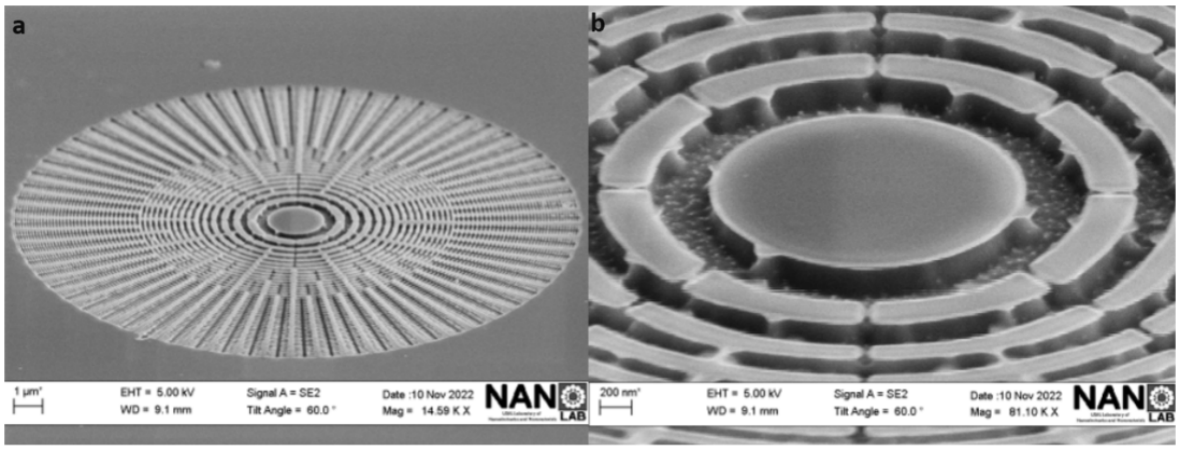

Figure 4.14: Tilted (60°C) Scanning electron microscope images captured from a distance (a) and in close-up detail (b) of FZP with 100 zones, a diameter of 20 µm and an Outermost Zone Width of 50 nm after 15s of silicon etching with increasing in oxygen gas flow to 12 sccm and reducing the etching cryo temperature to -120°C. the under-etching (Negative taper) is slightly visible

Because the temperature that was being used was at the lowest possible point (-120°C) for silicon etching, we are now concentrating on the oxygen flow, which we have raised to 18 sccm as part of our continuous attempts to optimize the procedure. this step leads to eliminating completely the under-etching as seen in Figure 4.15.a . The next most critical factor, following the elimination of under-cutting in silicone, is over-etching, commonly referred to as positive taper which can be seen in the SEM image in figure 4.15.b , there was a significant positive taper and a narrowing at the lowermost.

Regarding cryogenic silicon etching, positive taper describes a progressive etching structure spreading toward the top, making the top larger than the bottom. This phenomenon is manifested as a progressive increase in the breadth or diameter of the

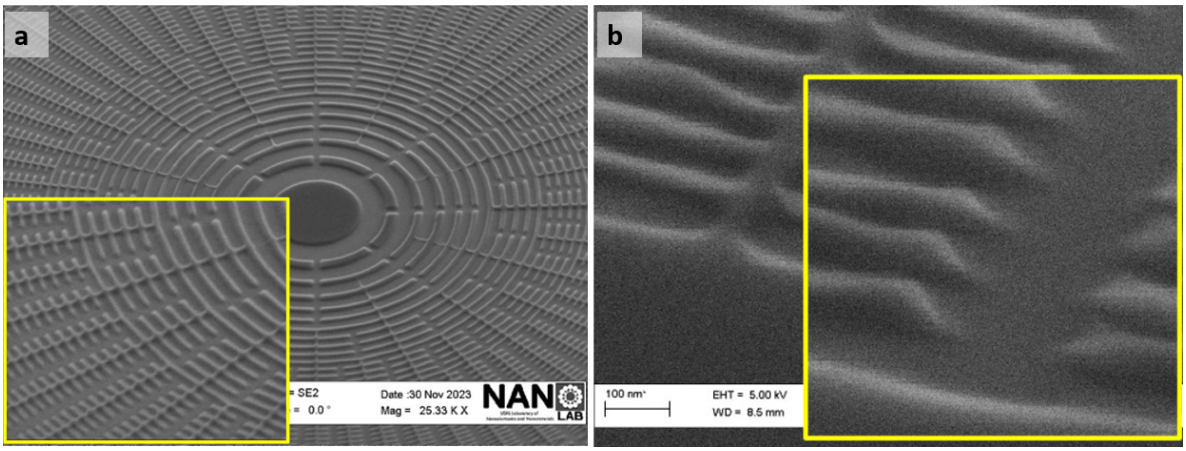

Figure 4.15: (a) Zone Plate following 15 seconds of silicon etching reveals a noteworthy outcome. With an elevated oxygen gas flow of 18 sccm, the under-cutting of silicon is completely eradicated. The resultant patterns exhibit well-defined characteristics, significantly improving etching precision. Notably, the absence of bent patterns underscores the effectiveness of the increased oxygen flow in refining the etching process and achieving the desired etch profile. (b)A titled (45°) Scanning Electron Microscope image captures the etching profile of the outer zone after a 15-second etching process employing 18 sccm of oxygen flow and a cryogenic temperature of -120°C. In the image, the resulting patterns exhibit an over-etched characteristic, showcasing a broader top compared to the bottom. This observation aligns with the effects of increased oxygen flow and the extreme cryogenic temperature, which collectively contribute to the pronounced widening of the etched structures.

etched feature as it extends deeper into the silicon material. It is specifically observed in the sidewall profile of the etched feature. the etch profile was transformed from a negative taper to a positive taper.With an increase in trench size, positive taper is visible. Due of the restricted oxygen transfer in smaller trenches, there is variance in the sidewall angle. Notably, inadequate oxygen delivery is the main cause of positive taper, especially in trenches with narrower openings. The creation of the SiO_xF_y passivation layer is facilitated by a greater oxygen flow in certain situations, which ultimately affects the trench profile and produces the observed positive taper [275] [262]. We can therefore conclude that thicker and harder passivation layers, which provide positive etch profiles, are produced by increasing the oxygen flow or decreasing the temperature. On the other hand, thinner and softer passivation layers are produced by decreasing the oxygen flow or raising the temperature, which results in negative etch profiles [273].

After careful examination, it was determined that using an oxygen flow rate of

18 sccm during the etching process resulted in an undesired positive sidewall profile. Acknowledging the necessity for enhancement in order to get almost vertical sidewalls, a calculated modification was executed by slightly decreasing the oxygen flow to 15 sccm. This intentional change was made after giving much thought to how to best balance resolving the identified problem with preserving ideal process parameters.

A detailed instance demonstrating the exceptional efficacy of a precisely calibrated mixture of O_2/SF_6 gases is shown in Figure 4.16. This combination was carefully tested at flow rates of 15/60 sccm, in conjunction with a temperature as low as -120°C and a carefully maintained pressure of 10 mTorr. Moreover, this arrangement was optimized by utilizing an ICP/RF power setting of 1000/04 W (See Table 4.5)).

Table 4.5: Selected parameters for silicon reactive ion etching, resulting in vertically etched features and precisely defined patterns, as shown in Fig.4.16

Silicon reactive ion etching	
Pressure	10 mTorr
Rf power	4 W
ICP power	1000 W
SF6 flow	60 sccm
O2 flow	15 sccm
Temperature	-120 °C
Time	2 mn
etching rate	2.25 µm/nm

resulting vertically well-defined and intact structures are shown in Fig.4.16, which presents SEM images of the etching profile after a two-minute process, clearly illustrating the well-defined patterns. A standard cleaning process of rinsing in acetone and isopropanol would complete the process by removing the remaining PMMA layer. Keskinbora et al. reported the fabrication of FZPs suited for soft X-ray microscopy with similar wavelength (1.2 keV) that were able to achieve a spatial resolution in the first order of 61 nm [276]. In those works, trapezoidal-like profiles were obtained by the etching process, detrimental for the fluence found at first order due to the lower

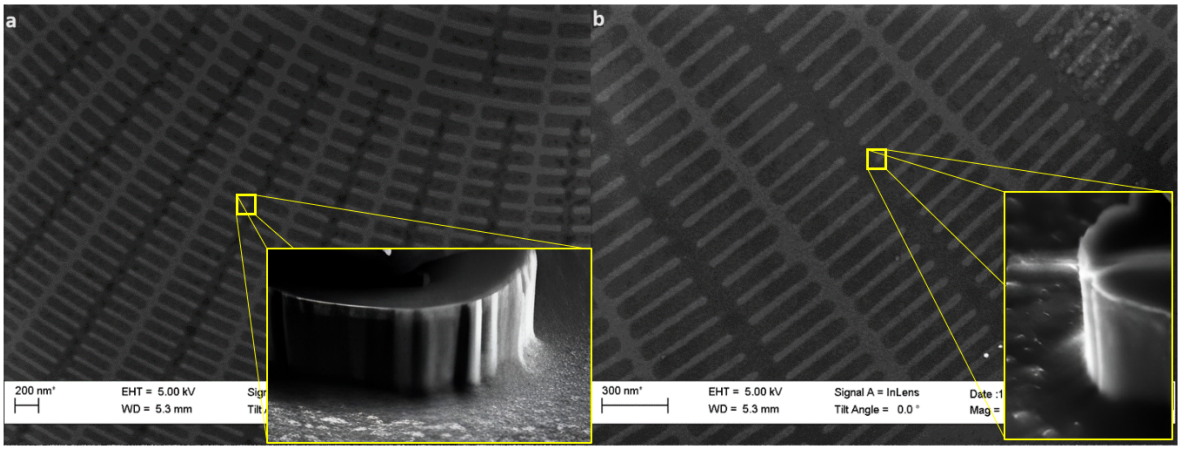

Figure 4.16: Scanning Electron Microscope images (a) from the left side and (b) from the right side of the lens showcase the etching profile of patterns after a two-minute etching process utilizing a 15 sccm oxygen flow and a cryogenic temperature of -120°C. The image vividly displays the vertically etched features and precisely defined patterns that resulted from this specific etching condition.

lens efficiency provoked by the nonvertical feature profiles and the roughness at the edges [211]. Such reduction in the performance of the FZP provokes an increment in the measurement dwell time which can be overcome with the sharper structures that we have fabricated. Moreover, with the correct definition for the outermost vertically well-defined structures by the cryo-etching, we are able to increase the lens efficiency [211] overcoming other dry etching methods [277] where thorough etching was not achieved for comparable outermost zone widths, indispensable for the fabrication of an efficient FZP [210].

This particular arrangement produced very positive results that exceeded expectations by producing the needed vertical sidewalls for silicon etching. This accomplishment marked the effective completion of the complex Fresnel lens manufacture process and acted as a turning point. The accurate calibration of a number of factors, including the closely regulated gas flow rates and the painstakingly maintained temperature, is responsible for the configuration's performance. During the critical last stage of production, these characteristics were essential in sculpting the desired sidewall profile and guaranteeing an overall high-quality end product.

4.4.2 | Etching rate

In this section, we will delve into the examination of the etching rate in cryogenic silicon etching (In this part, the etching depth was determined using a profilometer, see section 3.2.5). Figure 4.17 represents the dependence of the etching rate on oxygen flow and temperature. In Figure 4.17.a ,we can notice that the etching rate decreases from 2.6 to 1.9 µm/mn while increasing the oxygen flow from 8 to 18 sccm.

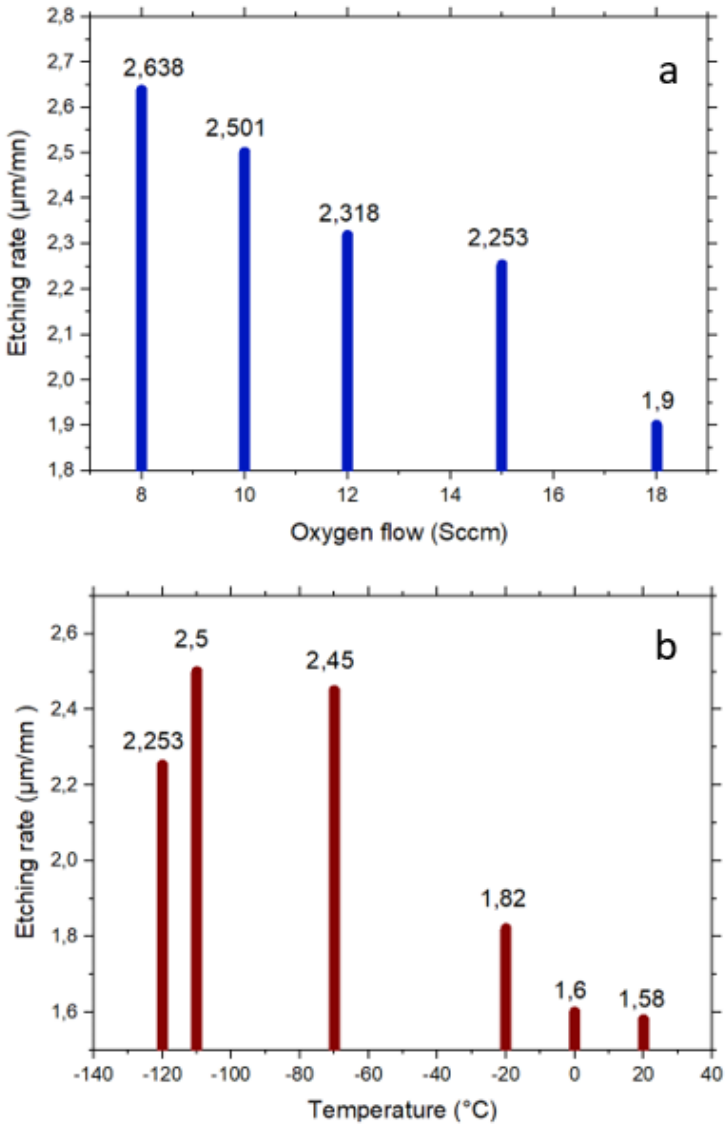

Figure 4.17: Result analysis of the silicon etch rate in the cryogenic etching process in relation to (a) O_2 gas flow at a constant temperature of -120C and (b) temperature with constant O_2 flow of 15 Sccm, where all the etching parameters were maintained, only the temperature and the oxygen flow were changed.

A number of chemical reactions interact at the surface of the material being etched to cause the complex phenomena known as the drop in etch rate. The development of the SiO_xF_y inhibitory coating is thought to be a key factor in this process. The formation of this film is thought to occur when the O_2 ratio rises enough to the point where fluorine is replaced, causing a drop in the reactive species. By acting as a barrier, this inhibitory coating lowers the etch rate by stopping the creation of etch products [278, 279].

Moreover, it has been seen that sulfur present on the surface at low O_2 concentrations can impede the adsorption of oxygen atoms. This will inhibit how fast the etching process proceeds. The complexity of etching and the need for an in-depth understanding of underlying mechanisms to manage and optimize etch rates in practical applications are also demonstrated by these subtle interplays between various chemical species [280, 281].

Opposite of this, our observation, as indicated in Figure 4.17.b showed an increased etching rate at lower cryogenic temperatures a comprehensive study of the experimental data indicates that with a decrease in temperature, there is a better efficiency for etching. For instance, at -110°C, below zero temperature, the etching speed significantly improved and reached an extraordinary level of 2.5µm/min. This change in rates with temperature demonstrates how complex cryogenics is able to influence the dissolution process.

The dynamic relationship between temperature and etching profile is illustrated visually in Figure 4.18, which comes after a detailed investigation of the subtle effects of temperature variations on the etching rate. This figure provides a thorough understanding of the numerous nuances of the process by carefully comparing the etching profiles at different temperatures. A distinguishing pattern becomes apparent upon closer examination. The cryogenic temperature drops from 20 to -20, -70, and -120 °C, and over-etching angles rise progressively to 51°, 69°, 83°, and 87°, at that order. The relationship between temperature modulation and the resulting over-etching properties is clearly demonstrated by this astute finding. The etching profile has a notable positive taper, as revealed by the examination conducted at room temperature (20°C) and

at somewhat lower temperatures (-20°C). The pronounced over-etching patterns and a discernible increase in sidewall roughness attest to this. These results indicate how the overall geometry and texture of the etched patterns are affected by even small changes in temperature throughout the etching process.

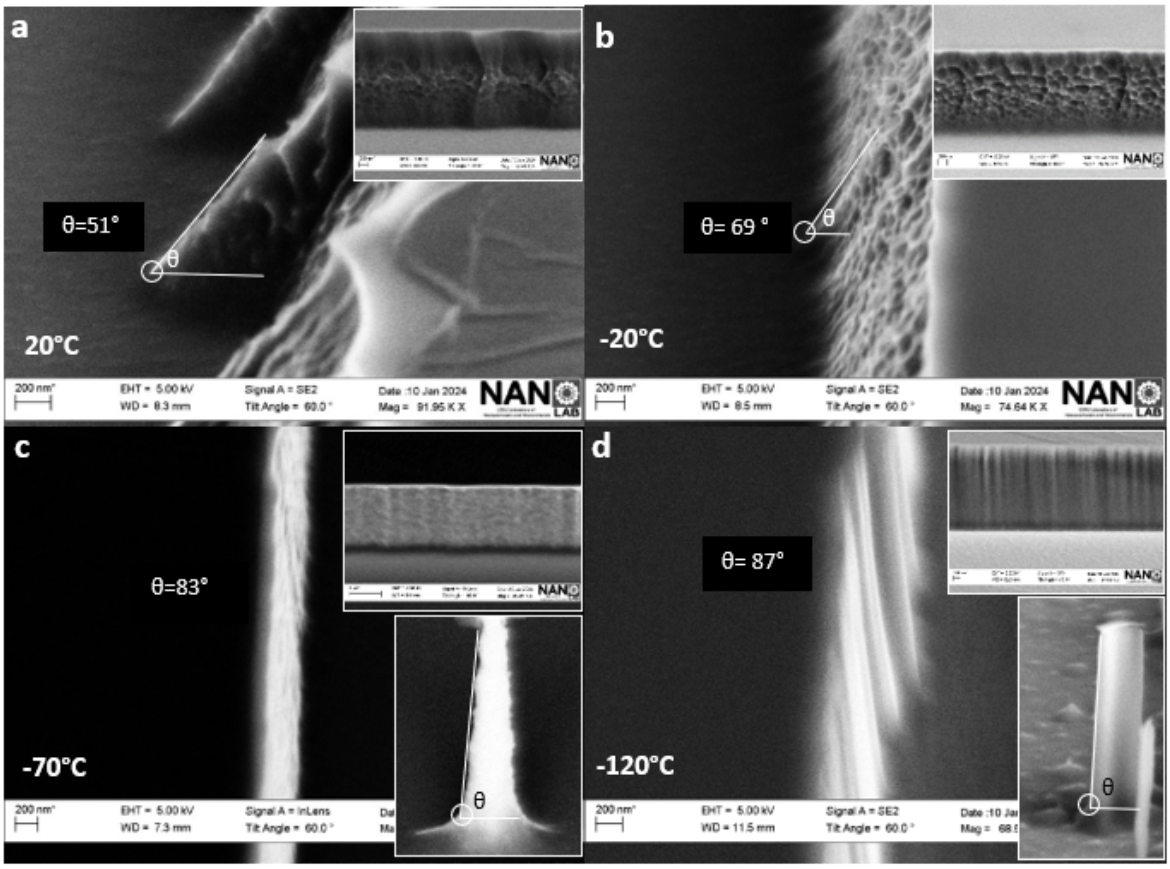

Figure 4.18: Scanning Electron Microscope images provide a detailed analysis of the etching profile at various temperatures. The images capture the sidewalls from different angles, showcasing the etching process in a comprehensive manner. At room temperature (20°C) and at -20°C respectively figs. (a) and (b), the SEM images reveal that the sidewalls appear extremely rough. The over-etching is clearly visible, indicating an intense etching process. The big illustration in the SEM image displays the sidewalls from a side angle of view, giving a larger perspective of the etching profile. In contrast, at low temperatures (-70°C and -120°C) respectively as seen in Figs. (c) and (d), the sidewalls undergo a significant change. The SEM images exhibit a softer texture on the sidewalls, indicating a less aggressive etching process. The small illustration in the upper right corner of the SEM image showcases the sidewalls from a facing angle of view, providing a closer look at the etching profile. Furthermore, at these low temperatures, the etching tends to be more vertical in nature. This vertical etching pattern is clearly depicted in the small illustrations in the right bottom corner of the SEM image. The sidewalls appear smoother and more uniform, suggesting a controlled and precise etching process.

On the other hand, a different pattern appears when the temperature drops even lower. The tendency toward vertical etching emerges at -120°C, and the over-etching decreases. Together with this radical change in etching behavior, soft sidewalls occur, emphasizing the complex relationship between temperature and the structural properties of the etched patterns that arise. In general, the SEM pictures shown in Figure 4.18 provide crucial details regarding the temperature-dependent etching profile. At higher temperatures, the sidewalls become more rounded and defined; but, at lower temperatures, they also acquire a finer texture and vertical etchings. These results provide information about how to enhance the etching procedure.

In this final section, we will mention and provide a brief description of the shadow mask evaporation process, which is an extra method that can be employed to enhance the etching results. The most important step in the creation of electronic devices using nanomaterials is electrode deposition. The most extensively used technology for depositing electrodes is presumably lithographic in nature, either photolithography or electron beam lithography, which call for pricey, specialized facilities in addition to a solid technical foundation in micro-fabrication. Different strategies for less costly lithography setups using nanomaterials have been demonstrated in recent publications [282, 283]. However, in order to guarantee the adhesion of the resists for the development and lift-off phases, these lithographic techniques require chemical treatment procedures, which may cause harm to some nanomaterials that are more environmentally sensitive.

Conversely, direct metal evaporation via a shadow mask offers a number of benefits over traditional lithographic methods [284–287]. It doesn't need a clean room setting, is simple to deploy, and is rather inexpensive. Furthermore, labs lacking the necessary infrastructure or experience in microfabrication can still simply implement it. The fact that the procedure is "all-dry," or acceptable with nanomaterials that are prone to degradation or destruction throughout the chemical and optical operations needed in lithographic techniques, is another significant feature of the technology [288–290]. One benefit of pre-patterned electrodes is that they allow for a nanomaterial construction in the instrument panel, which is essential for materials that are sensitive to air [291]

[292].

Usually, the creation of shadow masks necessitates an expensive, specialized facility akin to that used for lithographic processes [293] [294]. The majority of research teams that employ shadow mask deposition purchase masks from the commercial market or contract with micro-fabrication foundries to handle the fabrication, which reduces the flexibility of the technique and renders it unsuitable for quick prototyping. This raises the question of whether it is possible to construct shadow masks in an economical and adaptable manner, enabling research groups to create unique masks on their own without having to outsource manufacturing or invest in expensive infrastructure.

A novel electroless plating technique using droplets to deposit gold and silver nanoparticles on a silicon substrate is presented by Chia-Wen et al., where they construct different geometries and designs on the silicon surface by combining the techniques of shadow mask and handwriting[295]. Likewise, according to Ho Jin et al., Y2O3-MgO nanocomposite with an aspect ratio of 50:50 exhibits plasma etching behavior when used in ceramic components of etching equipment operating at high power levels and in various plasma gas atmospheres. where the sample was partially covered with a shadow mask so that just the region intended for plasma etching was visible [296].

A work on laser ablation mask creation employing custom optical systems was recently published by Tomczyk et al. However, the resolution obtained by these systems was limited to the range of 50 to 100 m, and they were usually made up of pricey components [297]. Many uses of nanomaterials may call for electrodes in the 10–50 m range, therefore, this might not be adequate in all cases. In addition, many research groups would find the stated laser ablation systems too costly and difficult to utilize to be practical. Recent research on the creation of shadow masks with an absolute minimum pattern dimension of 100 m using the CO2 laser to eliminate filter paper was also reported by Elhami Nik et al [298].

In our study, during the fresnel lens fabrication, after 2 minutes of silicon etching, we tried to apply the shadow mask technique by covering the lens with gold in order to protect the patterns and etch it more so we could get deeper patterns. Our sample

was tilted around thirty degrees during the evaporation process with the intention of reaching and coating the sidewalls that are not shielded by the chromium mask, allowing us to further etch the silicon. In our e-beam evaporator, the base pressure of the main chamber is normally in the range of 10^{-10} mbar. The sample is loaded from the load chamber when the pressure reaches a value of 10^{-6} mbar. With our e-beam gun for Telemark, we applied 8 kV for the acceleration of the electrons on the crucible. The gold was previously melted, and for good evaporation, we need to increase little by little the current emission to avoid the spitting problems of the material. In our e-beam evaporator, gold starts to evaporate with a current emission of 160–170 mA, but we have to achieve 220 mA to obtain a deposition rate of 0.1 nm/s. When the final deposition is obtained, we remove the sample from the main chamber to the load lock and switch off the system. When a layer of 20 nm-thick gold was used to seal the etched patterns on silicon, an outstanding improvement in the etching process was realized. The ability to make more complex and deeper patterns was now achievable by extending the etching time beyond 03 minutes while preventing the problem of under-etching entirely. This improvement can be explained by the fact that the extra layer of gold played a protective role. The etching process was controlled and made more precise by shielding the side walls of the structures against over-etching through the use of a gold layer.

As illustrated in Figure 4.19, the inclusion of this layer brought about a drastic improvement in this procedure. The protective characteristics of the gold layer were very important when it came to protecting the etched patterns' integrity and desired shape. The latter served as a blockade against too much material cutting hence keeping the sidewalls' structural form. This safety measure made sure there was controlled and predictable etching which ended up giving patterns of greater depth and definition.

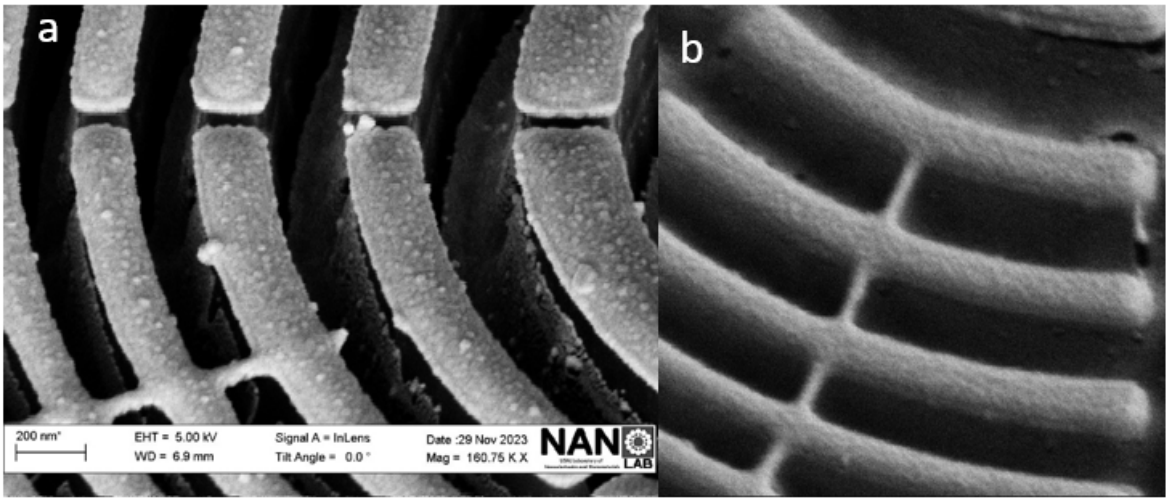

Figure 4.19: The scanning electron microscopy images provide evidence of the outcome of the shadow mask technique. image (a) illustrates the FZP patterns after the evaporation of a 20 nm layer of gold that covers them. Image (b) shows the resultant silicon patterns after the cryogenic etching of the silicon for 03 minutes. Here, it is apparent that the patterns have become deeper without under-etching.

4.5 | Conclusions

X-rays, widely used for their ability to penetrate matter and unveil intricate structural details at electronic, atomic and molecular levels, with unprecedented resolution, in space and time, serve as an indispensable tool across numerous scientific fields such as materials science, medicine, chemistry, and physics. The full exploitation of last generation Free Electron Lasers and synchrotron light sources requires the use of state of the art devices able to focus X-rays at their diffraction limit, at tens of nanometer resolution scale and beyond. Besides the aforementioned established players in the field, laser-driven X-ray sources are emerging as a promising and rapidly evolving field, requiring a set of new tools to get advantage of their capabilities. Grazing incidence mirrors and FZPs are currently the optical devices able to reach the highest imaging resolutions in the soft X-ray range, though FZPs offer unrivaled performances in terms of compactness, joint with superior stability with respect to environmental parameters. The key factors and challenges in FZP manufacturing can be condensed in an extreme control (i.e., required resolutions of nm-scale) of the manufacturing process of a full 3D

device over tens of µm range (i.e., the overall transverse size) and thicknesses on the µm scale.

Our research presents an advanced method for crafting nm-size Fresnel zone plates combining precise CAD design with etching at cryogenic temperatures, a technique that surpasses traditional etching methods both in the definition of the vertical edges of such structures. This approach is ideal for producing complex structures with high accuracy. We've successfully created a silicon FZP with 100 zones, measuring 20µm in diameter with an outermost zone just 50nm wide and a very high aspect ratio, suitable for a direct employment at lower photon energies, as much as a deposition mask for high-Z materials at higher photon energies. Our method combines Electron Beam Lithography for precise microstructure definition with a chromium mask, ensuring flawless FZP fabrication via cryoetching. Through refinement of the chromium mask and exploration of different designs, we successfully addressed the issue of pattern collapse. Despite challenges with PMMA resist, we effectively utilized it as a mask for chromium layer etching. By employing cryogenic etching techniques and selecting an optimal process recipe, we achieved a silicon etch depth of approximately 4.3 µm, along with well-defined vertical sidewalls. Additionally, the incorporation of a 20-nm thick gold layer, although complex and time-consuming, provided crucial protection to the outermost regions, enabling the production of high-quality patterns with high aspect ratios. This approach effectively prevents undesired under- or over-etching, making it well-suited for generating nm-scale patterns with low roughness profiles.

We can therefore conclude that it is feasible to fabricate nanometric devices with narrow patterns and obtain clear, well-defined features by utilizing the EBL and cryogenic etching, which is accomplished by first selecting an appropriate EBL design and an appropriate underlayer material type and thickness (between the resist and silicon substrate). In addition to selecting suitable etching recipes with regard to the kinds of gases employed and their proportions, as well as the pressure, RF power, ICP power, process time, and temperature.

5 | Nanoscale characterization of ReS_2

5.1 | Introduction

Due to their remarkable mechanical, optical, and electrical capabilities, two dimensional materials (2DMs) have enormous application potential in addition to being of great research interest. Chapter 2 (Introduction) includes a detailed description of these materials, as well as the main motivation for the current research. In the context of this thesis, we have performed a thorough characterization of ReS_2, aiming at its application on different optoelectronic devices. Nevertheless, the main results presented here are obtained via surface, structural and chemical characterization techniques, and they focus on deciphering their behaviour at the nanoscale. Specifically, this chapter will cover the characterization of ReS_2 by means of a variety of instruments, including the profilometer, Atomic force microscopy, and Raman spectroscopy.

5.2 | Motivation

Over the past ten years, layered transition metal dichalcogenides have attracted a lot of interest because of their two-dimensional nature, easily tunable bandgaps (which can shift from indirect in bulk to direct in monolayer form), strong spin–orbit coupling and prominent excitonic effects, which makes their application in nanoelectronics, optoelectronics, and energy storage system very promising.[299, 300]. Among the TMDs family, Re-based TMDs (ReS_2 and $ReSe_2$) are receiving a lot of focus due to their particular structural and electronic features that set them apart from more commonly studied group VI TMDs (like MoS_2 or WS_2). They present substantial exciton transitions. In contrast to group VI crystals, these materials exhibit optical anisotropy as a result of their decreased crystal symmetry [301–303]. This anisotropy allows to explore novel applications such as polarization-sensitive optoelectronic devices, and their prominent excitonic transitions open up opportunities for next-generation optoelectronics and quantum technologies.

Although numerous research groups have examined the band structure and optical properties of atomically thin ReS_2, many questions remain about its fundamental aspects. For instance, there is disagreement among the publications regarding the labeling of the various excitonic transitions and the nature of the fundamental bandgap (direct or indirect)[304–307]. Furthermore, ReS_2 multilayers exhibit two stable stacking orders at room temperature [308, 309], each with significantly distinct optical characteristics. The occurrence of numerous stable crystalline structures, each with a distinct band dispersion, may therefore be the cause of the seemingly contradicting results for the bandgap and optical response of ReS_2 crystals published in the literature. The optical response of the photodetectors, which is dominated by exciton transitions even at moderate temperatures, is greatly influenced by the strong Coulomb interaction and the low symmetry of the ReS_2 crystalline structure.

In sharp contrast to MoX_2 or WX_2, which form crystalline phases of the 2H-hexagonal, ReS_2 is a semiconducting TMD with a 1T-distorted crystalline structure with two nonequivalent perpendicular directions that are either parallel or perpendicular to the b crystalline axis [112], where the rhenium (Re) atoms form clusters (Re_4 chains) that break the higher symmetry seen in MoX_2-type structures (See figure 5.1). The stacking between layers in multilayer crystals exhibits two distinct stable configurations, referred to as AA and AB stacking in the literature [308, 309]. The succeeding layers in AA-stacked crystals are stacked exactly on top of one another, whereas in AB stacking, the successive layers are displaced across the (a) crystalline axis by around 2.5 Å. Photoluminescence and polarization-resolved Raman spectroscopy can be used to determine the stacking configuration and the orientation of the ReS_2 crystalline axis. It has also been shown that the orientation of the material with respect to the crystal axes affects the various properties of ReS_2, such as electrical conductivity, optical absorption, etc[310–313].

ReS_2's distorted structure has an impact on a number of its characteristics, including the interlayer decoupling, which is a reduced coupling that results from the distorted structure and reduces interactions between neighboring layers. One significant result of the weak interlayer interactions is that its bandgap remains nearly direct even in

bulk form (1.5 eV), therefore maintaining strong optical transitions and high photoluminescence efficiency even in bulk or multi-layer forms. Conversely, in most TMDs, the bandgap shifts from indirect (bulk) to direct (monolayer) due to interlayer coupling effects [116].

The enhanced photoluminescence efficiency stems from the excitons' behaviour in the material. An exciton is a known state in which an electron is stimulated from the valence band to the conduction band and a hole is attracted to it by the Coulomb force [314]. In other words, there is a relationship between excitons and band gap. In materials with a direct band gap, excitons can recombine directly by releasing a photon, which results in faster and more efficient photoluminescence than in materials with an indirect band gap, where the process is slower and less efficient. This makes it possible for multilayer ReS_2 to exhibit high photoluminescence (PL), which is uncommon for TMDs [315]. Furthermore, excitons exhibit polarization dependence (which is related to the strong in-plane anisotropy of ReS_2); the intensities of these excitonic features vary with the linear polarization of light, where each exciton reaches its maximum strength at a distinct polarization angle[316]. In their work, D. Vaquero et al focus on the optoelectronic response of few-layer ReS_2 phototransistors. They discover three primary excitonic characteristics, whose brightness changes as a function of the polarization of input light, by using low-temperature photocurrent spectroscopy [317, 318]. They also computed the band structure of ReS_2 using density functional theory (DFT) first principles in order to understand the origin of the excitonic features seen in the spectra. Exciton absorption spectra have been derived from this band structure, which enabled them to determine the excitonic origin of the different features seen in the optical spectra. In close agreement with the spectrum features published in the literature for low-temperature photoluminescence spectroscopy in ReS_2, the obtained result demonstrated that the experimentally measured photoresponse shows multiple exciton-like patterns in the energy range from 1.45 eV to 1.7 eV [319, 320]. Therefore, by altering the polarization of the incident light, ReS_2's basic characteristics, such as transport and lifetime, may be changed selectively [321].

The electrical and photovoltaic properties of a ReS_2 van der Waals heterostructure

were investigated by Ah−Jin Cho et al.[322] and they show that a multilayer ReS_2 heterostructure exhibited diode−like rectifying performance. Their research shows how Re−based TMD semiconductors can be integrated to build a van der Waals heterostructure for practical use. In order to differentiate intrinsic bulk photovoltaic signals from other extrinsic photocurrent contributions resulting from interfacial effects, Maria et al.[323] develop high-quality, lateral devices based on atomically thin ReS_2 with minimum contact resistance.

Ferroelectricity on ReS_2

Ferroelectricity is the property by which a material exhibits a spontaneous electric polarization (an internal electric dipole moment) that can be switched by an external electric field. In most conventional ferroelectrics it is caused by the crystal's internal ions shift, moving slightly away from symmetrical positions and breaking inversion symmetry, which causes the reversible orientation of dipoles [324].

Low-dimensional ferroelectric materials have drawn a lot of interest in response to the increasing need for integration and miniaturization in devices fueled by developments in nanoelectronics [325, 326]. Ferroelectricity in 2D vdW materials has attracted a lot of attention, opening up new possibilities in ultrathin, non-volatile ferroelectric memories, reconfigurable electronics, and nanoscale sensors and actuators [327–329]. In 2D materials, ferroelectricity combines the unique properties of atomic-scale thickness, flexible mechanics, and strong electrostatic tunability.

In *sliding ferroelectrics*, the out-of-plane (vertical) polarization arises precisely because the layers are stacked in a way that breaks inversion symmetry, and shifting one layer in-plane relative to the other (i.e., changing their stacking order) reverses that polarization. Therefore, the vertical ferroelectric polarization in 2D sliding ferroelectrics is inherently linked to the vdW layers' stacking arrangement, which is controllable by in-plane shear motion between them [330, 331]. Room-temperature sliding ferroelectricity in few-layered semiconducting ReS_2 was reported by Wan et al[332]. This research proved that monolayer 1T'-ReS_2 is not ferroelectric; however, two-dimensional 1T'-ReS_2 with layer number $N \geq 2$ exhibits room-temperature vertical ferroelectricity. While interlayer interactions in higher-symmetry TMDs can decrease ferroelectricity in thicker

layers, the weak coupling in ReS_2 guarantees that polarization endures even in bulk-like or multilayer structures. The two degenerate structures (states A and A') were found to have spontaneous vertical polarization with opposite polarization directions (See Figure 5.1), whereas state B is nonpolar along the z-axis direction, meaning that it has spontaneous electric polarization in specific stacking configurations, which allows ferroelectricity. Consequently, the electric polarization that arises from the uncompensated charge transfer between layers can be changed by interlayer sliding.

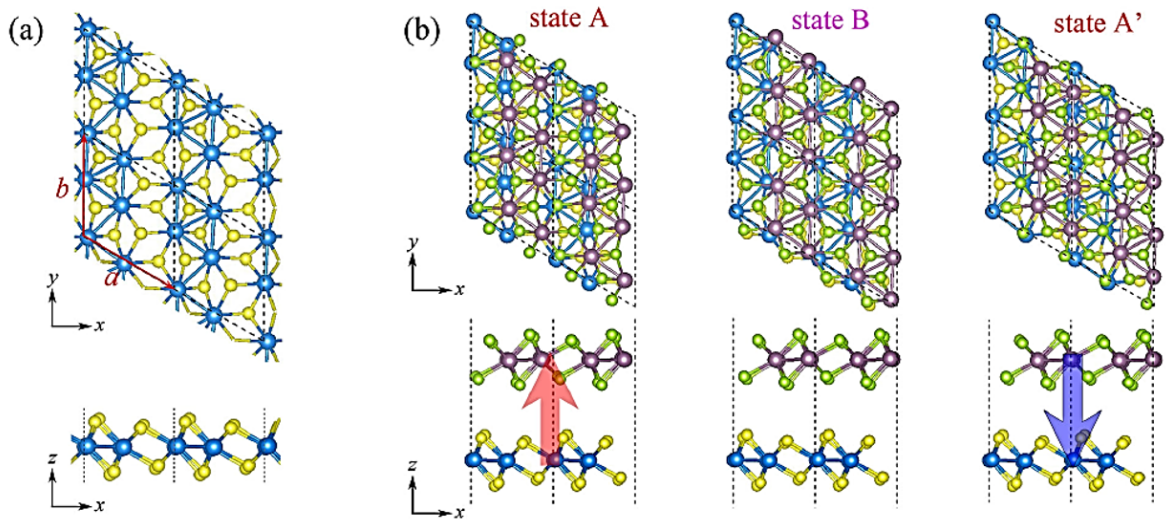

Figure 5.1: (a) Top and side views for the crystal structures of monolayer ReS_2.(b) Top and side views of the high-symmetry nonpolar structure (state B) and the two energy-degenerate ferroelectric structures of bilayer ReS_2 (states A and A').The direction of polarization is shown by the arrows.image adapted from [332].

While it's widely agreed that ReS_2 can exhibit out-of-plane polarization due to its unique chain-based structure and stacking arrangement, many fundamental questions remain. These include how domains switch in actual devices, how substrate or doping changes influence that switching, if the ferroelectricity translates to thicker layers, and how well ReS_2's ferroelectric behavior holds up over time. The current research is using advanced imaging methods (like in situ electron microscopy or near-field spectroscopy), along with strain and doping techniques, to uncover the microscopic switching pathways and overall stability of ReS_2 ferroelectricity.

In this chapter we will explore the origin of contrasting signals observed in Kelvin Probe Force Microscopy (KPFM) measurements of ReS_2 flakes that do not correlate

with topographic features. KPFM is a valuable tool to investigate the role of interlayer interactions, stacking configurations, and sliding ferroelectricity phenomena. We particularly explore the formation and stability of spontaneous vertical polarization domains arising from interlayer charge transfer and polarization induced by lateral sliding of layers. By examining different thicknesses and stacking sequences of ReS_2, we aim to understand how interlayer sliding influences polarization and results in distinct KPFM contrasts. These results could lead to a deeper understanding of ferroelectricity in two-dimensional van der Waals systems, enabling novel nanoelectronic applications based on controlled interlayer sliding.

5.3 | Exfoliation and transfer of the ReS_2 flakes.

The mechanical exfoliation of two-dimensional (2D) materials, demonstrated by the isolation of graphene in 2004, fundamentally relies on the systematic thinning of bulk van der Waals crystals using adhesive tape [333]. This approach exploits the weak interlayer bonding in layered materials to obtain atomic monolayers through repeated peeling of the bulk material using an adhesive tape [334].

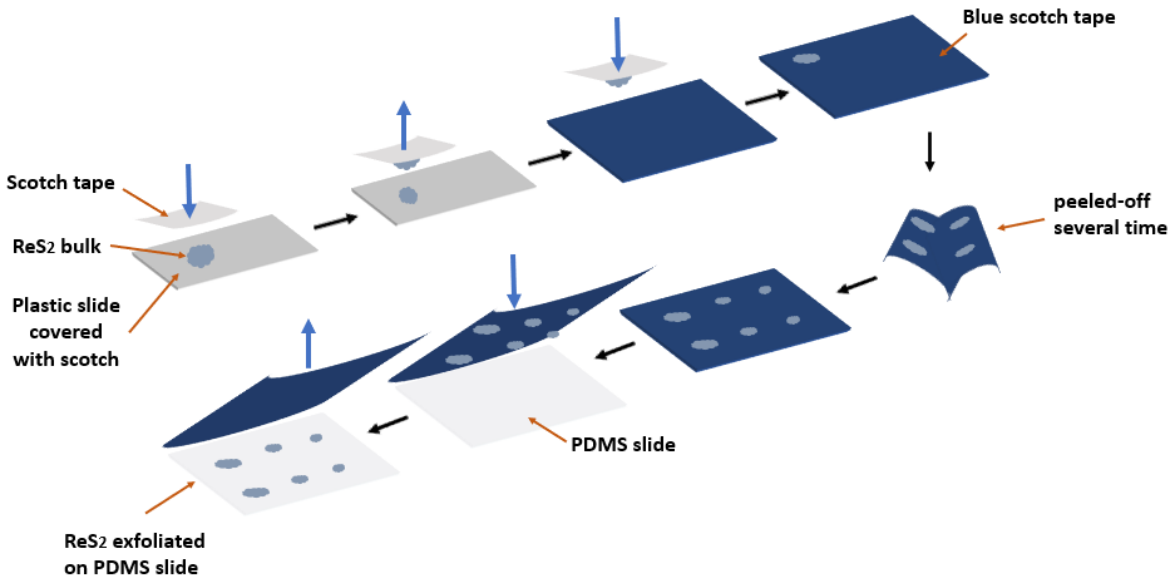

Figure 5.2: Schematic illustration demonstrates the steps of ReS_2 exfoliation on PDMS slide.

High-quality flakes are produced by a standard scotch-tape technique, which we

employed for the ReS_2. The procedure begins with bulk ReS_2 being placed on a tiny piece of Scotch tape that is placed on a plastic slide, creating a tool that resembles a stamp. After that, we gently press on the stamp we created using another piece of scotch tape and transfer a little amount of our ReS_2 to a blue scotch tape, forming small smudges, then we start to peel-off the scotch-tape several times to reduce progressively the thickness of the ReS_2 flakes. Then, the tape with the flakes is placed onto the transparent Polydimethylsiloxane (PDMS) slide, applying a light pressure. Following, the tape is removed slowly to release flakes of different thicknesses in the PDMS slide. The whole process is schematized in Figure 5.2.

Also referred to as the Scotch tape or peel-off method, it has shown significant potential for producing monolayer 2D TMD materials due to its low cost, easy manipulation, and universality for all 2D materials. However, it is still challenging to regulate the thickness, size, as well as the shape of exfoliated nanoflakes. Besides, when Scotch tape is utilized in this type of preparation, it tends to leave sticky residues on the substrate. To circumvent this problem, blue tape is at times used on account of its less amount of adhesive [335].

Due to the transparency of the PDMS films, we can observe the flakes Transmission Optical Microscopy (TOM) while using them as a substrate. This makes it possible for us to use the camera software on the microscope to assess the absorption of red, green, and blue (RGB) channels in various flakes. By performing a correlation between the absorption and the number of layers (determined via Raman spectroscopy, AFM or profilometer measurements), we can determine the thickness of the exfoliated flakes right in the PDMS, allowing us to select the most promising for their subsequent transfer to a different substrate. This method has proven to be effective for various Van der Waals materials [336].

Following the exfoliation stages, we moved to the transfer procedure where the ReS_2 was transferred from PDMS to another substrate, either Silicon dioxide SiO_2 or metallic (such as Au or Pt). The PDMS is suited for achieving deterministic mechanical transfer of exfoliated flakes because to its viscoelastic characteristic.

Once the selected exfoliated flake on the PDMS has been optically identified, the

area of interest is separated by cutting the PDMS slide so that the flake is near the upper edge of the strip. The PDMS strip is positioned in the stage of the transfer system with the aid of tape and a glass slide. The stages are used to precisely align the substrate and the flake that is deposited on the PDMS after the substrate is fixed using vacuum and placed on the hot plate. The PDMS is then adhered to the SiO_2 substrate by means of the z-stage. The whole process is schematized in Figure 5.3. This is a crucial step because sometimes the PDMS needs to be gently tapped with the tweezers to stick to the substrate. After that, the substrate is heated to 80–100 degrees Celsius. Ultimately, the PDMS separates slowly because, at low detachment speeds, the material's viscoelasticity renders it non-stick. The stack is finished once the PDMS has been completely detached. Using the 2D-Transfer setup (see section 3.2.4) the ReS_2 was transferred by following the steps just describes-

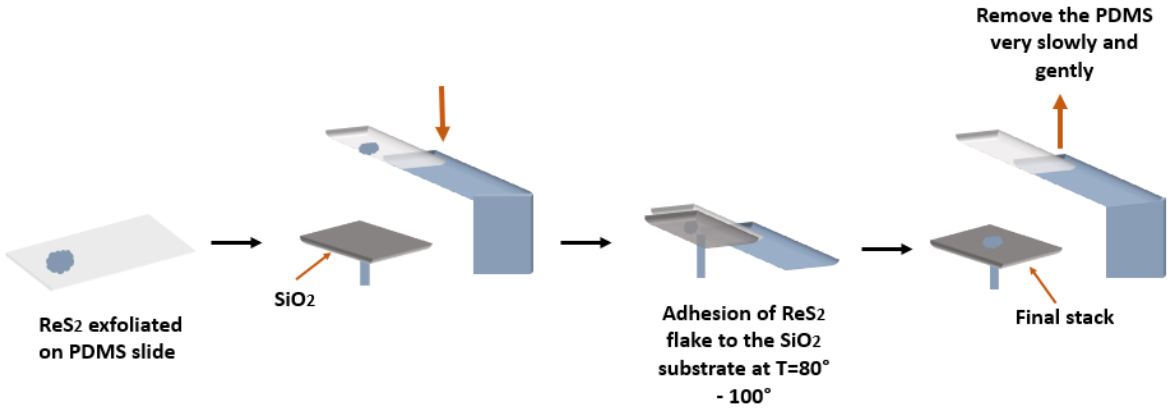

Figure 5.3: Schematic illustration depicting the steps of ReS_2 transfer from PDMS to a SiO_2 substrate

The outcome of the ReS_2 flakes' exfoliation and transfer is displayed in Figure 5.4. An optical picture of a few layers of ReS_2 as flakes of varying heights exfoliated on the PDMS is shown in panel (a). The transferred ReS_2 flakes on the SiO_2 substrate are shown in panel (b), where it is evident that the flakes maintain their shapes, suggesting that the transfer of our ReS_2 flakes was successful.

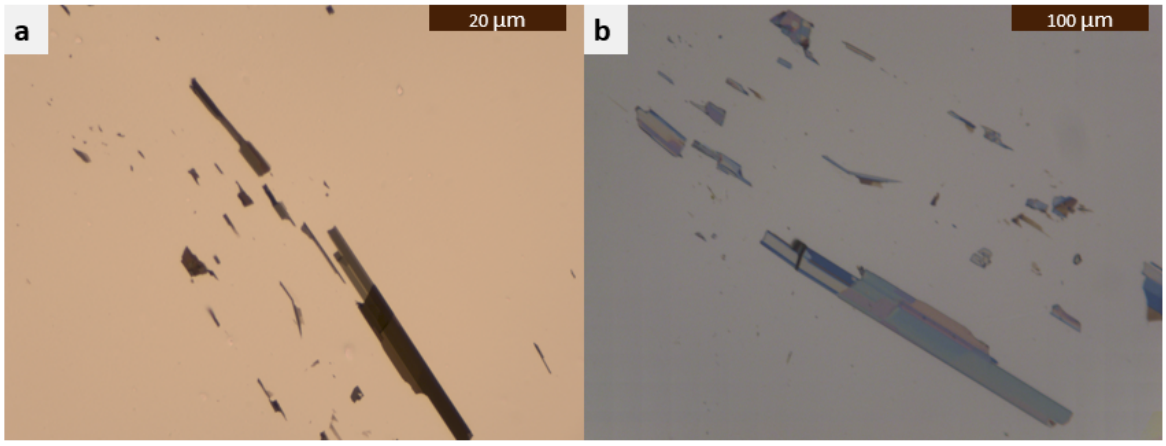

Figure 5.4: Optical picture of the exfoliation and transfer of ReS_2 flakes results .(a) Exfoliated of ReS_2 on the PDMS.(b) The transferred ReS_2 flakes on the SiO_2 substrate

5.4 | Raman characterization of ReS_2

Raman spectroscopy is a quick, practical, and nondestructive method for determining the basic characteristics of 2D materials at both the lab and mass-production scales [337–339]. Generally speaking, Raman peaks of lattice vibrations i.e., phonons, in 2DMs show a number of notable characteristics, such as line shape, peak position (Pos), full width at half maximum (FWHM), and intensity (I). These characteristics can be used to characterize the physical and chemical properties of 2DMs, including electronic states, quantum interference, phonon frequency, electron-phonon coupling, and decay rates of intermediate electronic states involved in Raman scattering processes [337].

Two different types of Raman modes exist in 2DMs, based on the atomic displacement of lattice vibrations: intralayer and interlayer modes. These modes originate from intralayer chemical bonds and the contact between layers through van der Waals interaction (vdW) respectively [340].

Intralayer Raman mode characteristics reveal material compositions and structural stages through analysis of spectral parameters such as peak positions, intensities, and full-width-at-half-maximum (FWHM). The fundamental properties of 2DMs can be studied in relation to external perturbations, such as the dependence of temperature on phonon anharmonicity, electron-phonon coupling (EPC) and thermal expansion [341,

342], the dependence of electrostatic doping on EPC [343, 344], the dependence of strain on elastic constant [345, 346], the dependence of defect concentration on phonon confinement effect [347–350], the dependence of magnetic field on Fermi velocity and many-body effect [351, 352], and the dependence of excitation energy (Eex) on band structure, double resonance Raman process [338, 353], interlayer EPC27, and phonon dispersion [354–356].

In this study, we have exfoliated and transferred several ReS_2 flakes of different heights, and Raman spectroscopy was employed to determine the number of layers and the stacking mode (AA or AB) (see Figure 5.5). The LabRAM HR employed system enables both micro and macro measurements. It includes objectives with magnifications of 10x and 50x, both featuring long working distances, and a high-resolution 100x objective with a significantly shorter working distance. All spectra were collected using the highest-resolution (100x) objective, resulting in an injection spot size of approximately 1 µm. Scattered light analysis is performed using two different diffraction gratings, one with 1800 grooves/mm and another with 600 grooves/mm. Raman spectra acquisition utilizes a 256x1024 pixel Synapse CCD detector, providing a spectral detection range from 200 to 1050 nm.

Similar to MoS_2 [357], the thickness of ReS_2 flakes can be determined by measuring the energetic difference of specific high-energy modes of ReS_2 ranging from one layer to four layers [301]. Moreover, Raman spectroscopy offers an effective way to differentiate AA and AB stacking modes (See Figure 5.1). As shown in the spectra in Figure 5.5.a. extracted from literature[308], in AA stacking, the Raman-active modes I and III are separated by roughly 13 cm^{-1}, while in AB stacking, this gap increases to about 20 cm^{-1} as a result of stronger interlayer interactions affecting phonon dynamics. Figure 5.5 b shows the values of the difference between mode I and III for AA and AB stacked flakes over 4 layers. Furthermore, AB-stacked ReS_2 typically exhibits broader Raman peaks and lower intensity, which can be attributed to variations in symmetry and interlayer coupling. For flakes below 5 to 6 layers, we can see the evolution of this difference with the number of layers. During this work, we have employed this technique to characterize the amount of layers and the type of stacking comparing with the values measured in

literature and AFM measurements.

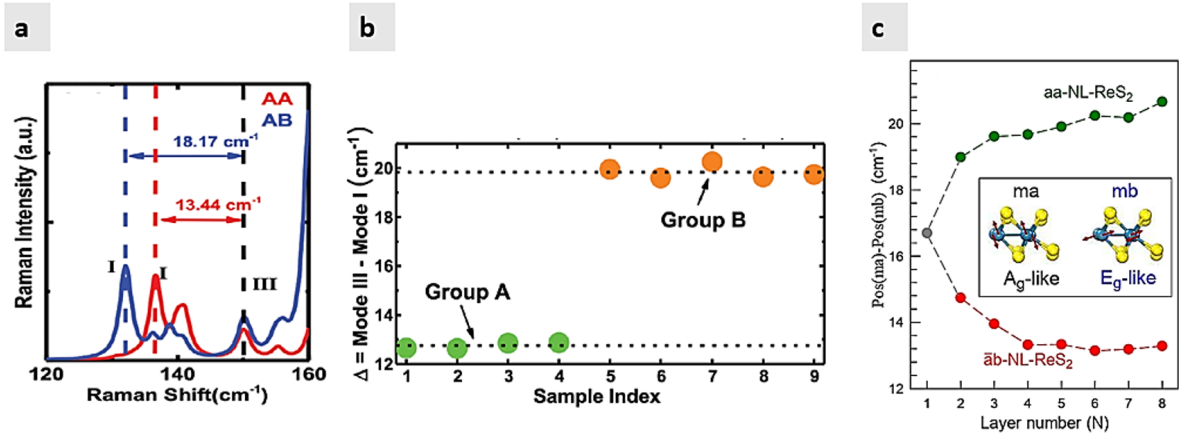

Figure 5.5: (a) The Raman spectra of mode I and mode III in both stackings (AA and AB) for 9 bulk ReS_2 samples. (b) The difference between mode III and mode I, which distinctly displays two distinct groups that correspond to the stacking of AA (group A) and AB (group B). (c) The peak frequency difference between modes I and III as a function of layer number for AA and AB stacking. Results taken from [308, 358]

During this work, we mechanically exfoliated several flakes from a single bulk crystal obtained from HQGraphene onto different substrates. Despite originating from the same parent material, Raman spectroscopy identified both AA and AB stacking configurations within the exfoliated flakes. Preliminary characterization showed that AA-stacked regions exhibited a consistent 13 cm ^{1} separation between Mode I and III, while AB-stacked regions displayed a larger 20 cm ^{1} splitting. Figure 5.6 shows the results of the Raman characterization of two flakes stacked in the AA and AB modes. In panels b, c, and e, we can see the Raman spectra of flakes depicted in the optical images in a and d, respectively. The difference between the peaks is noticeable, as the intensity of Mode III.

We restrict our attention to the range of Raman shifts between 120 and 240 cm^{-1}, since the strongest modes occur in this frequency range, where we label the individual peaks with Roman numerals from I to V as seen in Figures 5.6.b, and 5.6.c, and 5.6.e. The III − I frequency difference 5.6.f. can be used to calculate the number of layers in each region as well as to determine the stacking mode. A_g-(cross-plane) mode is correlated with I mode, and E_g-like (in-plane) mode is correlated with III mode. The

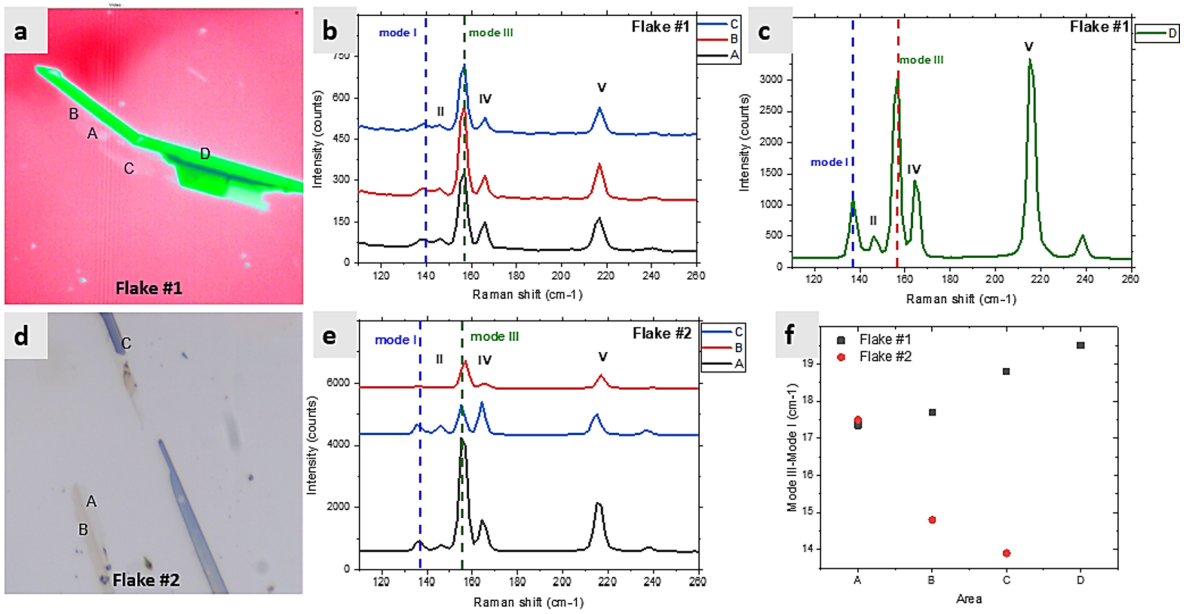

Figure 5.6: Optical microscope images of ReS_2 flakes #1 and #2 are shown in (a) and (d). Panels (b), (c) and (e) present the Raman spectra of transferred ReS_2 flakes #1 and #2 in the range of 120–240 cm^{-1}. (f) The differences between peaks III and I for flakes #1 and #2 allow us to determine both the type of stacking and the number of layers in each case.

mode I peak can be seen at either 136 or 138 cm^{-1}, whereas the mode III peak is reliably found at 156 cm^{-1} In both Flakes #1 #2. For Flake #1 (Fig.5.6.a.) areas A, B, C, and D, the differences are 17.3 cm^{-1}, 17.7 cm^{-1}, 18.8 cm^{-1}, and 19.7 cm^{-1} respectively. This leads to the conclusion that areas A and B are one layer, C is two layers and D is three layers in AB stacking mode. In Flake #2 (Fig.5.6.d.) for areas A, B, and C, the differences are 17.5cm^{-1}, 14.8 cm^{-1}, and 13.9 cm^{-1} respectively, allowing us to conclude that area A is one layer, area B is two layers, and area C is three layers in AA stacking mode [301, 308]. Regarding the Raman peak signal for mode V, it remains consistent at 216 cm^{-1} over the entire regions. This mode is related to mixed in-plane and out-of-plane vibrations of sulfur atoms [359]. Typically, Mode V shows minimal frequency shifts (<1 cm ^{1}) with thickness variations from monolayer to bulk [360]. However, it exhibits strong polarization dependence, with maximum intensity observed at specific crystallographic orientations [301]. This mode is also highly sensitive to uniaxial strain, as explored by A. Castellanos group [361]. In our case, the consistency in the mode V intensity and positons suggests that the fundamental crystal structure and symmetry of ReS_2 are preserved in all the areas under study.

5.5 | Nanoscale characterization of the surface potential in ReS_2 flakes

Kelvin Probe Force Microscopy is a powerful tool for investigating the electronic and surface properties. In the case of our of few-layer transition metal dichalcogenides , it can provide spatially resolved measurements of the work function, which is crucial for understanding layer-dependent electronic properties and identifying the impact of defects, grain boundaries, and chemical impurities [362]. KPFM has been proven fundamental in mapping charge distributions, revealing charge trapping, and analyzing intrinsic and extrinsic doping effects. By examining substrate interactions, KPFM helps quantify substrate-induced effects, such as dielectric screening and work function shifts, essential for optimizing device performance. Additionally, it provides detailed information about the local electronic properties of edges, defects, and grain boundaries, which play a critical role in charge transport [363, 364]. Aiming at gaining a deeper insight in the electronic and crystalline structure of ReS_2, we performed detailed KPFM measurements of exfoliated and transferred films of different thicknesses, finding striking contrasts not correlated with the topography.

As explained in section 3.2.3, The KPFM tip scans the flake to simultaneously get the distribution of electrostatic potential and the topography along the flake. Typical KPFM images of a 20 nm-thick ReS_2 flake are shown in Figure 5.7, where (a) is a topographical image and (b) is a surface potential image. This figure shows the presence of remarkable contrasts arising in the Surface Potential images in flakes of similar thickness. In scanning probe microscopy studies of TMDs, EFM and KPFM have revealed critical electronic contrasts invisible in topography, providing insights into defect states, doping effects, and interfacial charge transfer [362, 365–367]. For example, by KFM, 80 mV CPD drops in MoS_2 were observed due to effect-induced Fermi-level shifts [365]. Also, substrate-dependent interfacial charge transfer (150–100 mV CPD modulations in WS_2 due to humidity or metal contacts) were observed by P. A. Markeev et al. [362]. These techniques also allow the observation of dynamic charge redistribution processes and dielectric variations undetectable by conventional AFM [368, 369].

In heterostructures, KPFM can determine the important junction characteristics, such as the widths of the depletion layer and the lateral built-in potential [370]. Because surface potential can provide information about the stacking order, researchers use the KPFM in TMDs to retrieve information about the stacking configuration. Junxi et al.[371] differentiate between Bernal (ABAB) and rhombohedral (ABCA) stacked graphene using a combination of lateral Piezoresponse Force Microscopy (LPFM) and Scanning Kelvin Probe Microscopy (SKPM). They then directly correlate these stacking configurations with local surface potential and discover that the ABCA domains' surface potential is approximately 15 mV higher (smaller work function) than the ABAB domains. EFM and KPFM are used by Jing et al. [372] to examine the stacking configuration in 3R-MoS_2. Using bilayer 3R-MoS_2 as a model, they found that a single flake can exhibit two symmetric stacking arrangements. The stacking configuration known as AB stacking is when the sulfur atom in the top layer is positioned above the molybdenum atom in the bottom layer, while BA stacking represents the reflected counterpart of the AB stacking configuration. Because the spontaneous polarization in the AB stacking has been shown to be upward [373], the resulting downward depolarization electric field raises the surface potential. On the other hand, a decreased surface potential results from the polarization and depolarization fields being reversed in the BA stacking.

In general, studying these contrasts have allowed to prove how localized doping, interfacial interactions, and defect configurations govern nanoscale electronic behavior in TMDs, making EFM/KPFM critical for linking atomic-scale electronic structure to macroscale device performance.

In order to exclude or minimize the influence of the substrate on the KPFM measurements, we transferred flakes onto different substrates and comparing measurements on transferred flakes. This allowed us to rule out substrate-induced effects such as charge transfer, dielectric screening, and electrostatic coupling, ensuring that the observed KPFM contrast reflects intrinsic properties of the ReS_2 layers rather than substrate artifacts [374]. Gold (Au), platinum (Pt), and native silicon dioxide (SiO_2) were employed (see Figure 5.8). The results showed that the same contrast was seen independent of the

substrate type, indicating similar behavior across all substrate types. The consistency here suggests that the observed contrasts are independent of the substrate material.

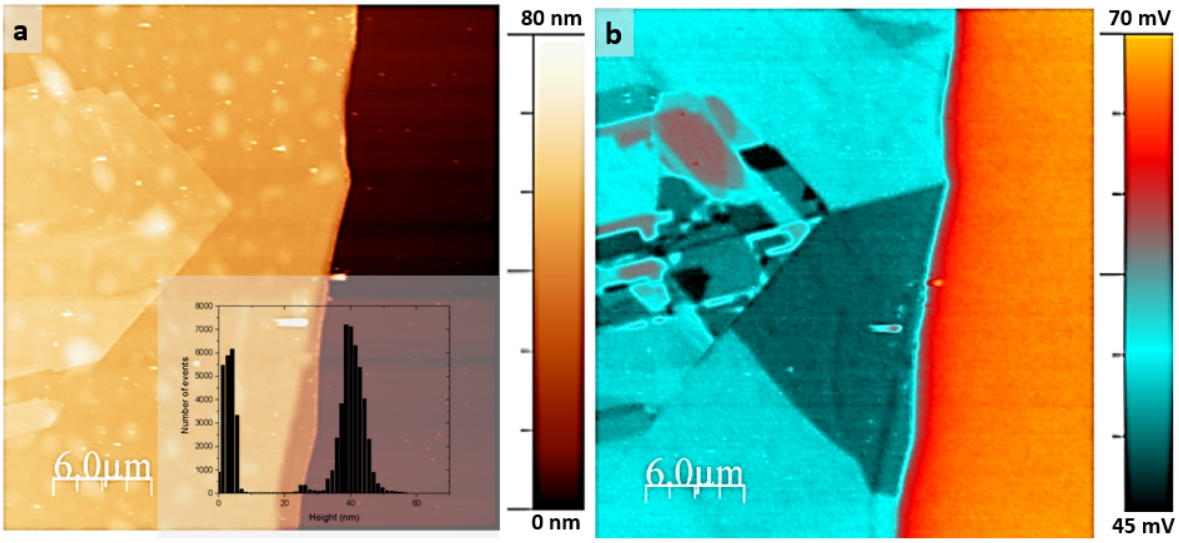

Figure 5.7: Typical KPFM images of a 20 nm-thick ReS_2 flake on a SiO_2 substrate, where (a) is a topographical image and (b) is a surface potential image

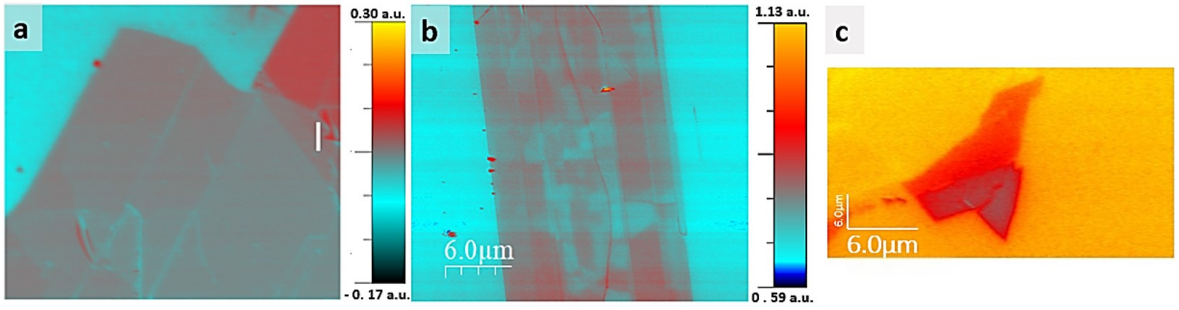

Figure 5.8: KPFM images of ReS_2 flake transferred in different substrates,(a) native silicon dioxide (SiO_2),(b) Gold (Au),(c) platinum (Pt).

After ruling out the influence of the substrate, we hypothesized that the observed contrasts were the result of different stacking configurations within the flakes. Since the number of flake layers and the type of stacking are two of the many characteristics that can be inferred from the Raman spectra, we employed Raman spectroscopy on thin wafers that displayed distinct contrast between regions to confirm the stacking mode of each of these regions. Raman spectra were taken at multiple locations on a ReS_2 flake: A, B, C, D, E, F, and Ds, as shown in the Figure 5.9. These regions had varying thicknesses of 5.5 nm, 35.92 nm, 5.5 nm, 44.8 nm, 59.2 nm, 43.4 nm, and 5.5 nm respectively, measured by AFM respect to the substrate. Figure 5.10.b displays the

calculated difference between peak III and peak I of the Raman spectra . All the values are around 19.45, with the differences between them attributed to the experimental error. Therefore, in this flake we can conclude that the type of stacking in all the electrostatic regions observed in the KPFM image is AB.

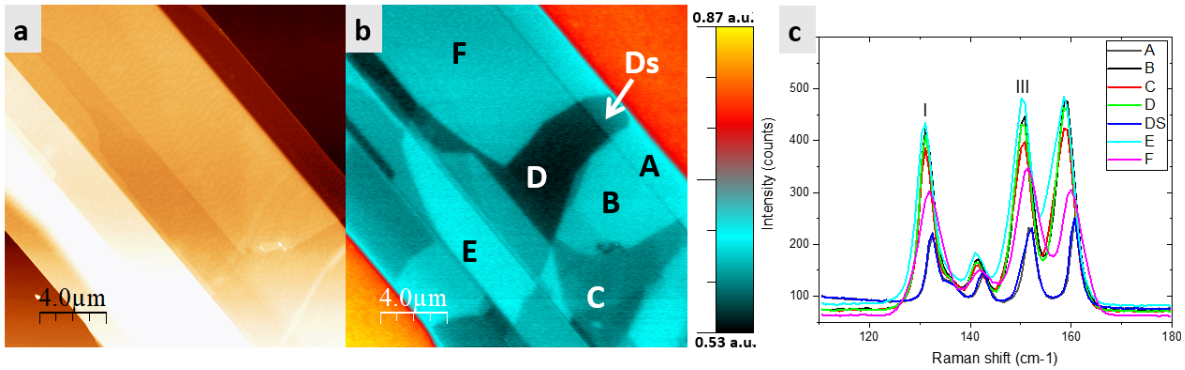

Figure 5.9: (a) KPFM topographical image, (b) surface potential image of a thin ReS_2 flake on a SiO_2 substrate, and (c) Raman spectra measured in regions A, B, C, D, E, F, and Ds.

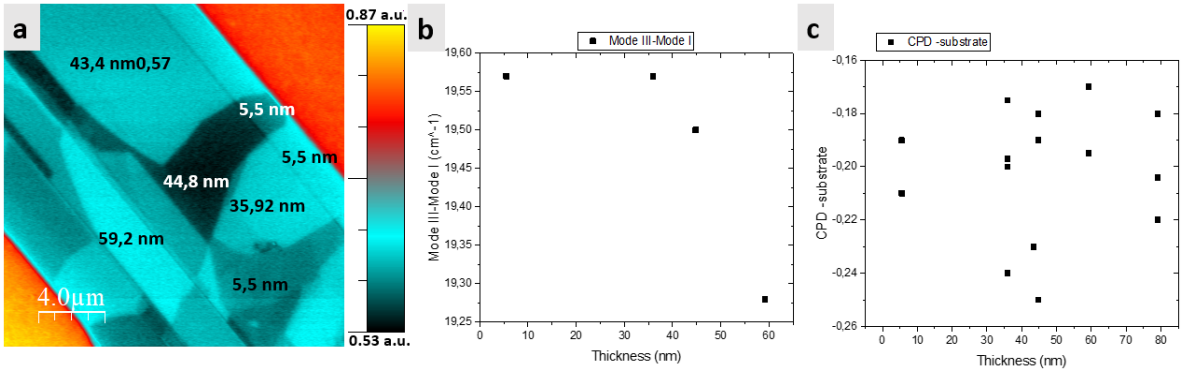

Figure 5.10: (a) Surface potential image of a thin ReS_2 flake on a SiO_2 substrate where the thicknesses of different regions are shown (A, B, C, D, E, F, and Ds, with thicknesses of 5.5 nm, 35.92 nm, 5.5 nm, 44.8 nm, 59.2 nm, 43.4 nm, and 5.5 nm, respectively). (b) The difference between peak III and peak I of Raman spectra is plotted in function of region's thickness. (c) CPD contrast distribution over the thin ReS_2 flake in function of thickness.

Regions A and Ds, which are depicted in Figure 5.9.b., present a significant difference in their surface potential contrast (different CPD), with area Ds being darker than area A. On the other hand, the two regions have the same thickness related to the substrate (5.5 nm), and have the same stacking mode (AB), concluded from the Raman analysis.

In conclusion, the Raman spectra show no peak shifts or splitting across electrostatic

domains, indicating that the observed potential contrast does not arise from structural domain differences, but likely from variations in interlayer electrostatics. This supports the interpretation that the contrast is due to sliding ferroelectricity in ReS_2, rather than ferroelasticity or strain.

Temperature dependency of the electrostatic domains

Temperature variations significantly impact strain production in TMDs, where uniform biaxial tensile strain can be induced by taking advantage of a huge mismatch between the thermal expansion of a 2D semiconducting material and the substrate on which it is laying (see Figure 5.11). Therefore, the substrate can be purposefully chosen to have a relatively large positive value. As a result, the 2D material will undergo a tensile biaxial strain when the substrate is heated [375]. The thermal expansion coefficients of the substrates used in our study are summarized in table 5.1. For example, Plechinger et al. managed to apply 0.23% of biaxial tensile strain on $MoSe_2$ by raising the sample's temperature by 150° C utilizing poly-dimethyl siloxane rather than traditional dielectric substrates [376].

Table 5.1: Thermal expansion coefficients of different substrates used in our study.

Thermal Expansion Coefficients (ppm/°C)	
Gold (Au)	14.2 [378]
Silicon Dioxide (SiO_2)	0.5 [379]
Platinum (Pt)	8.9 [380]
Polycarbonate	65 [381]

Strain effectively affects the electrical, transport, and optical properties of 2D material [382, 383]. In the case of ReS_2, strain engineering significantly influences its electronic, optical, and vibrational properties due to its anisotropic crystal structure. Tensile strain modulates the band gap and induces excitonic peak redshifts, with the effects being most pronounced when strain is applied along the b-axis [384]. Raman modes also exhibit direction-dependent shifts, highlighting the material's anisotropic mechanical response. Mode V shows a maximal gauge factor of 3.18 cm^{-1}/ strain when strained parallel to the b-axis, while Mode III responds most strongly when strain is

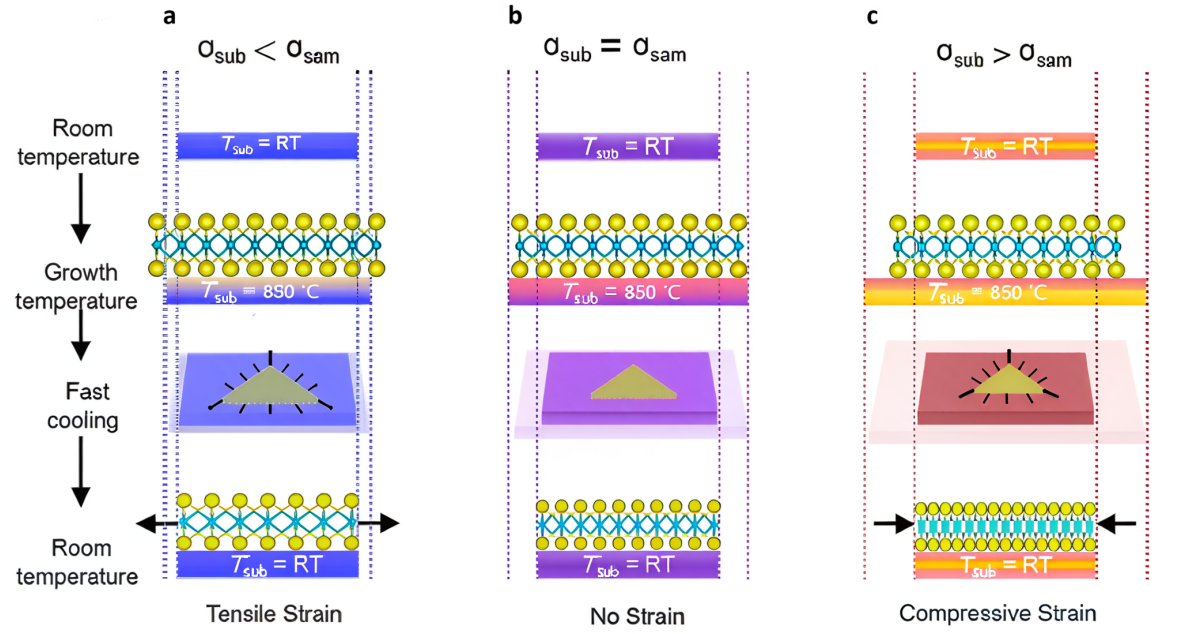

Figure 5.11: Process diagram showing how the thermal expansion coefficient (TEC) mismatch between the substrate and TMD causes strain in 2D materials.(a) When the substrate TEC is lower than that of the 2D material, tensile strain is attained,(b) When the TEC of the 2D material and the substrate match, relaxed samples are produced, and (c) When the TEC of the substrate is higher than that of the 2D material, compressive strain is reached. Schematic extracted from [377]

.

applied at 30° relative to the b-axis. This directional sensitivity allows precise tuning of optoelectronic properties, making ReS_2 highly promising for flexible electronics and photonic devices [385].

Ferroelasticity is a property of materials that can switch between two or more stable strain states when mechanical stress or, in some cases, an electric field is applied. These strain states remain even after the force is removed, similar to how ferroelectric materials retain polarization. Ferroelasticity in ReS_2, arising from its distorted 1T triclinic structure, has been experimentally demonstrated, establishing ReS_2 as a 2D multiferroic material with coupled ferroelastic and ferroelectric orders [386, 387]. While not directly related to ferroelasticity, the Raman response of ReS_2 is sensitive to interlayer coupling and stacking order, which can be influenced by strain and domain formation. Mode V can potentially be used to probe subtle changes in interlayer interactions associated with ferroelastic domain formation [388]. Building on the mentioned sensitivity of ReS_2's anisotropic properties to strain, we explored ferroelasticity as a potential origin

to the different electrostatic zones found in the surface potential images by KPFM. In order to do that, we tuned the substrate temperature during the KPFM measurement using a commercial AFM (Cypher ES, Oxford Instruments). Our goal was to observe how thermally induced strain affected interlayer interactions, ferroelectric polarization, and domain evolution. As discussed before, ReS_2 has a weak interlayer coupling. By inducing anisotropic thermal expansion, temperature changes can generate strain that modifies interlayer spacing [375, 384], potentially influencing sliding ferroelectricity and charge transfer [363]. This strain could also drive domain wall motion or restructuring, altering surface potential contrasts observed in KPFM [389]. Additionally, thermal expansion is capable of inducing slip motion between the layers, modifying stacking configurations and polarization states [390].

The temperature dependency of the contact potential difference of the ReS_2 flakes deposited in a gold (Au) substrate is shown in Figure 5.12. First, we confirm that the transferred flake presents several different contrasts (Fig. 5.12, panel a). With increasing temperature, it can be observed how the electrostatic domain boundaries don't apparently change, maintaining the same shapes through the experiment, suggesting that no slip motion is induced or domain walls are induced.

Nevertheless, we observed an enhancement of some contrasts of surface potential images and a decrease of others upon temperature variations. As shown in Fig. 5.12.f, the contrast is significantly more pronounced at the higher temperature (200 °C), where darker areas are visible. The altered contrast of domains observed in KPFM for ReS_2 flakes at higher temperatures could imply enhanced electronic heterogeneity between domains due to thermally activated processes. Several mechanisms can be behind this phenomena: charge redistribution, potential subtle structural or phase changes in the distorted 1T' crystal structure, alterations in band alignment and work function variations due to electron-phonon interactions and charge redistribution, and possible grain boundary effects. These thermally-driven changes would be able to amplify the differences in surface potential between adjacent domains, resulting in more pronounced KPFM contrasts.

Figure 5.13 shows the topographical image of an area from the same area of Fig.

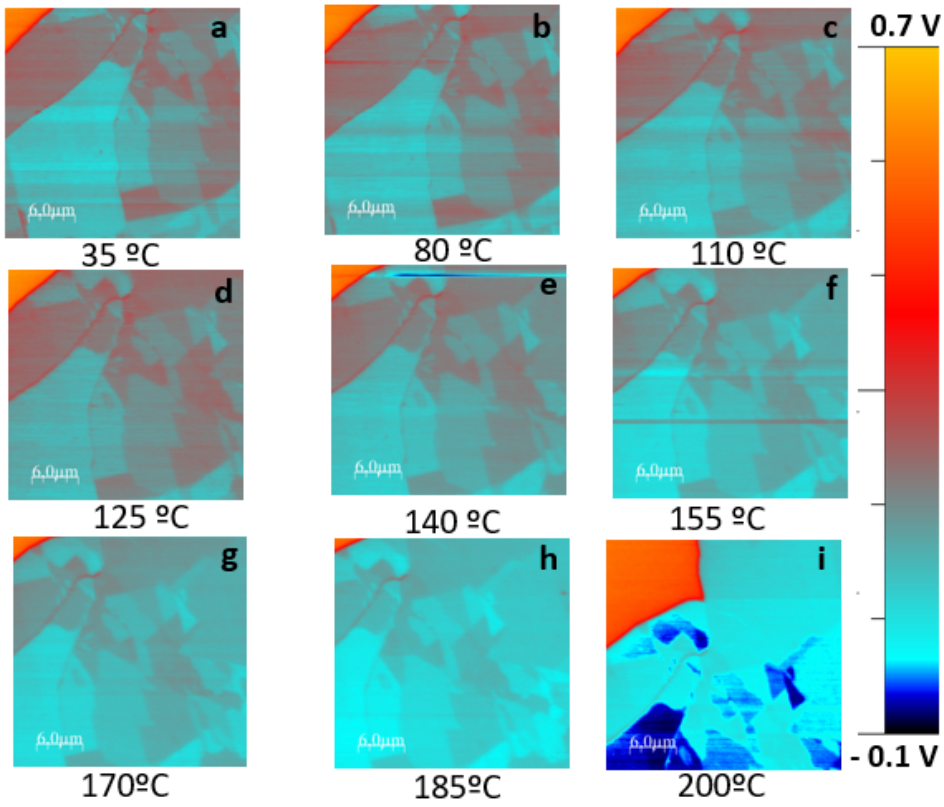

Figure 5.12: Surface potential images show the temperature dependency of the ReS_2 flakes deposited in a gold (Au) substrate, where enhancement of some contrasts of surface potential images and a decrease of others upon temperature variation is shown.

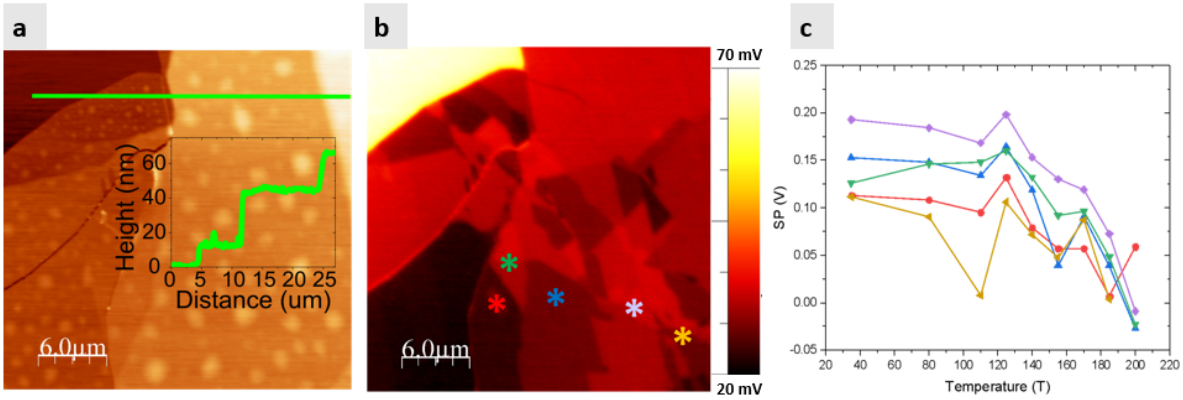

Figure 5.13: Topographical (left) and Surface potential image (right) of a 65 nm thick ReS_2 flake. Surface potential evolution with T (corrected by the substrate value) for the marked areas,

5.12. Firstly, we can observe how the different topographical steps don't correlate with all the observed contrasts in the Surface potential image (b).The evolution of the surface potential (corrected by the substrate value) with temperature for the marked areas is plotted in the graph in (c). We can see that the contrast for those areas evolves towards

lower surface potential values, inverting their contrast with surrounding areas at certain temperatures. At a temperature around 140ºC, a more pronounced drop in the surface potential is observed.

Figure 5.14 displays another ReS_2 flake transferred flakes on a platinum substrate. The topography is shown in panel f, where the height of each flake, obtained via profiles and histograms in relation to the substrate is indicated for each area. Panels a-e show the dependence of the surface potential with temperature. The evolution with temperature of values of the relative Surface Potential for each area are plotted in the graph in (g). Up to 150ºC, we observe a tendency for it to increase, and thereafter an inverse tendency. This holds true for the majority of areas with varying thicknesses, including thin ones like area A, which has a thickness of 3.2 nm. The surface potential image in panel h reveals that the original contrasts aren't recovered after the experiment. The complete inversion of contrast in some ReS_2 flakes after heating to 240°C and cooling back to room temperature likely indicates a permanent or quasi-permanent change in the electronic or structural properties of the material.In the case of layered 2D materials such as ReS_2, it suggests domain rearrangements or local stacking/sliding events that can be activated thermally [391]. Once triggered at elevated temperature and cooled back down, the new configuration remains pinned and therefore yields a different KPFM contrast from before. It can also indicate the introduction of defects or adsorbates that alter the local doping in a non-reversible way. In general, the fact that the contrast does not recover implies an irreversible change in local polarization, doping, or crystal structure that was enabled by the heating step and remains stable at room temperature.

Many studies report that strain may be generated during sliding in TMDs. Himanshu et al.[392] showed that the sliding action of an AFM tip on WS_2 monolayers causes localized lateral stress and strain. Furthermore, given the weak vdW bonding between layers, it has been shown that sliding may occur during exfoliation as a result of the shear force [372]. It can be inferred from all of this that there is a relationship between sliding strain and exfoliation. Some layers can fail to separate completely during mechanical exfoliation and instead experience sliding, and a shear strain may be created

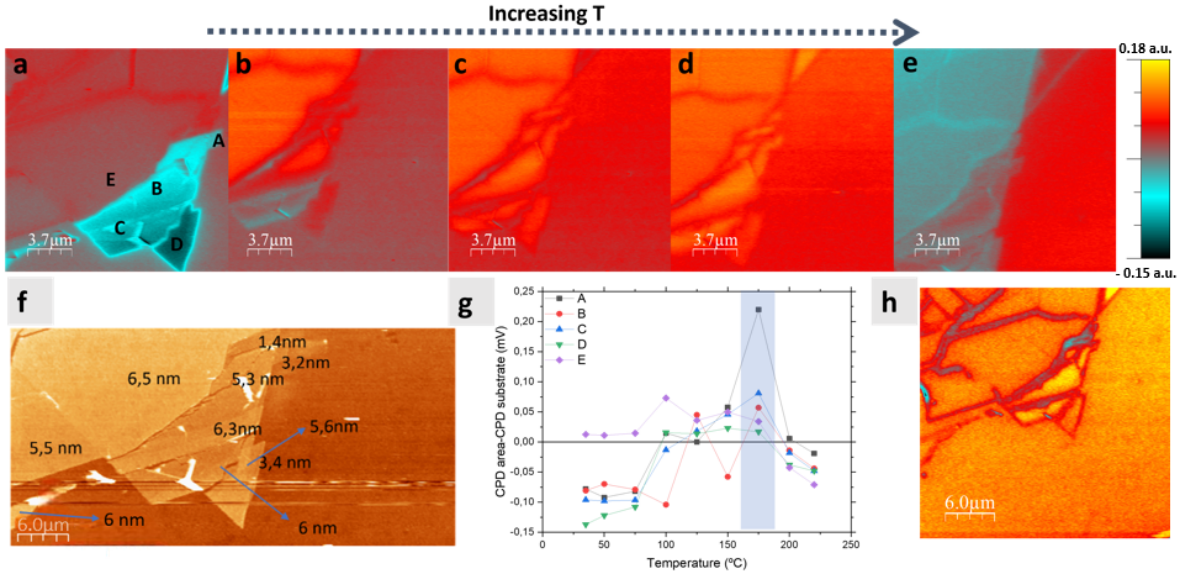

Figure 5.14: (a,b,c,d and, e) Surface potential images show the temperature dependency of the ReS_2 flakes deposited in platinum (Pt) substrate.(f) Topographical image of the same area with the heights respect to the substrate of the different areas marked in a. (g) Temperature evolution of the CPD difference (respect to the substrate) for the areas marked in (a). (h) Surface potential image at room temperature after the experiment, where we can see that a irreversible change was induced.

during this interlayer sliding as the bottom of the ReS_2 flake is bonded to the substrate. It has also been reported interlayer sliding can produce ferroelectricity in bilayer or few-layer van der Waals materials [393]. Despite the fact that their bulk-phase structure is not polarized, several 2D layered materials can display the unique property of "sliding ferroelectricity", which is a phenomenon in 2D van der Waals materials where the vertical electric polarization can be switched by in-plane interlayer sliding [394, 395]. Our findings suggest that arising ferroelectric domains that are impacted by the strain can be linked to the appearance of contrast in the surface potential pictures of the ReS_2 flake. We observe that the CPD of various regions of our ReS_2 flake exhibits an inverse tendency over 140- 150ºC(see figure 5.14.g), coinciding with the reported transition from the ferroelectric phase to the paraelectric one [396]. According to Yi Wan et al.[332], the second harmonic generation measurements for bilayer 1T'-ReS_2 indicate that the ferroelectric transition temperature is around 405 K (130ºC), close to the temperature at which we observe the inversion tendency.

We subsequently performed a Raman Mapping on the same sample (see Figure 5.15)

after the KPFM measurements. Panel (c) shows the different spectra obtained in the points marked in the topographical image in (c) The difference (mode III-mode I) usually gives information regarding the layer number, and it does not correlate with CPD. As for mode V (Fig 5.15.c), as explained before, is also sensitive to uniaxial strain. We extracted the peak position and intensity from the peaks, observing no evident correlation between the contrast in KPFM and the Mode V peak position. While the absence of significant shifts in Mode V might suggest low strain in certain directions, it does not necessarily indicate that the material is entirely strain-free. The complex strain response in ReS_2 is highly anisotropic, with different Raman modes exhibiting varying sensitivities to strain depending on the type and direction of applied stress relative to the crystal structure [361]. However, the lack of correlation between the different electrostatic potential areas and the shifts in Mode V suggests that the observed electrostatic potential variations are definetely not solely attributable to strain effects, accordingly with the temperature dependence results. The unique crystal structure of ReS_2 allows for complex interplays between structural modifications and electronic properties, which can manifest in ways not directly reflected in certain Raman modes. Therefore, while strain may contribute to the observed electrostatic potential landscape, other factors likely play significant roles in shaping the material's electronic heterogeneity.

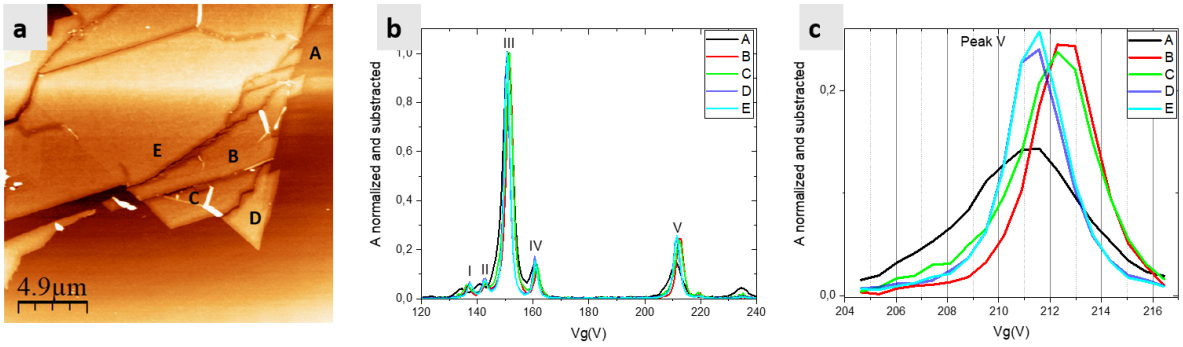

Figure 5.15: (a)ReS_2's topographical image. (b)Raman spectra measured in regions A, B, C, D, and E. (c) Zoom in on peak V.

5.6 | Correlated UVPEEM and KPFM measurements

Collaborating with S. Ruiz-Gomez, M. Foerster, and L. Aballe, this study was conducted on the In Situ Correlative Facility for Advanced Energy Materials, also known as In-CAEM (Instalación Correlativa In-situ para Materiales Avanzados para Energía). the ReS_2 flakes were analyzed by UV-PEEM then correlate the result with KPFM results.

UVPEEM is a powerful surface analysis method used to study electronic structures and chemical compositions at the microscopic level [397]. UVPEEM relies on the photoelectric effect . A sample is illuminated with ultraviolet (UV) light, which excites electrons from the sample's surface into the vacuum. The energy and angular distribution of these emitted electrons are analyzed to obtain spatially resolved information about the electronic structure and surface properties [398]. In 2D materials, UVPEEM provides insights into the electronic band structure of materials, enables visualization of surface chemical composition and measures the work function variations across a material's surface [399]. Variations in local work function affect both the surface potential (KPFM) and the energy of emitted photoelectrons (UVPEEM). Sliding ferroelectricity in ReS_2 might alter the surface potential and influence the density of electronic states observed in UVPEEM.

Results of UV-PEEM on a ReS_2 flake are displayed in Figure 5.16.c. As preliminary findings, we can state that UV-PEEM results are consistent with KPFM findings, and that the changes in work functions that correlate to KPFM contrasts could be correlated to the disparities in electronic structure in the domains that cause surface potential contrasts.

If the contrasts observed in KPFM and UVPEEM coincide, it implies that both techniques are sensing the same spatial variations in the local electronic structure, specifically variations in surface potential and work function. This spatial correlation suggests that the observed domains are characterized by distinct electronic environments, likely arising from different stacking orders or polarization states. In materials like ReS_2, which exhibit weak interlayer coupling and can host interfacial sliding ferroelectricity,

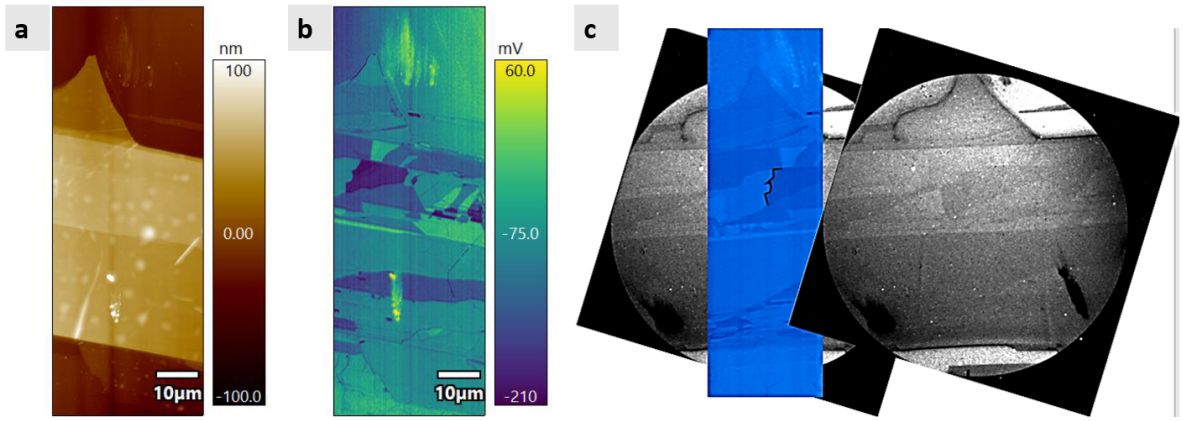

Figure 5.16: (a) Topographical image of ReS_2 flake, (b) Surface potential image of ReS_2 flake. (c)UV-PEEM image of ReS_2 flake that provides high-resolution spatial maps of the electronic structure of the surface.

these domains may correspond to regions with differing vertical polarization resulting from interlayer shifts. Since KPFM maps the local surface potential and UVPEEM is sensitive to the local work function and occupied electronic states, their matching patterns imply that the differences in polarization or charge distribution are robust and intrinsic, very likely not induced by external factors like topography or contamination. This kind of correlation strongly supports the presence of stable, switchable electronic domains, possibly linked to sliding ferroelectricity as described in works as Wan et al.[332]and Meng et al.[400].

5.7 | Conclusion

TMDs have opened up a vast range of opportunities for nanoelectronic and optoelectronic devices, due to their extraordinary mechanical, optical, and electrical properties. We have focused on the Disulfide rhenium ReS_2 in our study.

ReS_2 known for its distorted 1T' structure and weak interlayer coupling, mechanical exfoliation followed by PDMS transfer onto various substrates (SiO_2, Au, and Pt), followed by careful analysis by Raman spectroscopy, revealed the number of layers and two stacking configurations in flakes. In Flake #1, areas A, B, C, and D have III−I frequency differences of 17.3 cm^{-1}, 17.7 cm^{-1}, 18.8 cm^{-1}, and 19.7 cm^{-1}, indicating that areas A and B are one layer, C is two layers, and D is three layers in AB stacking

mode. In the other hand in Flake #2, areas A, B, and C have III−I frequency differences of 17.5 cm^{-1}, 14.8 cm^{-1}, and 13.9 cm^{-1}, indicating that area A is one layer, B is two layers, and C is three layers in AA stacking mode.

Kelvin probe force microscopy (KPFM) measurements revealed striking differences in surface potential that do not correspond with topography features or stacking order, suggesting that sliding ferroelectricity or domain-related charge redistribution is responsible for these electronic inhomogeneities. Correlative ultraviolet photoemission electron microscopy (UVPEEM) measurements confirmed this behavior by showing matching work-function contrasts. Moreover, temperature-dependent KPFM experiments indicated irreversible reorganization of the electrostatic domains at elevated temperatures, consistent with recent reports that ReS_2 can exhibit thermally activated domain reshuffling. These findings demonstrate how the interplay between interlayer coupling and lattice distortions strongly affect the electrostatic landscape of ReS_2, paving the way for potential for advanced optoelectronic, memory, and sensing applications.

6 | Conclusions

Nanoscience and nanotechnology continue to lead groundbreaking developments across diverse fields such as electronics, magnetism, chemistry, biology, and medicine. Their rapid evolution is propelled by the realistic prospects of technological breakthroughs. However, the success of these advancements critically depends on the availability of probing and fabrication tools that are compatible with the nanoscale products and samples under investigation. Historically, the microelectronics industry has served as a template for nanofabrication, inspiring bioengineering applications that range from traditional techniques like photolithography and electron-beam lithography (EBL) to next-generation lithography such as nanoimprint lithography (NIL). These methods have enabled the fabrication of topographically patterned substrates for cell studies, with a wide variety of lateral dimensions, from tens of nanometers to hundreds of micrometers, and geometries such as fibers and pores. Among these, EBL stands out for its precision in generating nanometric patterns in a highly controlled and reproducible way.

Currently, top-down nanofabrication remains the most mature approach for nanoscale patterning. In research settings, this generally involves a combination of metal lift-off processes, nanolithography, and dry etching techniques, closely aligned with those used in semiconductor fabrication. Dry etching, in particular, employs reactive agents to selectively remove material, with the etching direction dictating whether the resulting structures are anisotropic or isotropic. In this thesis, Fresnel zone plate (FZP) structures were successfully fabricated by integrating electron beam lithography with dry etching for pattern transfer. A core challenge in FZP fabrication lies in producing extremely dense line patterns with nanometer-scale precision. This becomes even more complex when striving for full 3D devices that span tens of micrometers in diameter and several micrometers in thickness. A critical parameter in FZP fabrication is the Δr limit, which determines the aspect ratio $t/\Delta r$. In this study, a Δr of 50 nm yielded an aspect ratio of 86. This high aspect ratio, while crucial for performance, introduced significant challenges, particularly in managing the fragility of the outermost zones, which

are prone to collapse due to proximity effects inherent in EBL.

Despite the drawbacks encountered throughout the process, we successfully fabricated a silicon FZP with 100 zones, a 20µm diameter, and an outermost zone width of just 50 nm. This high-precision structure is suitable for use at low photon energies, and as a deposition mask for high-Z materials at higher photon energies. The fabrication process was refined through the combined use of cryogenic etching and an optimized chromium mask, which effectively mitigated pattern collapse. Even though PMMA resist presented challenges, it was ultimately employed as a successful mask for chromium layer etching. The final structure demonstrated excellent verticality and an etch depth of approximately 4.3 µm. A 20 nm gold coating provided critical protection to the most delicate features, facilitating the production of high-aspect-ratio patterns with low roughness and minimal etching artifacts.

Looking ahead, the emergence of 2D materials, especially in applications like quantum computing, is set to redefine next-generation electronics. The unique properties conferred by reduced dimensionality make 2D materials such as ReS_2 highly attractive for devices that bulk materials cannot efficiently support. Promising applications span transistors, sensors, topological insulators, battery electrodes, and valleytronics.. We have explored the characterization of ReS_2, an anisotropic layered material with unconventional electrical, optical, vibrational, and magnetic properties that remain consistent across bulk and monolayer forms. The interplay of interlayer coupling and stacking order in ReS_2 influences light polarization, bandgap tunability, and quantum phases. Its heterostructures—rather than isolated layers—are poised to play a critical role in future technologies, ranging from optoelectronics to energy conversion.

Using Raman spectroscopy, AFM, and KPFM, we characterized the number of layers and stacking configurations (AA and AB) of ReS_2 flakes transferred onto SiO_2, Au, and Pt substrates. KPFM revealed significant electronic inhomogeneities unrelated to topography or stacking order, suggesting ferroelectric domain behavior. This was further validated by UVPEEM, and temperature-dependent KPFM confirmed the thermal activation of these domains. These findings emphasize the crucial role of interlayer dynamics and lattice distortions in shaping the electrostatic environment, unlocking

new possibilities for advanced memory, sensing, and optoelectronic applications.

Looking forward for future work, there are several promising experiments and approaches to further advance the findings of this thesis. One critical direction involves the continued optimization of electron beam lithography parameters and cryogenic etching protocols. Fine-tuning these processes could enable the fabrication of even smaller, more precise nanostructures with improved uniformity and reduced pattern collapse, pushing the boundaries of current resolution capabilities. Additionally, the development of hybrid Fresnel zone plate designs that incorporate other nanophotonic elements or functional materials, such as phase-change compounds, could open new possibilities for tunable or multifunctional optical components. Exploration of alternative mask materials beyond chromium is also a valuable pursuit. Materials that offer higher etch resistance and better process compatibility may enhance pattern transfer efficiency, particularly in high-aspect-ratio structures where mechanical stability is crucial.

Parallel to advancements in the fabrication of FZPs, further efforts should be made to integrate ReS_2 into working devices. Given its unique anisotropic properties, ReS_2 heterostructures with other two-dimensional materials hold great potential for flexible electronics, optoelectronic systems, neuromorphic computing, and next- generation memory architectures. Moreover, the use of in-situ characterization techniques during fabrication and thermal processing would provide real-time insights into the evolution of structural, electronic, and interfacial properties. Such methods could be especially beneficial for understanding defect dynamics and optimizing growth conditions. Finally, a deeper investigation into the thermal behavior of ferroelectric domains in ReS_2 is warranted. Understanding the switching mechanisms and stability of these domains at elevated temperatures could pave the way for robust, high- performance sensors and memory devices capable of operating under demanding environmental conditions. These future efforts will not only enhance the utility of nanofabricated structures but also unlock new technological potentials of emerging 2D materials.

7 | Conclusiones

La nanociencia y la nanotecnología siguen liderando avances revolucionarios en campos tan diversos como la electrónica, el magnetismo, la química, la biología y la medicina. Su rápida evolución está impulsada por las perspectivas realistas de avances tecnológicos. Sin embargo, el éxito de estos avances depende en gran medida de la disponibilidad de herramientas de sondeo y fabricación compatibles con los productos y muestras a nanoescala que se investigan. Históricamente, la industria microelectrónica ha servido de modelo para la nanofabricación, inspirando aplicaciones de bioingeniería que van desde técnicas tradicionales como la fotolitografía y la litografía por haz de electrones (EBL) hasta la litografía de nueva generación, como la litografía de nanoimpresión (NIL). Estos métodos han permitido la fabricación de sustratos con patrones topográficos para estudios celulares, con una amplia variedad de dimensiones laterales, desde decenas de nanómetros a cientos de micrómetros, y geometrías como fibras y poros. Entre ellas, la EBL destaca por su precisión a la hora de generar patrones nanométricos de forma altamente controlada y reproducible.

En la actualidad, la nanofabricación descendente sigue siendo el enfoque más maduro para la creación de patrones a nanoescala. En el ámbito de la investigación, se trata generalmente de una combinación de procesos de despegue de metales, nanolitografía y técnicas de grabado en seco, muy similares a las utilizadas en la fabricación de semiconductores. El grabado en seco, en particular, emplea agentes reactivos para eliminar material de forma selectiva, y la dirección del grabado determina si las estructuras resultantes son anisótropas o isótropas. En esta tesis, se fabricaron con éxito estructuras de placa de zona Fresnel (FZP) integrando la litografía por haz de electrones con el grabado en seco para la transferencia de patrones. Uno de los principales retos de la fabricación de FZP es producir patrones de líneas extremadamente densos con una precisión nanométrica. Esta tarea se complica aún más cuando se trata de fabricar dispositivos tridimensionales que abarcan decenas de micrómetros de diámetro y varios micrómetros de grosor. Un parámetro crítico en la fabricación de FZP es el límite Δr, que determina la relación de aspecto $t/\Delta r$. En este estudio, un Δr de 50 nm dio lugar a

una relación de aspecto de 86. Esta elevada relación de aspecto, aunque crucial para el rendimiento, introdujo importantes retos, sobre todo en la gestión de la fragilidad de las zonas más externas, propensas al colapso debido a los efectos de proximidad inherentes a la EBL.

A pesar de los inconvenientes encontrados a lo largo del proceso, hemos fabricado con éxito una FZP de silicio con 100 zonas, un diámetro de 20µm y una anchura de la zona más externa de tan sólo 50 nm. Esta estructura de alta precisión es adecuada para su uso a bajas energías fotónicas y como máscara de deposición para materiales de alta Z a energías fotónicas más altas. El proceso de fabricación se perfeccionó mediante el uso combinado de grabado criogénico y una máscara de cromo optimizada en, que mitigó eficazmente el colapso del patrón. Aunque la resistencia de PMMA presentaba dificultades, al final se empleó con éxito como máscara para el grabado de la capa de cromo. La estructura final demostró una excelente verticalidad y una profundidad de grabado de aproximadamente 4,3 µm. Un recubrimiento de oro de 20 nm proporcionó una protección crítica a las características más delicadas, facilitando la producción de patrones de alta relación de aspecto con baja rugosidad y mínimos artefactos de grabado.

De cara al futuro, la aparición de materiales 2D, especialmente en aplicaciones como la computación cuántica, está llamada a redefinir la electrónica de próxima generación. Las propiedades únicas conferidas por la dimensionalidad reducida hacen que los materiales 2D, como el ReS_2, resulten muy atractivos para dispositivos que los materiales a granel no pueden soportar eficientemente. Las prometedoras aplicaciones de abarcan transistores, sensores, aislantes topológicos, electrodos de baterías y valleytrónica. Hemos estudiado la caracterización del ReS_2, un material anisótropo en capas con propiedades eléctricas, ópticas, vibracionales y magnéticas poco convencionales que se mantienen constantes en las formas a granel y monocapa. La interacción del acoplamiento entre capas y el orden de apilamiento en el ReS_2 influye en la polarización de la luz, la sintonización de la banda prohibida y las fases cuánticas. Sus heteroestructuras-en lugar de las capas aisladas de-están preparadas para desempeñar un papel fundamental en las tecnologías del futuro, desde la optoelectrónica hasta la

conversión de energía.

Mediante espectroscopia Raman, AFM y KPFM, hemos caracterizado el número de capas y las configuraciones de apilamiento (AA y AB) de las escamas de ReS_2 transferidas a sustratos de SiO_2, Au y Pt. La KPFM reveló importantes inhomogeneidades electrónicas no relacionadas con la topografía o el orden de apilamiento, lo que sugiere un comportamiento de dominio ferroeléctrico. Esto se validó mediante UVPEEM, y la KPFM dependiente de la temperatura confirmó la activación térmica de estos dominios en. Estos resultados ponen de relieve el papel crucial de la dinámica entre capas y las distorsiones de la red en la formación del entorno electrostático, y abren nuevas posibilidades para aplicaciones avanzadas de memoria, detección y optoelectrónica.

De cara al futuro, existen varios experimentos y enfoques prometedores para seguir avanzando en los hallazgos de esta tesis. Una dirección fundamental es, donde se siguen optimizando los parámetros de la litografía por haz de electrones y los protocolos de grabado criogénico. El perfeccionamiento de estos procesos podría permitir la fabricación de nanoestructuras aún más pequeñas y precisas, con una uniformidad mejorada y un colapso reducido del patrón, ampliando los límites de las capacidades de resolución actuales. Además, el desarrollo de diseños híbridos de placas de zona Fresnel que incorporen otros elementos nanofotónicos o materiales funcionales, como compuestos de cambio de fase, podría abrir nuevas posibilidades para componentes ópticos sintonizables o multifuncionales. La exploración de materiales de máscara alternativos al cromo también es un objetivo valioso. Los materiales que ofrecen una mayor resistencia a la corrosión y una mejor compatibilidad con los procesos pueden mejorar la eficacia de la transferencia de patrones, sobre todo en estructuras de alta relación de aspecto en las que la estabilidad mecánica es crucial.

Paralelamente a los avances en la fabricación de FZP, deberían realizarse más esfuerzos para integrar el ReS_2 en dispositivos operativos. Dadas sus propiedades anisotrópicas únicas, Las heteroestructuras de ReS_2 con otros materiales bidimensionales tienen un gran potencial para la electrónica flexible, los sistemas optoelectrónicos, la computación neuromórfica y las arquitecturas de memoria de nueva generación. Además, el uso de técnicas de caracterización in situ durante la fabricación y el procesamiento tér-

mico proporcionaría información en tiempo real sobre la evolución de las propiedades estructurales, electrónicas e interfaciales. Estos métodos podrían ser especialmente beneficiosos para comprender la dinámica de los defectos y optimizar las condiciones de crecimiento. Por último, está justificada una investigación más profunda del comportamiento térmico de los dominios ferroeléctricos en ReS_2. La comprensión de los mecanismos de conmutación y la estabilidad de estos dominios a temperaturas elevadas podría allanar el camino hacia sensores y dispositivos de memoria robustos y de alto rendimiento, capaces de funcionar en las exigentes condiciones ambientales. Estos esfuerzos futuros no sólo mejorarán la utilidad de las estructuras nanofabricadas, sino que también desvelarán nuevos potenciales tecnológicos de los materiales emergentes 2D.

List of Acronyms

FZP: Fresnel Zone Plate

ML-FZP: Multi-Layer fresnel zone plate

EBL: Electron Beam Lithography

STXM: Scanning Transmission X-ray microscope

TXM: Transmission X-ray Microscope

SEM: Scanning Electron Microscopy

AFM: Atomic Force Microscopes

KPFM: Kelvin Probe Force Microscopy

ICP/RIE: Inductively Coupled Plasma/Reactive Ion Etching

TMDs: Transition Metal Dichalcogenides

OSA: Order Selecting Aperture

PEEM: Photoemission Electron Microscopy

PMMA: Polymethylmethacrylate

LFR: Linear Fresnel Reflector

CVD: Chemical Vapor Deposition

FEG: Field Emitter Gun

FE-SEM: Field Emission Scanning Electron Microscope

CPD: Contact Potential Difference

NA: Numerical Aperture

HSQ: Hydrogen Silses Quioxane

CAD: Computer-Aided Design

TEC: Thermal Expansion Coefficient

8 | References

[1] O. Haeberlé, K. Belkebir, H. Giovaninni, and A. Sentenac, "Tomographic diffractive microscopy: basics, techniques and perspectives," *Journal of Modern Optics*, vol. 57, no. 9, pp. 686–699, 2010.

[2] C. J. Bouwkamp, "Diffraction theory," *Reports on progress in physics*, vol. 17, no. 1, p. 35, 1954.

[3] H. Wang, C. J. Sheppard, K. Ravi, S. T. Ho, and G. Vienne, "Fighting against diffraction: apodization and near field diffraction structures," *Laser & Photonics Reviews*, vol. 6, no. 3, pp. 354–392, 2012.

[4] F. Kneubühl, "Diffraction grating spectroscopy," *Applied optics*, vol. 8, no. 3, pp. 505–519, 1969.

[5] B. Bhaduri, H. Pham, M. Mir, and G. Popescu, "Diffraction phase microscopy with white light," *Optics letters*, vol. 37, no. 6, pp. 1094–1096, 2012.

[6] G. R. Bigg, "Back to basics: Light in the atmosphere: Part 2—the effects of water and ice," *Weather*, vol. 52, no. 8, pp. 258–261, 1997.

[7] G. R. Bigg, "Back to basics: Light in the atmosphere: Part 2-the effects of water,"

[8] M. Ayub, R. Nawaz, and A. Naeem, "Diffraction of sound waves by a finite barrier in a moving fluid," *Journal of mathematical analysis and applications*, vol. 349, no. 1, pp. 245–258, 2009.

[9] X. Yu, "Diffraction of water waves by porous breakwaters," *Journal of waterway, port, coastal, and ocean engineering*, vol. 121, no. 6, pp. 275–282, 1995.

[10] C. Davisson and L. H. Germer, "Diffraction of electrons by a crystal of nickel," *Physical review*, vol. 30, no. 6, p. 705, 1927.

[11] A. Zeilinger, R. Gähler, C. Shull, W. Treimer, and W. Mampe, "Single-and double-slit diffraction of neutrons," *Reviews of modern physics*, vol. 60, no. 4, p. 1067, 1988.

[12] J. B. Keller, "Diffraction by an aperture," *Journal of Applied Physics*, vol. 28, no. 4, pp. 426–444, 1957.

[13] G. Arfken, *International edition university physics*. Elsevier, 2012.

[14] J. Jewett and R. Serway, *Physics for scientists and engineers with modern, chapters 1-46*, ch. 38, pp. 1009–1039. Florence, KY: Brooks/Cole, 8 ed., 2009.

[15] J. Jewett and R. Serway, *Physics for scientists and engineers with modern, chapters 1-46*, ch. 35, pp. 1009–1039. Florence, KY: Brooks/Cole, 8 ed., 2009.

[16] F. A. Jenkins and H. E. White, *Fundamentals of optics*. Tata McGraw-Hill Education, 2018.

[17] G. S. Raghuvanshi, *Engineering Physics*. Delhi, India: PHI Learning, 3 ed., Aug. 2016.

[18] M. S. Naidu, *Engineering Physics-I (for WBUT)*. Delhi, India: Pearson Education, Dec. 2010.

[19] Raghuvanshi, G. S. Raghuvanshi, and G S, *Engineering physics, 1/e*. Delhi, India: PHI Learning.

[20] A. M. Gretarsson, *A first course in laboratory optics*. Cambridge, England: Cambridge University Press, June 2021.

[21] M. Born and E. Wolf, *Principles of optics: electromagnetic theory of propagation, interference and diffraction of light*. Elsevier, 2013.

[22] T. Reisinger, "Free-standing, axially-symmetric diffraction gratings for neutral matter-waves: experiments and fabrication," 2011.

[23] E. Hecht, *Optics, 5e*. Pearson Education India, 2002.

[24] D. K. Jha, *Contemporary Optics*. New Delhi, India: Discovery Publishing, Apr. 2009.

[25] N. Singh, *Waves and optics*. I K International, Oct. 2023.

[26] M N Avadhanulu & TVS Arun Murthy, *Waves and Optics: As per CBCS*. S. Chand Publishing.

[27] N. Subrahmanyam, B. V. Lal, and M. N. Avadhanulu, *A textbook of optics*. New Delhi, India: S Chand, Dec. 2006.

[28] C. L. Arora, *Physics for degree student B.sc. Second year*. New Delhi, India: S Chand, Dec. 2013.

[29] A. S. Vasudeva, *Modern Engineering Physics*. New Delhi, India: S Chand, Dec. 2010.

[30] M. Young, *Optics and lasers*. Advanced Texts in Physics, Berlin, Germany: Springer, 5 ed., Sept. 2000.

[31] M. H. Freeman, *Optics*. Woburn, MA: Butterworth-Heinemann, 10 ed., Aug. 1990.

[32] *Krishina's engineering physics; Volume III; Optics; 2001*. Krishna Prakashan Media.

[33] S. Singh, *An Introduction to Engineering Physics*. New Delhi, India: Discovery Publishing, Apr. 2009.

[34] D. S. Goodman, "General principles of geometric optics," *Hand Book of Optics*, vol. 1, pp. 68–69, 1996.

[35] N. Singh, *Waves and optics*. I K International, Oct. 2023.

[36] P. W. Hawkes and E. Kasper, *Principles of electron optics*. Academic Press, May 2014.

[37] R. K. Verma, *Wave Optics*. New Delhi, India: Discovery Publishing, Aug. 2008.

[38] L. Rayleigh, "Wave theory," in *Encyclopedia Britannica*, vol. 24, p. 429, ninth ed., 1988.

[39] L. Rayleigh, "Rayleigh's first entry in his notebook," 1871. Rayleigh's first entry in his notebook, describing the first successful demonstration, is dated 11 April 1871.

[40] E. Di Fabrizio, F. Romanato, M. Gentili, S. Cabrini, B. Kaulich, J. Susini, and R. Barrett, "High-efficiency multilevel zone plates for kev x-rays," *Nature*, vol. 401, no. 6756, pp. 895–898, 1999.

[41] D. Attwood, *Soft x-rays and extreme ultraviolet radiation: principles and applications*. Cambridge university press, 2000.

[42] S.-R. Wu, Y. Hwu, and G. Margaritondo, "Hard-x-ray zone plates: recent progress," *Materials*, vol. 5, no. 10, pp. 1752–1773, 2012.

[43] A. G. Michette, *Optical systems for soft X rays*. Springer, 1884.

[44] S. Eder, X. Guo, T. Kaltenbacher, M. Greve, M. Kalläne, L. Kipp, and B. Holst, "Focusing of a neutral helium beam with a photon-sieve structure," *Physical Review A*, vol. 91, no. 4, p. 043608, 2015.

[45] J. Kirz, "Phase zone plates for x rays and the extreme uv," *JOSA*, vol. 64, no. 3, pp. 301–309, 1974.

[46] D. R. Reid and G. S. Smith, "A comparison of the focusing properties of a fresnel zone plate with a doubly-hyperbolic lens for application in a free-space, focused-beam measurement system," *IEEE Transactions on Antennas and Propagation*, vol. 57, no. 2, pp. 499–507, 2009.

[47] B. Yang, "Fresnel and refractive lenses for x-rays," *Nuclear Instruments and Methods in Physics Research Section A: Accelerators, Spectrometers, Detectors and Associated Equipment*, vol. 328, no. 3, pp. 578–587, 1993.

[48] K. Awasthi, D. S. Reddy, and M. K. Khan, "Design of fresnel lens with spherical facets for concentrated solar power applications," *International Journal of Energy Research*, vol. 44, no. 1, pp. 460–472, 2020.

[49] J. Rodríguez, H. D. Hristov, and W. Grote, "Fresnel zone plate and ordinary lens antennas: Comparative study at microwave and terahertz frequencies," in *2011 41st European Microwave Conference*, pp. 894–897, IEEE, 2011.

[50] K. Garcia, *Wilhelm roentgen and the discovery of X-rays*. Unlocking the Secrets of Science, Mitchell Lane, Dec. 2005.

[51] G. Schmahl, D. Rudolph, B. Niemann, and O. Christ, "Zone-plate x-ray microscopy," *Quarterly Reviews of Biophysics*, vol. 13, no. 3, pp. 297–315, 1980.

[52] G. Schneider, P. Guttmann, S. Heim, S. Rehbein, F. Mueller, K. Nagashima, J. B. Heymann, W. G. Müller, and J. G. McNally, "Three-dimensional cellular ultrastructure resolved by x-ray microscopy," *Nature methods*, vol. 7, no. 12, pp. 985–987, 2010.

[53] W. Chao, B. D. Harteneck, J. A. Liddle, E. H. Anderson, and D. T. Attwood, "Soft x-ray microscopy at a spatial resolution better than 15 nm," *Nature*, vol. 435, no. 7046, pp. 1210–1213, 2005.

[54] J. Chen, C. Wu, J. Tian, W. Li, S. Yu, and Y. Tian, "Three-dimensional imaging of a complex concaved cuboctahedron copper sulfide crystal by x-ray nanotomography," *Applied Physics Letters*, vol. 92, no. 23, 2008.

[55] P. Fischer, "Magnetic imaging with polarized soft x-rays," *Journal of Physics D: Applied Physics*, vol. 50, no. 31, p. 313002, 2017.

[56] E. Zschech, W. Yun, and G. Schneider, "High-resolution x-ray imaging—a powerful nondestructive technique for applications in semiconductor industry," *Applied Physics A*, vol. 92, no. 3, pp. 423–429, 2008.

[57] Y. Li, W. Lu, S. Wang, Q. Yuan, X. Kong, L. Han, and Y. Xia, "Fabrication of multilayer fresnel zone plate for hard x-ray microscopy by atomic layer deposition and focused ion beam milling," *Vacuum*, vol. 209, p. 111776, 2023.

[58] P. Horowitz and J. A. Howell, "A scanning x-ray microscope using synchrotron radiation," *Science*, vol. 178, no. 4061, pp. 608–611, 1972.

[59] D. Nolle, M. Weigand, G. Schütz, and E. Goering, "High contrast magnetic and nonmagnetic sample current microscopy for bulk and transparent samples using soft x-rays," *Microscopy and Microanalysis*, vol. 17, no. 5, pp. 834–842, 2011.

[60] H. Stoll, M. Noske, M. Weigand, K. Richter, B. Krüger, R. M. Reeve, M. Hänze, C. F. Adolff, F.-U. Stein, G. Meier, *et al.*, "Imaging spin dynamics on the nanoscale using x-ray microscopy," *Frontiers in Physics*, vol. 3, p. 26, 2015.

[61] F. Groß, N. Träger, J. Förster, M. Weigand, G. Schütz, and J. Gräfe, "Nanoscale detection of spin wave deflection angles in permalloy," *Applied Physics Letters*, vol. 114, no. 1, 2019.

[62] S. Chung, Q. T. Le, M. Ahlberg, A. A. Awad, M. Weigand, I. Bykova, R. Khymyn, M. Dvornik, H. Mazraati, A. Houshang, *et al.*, "Direct observation of zhang-li torque expansion of magnetic droplet solitons," *Physical review letters*, vol. 120, no. 21, p. 217204, 2018.

[63] N. Ohmer, B. Fenk, D. Samuelis, C.-C. Chen, J. Maier, M. Weigand, E. Goering, and G. Schütz, "Phase evolution in single-crystalline lifepo4 followed by in situ scanning x-ray microscopy of a micrometre-sized battery," *Nature communications*, vol. 6, no. 1, p. 6045, 2015.

[64] J. Lim, Y. Li, D. H. Alsem, H. So, S. C. Lee, P. Bai, D. A. Cogswell, X. Liu, N. Jin, Y.-s. Yu, *et al.*, "Origin and hysteresis of lithium compositional spatiodynamics within battery primary particles," *Science*, vol. 353, no. 6299, pp. 566–571, 2016.

[65] W. E. Gent, K. Lim, Y. Liang, Q. Li, T. Barnes, S.-J. Ahn, K. H. Stone, M. McIntire, J. Hong, J. H. Song, *et al.*, "Coupling between oxygen redox and cation migration explains unusual electrochemistry in lithium-rich layered oxides," *Nature communications*, vol. 8, no. 1, p. 2091, 2017.

[66] I. Mohacsi, I. Vartiainen, B. Rösner, M. Guizar-Sicairos, V. A. Guzenko, I. McNulty, R. Winarski, M. V. Holt, and C. David, "Interlaced zone plate optics for hard x-ray imaging in the 10 nm range," *Scientific Reports*, vol. 7, no. 1, p. 43624, 2017.

[67] Y. Takeichi, N. Inami, H. Suga, K. Ono, and Y. Takahashi, "Development of a compact scanning transmission x-ray microscope (stxm) at the photon factory," *Chemistry Letters*, vol. 43, no. 3, pp. 373–375, 2014.

[68] R. Leutz, A. Suzuki, A. Akisawa, T. Kashiwagi, and J. Toksoy, "Developments and designs of solar engineering fresnel lenses," in *Proceedings Symposium on Energy Engineering*, vol. 2, pp. 759–765, 2000.

[69] R. Leutz and A. Suzuki, *Nonimaging Fresnel lenses: design and performance of solar concentrators*, vol. 83. Springer, 2012.

[70] O. Miller, J. McLeod, and W. Sherwood, "Thin sheet plastic fresnel lenses of high aperture," *JOSA*, vol. 41, no. 11, pp. 807–815, 1951.

[71] A. Tsangrassoulis, L. Doulos, M. Santamouris, M. Fontoynont, F. Maamari, M. Wilson, A. Jacobs, J. Solomon, A. Zimmerman, W. Pohl, *et al.*, "On the energy efficiency of a prototype hybrid daylighting system," *Solar Energy*, vol. 79, no. 1, pp. 56–64, 2005.

[72] T. Yabe, T. Ohkubo, S. Uchida, K. Yoshida, M. Nakatsuka, T. Funatsu, A. Mabuti, A. Oyama, K. Nakagawa, T. Oishi, *et al.*, "High-efficiency and economical solar-energy-pumped laser with fresnel lens and chromium codoped laser medium," *Applied physics letters*, vol. 90, no. 26, 2007.

[73] I. Oshida, "Step lenses and step prisms for utilization of solar energy," in *Proc. UN Conf. on New Sources of Energy*, vol. 35, 1961.

[74] R. Donovan and S. Broadbent, "Photovoltaic concentrating array," in *13th Intersociety Energy Conversion Engineering Conference*, vol. 2, pp. 1593–1599, 1978.

[75] G. Francia, "Pilot plants of solar steam generating stations," *Solar Energy*, vol. 12, no. 1, pp. 51–64, 1968.

[76] J.-S. Lin, W.-C. Huang, H.-C. Hsu, M.-W. Chang, and C.-P. Liu, "A study for the special fresnel lens for high efficiency solar concentrators," in *Nonimaging Optics and Efficient Illumination Systems II*, vol. 5942, pp. 293–301, SPIE, 2005.

[77] A. Akisawa, T. Sato, T. Miyazaki, T. Kashiwagi, and M. Hiramatsu, "High concentration non-imaging fresnel lens design with flat upper surface," in *High and Low Concentration for Solar Electric Applications II*, vol. 6649, pp. 133–140, SPIE, 2007.

[78] M. R. Squillante, R. A. Myers, M. Woodring, J. F. Christian, F. Robertson, R. Farrell, A. I. Kogan, T. C. Tiernan, and G. Entine, "Apd-based x-ray imaging telescope using fresnel zone plates for extremely high spatial resolution," in *Penetrating Radiation Systems and Applications VII*, vol. 5923, pp. 188–195, SPIE, 2005.

[79] H. Barrett, W. Stoner, D. Wilson, and G. DeMeester, "Coded apertures derived from the fresnel zone plate," *Optical Engineering*, vol. 13, no. 6, pp. 539–549, 1974.

[80] W. Rogers, K. Han, L. Jones, and W. Beierwaltes, "Application of a fresnel zone plate to gamma-ray imaging," *Journal of Nuclear Medicine*, vol. 13, no. 8, pp. 612–615, 1972.

[81] N. Nakamura, Y. Kamiya, T. Koseki, H. Takaki, N. Aoki, and K. Nakayama, "Design of a beam size monitor using fresnel zone plates," in *PACS2001. Proceedings of the 2001 Particle Accelerator Conference (Cat. No. 01CH37268)*, vol. 2, pp. 1628–1630, IEEE, 2001.

[82] S. Wang and X.-C. Zhang, "Terahertz technology: terahertz tomographic imaging with a fresnel lens," *Optics and Photonics News*, vol. 13, no. 12, pp. 59–59, 2002.

[83] P. Kumbhakar, J. S. Jayan, A. S. Madhavikutty, P. Sreeram, A. Saritha, T. Ito, and C. S. Tiwary, "Prospective applications of two-dimensional materials beyond laboratory frontiers: A review," *IScience*, vol. 26, no. 5, 2023.

[84] K. S. Novoselov, A. K. Geim, S. V. Morozov, D.-e. Jiang, Y. Zhang, S. V. Dubonos, I. V. Grigorieva, and A. A. Firsov, "Electric field effect in atomically thin carbon films," *science*, vol. 306, no. 5696, pp. 666–669, 2004.

[85] F. R. Fan, R. Wang, H. Zhang, and W. Wu, "Emerging beyond-graphene elemental 2d materials for energy and catalysis applications," *Chemical Society Reviews*, vol. 50, no. 19, pp. 10983–11031, 2021.

[86] C. Sanchez, P. Belleville, M. Popall, and L. Nicole, "Applications of advanced hybrid organic–inorganic nanomaterials: from laboratory to market," *Chemical Society Reviews*, vol. 40, no. 2, pp. 696–753, 2011.

[87] V. A. Cao, M. Kim, W. Hu, S. Lee, S. Youn, J. Chang, H. S. Chang, and J. Nah, "Enhanced piezoelectric output performance of the sns2/sns heterostructure thin-film piezoelectric nanogenerator realized by atomic layer deposition," *ACS nano*, vol. 15, no. 6, pp. 10428–10436, 2021.

[88] W. Wu, L. Wang, Y. Li, F. Zhang, L. Lin, S. Niu, D. Chenet, X. Zhang, Y. Hao, T. F. Heinz, *et al.*, "Piezoelectricity of single-atomic-layer mos2 for energy conversion and piezotronics," *Nature*, vol. 514, no. 7523, pp. 470–474, 2014.

[89] K.-A. N. Duerloo, M. T. Ong, and E. J. Reed, "Intrinsic piezoelectricity in two-dimensional materials," *The Journal of Physical Chemistry Letters*, vol. 3, no. 19, pp. 2871–2876, 2012.

[90] S. Kim, T. Y. Kim, K. H. Lee, T.-H. Kim, F. A. Cimini, S. K. Kim, R. Hinchet, S.-W. Kim, and C. Falconi, "Rewritable ghost floating gates by tunnelling triboelectrification for two-dimensional electronics," *Nature communications*, vol. 8, no. 1, p. 15891, 2017.

[91] S. D. Negedu, R. Tromer, C. C. Gowda, C. F. Woellner, F. E. Olu, A. K. Roy, P. Pandey, D. S. Galvao, P. M. Ajayan, P. Kumbhakar, *et al.*, "Two-dimensional cobalt telluride as a piezo-tribogenerator," *Nanoscale*, vol. 14, no. 21, pp. 7788–7797, 2022.

[92] K. S. Novoselov, D. Jiang, F. Schedin, T. Booth, V. Khotkevich, S. Morozov, and A. K. Geim, "Two-dimensional atomic crystals," *Proceedings of the National Academy of Sciences*, vol. 102, no. 30, pp. 10451–10453, 2005.

[93] K. F. Mak, C. Lee, J. Hone, J. Shan, and T. F. Heinz, "Atomically thin mos 2: a new direct-gap semiconductor," *Physical review letters*, vol. 105, no. 13, p. 136805, 2010.

[94] H. Liu, A. T. Neal, Z. Zhu, D. Tomanek, and P. D. Ye, "Phosphorene: a new 2d material with high carrier mobility," *arXiv preprint arXiv:1401.4133*, 2014.

[95] G. Serpico and N. Poccia, "Perspective in the twistronics of high-temperature superconductors," in *Encyclopedia of Condensed Matter Physics (Second Edition)* (T. Chakraborty, ed.), pp. 712–724, Oxford: Academic Press, second edition ed., 2024.

[96] C. R. Dean, A. F. Young, I. Meric, C. Lee, L. Wang, S. Sorgenfrei, K. Watanabe, T. Taniguchi, P. Kim, K. L. Shepard, *et al.*, "Boron nitride substrates for high-quality graphene electronics," *Nature nanotechnology*, vol. 5, no. 10, pp. 722–726, 2010.

[97] D. Sander, S. O. Valenzuela, D. Makarov, C. H. Marrows, E. E. Fullerton, P. Fischer, J. McCord, P. Vavassori, S. Mangin, P. Pirro, B. Hillebrands, A. D. Kent, T. Jungwirth, O. Gutfleisch, C. G. Kim, and A. Berger, "The 2017 magnetism roadmap," *J. Phys. D Appl. Phys.*, vol. 50, p. 363001, Sept. 2017.

[98] L. Britnell, R. Gorbachev, R. Jalil, B. Belle, F. Schedin, A. Mishchenko, T. Georgiou, M. Katsnelson, L. Eaves, S. Morozov, *et al.*, "Field-effect tunneling transistor based on vertical graphene heterostructures," *Science*, vol. 335, no. 6071, pp. 947–950, 2012.

[99] K. Roy, M. Padmanabhan, S. Goswami, T. P. Sai, G. Ramalingam, S. Raghavan, and A. Ghosh, "Graphene–mos2 hybrid structures for multifunctional photoresponsive memory devices," *Nature nanotechnology*, vol. 8, no. 11, pp. 826–830, 2013.

[100] S. Zeng, S. Hu, J. Xia, T. Anderson, X.-Q. Dinh, X.-M. Meng, P. Coquet, and K.-T. Yong, "Graphene–mos2 hybrid nanostructures enhanced surface plasmon

resonance biosensors," *Sensors and Actuators B: Chemical*, vol. 207, pp. 801–810, 2015.

[101] K.-J. Huang, L. Wang, J. Li, and Y.-M. Liu, "Electrochemical sensing based on layered mos2–graphene composites," *Sensors and Actuators B: Chemical*, vol. 178, pp. 671–677, 2013.

[102] K. S. Novoselov, A. Mishchenko, A. Carvalho, and A. Castro Neto, "2d materials and van der waals heterostructures," *Science*, vol. 353, no. 6298, p. aac9439, 2016.

[103] E. Gao, S.-Z. Lin, Z. Qin, M. J. Buehler, X.-Q. Feng, and Z. Xu, "Mechanical exfoliation of two-dimensional materials," *Journal of the Mechanics and Physics of Solids*, vol. 115, pp. 248–262, 2018.

[104] M. Zhao, C. Casiraghi, and K. Parvez, "Electrochemical exfoliation of 2d materials beyond graphene," *Chemical Society Reviews*, 2024.

[105] O. Song and J. Kang, "Solution-processed 2d materials for electronic applications," *ACS Applied Electronic Materials*, vol. 5, no. 3, pp. 1335–1346, 2023.

[106] K. Thambiratnam, S. A. Reduan, Z. C. Tiu, and H. Ahmad, "Application of two-dimensional materials in fiber laser systems," in *Nano-Optics*, pp. 227–264, Elsevier, 2020.

[107] P. Chavalekvirat, W. Hirunpinyopas, K. Deshsorn, K. Jitapunkul, and P. Iamprasertkun, "Liquid phase exfoliation of 2d materials and its electrochemical applications in the data-driven future," *Precision Chemistry*, 2024.

[108] H. Zhang, "Introduction: 2d materials chemistry," 2018.

[109] S. Bhowmik and A. G. Rajan, "Chemical vapor deposition of 2d materials: A review of modeling, simulation, and machine learning studies," *Iscience*, vol. 25, no. 3, 2022.

[110] M. Houssa, A. Dimoulas, and A. Molle, eds., *2D materials for nanoelectronics*. Series in Materials Science and Engineering, London, England: CRC Press, Mar. 2021.

[111] M. Chhowalla, H. S. Shin, G. Eda, L.-J. Li, K. P. Loh, and H. Zhang, "The chemistry of two-dimensional layered transition metal dichalcogenide nanosheets," *Nature chemistry*, vol. 5, no. 4, pp. 263–275, 2013.

[112] J. A. Wilson and A. Yoffe, "The transition metal dichalcogenides discussion and interpretation of the observed optical, electrical and structural properties," *Advances in Physics*, vol. 18, no. 73, pp. 193–335, 1969.

[113] M. M. Fadhel, N. Ali, H. Rashid, N. M. Sapiee, A. E. Hamzah, M. S. D. Zan, N. A. Aziz, and N. Arsad, "A review on rhenium disulfide: Synthesis approaches, optical properties, and applications in pulsed lasers," *Nanomaterials*, vol. 11, no. 9, p. 2367, 2021.

[114] M. Rahman, K. Davey, and S.-Z. Qiao, "Advent of 2d rhenium disulfide (res2): fundamentals to applications," *Advanced Functional Materials*, vol. 27, no. 10, p. 1606129, 2017.

[115] W. Noddack, "Die ekamangane," *Naturwiss*, vol. 13, pp. 567–574, 1925.

[116] S. Tongay, H. Sahin, C. Ko, A. Luce, W. Fan, K. Liu, J. Zhou, Y.-S. Huang, C.-H. Ho, J. Yan, *et al.*, "Monolayer behaviour in bulk res2 due to electronic and vibrational decoupling," *Nature communications*, vol. 5, no. 1, p. 3252, 2014.

[117] X. Li, C. Chen, Y. Yang, Z. Lei, and H. Xu, "2d re-based transition metal chalcogenides: progress, challenges, and opportunities," *Advanced Science*, vol. 7, no. 23, p. 2002320, 2020.

[118] Q. Zhang and L. Fu, "Novel insights and perspectives into weakly coupled res2 toward emerging applications," *Chem*, vol. 5, no. 3, pp. 505–525, 2019.

[119] E. Zhang, Y. Jin, X. Yuan, W. Wang, C. Zhang, L. Tang, S. Liu, P. Zhou, W. Hu, and F. Xiu, "Res2-based field-effect transistors and photodetectors," *Advanced Functional Materials*, vol. 25, no. 26, pp. 4076–4082, 2015.

[120] A. Zulkefli, B. Mukherjee, T. Iwasaki, R. Hayakawa, S. Nakaharai, and Y. Wakayama, "Gate-bias tunable humidity sensors based on rhenium disulfide

field-effect transistors," *Japanese Journal of Applied Physics*, vol. 60, no. SB, p. SBBH01, 2020.

[121] D. P. Thanu, E. S. Srinadhu, M. Zhao, N. V. Dole, and M. Keswani, "Fundamentals and applications of plasma cleaning," *Developments in surface contamination and cleaning: applications of cleaning techniques*, pp. 289–353, 2019.

[122] S. Deiries, A. Silber, O. Iwert, E. Hummel, and J. L. Lizon, "Plasma cleaning," in *Scientific detectors for astronomy 2005: Explorers of the Photon Odyssey*, pp. 129–136, Springer, 2006.

[123] N. Sahu, B. Parija, and S. Panigrahi, "Fundamental understanding and modeling of spin coating process: A review," *Indian Journal of Physics*, vol. 83, no. 4, pp. 493–502, 2009.

[124] S. Nandy and K. H. Chae, "Chemical synthesis of ferrite thin films," in *Ferrite Nanostructured Magnetic Materials*, pp. 309–334, Elsevier, 2023.

[125] C. A. Bishop, "Chapter 15 - electron beam (e-beam) evaporation," in *Vacuum Deposition Onto Webs, Films and Foils (Third Edition)* (C. A. Bishop, ed.), pp. 289–299, Boston: William Andrew Publishing, third edition ed., 2015.

[126] T. Kerdcharoen and C. Wongchoosuk, "11 - carbon nanotube and metal oxide hybrid materials for gas sensing," in *Semiconductor Gas Sensors* (R. Jaaniso and O. K. Tan, eds.), Woodhead Publishing Series in Electronic and Optical Materials, pp. 386–407, Woodhead Publishing, 2013.

[127] V. Clericò *et al.*, "Fabrication and characterization of quantum materials: graphene heterostructures and topological insulators," 2020.

[128] R. C. H. Cik, C. T. Foo, and A. F. O. Nor, "Field emission scanning electron microscope (fesem) facility in bti," 2015.

[129] J. I. Goldstein, D. E. Newbury, P. Echlin, D. C. Joy, C. E. Lyman, E. Lifshin, L. Sawyer, J. R. Michael, J. I. Goldstein, D. E. Newbury, *et al.*, "Special topics in scanning electron microscopy," *Scanning Electron Microscopy and X-ray Microanalysis: Third Edition*, pp. 195–270, 2003.

[130] A. Alyamani and O. Lemine, "Fe-sem characterization of some nanomaterial," in *Scanning electron microscopy*, IntechOpen, 2012.

[131] R. S. Prabhu, R. Priyanka, M. Vijay, and G. K. Vikashini, "Field emission scanning electron microscopy (fesem) with a very big future in pharmaceutical research," *Research Article—Pharmaceutical Sciences—OA Journal—MCI Approved—Index Copernicus*, vol. 11, pp. 2321–3272, 2021.

[132] P. Breton, "From microns to nanometers: early landmarks in the science of scanning electron microscope imaging," *Scanning Microsc*, vol. 13, no. 1, pp. 1–6, 1999.

[133] V. Clericò, M. Amado, and E. Diez, "Electron beam lithography and its use on 2d materials," in *Nanofabrication: Nanolithography techniques and their applications*, pp. 3–1, IOP Publishing Bristol, UK, 2020.

[134] H. Yao and K. Kimura, "Field emission scanning electron microscopy for structural characterization of 3d gold nanoparticle superlattices," *Modern research and educational topics in microscopy*, vol. 2, pp. 568–576, 2007.

[135] J. M. De Teresa, *Nanofabrication: Nanolithography techniques and their applications*. IOP Publishing, 2020.

[136] A. Abbas, "Nanofabrication using electron beam lithography: novel resist and applications," Master's thesis, University of Waterloo, 2013.

[137] D. Tennant and A. Bleier, "Electron beam lithography of nanostructures," *Handb. Nanofabrication*, vol. 4, pp. 121–148, 2010.

[138] M. J. Madou, *Fundamentals of microfabrication: the science of miniaturization*. CRC press, 2018.

[139] M. Altissimo, "E-beam lithography for micro-/nanofabrication," *Biomicrofluidics*, vol. 4, no. 2, 2010.

[140] C. Vieu, F. Carcenac, A. Pepin, Y. Chen, M. Mejias, A. Lebib, L. Manin-Ferlazzo, L. Couraud, and H. Launois, "Electron beam lithography: resolution limits and applications," *Applied surface science*, vol. 164, no. 1-4, pp. 111–117, 2000.

[141] A. Grigorescu and C. Hagen, "Resists for sub-20-nm electron beam lithography with a focus on hsq: state of the art," *Nanotechnology*, vol. 20, no. 29, p. 292001, 2009.

[142] R. Harris, "Polymethyl methacrylate as an electron sensitive resist," *Journal of The Electrochemical Society*, vol. 120, no. 2, p. 270, 1973.

[143] M. Peuker, M. Lim, H. I. Smith, R. Morton, A. van Langen-Suurling, J. Romijn, E. van der Drift, and F. van Delft, "Hydrogen silsesquioxane, a high-resolution negative tone e-beam resist, investigated for its applicability in photon-based lithographies," *Microelectronic Engineering*, vol. 61-62, pp. 803–809, 2002. Micro- and Nano-Engineering 2001.

[144] B. Bhushan, ed., *Encyclopedia of nanotechnology*. Encyclopedia of Nanotechnology, Dordrecht, Netherlands: Springer, 2 ed., Aug. 2012.

[145] P. Rai-Choudhury, *Handbook of microlithography, micromachining, and microfabrication: microlithography*, vol. 39. SPIE press, 1997.

[146] D. Bodas, S. J. Patil, V. Krishnamurthy, and S. Gangal, "Pmma as an etch mask for silicon micromachining a feasibility study.," *Journal of the Indian Institute of Science*, vol. 81, no. 6, p. 645, 2001.

[147] H. Yang, A. Jin, Q. Luo, J. Li, C. Gu, and Z. Cui, "Electron beam lithography of hsq/pmma bilayer resists for negative tone lift-off process," *Microelectronic Engineering*, vol. 85, no. 5-6, pp. 814–817, 2008.

[148] P. Rai-Choudhury, *Handbook of Microlithography, Micromachining and Microfabrication: Handbook of Microlithography, Micromachining and Microfabrication Vol.1 Vol.1*. Press Monographs, Bellingham, WA: SPIE Press, Oct. 1999.

[149] P. Candeloro, D. Panella, S. A. Pullano, M. L. Coluccio, and G. Perozziello, "Chapter 6 - fabrication technologies," in *Microfluidics for Cellular Applications* (G. Perozziello, U. Krühne, and P. Luciani, eds.), Micro and Nano Technologies, pp. 223–274, Elsevier, 2023.

[150] M. Toofan and J. Toofan, "Chapter 5 - a brief review of the cleaning process for electronic device fabrication," in *Developments in Surface Contamination and Cleaning* (R. Kohli and K. Mittal, eds.), pp. 185–212, Oxford: William Andrew Publishing, 2015.

[151] V. Kumar, M. Pallapa, P. Rezai, and P. Selvaganapathy, "Polymers," in *Reference Module in Materials Science and Materials Engineering*, Elsevier, 2016.

[152] "Chapter 5 - promising future processing technology," in *Advances in CMP Polishing Technologies* (T. Doi, I. D. Marinescu, and S. Kurokawa, eds.), pp. 229–295, Oxford: William Andrew Publishing, 2012.

[153] S. Franssila, *Introduction to microfabrication*. John Wiley & Sons, 2010.

[154] T. Jawhari, "Raman spectroscopy as a powerful analytical tool: probing the structure of matter," *Capítol del llibre: Handbook of instrumental techniques for materials, chemical and biosciences research, Centres Científics i Tecnològics. Universitat de Barcelona, Barcelona, 2012. Part II. Chemical technologies (ChT), ChT. 2, 12 p.*, 2012.

[155] S. Nandi, "RAMAN SPECTROSCOPY," 2021.

[156] S. Chatterjee, S. S. Gadad, and T. K. Kundu, "Atomic force microscopy: a tool to unveil the mystery of biological systems," *Resonance*, vol. 15, pp. 622–642, 2010.

[157] Y. Gan, "Atomic and subnanometer resolution in ambient conditions by atomic force microscopy," *Surface Science Reports*, vol. 64, no. 3, pp. 99–121, 2009.

[158] M. D. Ward, "Bulk crystals to surfaces: Combining x-ray diffraction and atomic force microscopy to probe the structure and formation of crystal interfaces," *Chemical Reviews*, vol. 101, no. 6, pp. 1697–1726, 2001.

[159] E. Meyer, H. J. Hug, and R. Bennewitz, *Scanning probe microscopy: the lab on a tip*. Springer, 2004.

[160] N. Masaki, K. Machida, H. Kado, K. Yokoyama, and T. Tohda, "Molecular-resolution images of aspirin crystals with atomic force microscopy," *Ultramicroscopy*, vol. 42, pp. 1148–1154, 1992.

[161] B. Bhushan, "Nanotribology and nanomechanics in nano/biotechnology," *Philosophical Transactions of the Royal Society A: Mathematical, Physical and Engineering Sciences*, vol. 366, no. 1870, pp. 1499–1537, 2008.

[162] H. Assender, V. Bliznyuk, and K. Porfyrakis, "How surface topography relates to materials' properties," *Science*, vol. 297, no. 5583, pp. 973–976, 2002.

[163] P. Neogi, "Length scales and roughness on a growing solid surface: a review," *Journal of Electroanalytical Chemistry*, vol. 595, no. 1, pp. 1–10, 2006.

[164] K. D. Jandt, "Atomic force microscopy of biomaterials surfaces and interfaces," *Surface Science*, vol. 491, no. 3, pp. 303–332, 2001.

[165] A. Agnihotri, J. T. Garrett, J. Runt, and C. A. Siedlecki, "Atomic force microscopy visualization of poly (urethane urea) microphase rearrangements under aqueous environment," *Journal of Biomaterials Science, Polymer Edition*, vol. 17, no. 1-2, pp. 227–238, 2006.

[166] O. Marti, T. Stifter, H. Waschipky, M. Quintus, and S. Hild, "Scanning probe microscopy of heterogeneous polymers," *Colloids and Surfaces A: Physicochemical and Engineering Aspects*, vol. 154, no. 1-2, pp. 65–73, 1999.

[167] A. Simon and M.-C. Durrieu, "Strategies and results of atomic force microscopy in the study of cellular adhesion," *Micron*, vol. 37, no. 1, pp. 1–13, 2006.

[168] F. Variola, "Atomic force microscopy in biomaterials surface science," *Physical Chemistry Chemical Physics*, vol. 17, no. 5, pp. 2950–2959, 2015.

[169] D. Guo, G. Xie, and J. Luo, "Mechanical properties of nanoparticles: basics and applications," *Journal of physics D: applied physics*, vol. 47, no. 1, p. 013001, 2013.

[170] R. W. Carpick and M. Salmeron, "Scratching the surface: fundamental investigations of tribology with atomic force microscopy," *Chemical reviews*, vol. 97, no. 4, pp. 1163–1194, 1997.

[171] J. N. Israelachvili, *Intermolecular and surface forces*. Academic press, 2011.

[172] B. Kyeyune, "Atomic force microscopy," 2017.

[173] B. Kyeyune *et al.*, "Surface potential response of wurzite and zinc blende structures in gap nanowires," 2018.

[174] S. Sadewasser and T. Glatzel, *Kelvin Probe Force Microscopy: From Single Charge Detection to Device Characterization*, vol. 65. Springer, 2018.

[175] T. Glatzel, U. Gysin, and E. Meyer, "Kelvin probe force microscopy for material characterization," *Microscopy*, vol. 71, no. Supplement_1, pp. i165–i173, 2022.

[176] O. Vatel and M. Tanimoto, "Kelvin probe force microscopy for potential distribution measurement of semiconductor devices," *Journal of applied physics*, vol. 77, no. 6, pp. 2358–2362, 1995.

[177] A. Zahmatkeshsaredorahi, D. S. Jakob, and X. G. Xu, "Pulsed force kelvin probe force microscopy a new type of kelvin probe force microscopy under ambient conditions," *The Journal of Physical Chemistry C*, vol. 128, no. 24, pp. 9813–9827, 2024.

[178] A. Perez-Rodriguez, I. Temino, C. Ocal, M. Mas-Torrent, and E. Barrena, "Decoding the vertical phase separation and its impact on c8-btbt/ps transistor properties," *ACS applied materials & interfaces*, vol. 10, no. 8, pp. 7296–7303, 2018.

[179] I. Gelmetti, N. F. Montcada, A. Pérez-Rodríguez, E. Barrena, C. Ocal, I. García-Benito, A. Molina-Ontoria, N. Martín, A. Vidal-Ferran, and E. Palomares, "Energy alignment and recombination in perovskite solar cells: weighted influence

on the open circuit voltage," *Energy & Environmental Science*, vol. 12, no. 4, pp. 1309–1316, 2019.

[180] S. Sadewasser, "Optoelectronic studies of solar cells," *Kelvin Probe Force Microscopy: Measuring and Compensating Electrostatic Forces*, pp. 151–174, 2011.

[181] M. Wohlfahrt, M. J. Uren, Y. Yin, K. B. Lee, and M. Kuball, "Vertical field inhomogeneity associated with threading dislocations in gan high electron mobility transistor epitaxial stacks," *Applied Physics Letters*, vol. 119, no. 24, 2021.

[182] J. Nie, Y. Zhang, J. Wang, L. Li, and Y. Zhang, "Recent progress in regulating surface potential for high-efficiency perovskite solar cells," *ACS Energy Letters*, vol. 9, no. 4, pp. 1674–1681, 2024.

[183] Y. Li, X. Zhu, F. Liu, Z. Sui, B. Wang, C. Jiang, and L. Liao, "Enhancing hole-injection efficiency of top-emitting organic light-emitting diodes based on al/monx anodes," *Materials Letters*, vol. 331, p. 133424, 2023.

[184] M. Vishwakarma, D. Varandani, C. Andres, Y. E. Romanyuk, S. G. Haass, A. N. Tiwari, and B. R. Mehta, "A direct measurement of higher photovoltage at grain boundaries in cds/cztse solar cells using kpfm technique," *Solar Energy Materials and Solar Cells*, vol. 183, pp. 34–40, 2018.

[185] J. J. Kopanski, "Scanning capacitance microscopy for electrical characterization of semiconductors and dielectrics," in *Scanning Probe Microscopy: Electrical and Electromechanical Phenomena at the Nanoscale*, pp. 88–112, Springer, 2007.

[186] A. Gil, J. Colchero, J. Gómez-Herrero, and A. Baró, "Electrostatic force gradient signal: resolution enhancement in electrostatic force microscopy and improved kelvin probe microscopy," *Nanotechnology*, vol. 14, no. 2, p. 332, 2003.

[187] T. Glatzel, M. C. Lux-Steiner, E. Strassburg, A. Boag, and Y. Rosenwaks, "Principles of kelvin probe force microscopy," *Scanning Probe Microscopy: Electrical and Electromechanical Phenomena at the Nanoscale*, pp. 113–131, 2007.

[188] M. Labani, V. Clericò, E. Diez, G. Gatti, M. Amado, and A. Pérez-Rodríguez, "Optimization of soft x-ray fresnel zone plate fabrication through joint electron beam lithography and cryo-etching techniques," *Nanomaterials*, vol. 14, no. 23, p. 1898, 2024.

[189] M. Brzhezinskaya, A. Firsov, K. Holldack, T. Kachel, R. Mitzner, N. Pontius, J.-S. Schmidt, M. Sperling, C. Stamm, A. Föhlisch, *et al.*, "A novel monochromator for experiments with ultrashort x-ray pulses," *Journal of synchrotron radiation*, vol. 20, no. 4, pp. 522–530, 2013.

[190] T. Kroll, J. Kern, M. Kubin, D. Ratner, S. Gul, F. D. Fuller, H. Löchel, J. Krzywinski, A. Lutman, Y. Ding, *et al.*, "X-ray absorption spectroscopy using a self-seeded soft x-ray free-electron laser," *Optics Express*, vol. 24, no. 20, pp. 22469–22480, 2016.

[191] T. Kawazoe, T. Takahashi, and M. Ohtsu, "Evaluation of the dynamic range and spatial resolution of nonadiabatic optical near-field lithography through fabrication of fresnel zone plates," *Applied Physics B*, vol. 98, pp. 5–11, 2010.

[192] M. Mayer, K. Keskinbora, C. Grévent, A. Szeghalmi, M. Knez, M. Weigand, A. Snigirev, I. Snigireva, and G. Schütz, "Efficient focusing of 8 kev x-rays with multilayer fresnel zone plates fabricated by atomic layer deposition and focused ion beam milling," *Journal of Synchrotron Radiation*, vol. 20, no. 3, pp. 433–440, 2013.

[193] S. S. Sarkar, H. H. Solak, J. Raabe, C. David, and J. F. van der Veen, "Fabrication of fresnel zone plates with 25 nm zone width using extreme ultraviolet holography," *Microelectronic Engineering*, vol. 87, no. 5-8, pp. 854–858, 2010.

[194] T. Okabe, K. Utsumi, K. Ogino, Y. Shinonaga, M. Miyatake, S. Yoshimoto, J. Taniguchi, and S. Sasaki, "Electron beam mastering system using a vacuum-compatible hydrodynamic spindle," *Microelectronic Engineering*, vol. 142, pp. 64–69, 2015.

[195] E. T. F. Rogers, J. Lindberg, T. Roy, S. Savo, J. E. Chad, M. R. Dennis, and N. I. Zheludev, "A super-oscillatory lens optical microscope for subwavelength imaging," *Nature Materials*, vol. 11, no. 5, pp. 432–435, 2012.

[196] X.-T. Kong, A. A. Khan, P. R. Kidambi, S. Deng, A. K. Yetisen, B. Dlubak, P. Hiralal, Y. Montelongo, J. Bowen, S. Xavier, *et al.*, "Graphene-based ultrathin flat lenses," *ACS Photonics*, vol. 2, no. 2, pp. 200–207, 2015.

[197] X. Li, L. Wei, R. H. Poelma, S. Vollebregt, J. Wei, H. P. Urbach, P. M. Sarro, and G. Q. Zhang, "Stretchable binary fresnel lens for focus tuning," *Scientific Reports*, vol. 6, no. 1, p. 25348, 2016.

[198] X. Zheng, B. Jia, H. Lin, L. Qiu, D. Li, and M. Gu, "Highly efficient and ultra-broadband graphene oxide ultrathin lenses with three-dimensional subwavelength focusing," *Nature Communications*, vol. 6, no. 1, p. 8433, 2015.

[199] M. J. Low, H. Lee, C. H. J. Lim, C. S. Sandeep, V. M. Murukeshan, S.-W. Kim, and Y.-J. Kim, "Laser-induced reduced-graphene-oxide micro-optics patterned by femtosecond laser direct writing," *Applied Surface Science*, vol. 526, p. 146647, 2020.

[200] M. A. Mohammad, M. Muhammad, S. K. Dew, and M. Stepanova, "Fundamentals of electron beam exposure and development," in *Nanofabrication: Techniques and Principles*, pp. 11–41, Springer, 2011.

[201] R. G. Brault, R. L. Kubena, and R. A. Metzger, "Bilevel polysiloxane resist for ion-beam and electron-beam lithography," in *Advances in Resist Technology and Processing II*, vol. 539, pp. 70–73, SPIE, 1985.

[202] A. Lyons and J. Hartley, "Proximity effect correction parameters for patterning of euv reticles with gaussian electron-beam lithography," in *Photomask Technology 2012*, vol. 8522, pp. 715–724, SPIE, 2012.

[203] G. Zhao and Y. Li, "A comparison study of tantalum-nitrogen and chromium absorber in extreme ultraviolet mask fabrication using electron-beam lithography

simulation," in *Photomask and Next-Generation Lithography Mask Technology XIV*, vol. 6607, pp. 915–922, SPIE, 2007.

[204] M. N. Hossain, J. Justice, P. Lovera, B. McCarthy, A. O'Riordan, and B. Corbett, "High aspect ratio nano-fabrication of photonic crystal structures on glass wafers using chrome as hard mask," *Nanotechnology*, vol. 25, no. 35, p. 355301, 2014.

[205] C. David, S. Gorelick, S. Rutishauser, J. Krzywinski, J. Vila-Comamala, V. Guzenko, O. Bunk, E. Färm, M. Ritala, M. Cammarata, *et al.*, "Nanofocusing of hard x-ray free electron laser pulses using diamond based fresnel zone plates," *Scientific Reports*, vol. 1, no. 1, p. 57, 2011.

[206] T. Reisinger, S. Eder, M. M. Greve, H. I. Smith, and B. Holst, "Free-standing silicon-nitride zoneplates for neutral-helium microscopy," *Microelectronic engineering*, vol. 87, no. 5-8, pp. 1011–1014, 2010.

[207] P. Takman, *Compact Soft X-Ray Microscopy: Sources, Optics and Instrumentation.* PhD thesis, KTH, 2007.

[208] K. Parfeniukas *et al.*, "Improved tungsten nanofabrication for hard x-ray zone plates," *Microelectronic Engineering*, vol. 152, pp. 6–9, 2016.

[209] Z. Liu, Y. Wu, B. Harteneck, and D. Olynick, "Super-selective cryogenic etching for sub-10 nm features," *Nanotechnology*, vol. 24, no. 1, p. 015305, 2012.

[210] E. D. Fabrizio *et al.*, "High-performance multilevel blazed x-ray microscopy fresnel zone plates: Fabricated using x-ray lithography," *Journal of Vacuum Science & Technology B: Microelectronics and Nanometer Structures Processing, Measurement, and Phenomena*, vol. 12, no. 6, pp. 3979–3985, 1994.

[211] J. Zhu, Y. Chen, S. Xie, L. Zhang, C. Wang, and R. Tai, "Nanofabrication of 30 nm au zone plates by e-beam lithography and pulse voltage electroplating for soft x-ray imaging," *Microelectronic Engineering*, vol. 225, p. 111254, 2020.

[212] W. Loesberg, J. Te Riet, F. Van Delft, P. Schön, C. Figdor, S. Speller, J. Van Loon, X. Walboomers, and J. Jansen, "The threshold at which substrate nanogroove di-

mensions may influence fibroblast alignment and adhesion," *Biomaterials*, vol. 28, no. 27, pp. 3944–3951, 2007.

[213] A. M. Rajnicek and C. D. McCaig, "Guidance of cns growth cones by substratum grooves and ridges: effects of inhibitors of the cytoskeleton, calcium channels and signal transduction pathways," *Journal of cell science*, vol. 110, no. 23, pp. 2915–2924, 1997.

[214] M. Larkin and R. Matta, "The electron beam fabrication of small geometry transistors," *Solid-State Electronics*, vol. 10, no. 5, pp. 491–496, 1967.

[215] H. Ku and L. Scala, "Polymeric electron beam resists," *Journal of The Electrochemical Society*, vol. 116, no. 7, p. 980, 1969.

[216] "Chapter 5 - manipulation and patterning of surfaces (nanolithography)," in *Fundamentals and Applications of Nano Silicon in Plasmonics and Fullerines* (M. Nayfeh, ed.), Micro and Nano Technologies, pp. 89–137, Elsevier, 2018.

[217] Y.-H. Lee, R. Browning, N. Maluf, G. Owen, and R. Pease, "Low voltage alternative for electron beam lithography," *Journal of Vacuum Science & Technology B: Microelectronics and Nanometer Structures Processing, Measurement, and Phenomena*, vol. 10, no. 6, pp. 3094–3098, 1992.

[218] H. Yang, L. Fan, A. Jin, Q. Luo, C. Gu, and Z. Cui, "Low-energy electron-beam lithography of zep-520 positive resist," in *2006 1st IEEE International Conference on Nano/Micro Engineered and Molecular Systems*, pp. 391–394, IEEE, 2006.

[219] D. Kyser and N. Viswanathan, "Monte carlo simulation of spatially distributed beams in electron-beam lithography," *Journal of Vacuum Science and Technology*, vol. 12, no. 6, pp. 1305–1308, 1975.

[220] G. Brewer, *Electron-beam technology in microelectronic fabrication*. Elsevier, 2012.

[221] M. Kamp, M. Emmerling, S. Kuhn, and A. Forchel, "Nanolithography using a 100 kv electron beam lithography system with a schottky emitter," *Journal of Vacuum*

Science & Technology B: Microelectronics and Nanometer Structures Processing, Measurement, and Phenomena, vol. 17, no. 1, pp. 86–89, 1999.

[222] C. Lo, M. Rooks, W. Lo, M. Isaacson, and H. Craighead, "Resists and processes for 1 kv electron beam microcolumn lithography," *Journal of Vacuum Science & Technology B: Microelectronics and Nanometer Structures Processing, Measurement, and Phenomena*, vol. 13, no. 3, pp. 812–820, 1995.

[223] L. K. Mun, D. Drouin, E. Lavallée, and J. Beauvais, "The impact of charging on low-energy electron beam lithography," *Microscopy and Microanalysis*, vol. 10, no. 6, pp. 804–809, 2004.

[224] T. Chang, "Proximity effect in electron-beam lithography," *Journal of vacuum science and technology*, vol. 12, no. 6, pp. 1271–1275, 1975.

[225] B. Bhushan, *Encyclopedia of nanotechnology*, vol. 1. Springer Dordrecht, The Netherlands:, 2012.

[226] H. Demers, N. Poirier-Demers, M. R. Phillips, N. de Jonge, and D. Drouin, "Three-dimensional electron energy deposition modeling of cathodoluminescence emission near threading dislocations in gan and electron-beam lithography exposure parameters for a pmma resist," *Microscopy and Microanalysis*, vol. 18, no. 6, pp. 1220–1228, 2012.

[227] G. Owen, "Methods for proximity effect correction in electron lithography," *Journal of Vacuum Science & Technology B: Microelectronics Processing and Phenomena*, vol. 8, no. 6, pp. 1889–1892, 1990.

[228] G. P. Watson, S. D. Berger, J. A. Liddle, and W. K. Waskiewicz, "A background dose proximity effect correction technique for scattering with angular limitation projection electron lithography implemented in hardware," *Journal of Vacuum Science & Technology B: Microelectronics and Nanometer Structures Processing, Measurement, and Phenomena*, vol. 13, no. 6, pp. 2504–2507, 1995.

[229] V. Sundaram and S. Wen, "An easy method to perform e-beam negative tone lift-off fabrication on dielectric material with a sandwiched conducting polymer

layer," *Journal of Micromechanics and Microengineering*, vol. 21, no. 6, p. 065021, 2011.

[230] B. Munkhbat, B. Küçüköz, D. G. Baranov, T. J. Antosiewicz, and T. O. Shegai, "Nanostructured transition metal dichalcogenide multilayers for advanced nanophotonics," *Laser & Photonics Reviews*, vol. 17, no. 1, p. 2200057, 2023.

[231] M. Muhammad, S. C. Buswell, S. K. Dew, and M. Stepanova, "Nanopatterning of pmma on insulating surfaces with various anticharging schemes using 30 kev electron beam lithography," *Journal of Vacuum Science & Technology B*, vol. 29, no. 6, 2011.

[232] K. Scholten and E. Meng, "Electron-beam lithography for polymer biomems with submicron features," *Microsystems & nanoengineering*, vol. 2, no. 1, pp. 1–7, 2016.

[233] S. Gorelick, V. A. Guzenko, J. Vila-Comamala, and C. David, "Direct e-beam writing of dense and high aspect ratio nanostructures in thick layers of pmma for electroplating," *Nanotechnology*, vol. 21, no. 29, p. 295303, 2010.

[234] C. S. Tiwari, Y. S. Lim, R. Fulton, J. Srinivasan, M. Gisinger, P. Flynn, and L. H. Mak, "Characterization of the descum process for various silicon substrates doping," *ECS Transactions*, vol. 58, no. 6, p. 251, 2013.

[235] F. Rahman, D. J. Carbaugh, J. T. Wright, P. Rajan, S. G. Pandya, and S. Kaya, "A review of polymethyl methacrylate (pmma) as a versatile lithographic resist–with emphasis on uv exposure," *Microelectronic Engineering*, vol. 224, p. 111238, 2020.

[236] M. Ilie, B. Marculescu, N. Moldovan, N. Nastase, and M. Olteanu, "Adhesion between pmma mask layer and silicon wafer in koh aqueous solution," in *Materials and Device Characterization in Micromachining*, vol. 3512, pp. 422–430, SPIE, 1998.

[237] H. Abe, K. Nishioka, S. Tamura, and A. Nishimoto, "Microfabrication of anti-reflective chromium mask by gas plasma," *Japanese Journal of Applied Physics*, vol. 15, no. S1, p. 25, 1976.

[238] H. Nakata, K. Nishioka, and H. Abe, "Plasma etching characteristics of chromium film and its novel etching mode," *Journal of Vacuum Science and Technology*, vol. 17, no. 6, pp. 1351–1357, 1980.

[239] T. Yamazaki, Y. Suzuki, and H. Nakata, "Gas plasma etching of ion implanted chromium films," *Journal of Vacuum Science and Technology*, vol. 17, no. 6, pp. 1348–1350, 1980.

[240] G. Bell and H. Spierer, "Plasma etching of chrome masks using pbs resist," in *Optical/Laser Microlithography III*, vol. 1264, pp. 446–451, SPIE, 1990.

[241] F. Aydinoglu, F. Saffih, R. K. Dey, and B. Cui, "Chromium oxide as a hard mask material better than metallic chromium," *Journal of Vacuum Science & Technology B*, vol. 35, no. 6, 2017.

[242] J. Tonotani, S.-i. Ohmi, and H. Iwai, "Dry etching of cr2o3/cr stacked film during resist ashing by oxygen plasma," *Japanese journal of applied physics*, vol. 44, no. 1R, p. 114, 2005.

[243] J.-W. Tsai, C.-Y. Huang, Y.-H. Tai, H.-C. Cheng, F.-C. Su, F.-C. Luo, and H.-C. Tuan, "Reducing threshold voltage shifts in amorphous silicon thin film transistors by hydrogenating the gate nitride prior to amorphous silicon deposition," *Applied physics letters*, vol. 71, no. 9, pp. 1237–1239, 1997.

[244] C.-s. Chiang, C.-y. Chen, J. Kanicki, and K. Takechi, "Investigation of intrinsic channel characteristics of hydrogenated amorphous silicon thin-film transistors by gated-four-probe structure," *Applied physics letters*, vol. 72, no. 22, pp. 2874–2876, 1998.

[245] B. Wu, "Photomask plasma etching: A review," *Journal of Vacuum Science & Technology B: Microelectronics and Nanometer Structures Processing, Measurement, and Phenomena*, vol. 24, no. 1, pp. 1–15, 2006.

[246] D. Hoffman and J. A. Thornton, "Internal stresses in cr, mo, ta, and pt films deposited by sputtering from a planar magnetron source," *Journal of Vacuum Science and Technology*, vol. 20, no. 3, pp. 355–358, 1982.

[247] M. Bîrjega, N. Popescu-Pogrion, C. Sârbu, and V. Topa, "Particularities in the growth behaviour of vacuum-evaporated chromium thin films," *Thin Solid Films*, vol. 58, no. 1, pp. 217–221, 1979.

[248] M. Genshaw and R. Sirohi, "An ellipsometric study of chromium passivation," *Journal of The Electrochemical Society*, vol. 118, no. 10, p. 1558, 1971.

[249] P. M. Boltovets, S. A. Kravchenko, and B. A. Snopok, "Building interfacial nanostructures by size-controlled chemical etching," *Plasmonics*, vol. 5, pp. 395–403, 2010.

[250] V. T. Hoang Nguyen, F. Jensen, J. Hübner, E. Shkondin, R. Cork, K. Ma, P. Leussink, W. De Malsche, and H. Jansen, "Cr and crox etching using sf6 and o2 plasma," *Journal of Vacuum Science & Technology B*, vol. 39, no. 3, 2021.

[251] D. Staaks, Z. Yu, S. D. Dhuey, S. Sassolini, K. Y. Lee, I. W. Rangelow, and D. L. Olynick, "Temperature and oxygen concentration effects on anisotropy in chromium hard mask etching for nanoscale fabrication," *Journal of Vacuum Science & Technology A*, vol. 37, no. 6, 2019.

[252] D. Staaks, X. Yang, K. Y. Lee, S. D. Dhuey, S. Sassolini, I. W. Rangelow, and D. L. Olynick, "Low temperature dry etching of chromium towards control at sub-5 nm dimensions," *Nanotechnology*, vol. 27, no. 41, p. 415302, 2016.

[253] Z. Liu, X. Gu, J. Hwu, S. Sassolini, and D. L. Olynick, "Low-temperature plasma etching of high aspect-ratio densely packed 15 to sub-10 nm silicon features derived from ps-pdms block copolymer patterns," *Nanotechnology*, vol. 25, no. 28, p. 285301, 2014.

[254] H. Ekinci, N. M. Jahed, M. Soltani, and B. Cui, "The role of oxygen on anisotropy in chromium oxide hard mask etching for sub-micron fabrication," *IEEE Transactions on Nanotechnology*, vol. 20, pp. 33–38, 2020.

[255] K. Smith, J. Wasson, P. Mangat, W. Dauksher, and D. Resnick, "Cr absorber etch process for extreme ultraviolet lithography mask fabrication," *Journal of Vacuum*

Science & Technology B: Microelectronics and Nanometer Structures Processing, Measurement, and Phenomena, vol. 19, no. 6, pp. 2906–2910, 2001.

[256] K. Racka-Szmidt, B. Stonio, J. Żelazko, M. Filipiak, and M. Sochacki, "A review: Inductively coupled plasma reactive ion etching of silicon carbide," *Materials*, vol. 15, no. 1, p. 123, 2021.

[257] T. Defforge, X. Song, G. Gautier, T. Tillocher, R. Dussart, S. Kouassi, and F. Tran-Van, "Scalloping removal on drie via using low concentrated alkaline solutions at low temperature," *Sensors and Actuators A: Physical*, vol. 170, no. 1-2, pp. 114–120, 2011.

[258] V. J. Cadarso, N. Chidambaram, L. Jacot-Descombes, and H. Schift, "High-aspect-ratio nanoimprint process chains," *Microsystems & nanoengineering*, vol. 3, no. 1, pp. 1–12, 2017.

[259] S. Tachi, K. Tsujimoto, and S. Okudaira, "Low-temperature reactive ion etching and microwave plasma etching of silicon," *Applied physics letters*, vol. 52, no. 8, pp. 616–618, 1988.

[260] Z. Li, Y. Chen, X. Zhu, M. Zheng, F. Dong, P. Chen, L. Xu, W. Chu, and H. Duan, "Fabrication of single-crystal silicon nanotubes with sub-10 nm walls using cryogenic inductively coupled plasma reactive ion etching," *Nanotechnology*, vol. 27, no. 36, p. 365302, 2016.

[261] M. D. Henry, C. Welch, and A. Scherer, "Techniques of cryogenic reactive ion etching in silicon for fabrication of sensors," *Journal of Vacuum Science & Technology A: Vacuum, Surfaces, and Films*, vol. 27, no. 5, pp. 1211–1216, 2009.

[262] Y. Wu, D. Olynick, A. Goodyear, C. Peroz, S. Dhuey, X. Liang, and S. Cabrini, "Cryogenic etching of nano-scale silicon trenches with resist masks," *Microelectronic engineering*, vol. 88, no. 8, pp. 2785–2789, 2011.

[263] C. Welch, A. Goodyear, T. Wahlbrink, M. C. Lemme, and T. Mollenhauer, "Silicon etch process options for micro-and nanotechnology using inductively coupled plasmas," *Microelectronic Engineering*, vol. 83, no. 4-9, pp. 1170–1173, 2006.

[264] T. Tillocher, R. Dussart, L. J. Overzet, X. Mellhaoui, P. Lefaucheux, M. Boufnichel, and P. Ranson, "Two cryogenic processes involving sf6, o2, and sif4 for silicon deep etching," *Journal of The Electrochemical Society*, vol. 155, no. 3, p. D187, 2008.

[265] M. W. Pruessner, W. S. Rabinovich, T. H. Stievater, D. Park, and J. W. Baldwin, "Cryogenic etch process development for profile control of high aspect-ratio submicron silicon trenches," *Journal of Vacuum Science & Technology B: Microelectronics and Nanometer Structures Processing, Measurement, and Phenomena*, vol. 25, no. 1, pp. 21–28, 2007.

[266] I. W. Rangelow and H. Löschner, "Reactive ion etching for microelectrical mechanical system fabrication," *Journal of Vacuum Science & Technology B: Microelectronics and Nanometer Structures Processing, Measurement, and Phenomena*, vol. 13, no. 6, pp. 2394–2399, 1995.

[267] M. A. Lieberman and A. J. Lichtenberg, "Principles of plasma discharges and materials processing," *MRS Bulletin*, vol. 30, no. 12, pp. 899–901, 1994.

[268] S. Tachi, K. Tsujimoto, S. Arai, and T. Kure, "Low-temperature dry etching," *Journal of Vacuum Science & Technology A: Vacuum, Surfaces, and Films*, vol. 9, no. 3, pp. 796–803, 1991.

[269] C. B. Mullins and J. W. Coburn, "Ion-beam-assisted etching of si with fluorine at low temperatures," *Journal of applied physics*, vol. 76, no. 11, pp. 7562–7566, 1994.

[270] G. S. Oehrlein and Y. Kurogi, "Sidewall surface chemistry in directional etching processes," *Materials Science and Engineering: R: Reports*, vol. 24, no. 4, pp. 153–183, 1998.

[271] R. Dussart, T. Tillocher, P. Lefaucheux, and M. Boufnichel, "Plasma cryogenic etching of silicon: from the early days to today's advanced technologies," *Journal of Physics D: Applied Physics*, vol. 47, no. 12, p. 123001, 2014.

[272] V. Clericò, J. A. Delgado-Notario, M. Saiz-Bretín, A. V. Malyshev, Y. M. Meziani, P. Hidalgo, B. Méndez, M. Amado, F. Domínguez-Adame, and E. Diez, "Quantum nanoconstrictions fabricated by cryo-etching in encapsulated graphene," *Scientific Reports*, vol. 9, no. 1, p. 13572, 2019.

[273] Ü. Sökmen, A. Stranz, S. Fündling, S. Merzsch, R. Neumann, H.-H. Wehmann, E. Peiner, and A. Waag, "Shallow and deep dry etching of silicon using icp cryogenic reactive ion etching process," *Microsystem technologies*, vol. 16, pp. 863–870, 2010.

[274] M. Boufnichel, P. Lefaucheux, S. Aachboun, R. Dussart, and P. Ranson, "Origin, control and elimination of undercut in silicon deep plasma etching in the cryogenic process," *Microelectronic Engineering*, vol. 77, no. 3-4, pp. 327–336, 2005.

[275] K. A. Addae-Mensah, S. Retterer, S. R. Opalenik, D. Thomas, N. V. Lavrik, and J. P. Wikswo, "Cryogenic etching of silicon: an alternative method for fabrication of vertical microcantilever master molds," *Journal of microelectromechanical systems*, vol. 19, no. 1, pp. 64–74, 2009.

[276] K. Keskinbora, C. Grévent, M. Bechtel, M. Weigand, E. Goering, A. Nadzeyka, L. Peto, S. Rehbein, G. Schneider, R. Follath, *et al.*, "Ion beam lithography for fresnel zone plates in x-ray microscopy," *Optics Express*, vol. 21, no. 10, pp. 11747–11756, 2013.

[277] F. Uhlén, D. Nilsson, J. Rahomäki, L. Belova, C. G. Schroer, F. Seiboth, A. Holmberg, H. M. Hertz, and U. Vogt, "Nanofabrication of tungsten zone plates with integrated platinum central stop for hard x-ray applications," *Microelectronic Engineering*, vol. 116, pp. 40–43, 2014.

[278] A. M. Kamto Tegueu, *Fabrication and reliability testing of copper-filled through-silicon vias for three-dimensional chip stacking applications*. PhD thesis, University of Alabama Libraries, 2010.

[279] A. Campo, C. Cardinaud, and G. Turban, "Investigation of si and ge etching mech-

anisms in radiofrequency cf2-o2 plasma based on surface reactivities," *Plasma Sources Science and Technology*, vol. 4, no. 3, p. 398, 1995.

[280] G. S. Oehrlein, S. W. Robey, and J. L. Lindström, "Surface processes in cf4/o2 reactive etching of silicon," *Applied physics letters*, vol. 52, no. 14, pp. 1170–1172, 1988.

[281] K. Ninomiya, K. Suzuki, S. Nishimatsu, and O. Okada, "Role of sulfur atoms in microwave plasma etching of silicon," *Journal of applied physics*, vol. 62, no. 4, pp. 1459–1468, 1987.

[282] M. V. Pugachev, A. I. Duleba, A. A. Galiullin, and A. Y. Kuntsevich, "Micro-mask lithography for cheap and fast 2D materials microstructures fabrication," *Micromachines (Basel)*, vol. 12, p. 850, July 2021.

[283] M. S. Khan, R. lachmayer, and B. Roth, "Maskless lithography for versatile and low cost fabrication of polymer based micro optical structures," *OSA Continuum*, vol. 3, pp. 2808–2816, Oct 2020.

[284] Y. X. Zhou, A. T. Johnson, J. Hone, and W. F. Smith, "Simple fabrication of molecular circuits by shadow mask evaporation," *Nano Lett.*, vol. 3, pp. 1371–1374, Oct. 2003.

[285] D. H. Tien, J.-Y. Park, K. B. Kim, N. Lee, and Y. Seo, "Characterization of graphene-based FET fabricated using a shadow mask," *Sci. Rep.*, vol. 6, p. 25050, May 2016.

[286] W. Bao, G. Liu, Z. Zhao, H. Zhang, D. Yan, A. Deshpande, B. LeRoy, and C. N. Lau, "Lithography-free fabrication of high quality substrate-supported and freestanding graphene devices," *Nano Res.*, vol. 3, pp. 98–102, Feb. 2010.

[287] H. Yun, S. Kim, H. Kim, J. Lee, K. McAllister, J. Kim, S. Pyo, J. Sung Kim, E. E. B. Campbell, W. Hyoung Lee, and S. Wook Lee, "Stencil nano lithography based on a nanoscale polymer shadow mask: towards organic nanoelectronics," *Sci. Rep.*, vol. 5, p. 10220, May 2015.

[288] J. Liang, K. Xu, B. Toncini, B. Bersch, B. Jariwala, Y.-C. Lin, J. Robinson, and S. K. Fullerton-Shirey, "Impact of post-lithography polymer residue on the electrical characteristics of MoS_2 and WSe_2 field effect transistors," *Adv. Mater. Interfaces*, vol. 6, p. 1801321, Feb. 2019.

[289] X. Shen, H. Wang, and T. Yu, "How do the electron beam writing and metal deposition affect the properties of graphene during device fabrication?," *Nanoscale*, vol. 5, pp. 3352–3358, 2013.

[290] Y. Katagiri, T. Nakamura, A. Ishii, C. Ohata, M. Hasegawa, S. Katsumoto, T. Cusati, A. Fortunelli, G. Iannaccone, G. Fiori, S. Roche, and J. Haruyama, "Gate-tunable atomically thin lateral MoS_2 schottky junction patterned by electron beam," *Nano Lett.*, vol. 16, pp. 3788–3794, June 2016.

[291] Y. Cao, A. Mishchenko, G. L. Yu, E. Khestanova, A. P. Rooney, E. Prestat, A. V. Kretinin, P. Blake, M. B. Shalom, C. Woods, J. Chapman, G. Balakrishnan, I. V. Grigorieva, K. S. Novoselov, B. A. Piot, M. Potemski, K. Watanabe, T. Taniguchi, S. J. Haigh, A. K. Geim, and R. V. Gorbachev, "Quality heterostructures from two-dimensional crystals unstable in air by their assembly in inert atmosphere," *Nano Lett.*, vol. 15, pp. 4914–4921, Aug. 2015.

[292] A. Castellanos-Gomez, L. Vicarelli, E. Prada, J. O. Island, K. L. Narasimha-Acharya, S. I. Blanter, D. J. Groenendijk, M. Buscema, G. A. Steele, J. V. Alvarez, H. W. Zandbergen, J. J. Palacios, and H. S. J. van der Zant, "Isolation and characterization of few-layer black phosphorus," *2d Mater.*, vol. 1, p. 025001, June 2014.

[293] M. Aljada, K. Mutkins, G. Vamvounis, P. Burn, and P. Meredith, "High quality shadow masks for top contact organic field effect transistors using deep reactive ion etching," *J. Micromech. Microeng.*, vol. 20, p. 075037, July 2010.

[294] H. Zhang, X. Guo, W. Niu, H. Xu, Q. Wu, F. Liao, J. Chen, H. Tang, H. Liu, Z. Xu, Z. Sun, Z. Qiu, Y. Pu, and W. Bao, "Multilayer si shadow mask processing of wafer-scale MoS2 devices," *2d Mater.*, vol. 7, p. 025019, Feb. 2020.

[295] C.-W. Tsao and P.-C. Shen, "Maskless patterning of metal nanoparticles and silicon nanostructures by a droplet deposition and etching process," *Materials Advances*, vol. 4, no. 24, pp. 6730–6740, 2023.

[296] H. J. Ma, Y.-J. Park, M.-J. Kim, H.-N. Kim, J.-W. Ko, J.-W. Lee, J.-H. Kim, and H.-C. Lee, "Physiochemical etching characteristics and surface analysis of y2o3-mgo nanocomposite under different cf4/ar/o2 plasma atmospheres," *Applied Surface Science*, vol. 641, p. 158483, 2023.

[297] M. Tomczyk, P. Kubik, and W. Waliszewski, "Optimization of the ablative laser cutting of shadow mask for organic FET electrode fabrication," *Electronics (Basel)*, vol. 9, p. 2184, Dec. 2020.

[298] F. Elhami Nik, I. Matthiesen, A. Herland, and T. E. Winkler, "Low-cost PVD shadow masks with submillimeter resolution from laser-cut paper," *Micromachines (Basel)*, vol. 11, p. 676, July 2020.

[299] S. Manzeli, D. Ovchinnikov, D. Pasquier, O. V. Yazyev, and A. Kis, "2d transition metal dichalcogenides," *Nature Reviews Materials*, vol. 2, no. 8, pp. 1–15, 2017.

[300] A. Splendiani, L. Sun, Y. Zhang, T. Li, J. Kim, C.-Y. Chim, G. Galli, and F. Wang, "Emerging photoluminescence in monolayer mos2," *Nano letters*, vol. 10, no. 4, pp. 1271–1275, 2010.

[301] D. A. Chenet, B. Aslan, P. Y. Huang, C. Fan, A. M. Van Der Zande, T. F. Heinz, and J. C. Hone, "In-plane anisotropy in mono-and few-layer res2 probed by raman spectroscopy and scanning transmission electron microscopy," *Nano letters*, vol. 15, no. 9, pp. 5667–5672, 2015.

[302] J. Wang, Y. J. Zhou, D. Xiang, S. J. Ng, K. Watanabe, T. Taniguchi, and G. Eda, "Polarized light-emitting diodes based on anisotropic excitons in few-layer ReS2," *Adv. Mater.*, vol. 32, p. e2001890, Aug. 2020.

[303] B. Aslan, D. A. Chenet, A. M. Van Der Zande, J. C. Hone, and T. F. Heinz, "Linearly polarized excitons in single-and few-layer res2 crystals," *Acs Photonics*, vol. 3, no. 1, pp. 96–101, 2015.

[304] K. P. Dhakal, E. Lee, T. V. Anh, G. Ghimire, W. Choi, Y.-M. Kim, D. L. Duong, and J. Kim, "Investigation of exciton states of res2 by temperature-and polarization-dependent photoluminescence and oxygen plasma treatment," *Applied Surface Science*, vol. 638, p. 158093, 2023.

[305] S. Ojo, J. Onasanya, M. Benamara, B. Hamad, and M. Manasreh, "Optical spectroscopy of excitons in res2 monolayers grown by chemical vapor deposition," *Optical Materials*, p. 116729, 2025.

[306] M. Gehlmann, I. Aguilera, G. Bihlmayer, S. Nemšák, P. Nagler, P. Gospodaric, G. Zamborlini, M. Eschbach, V. Feyer, F. Kronast, *et al.*, "Direct observation of the band gap transition in atomically thin res2," *Nano letters*, vol. 17, no. 9, pp. 5187–5192, 2017.

[307] X. Su, B. Zhang, Y. Wang, G. He, G. Li, N. Lin, K. Yang, J. He, and S. Liu, "Broadband rhenium disulfide optical modulator for solid-state lasers," *Photonics Research*, vol. 6, no. 6, pp. 498–505, 2018.

[308] Y. Zhou, N. Maity, A. Rai, R. Juneja, X. Meng, A. Roy, Y. Zhang, X. Xu, J.-F. Lin, S. K. Banerjee, *et al.*, "Stacking-order-driven optical properties and carrier dynamics in res2," *Advanced Materials*, vol. 32, no. 22, p. 1908311, 2020.

[309] Y. Zhou, N. Maity, J.-F. Lin, A. K. Singh, and Y. Wang, "Nonlinear optical absorption of res2 driven by stacking order," *ACS Photonics*, vol. 8, no. 2, pp. 405–411, 2021.

[310] C. Ho, Y. Huang, and K. Tiong, "In-plane anisotropy of the optical and electrical properties of res2 and rese2 layered crystals," *Journal of alloys and compounds*, vol. 317, pp. 222–226, 2001.

[311] Z. Zhou, Y. Cui, P.-H. Tan, X. Liu, and Z. Wei, "Optical and electrical properties of two-dimensional anisotropic materials," *Journal of Semiconductors*, vol. 40, no. 6, p. 061001, 2019.

[312] X. Meng, Y. Zhou, K. Chen, R. H. Roberts, W. Wu, J.-F. Lin, R. T. Chen, X. Xu,

and Y. Wang, "Anisotropic saturable and excited-state absorption in bulk res2," *Advanced Optical Materials*, vol. 6, no. 14, p. 1800137, 2018.

[313] F. Mooshammer, S. Chae, S. Zhang, Y. Shao, S. Qiu, A. Rajendran, A. J. Sternbach, D. J. Rizzo, X. Zhu, P. J. Schuck, *et al.*, "In-plane anisotropy in biaxial res2 crystals probed by nano-optical imaging of waveguide modes," *ACS Photonics*, vol. 9, no. 2, pp. 443–451, 2022.

[314] P. Littlewood, "Semiconductors: Exciton theory," in *Encyclopedia of Condensed Matter Physics (Second Edition)* (T. Chakraborty, ed.), pp. 418–426, Oxford: Academic Press, second edition ed., 2024.

[315] G. Froehlicher, E. Lorchat, and S. Berciaud, "Direct versus indirect band gap emission and exciton-exciton annihilation in atomically thin molybdenum ditelluride (mote 2)," *Physical Review B*, vol. 94, no. 8, p. 085429, 2016.

[316] D. Vaquero, O. Arroyo-Gascón, J. Salvador-Sánchez, P. L. Alcázar-Ruano, E. Diez, A. Perez-Rodríguez, J. D. Correa, F. Dominguez-Adame, L. Chico, and J. Quereda, "Polarization-tuneable excitonic spectral features in the optoelectronic response of atomically thin ReS_2," *2d Mater.*, vol. 11, p. 015011, Jan. 2024.

[317] D. Vaquero, V. Clericò, J. Salvador-Sánchez, A. Martín-Ramos, E. Díaz, F. Domínguez-Adame, Y. M. Meziani, E. Diez, and J. Quereda, "Excitons, trions and rydberg states in monolayer mos2 revealed by low-temperature photocurrent spectroscopy," *Communications Physics*, vol. 3, no. 1, p. 194, 2020.

[318] D. Vaquero, J. Salvador-Sánchez, V. Clericò, E. Diez, and J. Quereda, "The low-temperature photocurrent spectrum of monolayer mose2: Excitonic features and gate voltage dependence," *Nanomaterials*, vol. 12, no. 3, p. 322, 2022.

[319] C.-H. Ho and Z.-Z. Liu, "Complete-series excitonic dipole emissions in few layer res2 and rese2 observed by polarized photoluminescence spectroscopy," *Nano Energy*, vol. 56, pp. 641–650, 2019.

[320] J. Jadczak, J. Kutrowska-Girzycka, T. Smoleński, P. Kossacki, Y. Huang, and L. Bryja, "Exciton binding energy and hydrogenic rydberg series in layered res 2," *Scientific reports*, vol. 9, no. 1, p. 1578, 2019.

[321] P. Schiettecatte, D. Poonia, I. Tanghe, S. Maiti, M. Failla, S. Kinge, Z. Hens, L. D. Siebbeles, and P. Geiregat, "Unraveling the photophysics of liquid-phase exfoliated two-dimensional res2 nanoflakes," *The Journal of Physical Chemistry C*, vol. 125, no. 38, pp. 20993–21002, 2021.

[322] A.-J. Cho, S. D. Namgung, H. Kim, and J.-Y. Kwon, "Electric and photovoltaic characteristics of a multi-layer res2/rese2 heterostructure," *APL Materials*, vol. 5, p. 076101, 07 2017.

[323] M. Ramos, T. Ahmed, B. Q. Tu, E. Chatzikyriakou, L. Olano-Vegas, B. Martín-García, M. R. Calvo, S. S. Tsirkin, I. Souza, F. Casanova, *et al.*, "Unveiling intrinsic bulk photovoltaic effect in atomically thin res2," *Nano Letters*, vol. 24, no. 46, pp. 14728–14735, 2024.

[324] Z. Fei, W. Zhao, T. A. Palomaki, B. Sun, M. K. Miller, Z. Zhao, J. Yan, X. Xu, and D. H. Cobden, "Ferroelectric switching of a two-dimensional metal," *Nature*, vol. 560, no. 7718, pp. 336–339, 2018.

[325] H. Han, Y. Kim, M. Alexe, D. Hesse, and W. Lee, "Nanostructured ferroelectrics: fabrication and structure–property relations," *Advanced Materials*, vol. 23, no. 40, pp. 4599–4613, 2011.

[326] L. Zhang, M. Liu, and A. Du, "Theoretical exploration and design of low-dimensional ferroelectrics," *Computational Materials Science*, vol. 233, p. 112724, 2024.

[327] S. Li, F. Wang, Y. Wang, J. Yang, X. Wang, X. Zhan, J. He, and Z. Wang, "Van der waals ferroelectrics: Theories, materials, and device applications," *Advanced Materials*, vol. 36, no. 22, p. 2301472, 2024.

[328] W. Niu, G. Ding, Z. Jia, X.-Q. Ma, J. Zhao, K. Zhou, S.-T. Han, C.-C. Kuo, and

Y. Zhou, "Recent advances in memristors based on two-dimensional ferroelectric materials," *Frontiers of Physics*, vol. 19, no. 1, p. 13402, 2024.

[329] C. Wang, L. You, D. Cobden, and J. Wang, "Towards two-dimensional van der waals ferroelectrics," *Nature Materials*, vol. 22, no. 5, pp. 542–552, 2023.

[330] M. Vizner Stern, Y. Waschitz, W. Cao, I. Nevo, K. Watanabe, T. Taniguchi, E. Sela, M. Urbakh, O. Hod, and M. Ben Shalom, "Interfacial ferroelectricity by van der waals sliding," *Science*, vol. 372, no. 6549, pp. 1462–1466, 2021.

[331] K. Yasuda, X. Wang, K. Watanabe, T. Taniguchi, and P. Jarillo-Herrero, "Stacking-engineered ferroelectricity in bilayer boron nitride," *Science*, vol. 372, no. 6549, pp. 1458–1462, 2021.

[332] Y. Wan, T. Hu, X. Mao, J. Fu, K. Yuan, Y. Song, X. Gan, X. Xu, M. Xue, X. Cheng, *et al.*, "Room-temperature ferroelectricity in 1 t -res 2 multilayers," *Physical Review Letters*, vol. 128, no. 6, p. 067601, 2022.

[333] V. B. Mbayachi, E. Ndayiragije, T. Sammani, S. Taj, E. R. Mbuta, *et al.*, "Graphene synthesis, characterization and its applications: A review," *Results in Chemistry*, vol. 3, p. 100163, 2021.

[334] Y. Huang, Y.-H. Pan, R. Yang, L.-H. Bao, L. Meng, H.-L. Luo, Y.-Q. Cai, G.-D. Liu, W.-J. Zhao, Z. Zhou, *et al.*, "Universal mechanical exfoliation of large-area 2d crystals," *Nature communications*, vol. 11, no. 1, p. 2453, 2020.

[335] Y. Li, G. Kuang, Z. Jiao, L. Yao, and R. Duan, "Recent progress on the mechanical exfoliation of 2d transition metal dichalcogenides," *Materials Research Express*, vol. 9, no. 12, p. 122001, 2022.

[336] Y. Niu, S. Gonzalez-Abad, R. Frisenda, P. Marauhn, M. Drüppel, P. Gant, R. Schmidt, N. S. Taghavi, D. Barcons, A. J. Molina-Mendoza, *et al.*, "Thickness-dependent differential reflectance spectra of monolayer and few-layer mos2, mose2, ws2 and wse2," *Nanomaterials*, vol. 8, no. 9, p. 725, 2018.

[337] M.-L. Lin and P.-H. Tan, "Ultralow-frequency raman spectroscopy of two-dimensional materials," *Raman Spectroscopy of Two-Dimensional Materials*, pp. 203–230, 2019.

[338] J.-B. Wu, M.-L. Lin, X. Cong, H.-N. Liu, and P.-H. Tan, "Raman spectroscopy of graphene-based materials and its applications in related devices," *Chemical Society Reviews*, vol. 47, no. 5, pp. 1822–1873, 2018.

[339] A. Jorio, M. S. Dresselhaus, R. Saito, and G. Dresselhaus, *Raman spectroscopy in graphene related systems*. John Wiley & Sons, 2011.

[340] P. Tan, W. Han, W. Zhao, Z. Wu, K. Chang, H. Wang, Y. Wang, N. Bonini, N. Marzari, N. Pugno, *et al.*, "The shear mode of multilayer graphene," *Nature materials*, vol. 11, no. 4, pp. 294–300, 2012.

[341] H.-N. Liu, X. Cong, M.-L. Lin, and P.-H. Tan, "The intrinsic temperature-dependent raman spectra of graphite in the temperature range from 4k to 1000k," *Carbon*, vol. 152, pp. 451–458, 2019.

[342] N. Bonini, M. Lazzeri, N. Marzari, and F. Mauri, "Phonon anharmonicities in graphite and graphene," *Physical review letters*, vol. 99, no. 17, p. 176802, 2007.

[343] S. Pisana, M. Lazzeri, C. Casiraghi, K. S. Novoselov, A. K. Geim, A. C. Ferrari, and F. Mauri, "Breakdown of the adiabatic born–oppenheimer approximation in graphene," *Nature materials*, vol. 6, no. 3, pp. 198–201, 2007.

[344] R. Beams, L. G. Cançado, and L. Novotny, "Raman characterization of defects and dopants in graphene," *Journal of Physics: Condensed Matter*, vol. 27, no. 8, p. 083002, 2015.

[345] J.-U. Lee, S. Woo, J. Park, H. C. Park, Y.-W. Son, and H. Cheong, "Strain-shear coupling in bilayer mos2," *Nature communications*, vol. 8, no. 1, p. 1370, 2017.

[346] T. Mohiuddin, A. Lombardo, R. Nair, A. Bonetti, G. Savini, R. Jalil, N. Bonini, D. Basko, C. Galiotis, N. Marzari, *et al.*, "Uniaxial strain in graphene by raman spectroscopy: G peak splitting, grüneisen parameters, and sample orientation,"

Physical Review B—Condensed Matter and Materials Physics, vol. 79, no. 20, p. 205433, 2009.

[347] T. Lin, X. Cong, M.-L. Lin, X.-L. Liu, and P.-H. Tan, "The phonon confinement effect in two-dimensional nanocrystals of black phosphorus with anisotropic phonon dispersions," *Nanoscale*, vol. 10, no. 18, pp. 8704–8711, 2018.

[348] W. Shi, X. Zhang, X.-L. Li, X.-F. Qiao, J.-B. Wu, J. Zhang, and P.-H. Tan, "Phonon confinement effect in two-dimensional nanocrystallites of monolayer mos2 to probe phonon dispersion trends away from brillouin-zone center," *Chinese Physics Letters*, vol. 33, no. 5, p. 057801, 2016.

[349] W. Shi, M.-L. Lin, Q.-H. Tan, X.-F. Qiao, J. Zhang, and P.-H. Tan, "Raman and photoluminescence spectra of two-dimensional nanocrystallites of monolayer ws2 and wse2," *2D Materials*, vol. 3, no. 2, p. 025016, 2016.

[350] A. Merlen, J. G. Buijnsters, and C. Pardanaud, "A guide to and review of the use of multiwavelength raman spectroscopy for characterizing defective aromatic carbon solids: From graphene to amorphous carbons," *Coatings*, vol. 7, no. 10, p. 153, 2017.

[351] T. Ando, "Magnetic oscillation of optical phonon in graphene," *Journal of the Physical Society of Japan*, vol. 76, no. 2, pp. 024712–024712, 2007.

[352] M. Goerbig, J.-N. Fuchs, K. Kechedzhi, and V. I. Fal'ko, "Filling-factor-dependent magnetophonon resonance in graphene," *Physical review letters*, vol. 99, no. 8, p. 087402, 2007.

[353] A. C. Ferrari and D. M. Basko, "Raman spectroscopy as a versatile tool for studying the properties of graphene," *Nature nanotechnology*, vol. 8, no. 4, pp. 235–246, 2013.

[354] X. Cong, Q.-Q. Li, X. Zhang, M.-L. Lin, J.-B. Wu, X.-L. Liu, P. Venezuela, and P.-H. Tan, "Probing the acoustic phonon dispersion and sound velocity of graphene by raman spectroscopy," *Carbon*, vol. 149, pp. 19–24, 2019.

[355] X. Cong, J.-B. Wu, M.-L. Lin, X.-L. Liu, W. Shi, P. Venezuela, and P.-H. Tan, "Stokes and anti-stokes raman scattering in mono-and bilayer graphene," *Nanoscale*, vol. 10, no. 34, pp. 16138–16144, 2018.

[356] M.-L. Lin, Q.-H. Tan, J.-B. Wu, X.-S. Chen, J.-H. Wang, Y.-H. Pan, X. Zhang, X. Cong, J. Zhang, W. Ji, *et al.*, "Moiré phonons in twisted bilayer mos2," *Acs Nano*, vol. 12, no. 8, pp. 8770–8780, 2018.

[357] C. Lee, H. Yan, L. E. Brus, T. F. Heinz, J. Hone, and S. Ryu, "Anomalous lattice vibrations of single-and few-layer mos2," *ACS nano*, vol. 4, no. 5, pp. 2695–2700, 2010.

[358] X.-F. Qiao, J.-B. Wu, L. Zhou, J. Qiao, W. Shi, T. Chen, X. Zhang, J. Zhang, W. Ji, and P.-H. Tan, "Polytypism and unexpected strong interlayer coupling in two-dimensional layered res 2," *Nanoscale*, vol. 8, no. 15, pp. 8324–8332, 2016.

[359] T. Wen, J. Li, M. Zhang, C. Jiao, S. Pei, Z. Wang, and J. Xia, "Discerning the vibrational nature of res2 raman modes using solid-angle-resolved raman spectroscopy," *ACS Photonics*, vol. 9, no. 11, pp. 3557–3562, 2022.

[360] Y. Feng, W. Zhou, Y. Wang, J. Zhou, E. Liu, Y. Fu, Z. Ni, X. Wu, H. Yuan, F. Miao, *et al.*, "Raman vibrational spectra of bulk to monolayer re s 2 with lower symmetry," *Physical Review B*, vol. 92, no. 5, p. 054110, 2015.

[361] H. Li, D.-Y. Lin, A. Di Renzo, S. Puebla, R. Frisenda, X. Gan, J. Quereda, Y. Xie, A. M. Al-Enizi, A. Nafady, *et al.*, "Stretching res2 along different crystal directions: Anisotropic tuning of the vibrational and optical responses," *Applied Physics Letters*, vol. 120, no. 6, 2022.

[362] P. A. Markeev, E. Najafidehaghani, Z. Gan, K. Sotthewes, A. George, A. Turchanin, and M. P. de Jong, "Energy-level alignment at interfaces between transition-metal dichalcogenide monolayers and metal electrodes studied with kelvin probe force microscopy," *The Journal of Physical Chemistry C*, vol. 125, no. 24, pp. 13551–13559, 2021.

[363] C. Wang, Y. Zhang, D. Zhang, Y. Sun, T. Zhang, and J. Li, "2d van der waals sliding ferroelectrics toward novel electronic devices," *Small*, p. 2408375, 2025.

[364] S. Du, J. Liu, and S. Zheng, "Emerging optoelectronic applications of sliding ferroelectricity," *Advanced Materials Technologies*, p. 2402121.

[365] X. Zheng, A. Calò, T. Cao, X. Liu, Z. Huang, P. M. Das, M. Drndic, E. Albisetti, F. Lavini, T.-D. Li, *et al.*, "Spatial defects nanoengineering for bipolar conductivity in mos2," *Nature communications*, vol. 11, no. 1, p. 3463, 2020.

[366] W. Su, N. Kumar, H. Shu, O. Lancry, and M. Chaigneau, "In situ visualization of optoelectronic behavior of grain boundaries in monolayer wse2 at the nanoscale," *The Journal of Physical Chemistry C*, vol. 125, no. 48, pp. 26883–26891, 2021.

[367] S. Deb, J. Krause, P. E. Faria Junior, M. A. Kempf, R. Schwartz, K. Watanabe, T. Taniguchi, J. Fabian, and T. Korn, "Excitonic signatures of ferroelectric order in parallel-stacked mos2," *Nature Communications*, vol. 15, no. 1, p. 7595, 2024.

[368] M. Checa, S. M. Neumayer, W.-Y. Tsai, and L. Collins, "Advanced modes of electrostatic and kelvin probe force microscopy for energy applications," in *Atomic Force Microscopy for Energy Research*, pp. 45–104, CRC Press, 2022.

[369] M. Checa, A. S. Fuhr, C. Sun, R. Vasudevan, M. Ziatdinov, I. Ivanov, S. J. Yun, K. Xiao, A. Sehirlioglu, Y. Kim, *et al.*, "High-speed mapping of surface charge dynamics using sparse scanning kelvin probe force microscopy," *Nature Communications*, vol. 14, no. 1, p. 7196, 2023.

[370] N. Zhou, R. Wang, X. Zhou, H. Song, X. Xiong, Y. Ding, J. Lü, L. Gan, and T. Zhai, "P-gase/n-mos2 vertical heterostructures synthesized by van der waals epitaxy for photoresponse modulation," *Small*, vol. 14, no. 7, p. 1702731, 2018.

[371] J. Yu, R. Giridharagopal, Y. Li, K. Xie, J. Li, T. Cao, X. Xu, and D. S. Ginger, "Imaging graphene moiré superlattices via scanning kelvin probe microscopy," *Nano Letters*, vol. 21, no. 7, pp. 3280–3286, 2021.

[372] J. Liang, D. Yang, Y. Xiao, S. Chen, J. I. Dadap, J. Rottler, and Z. Ye, "Shear strain-induced two-dimensional slip avalanches in rhombohedral mos2," *Nano Letters*, vol. 23, no. 15, pp. 7228–7235, 2023.

[373] J. Liang, D. Yang, J. Wu, J. I. Dadap, K. Watanabe, T. Taniguchi, and Z. Ye, "Optically probing the asymmetric interlayer coupling in rhombohedral-stacked mos 2 bilayer," *Physical Review X*, vol. 12, no. 4, p. 041005, 2022.

[374] F. Li, J. Qi, M. Xu, J. Xiao, Y. Xu, X. Zhang, S. Liu, and Y. Zhang, "Layer dependence and light tuning surface potential of 2d mos2 on various substrates," *Small*, vol. 13, no. 14, p. 1603103, 2017.

[375] R. Roldán, A. Castellanos-Gomez, E. Cappelluti, and F. Guinea, "Strain engineering in semiconducting two-dimensional crystals," *Journal of Physics: Condensed Matter*, vol. 27, no. 31, p. 313201, 2015.

[376] G. Plechinger, A. Castellanos-Gomez, M. Buscema, H. S. Van Der Zant, G. A. Steele, A. Kuc, T. Heine, C. Schueller, and T. Korn, "Control of biaxial strain in single-layer molybdenite using local thermal expansion of the substrate," *2D Materials*, vol. 2, no. 1, p. 015006, 2015.

[377] R. Xu, J. Guo, S. Mi, H. Wen, F. Pang, W. Ji, and Z. Cheng, "Advanced atomic force microscopies and their applications in two-dimensional materials: a review," *Materials Futures*, vol. 1, no. 3, p. 032302, 2022.

[378] S. J. Yoon, J. W. Kim, H. C. Kim, J. Kang, and J. Kim, "Thermal stress in flexible interdigital transducers with anisotropic electroactive cellulose substrates," *Journal of Physics D: Applied Physics*, vol. 50, no. 50, p. 505304, 2017.

[379] Z. Jiang and Y. Yuan, "Effects of particle size distribution of silica on properties of ptfe/sio2 composites," *Materials Research Express*, vol. 5, no. 6, p. 066306, 2018.

[380] T. Gray, "Thermal expansion for all the elements in the periodic table," 2025. Accessed: 2025-03-28.

[381] K. Ltd, "Linear thermal expansion of polycarbonate," 2025. Accessed: 2025-03-28.

[382] J. Haeni, P. Irvin, W. Chang, R. Uecker, P. Reiche, Y. Li, S. Choudhury, W. Tian, M. Hawley, B. Craigo, *et al.*, "Room-temperature ferroelectricity in strained srtio3," *Nature*, vol. 430, no. 7001, pp. 758–761, 2004.

[383] K. Lai, M. Nakamura, W. Kundhikanjana, M. Kawasaki, Y. Tokura, M. A. Kelly, and Z.-X. Shen, "Mesoscopic percolating resistance network in a strained manganite thin film," *Science*, vol. 329, no. 5988, pp. 190–193, 2010.

[384] S. Yu, H. Zhu, K. Eshun, C. Shi, M. Zeng, and Q. Li, "Strain-engineering the anisotropic electrical conductance in res2 monolayer," *Applied Physics Letters*, vol. 108, no. 19, 2016.

[385] Y. Zhao, Z. Du, L. Wang, M. Liu, B. Yao, X. Hu, L. Gao, F. Wu, C. Liu, X. Li, *et al.*, "Revealing the optical anisotropy of res2 nanostructures by strain engineering," *ACS Applied Nano Materials*, vol. 6, no. 11, pp. 9679–9686, 2023.

[386] L. Huang, F. Zheng, H. Chen, Q. H. Thi, X. Chen, H. Liu, C.-S. Lee, Q. Deng, J. Zhao, and T. H. Ly, "Mechanical origin of martensite-like structures in two-dimensional res2," *Communications Materials*, vol. 2, no. 1, p. 87, 2021.

[387] J. Jeong, H.-S. Kim, G. Kwon, K. Jeong, H. Lee, J. H. Lee, M. Park, C. Lee, S. Yu, H. Kim, *et al.*, "Ferroelastic–ferroelectric multiferroicity in van der waals rhenium dichalcogenides," *Advanced Materials*, vol. 34, no. 18, p. 2108777, 2022.

[388] Z. Zhou, B. Wei, C. He, Y. Min, C. Chen, L. Liu, and X. Wu, "Anisotropic raman scattering and mobility in monolayer 1td-res2 controlled by strain engineering," *Applied Surface Science*, vol. 404, pp. 276–281, 2017.

[389] C. Woods, P. Ares, H. Nevison-Andrews, M. Holwill, R. Fabregas, F. Guinea, A. Geim, K. Novoselov, N. Walet, and L. Fumagalli, "Charge-polarized interfacial superlattices in marginally twisted hexagonal boron nitride," *Nature communications*, vol. 12, no. 1, p. 347, 2021.

[390] S. Zhou, J. Chen, and J. H. Warner, "In situ atomic level studies of thermally controlled interlayer stacking shifts in 2d transition metal dichalcogenide bilayers," *Journal of Materials Research*, vol. 35, no. 11, pp. 1407–1416, 2020.

[391] N. Goyal, D. Mackenzie, V. Panchal, H. Jawa, O. Kazakova, D. H. Petersen, and S. Lodha, "Enhanced thermally aided memory performance using few-layer res2 transistors," *Applied Physics Letters*, vol. 116, no. 5, 2020.

[392] H. Rai, D. Thakur, A. Gadal, Z. Ye, V. Balakrishnan, and N. N. Gosvami, "Transforming friction: unveiling sliding-induced phase transitions in cvd-grown ws 2 monolayers under single-asperity sliding nanocontacts," *Nanoscale*, vol. 16, no. 14, pp. 7102–7109, 2024.

[393] F. Li, J. Fu, M. Xue, Y. Li, H. Zeng, E. Kan, T. Hu, and Y. Wan, "Room-temperature vertical ferroelectricity in rhenium diselenide induced by interlayer sliding," *Frontiers of Physics*, vol. 18, no. 5, p. 53305, 2023.

[394] L. Li and M. Wu, "Binary compound bilayer and multilayer with vertical polarizations: two-dimensional ferroelectrics, multiferroics, and nanogenerators," *ACS nano*, vol. 11, no. 6, pp. 6382–6388, 2017.

[395] M. Wu and J. Li, "Sliding ferroelectricity in 2d van der waals materials: Related physics and future opportunities," *Proceedings of the National Academy of Sciences*, vol. 118, no. 50, p. e2115703118, 2021.

[396] Q. Zhang, A. Solanki, K. Parida, D. Giovanni, M. Li, T. L. Jansen, M. S. Pshenichnikov, and T. C. Sum, "Tunable ferroelectricity in ruddlesden–popper halide perovskites," *ACS applied materials & interfaces*, vol. 11, no. 14, pp. 13523–13532, 2019.

[397] A. J. Winchester, T. J. Anderson, J. K. Hite, R. E. Elmquist, and S. Pookpanratana, "Methodology and implementation of a tunable deep-ultraviolet laser source for photoemission electron microscopy," *Ultramicroscopy*, vol. 253, p. 113819, 2023.

[398] P. Winkler, *In situ correlative microscopy of hydrogen oxidation on rhodium-based model catalysts*. PhD thesis, Technische Universität Wien, 2022.

[399] R. Hönig, P. Roese, K. Shamout, T. Ohkochi, U. Berges, and C. Westphal, "Structural, chemical, and magnetic properties of cobalt intercalated graphene on silicon carbide," *Nanotechnology*, vol. 30, no. 2, p. 025702, 2018.

[400] P. Meng, Y. Wu, R. Bian, E. Pan, B. Dong, X. Zhao, J. Chen, L. Wu, Y. Sun, Q. Fu, *et al.*, "Sliding induced multiple polarization states in two-dimensional ferroelectrics," *Nature Communications*, vol. 13, no. 1, p. 7696, 2022.